Imperial College London
Department of Mathematics

Dynamical Description of Spatio-temporally Varying Turbulent Energy Cascades

Henrik Stumberg Larssen
January 2023

Submitted in part fulfilment of the requirements
for the degree of Doctor of Philosophy in Mathematics of
Imperial College London

I certify that all work presented in this thesis is my own and that all other contributions have been appropriately referenced and acknowledged.

The copyright of this thesis rests with the author. Unless otherwise indicated, its contents are licensed under a Creative Commons Attribution-Non Commercial 4.0 International Licence (CC BY-NC). Under this licence, you may copy and redistribute the material in any medium or format. You may also create and distribute modified versions of the work. This is on the condition that: you credit the author and do not use it, or any derivative works, for a commercial purpose. When reusing or sharing this work, ensure you make the licence terms clear to others by naming the licence and linking to the licence text. Where a work has been adapted, you should indicate that the work has been changed and describe those changes. Please seek permission from the copyright holder for uses of this work that are not included in this licence or permitted under UK Copyright Law.

For Elisa

Abstract

The spatio-temporally varying turbulent energy cascade dynamics in forced homogeneous/periodic turbulence is investigated with direct numerical simulations (DNS) and Helmholtz decompositions. The local in space and time cascade dynamics vastly differs from its spatio-temporal average manifestation. At scales larger than the Taylor scale, the solenoidal interscale transfer at most locations at most times increases or decreases the energy at the given scale in the frame moving with larger scales, i.e. Lagrangian transport. The solenoidal interscale transfer derives from the non-local in space vortex stretching/compression and tilting effects of its spatial vicinity. The irrotational cascade dynamics reduces to an exact balance between irrotational transport, irrotational interscale transfer and pressure-velocity. The typical fluctuations of these processes vastly exceed their spatio-temporal average values and the typical dissipation fluctuations.

At scales below the Taylor scale, viscous effects increase in importance in the solenoidal dynamics. At the Kolmogorov scale solenoidal interscale transfer, Lagrangian transport and viscous effects are all important. In regions of low and moderate small-scale energy, and to a somewhat lesser extent in regions of high small-scale energy, there is rarely a local balance between interscale transfer and viscous effects. Lagrangian transport acts as a non-local in time and space link between interscale transfer and viscous effects.

The spatially-averaged manifestation of the local cascade dynamics is an unsteady and approximately unidirectional energy cascade, which can be approximated with a hypothesis connecting the present interscale transfer with the future dissipation. The hypothesis can be used to develop non-equilibrium corrections to the low-pass filtered dynamics and second-order structure function scaling consistent with DNSs. We use the phenomenology of a time-lagged energy cascade to motivate a new redistributive dissipation scaling. The non-equilibrium dissipation scaling typically reduces to the redistributive dissipation scaling at low and moderate Reynolds numbers.

Acknowledgements

First and foremost I thank my supervisor for his outstanding guidance during these years. Prof. Christos Vassilicos' knowledge of turbulence helped sort the good ideas from the bad and ugly ideas. His attitude towards science and turbulence inspired me to always learn more and to reach for the highest standards. I thank Dr Mehrnaz Anvari for her guidance on our project on turbulence and information theory (which unfortunately did not bear fruits). I am also grateful to Prof. Bjørnar Pettersen for sharing his knowledge and enthusiasm and for encouraging me to pursue turbulence research.

I would like to acknowledge funding from the EPSRC-funded Centre for Doctoral Training in Fluid Dynamics across Scales to whom I am incredibly grateful. I am also thankful to Engys LTD and Dr Eugene de Villiers for employing me in my MRes year, making me eligible for the EPSRC funding. I also express my gratitude to Clodagh Li for her support throughout my time at Imperial. A word of appreciation to Lånekassen for their generous and sustained support over the years.

I am thankful to my CDT colleagues and friends Lorna, Ali, Geraldine, Sophia, James, Andy and Sam, who quickly made me feel welcome in London and at Imperial. I am especially thankful to Ali for our many discussions. Thanks to Daniel, Even, Magnus and Simen for accepting me as the quirky one in your midst and for affording me welcome breaks from the PhD.

I wish to thank my brother and parents for supporting me in pursuing my dreams. Their interest and pride in my (or rather our) achievements have always been a motivation.

Finally, I am forever indebted to my wonderful wife Elisa for supporting me through this PhD. You have kept me steady and provided invaluable breathing space and perspectives during these hectic years. Thank you for your sacrifices, encouragement and patience which allowed me to write this PhD thesis.

Contents

Abstract **5**

Acknowledgements **7**

Table of Contents **9**

Nomenclature **11**

List of Figures **15**

List of Tables **17**

1 Introduction **19**
1.1 An Overview of Classical Turbulence Theory 20
1.2 Real Turbulence Compared to K41 Turbulence 23
1.3 Thesis Objectives and Outline 25

2 Numerical Methodology **27**
2.1 Solver Description 28
2.1.1 A Pseudospectral Method for the Vorticity Equation 28
2.1.2 Large-scale Body Forcings 31
2.1.3 Initial Conditions 32
2.1.4 Temporal Evolution 33
2.1.5 In-situ Processing and Output 34
2.2 Numerical Setup 36
2.2.1 Resolution Requirements and Large-scale Periodicity 36
2.2.2 DNS Data Description 36
2.3 KHMH Post-processing 38

3 Interscale and Interspace Energy Transfer Dynamics in Homogeneous Turbulence **43**
3.1 Helmholtz Decomposition of Two-point Navier-Stokes Dynamics and Corresponding Turbulent Energy Exchanges 45
3.1.1 Solenoidal and Irrotational Acceleration Fluctuations 46

3.1.2 From One-point to Two-point Navier-Stokes Dynamics 50
3.1.3 Interscale Transfer and Physical Space Transport Accelerations . . 55
3.1.4 From NSD Dynamics to KHMH Dynamics 60
3.2 Fluctuating KHMH Dynamics 67
3.2.1 Correlations between Different KHMH Terms 67
3.2.2 Conditional KHMH Statistics 70
3.3 Homogeneity and Inhomogeneity Contributions to Interscale Transfers . . 73
3.4 General Irrotational and Solenoidal KHMH Equations 77
3.5 Summary 83

4 Energy Transfer Dynamics at Small Scales **85**
4.1 Average and Fluctuating KHMH Dynamics 86
4.2 Small-scale Interscale Transfer and Viscous Terms in Low and High Two-point Energy Regions 90
4.3 Small-scale Dynamics across Two-point Energy Levels 95
4.4 Summary 98

5 Spatially Averaged Unsteady Energy Exchanges **99**
5.1 Spatially Averaged KHMH Dynamics in Homogeneous Turbulence 100
5.2 A Formalised Time-lag Hypothesis for Homogeneous Turbulence 105
5.3 Time-lag Corrections to Local Equilibrium 113
5.3.1 Non-equilibrium Dynamics from Time-lag Corrections 113
5.3.2 Non-equilibrium Second-order Structure Function Scaling from Time-lag Corrections 119
5.3.3 Local Delay Scaling and Comparison with Similar Studies 124
5.4 Time-lags and Dissipation Scaling Laws 126
5.5 Summary 130

6 Conclusion **133**

Bibliography **137**

Appendices **147**

A Derivation of the KHMH Equation **148**

B Helmholtz-decomposed Dynamics in Fourier Space **153**

C Spatially Averaged KHMH Terms in Fourier Space **157**

D Time-lags and Grid Turbulence **161**

Nomenclature

Acronyms

CFL	Courant-Friedrichs-Lewy
DNS	Direct Numerical Simulation
FFT	Fast Fourier Transform
K41	Kolmogorov's original theory of turbulence
K62	Kolmogorov's refined theory of turbulence
KH	Kármán-Howarth equation (see equation (1.3))
KHMH	Kármán-Howarth-Monin-Hill equation (see equation (3.19))
LES	Large-Eddy Simulation
LHS	Left-hand side
NS	Incompressible Navier-Stokes equations (see equation (1.1))
NSD	Navier-Stokes Difference equations (see equation (3.14))
PDF	Probability Density Function
RANS	Reynolds-Averaged Navier-Stokes equations
RHS	Right-hand side

Greek Letters

$\boldsymbol{\omega}$	Fluid vorticity $\nabla_{\boldsymbol{x}} \times \boldsymbol{u}$
δ_{ij}	Kronecker delta
ϵ	Viscous (pseudo-)dissipation rate $\nu(\partial u_i/\partial x_j)^2$
ϵ_0	Characteristic large-scale input/global dissipation scale
ϵ_{ijk}	Levi-Civita tensor

η	Kolmogorov scale $\langle\epsilon\rangle_{\boldsymbol{x}}^{-1/4}\nu^{3/4}$
λ	Taylor scale $15(\nu u^2/\langle\epsilon\rangle_{\boldsymbol{x}})^{1/2}$
ϵ^*	KHMH two-point viscous pseudo-dissipation (see equation (3.20))
$\mathit{\Pi}$	KHMH interscale transfer (see equation (3.20))
$\mathit{\Pi}_H$	KHMH homogeneity interscale transfer (see equation (3.29))
$\mathit{\Pi}_I$	KHMH inhomogeneity interscale transfer (see equation (3.29))
ν	Fluid kinematic viscosity
$\overline{\mathit{\Pi}}$	KHMH equilibrium interscale transfer $-C_{\mathit{\Pi}}\langle\epsilon^*\rangle_{\boldsymbol{x}}$
$\overline{\tau}$	Interscale transfer and dissipation scale-dependent time delay
ρ	Fluid density
τ	Interscale transfer and dissipation time delay (see equation (5.11))
τ^*	Interscale transfer and dissipation "local" time delay (see equation (5.31))
$\widetilde{\mathit{\Pi}}$	KHMH non-equilibrium interscale transfer $\langle\mathit{\Pi}\rangle_{\boldsymbol{x}}^{a} - \overline{\mathit{\Pi}}$

Operators

$\xi(\phi\|\zeta)$	Operator ξ (e.g. σ) acting on ϕ conditioned on condition ζ
$\boldsymbol{q}_I$	Irrotational part of NS term $\boldsymbol{q}$
$\boldsymbol{q}_S$	Solenoidal part of NS term $\boldsymbol{q}$
$\boldsymbol{q}_{\overline{I}}$	Irrotational part in centroid space of NSD term $\boldsymbol{q}$
$\boldsymbol{q}_{\overline{S}}$	Solenoidal part in centroid space of NSD term $\boldsymbol{q}$
$\delta\phi$	ϕ difference $\phi^+ - \phi^-$
$\langle\phi\rangle$	Spatio-temporal average of ϕ
$\langle\phi\rangle_E$	Ensemble average of ϕ
$\langle\phi\rangle_t$	Time average of ϕ
$\langle\phi\rangle_{\boldsymbol{x}}$	Space average of ϕ
$\mathcal{Q}"$	$\mathcal{Q}$ temporal/ensemble fluctuation $\langle\mathcal{Q}\rangle_{\boldsymbol{x}} - \langle\mathcal{Q}\rangle$
$\mathcal{Q}'$	$\mathcal{Q}$ spatio-temporal fluctuation $\mathcal{Q} - \langle\mathcal{Q}\rangle$

$\mathcal{Q}_{\overline{I}}$	Irrotational (centroid space) part of KHMH term $\mathcal{Q}$ with NSD analogue $\boldsymbol{q}$ given by $2\delta\boldsymbol{u}\cdot\boldsymbol{q}_{\overline{I}}$
$\mathcal{Q}_{\overline{S}}$	Solenoidal (centroid space) part of KHMH term $\mathcal{Q}$ with NSD analogue $\boldsymbol{q}$ given by $2\delta\boldsymbol{u}\cdot\boldsymbol{q}_{\overline{S}}$
$\mathcal{Q}_S$	Solenoidal (physical space) part of KHMH term $\mathcal{Q}$ with NSD analogue $\delta\boldsymbol{q}$ given by $2\delta\boldsymbol{u}\cdot\delta\boldsymbol{q}_S$
ϕ^a	Orientation averaged ϕ (see equation (2.31))
ϕ^+	ϕ evaluated at $\boldsymbol{x}^+ = \boldsymbol{x} + 1/2\boldsymbol{r}$
ϕ^-	ϕ evaluated at $\boldsymbol{x}^- = \boldsymbol{x} - 1/2\boldsymbol{r}$
$\phi^<$	Low-pass filtered (in time) ϕ
$\sigma(\phi), \sigma_\phi$	Standard deviation of ϕ
$\mathrm{corr}(\phi_1, \phi_2)$	Pearson correlation coefficient of ϕ_1 and ϕ_2
$\mathrm{RMS}(\phi)$	Root-mean-square $\sqrt{\langle \phi^2 \rangle_t}$
$\widehat{\phi}(\boldsymbol{k})$	Fourier coefficient of ϕ at wavenumber $\boldsymbol{k}$

Roman Letters

$\boldsymbol{a}$	NS total acceleration $\boldsymbol{a}_l + \boldsymbol{a}_c$
$\boldsymbol{a}_c$	NS convective acceleration $\boldsymbol{u}\cdot\nabla_{\boldsymbol{x}}\boldsymbol{u}$
$\boldsymbol{a}_l$	NS local acceleration $\partial\boldsymbol{u}/\partial t$
$\boldsymbol{a}_p$	NS pressure gradient $-1/\rho\nabla_{\boldsymbol{x}}p$
$\boldsymbol{a}_{\mathcal{T}}$	NSD interspace transport $(\boldsymbol{u}^+ + \boldsymbol{u}^-)/2\cdot\nabla_{\boldsymbol{x}}\delta\boldsymbol{u}$
$\boldsymbol{a}_{\mathit{\Pi}}$	NSD interscale transfer $\delta\boldsymbol{u}\cdot\nabla_{\boldsymbol{r}}\delta\boldsymbol{u}$
$\boldsymbol{a}_\nu$	NS viscous term $\nu\nabla^2_{\boldsymbol{x}}\boldsymbol{u}$
$\boldsymbol{f}$	NS forcing term
$\boldsymbol{k}$	Wavenumber vector
$\boldsymbol{r}$	Separation vector $\boldsymbol{x}^+ - \boldsymbol{x}^-$
$\boldsymbol{u}$	Fluid velocity field
$\boldsymbol{x}$	Physical space or centroid location $(\boldsymbol{x}^+ + \boldsymbol{x}^-)/2$

$\mathcal{A}_c$	KHMH non-linear term $\mathcal{T} + \mathit{\Pi}$(see equation (3.20))
$\mathcal{A}_t$	KHMH time derivative term (see equation (3.20))
$\mathcal{D}$	KHMH viscous effects $\mathcal{D}_{r,\nu} + \mathcal{D}_{x,\nu} - \epsilon^*$
$\mathcal{D}_{r,\nu}$	KHMH viscous diffusion in scale space (see equation (3.20))
$\mathcal{D}_{x,\nu}$	KHMH viscous diffusion in centroid space (see equation (3.20))
$\mathcal{I}$	KHMH energy input rate (see equation (3.20))
$\mathcal{T}$	KHMH turbulent transport (see equation (3.20))
$\mathcal{T}_p$	KHMH pressure-velocity (see equation (3.20))
C_K	Kolmogorov constant (see equation (1.9))
$C_{\mathit{\Pi}}$	Formalised time-lag hypothesis prefactor (see equation (5.9))
C_τ	Local delay scaling prefactor (see equation (5.31))
E	$\boldsymbol{u}$ power spectrum (see equation (2.20))
K	Spatially-averaged turbulent kinetic energy $\langle u_i u_i \rangle_{\boldsymbol{x}}/2$
k	Wavenumber magnitude $\lvert \boldsymbol{k} \rvert$
$k_{\max}$	Maximum resolved wavenumber $\sqrt{2}/3N$
L	The integral length scale (see equation (2.22))
L_0	Characteristic large-scale input/global length scale
N	DNS simulation size with N^3 total wavenumber modes
p	Fluid pressure field
$r,\ r_d$	Length scale given by the separation magnitude $\lvert \boldsymbol{r} \rvert$
Re_λ	Taylor scale Reynolds number $u\lambda/\nu$
T	Integral time scale $\langle L \rangle_t / \langle u \rangle_t$
T_ϵ	Time scale of change of $\langle \epsilon \rangle_{\boldsymbol{x}}$ (see equation (5.15))
u	Velocity root-mean-square $\sqrt{2/3K}$
u_0	Characteristic large-scale input/global velocity scale

List of Figures

2.1 Yoffe's model spectrum used to set DNS initial conditions 33
2.2 Temporal evolution of the DNS turbulent kinetic energy. 38
2.3 Time-averaged three-dimensional energy spectra for the DNSs. 39
2.4 Sketch of the spherical averaging procedure used for KHMH post-processing 40
2.5 KHMH residuals at intermediate and large scales for DNS2-DNS3-DNS4 41
2.6 KHMH residuals at small scales for DNS1 42

3.1 PDFs of Navier-Stokes acceleration and force magnitudes. 48
3.2 Illustration of NSD centroid and separation vectors 51
3.3 NSD exceedance probabilities. 52
3.4 NSD space-time-average magnitudes and alignments 54
3.5 NSD space-time-average magnitudes and alignments with ABC forcing. . 55
3.6 NSD Helmholtz-decomposed average magnitudes. 57
3.7 NSD Helmholtz-decomposed average alignments 58
3.8 NSD Helmholtz-decomposed average magnitudes and alignments with ABC forcing. 59
3.9 KHMH average square and square fluctuating magnitudes 63
3.10 Test of two assumptions connecting NSD and KHMH relative magnitudes. 64
3.11 Comparison of NSD and KHMH relative average magnitudes. 65
3.12 KHMH average square and square fluctuating magnitudes with ABC forcing 66
3.13 Spherically averaged correlation coefficients between KHMH terms. . . . 67
3.14 Scatter plots of $\mathit{\Pi}'_{\overline{S}}$ and $\epsilon^{*'}$. 68
3.15 Scatter plots of $\mathcal{A}_t$ and $\mathcal{T}_{\overline{S}}$. 69
3.16 Scatter plots of $\mathcal{A}_t + \mathcal{T}_{\overline{S}}$ and $\mathit{\Pi}'_{\overline{S}}$. 70
3.17 KHMH correlation coefficients among relatively rare intense $\mathit{\Pi}^a_{\overline{S}}$ events. . 71
3.18 KHMH averages conditioned on relatively rare intense $\mathit{\Pi}^a_{\overline{S}}$ events. 72
3.19 PDFs of interscale transfer decompositions 74
3.20 KHMH skewness factors 75
3.21 Correlation coefficients between various interscale transfer decompositions 76
3.22 Average values of $\mathit{\Pi}$ decompositions conditioned on intense $\mathit{\Pi}$ events. . . 77
3.23 Average magnitude of solenoidal boundary term $\boldsymbol{a}_{\mathit{\Pi}_{\overline{SB}}}$ relative to the average magnitude of $\boldsymbol{a}_{\mathit{\Pi}_{\overline{S}}}$ as a function of the distance to the boundary. . . . 81

4.1 KHMH space-time-averages for DNS1. 86
4.2 KHMH standard deviations and flatness factors at small scales 88
4.3 KHMH skewness factors and correlation coefficients. 89
4.4 KHMH average viscous terms conditioned on various two-point energy levels 91
4.5 PDFs of $\mathit{\Pi}_{\overline{S}}^{a}$ and viscous terms at small scales in low- and high-two-point energy regions. 92
4.6 Scatter plots $(\mathcal{D}_{r,\nu}^{a} - \epsilon^{*a}, \mathit{\Pi}_{\overline{S}}^{a})$ and $(\mathcal{D}^{a}, \mathit{\Pi}_{\overline{S}}^{a})$ in low and high two-point energy regions. 94
4.7 KHMH standard deviations and correlation coefficients conditioned on the two-point energy 96

5.1 KHMH spatio-temporal averages across scales 102
5.2 KHMH temporal standard deviations 103
5.3 KHMH temporal correlation coefficients 103
5.4 DNS2 KHMH temporal standard deviations and correlation coefficients . 104
5.5 Time series of the spatially averaged interscale transfer, time derivative and dissipation terms for DNS3-DNS4 106
5.6 Formalised time-lag prefactor across scales 107
5.7 Scale-dependent time delays and associated correlation values 108
5.8 Correlation functions between the spatially averaged interscale transfer and disspation 109
5.9 Time series of the ratio of spatially averaged interscale transfer to spatially averaged dissipation with and without time-lag 110
5.10 Formalised time-lag hypothesis residuals across scales 111
5.11 Time series of relative non-equilibrium first- and second-order terms for the dissipation rate Taylor expansion 114
5.12 Average size of non-equilibrium first- and second-order corrections for the dissipation rate Taylor expansion 115
5.13 Assessment of non-equilibrium interscale transfer approximation 117
5.14 Assessment of non-equilibrium time derivative term approximation 118
5.15 Assessment of two low-pass weak Kovasznay closures 120
5.16 Assessment of $\langle\langle|\delta\boldsymbol{u}|^2\rangle_{\boldsymbol{x}}^{a}\rangle^{<}$ non-equilibrium predictions with a time-lagged low-pass weak Kovasznay closure 122
5.17 $\langle(|\delta\boldsymbol{u}|^2)^{a}\rangle$ and equilibrium and non-equilibrium predictions across scales . 123
5.18 Assessment of the local delay scaling 124
5.19 Time series of $u(t)/u_0$, $L(t)/L_0$ and $\epsilon(t)/\epsilon_0$ 127
5.20 Time series pertaining to the non-equilibrium and redistributive dissipation scalings 128

List of Tables

2.1 Key parameters of the DNS datasets 37
2.2 Specification of the temporal sampling of velocity, pressure and forcing fields in the DNSs 38

3.1 NS average acceleration and force magnitudes. 47
3.2 NS exceedance probabilities 48
3.3 NS average acceleration and force alignments. 49

4.1 Share of events with the interscale transfer and viscous terms being approximately equal with various small-scale $(|\delta \boldsymbol{u}|^2)^a$ conditioning. 93

A.1 Specification of NS, NSD and KHMH notation and the terms' direct and indirect relationships 152

1. Introduction

Fluid flows appearing in nature and engineering are typically turbulent. Even as turbulence is easy to observe, and the equations governing the motion of fluids became available in the 19th century, a deep understanding of turbulence is yet to be obtained. Fundamental aspects of turbulence must be clearly understood to improve turbulence models and subsequent engineering predictions and designs (Tsinober, 2009).

Arguably the most successful turbulence description to date is the Kolmogorov 1941 theory (abbreviated K41) (Kolmogorov, 1941a,b,c). In K41 turbulence is viewed as a wide range of dynamically interacting scales. The largest inviscid scales are dependent on flow-specific phenomena and the smallest scales are affected by viscosity. Under the hypotheses of statistical homogeneity and isotropy (i.e. the turbulence statistical properties are invariant under translations in space and rotations) and local equilibrium at intermediate scales (i.e. the energy transfer rate to smaller scales is equal to the rate at which energy is being converted to heat), K41 obtains predictions for the energy distribution at an intermediate range of scales. This prediction has been observed in a vast range of turbulent flow regions, both in flow regions where the hypotheses are plausibly satisfied and where they are not (Kraichnan, 1974; Alves Portela et al., 2017)

Notwithstanding its successes, the K41 theory has limitations. The K41 assumption of local equilibrium is not applicable in a wide range of scales (Goto and Vassilicos, 2015, 2016b). This effect of cascade unsteadiness remains to be accounted for in the description of the turbulent energy cascade. Moreover, the K41 mean-field description is not necessarily applicable locally in space and time. Such a hypothesis of equilibrium locally in space-time is the basis for the refined theory of Kolmogorov (1962) and later extensions, culminating in the multifractal formalism (Parisi and Frisch, 1985; Frisch, 1995). Recent investigations have shown that locally the cascade dynamics vastly differ from a local balance between interscale energy transfer and viscous dissipation (Yasuda and Vassilicos, 2018). The local cascade behaviour is central to large-eddy-simulation (LES) models of turbulence and the question of the smallest length scales in turbulent flows (Frisch and Vergassola, 1991).

Section 1.1 provides an overview of classical turbulence theory with a focus on the K41 theory. We discuss some shortcomings of the K41 theory in section 1.2 before listing the thesis objectives and outline in section 1.3.

1.1 An Overview of Classical Turbulence Theory

The equations governing incompressible Newtonian fluids are the (incompressible) Navier-Stokes equations (Batchelor, 1967)

$$\frac{\partial u_i}{\partial x_i} = 0, \tag{1.1a}$$

$$\frac{\partial u_i}{\partial t} + u_j \frac{\partial u_i}{\partial x_j} = -\frac{1}{\rho}\frac{\partial p}{\partial x_i} + \nu \frac{\partial^2 u_i}{\partial x_j \partial x_j}, \tag{1.1b}$$

where u_i is the fluid velocity components and p is the pressure at location $\boldsymbol{x}$ at time t, and ρ and ν are the density and kinematic viscosity of the fluid. If U and d denote characteristic velocity and length scales of $\boldsymbol{u}$, the flow becomes turbulent at sufficiently high Reynolds numbers

$$Re_d = \frac{Ud}{\nu}, \tag{1.2}$$

where the non-linear term dominates the viscous term at scale d (Reynolds, 1883; Davidson et al., 2011). At such Reynolds numbers the fields $\boldsymbol{u}$ and p can be thought of in terms of their mean and fluctuating parts (Reynolds, 1895). At first these turbulent fluctuations might seem random, but they are governed by a deterministic set of equations (1.1).

One possible organising principle of turbulent flows is the idea of a turbulent energy cascade first introduced by Richardson (1922); kinetic energy enters the flow at the largest scales, it is cascaded by inviscid processes to gradually smaller scales and at the smallest scales viscous dissipation is effective such that the energy is converted into heat. This picture emphasises the role of viscous dissipation at the end of a sequence of processes, and it represents a turbulent flow as a hierarchy of eddies ranging from the size of the largest energy-containing scales to the smallest scales allowed by dissipation.

An essential stepping stone in the further development of a cascade theory was the statistical theory of turbulence of G. I. Taylor (Taylor, 1935, 1938a,b). Taylor introduced the notions of statistically homogeneous and isotropic turbulence, where the average properties of the motion are independent of the position in the fluid and the direction of the axes of reference. The relative mathematical simplicity of isotropic turbulence led Kármán and Howarth (1938) to derive the Kármán-Howarth (KH) equation from the Navier-Stokes equations. This equation connects the evolution of mean values of the product of two and three components of the velocity field $\boldsymbol{u}$ at two locations in terms of only two unknown scale-dependent scalar functions. This equation can be written in terms of velocity structure functions (see e.g. Landau and Lifshitz (1987)) as

$$\frac{\partial \langle \delta u_r^2 \rangle_E}{\partial t} + \frac{1}{3r^4}\frac{\partial}{\partial r}\big(r^4 \langle \delta u_r^3 \rangle_E\big) = \frac{2\nu}{r^4}\frac{\partial}{\partial r}\big(r^4 \frac{\partial \langle \delta u_r^2 \rangle_E}{\partial r}\big) - \frac{4}{3}\langle \epsilon \rangle_E, \tag{1.3}$$

where $\langle \cdot \rangle_E$ denotes an ensemble average, $\langle \delta u_r^2 \rangle_E(r,t)$ and $\langle \delta u_r^3 \rangle_E(r,t)$ are the second and third order longitudinal velocity structure functions with

$$\delta u_r(\boldsymbol{x},\boldsymbol{r},t) = \big(\boldsymbol{u}(\boldsymbol{x}+\frac{1}{2}\boldsymbol{r},t) - \boldsymbol{u}(\boldsymbol{x}-\frac{1}{2}\boldsymbol{r},t)\big)\cdot\frac{\boldsymbol{r}}{r}, \tag{1.4}$$

$r = |\boldsymbol{r}|$ is the separation distance or scale and ϵ is the viscous (pseudo-)dissipation rate

$$\epsilon = \nu\frac{\partial u_i}{\partial x_j}\frac{\partial u_i}{\partial x_j}. \tag{1.5}$$

Equation (1.3) is an exact equation in homogeneous and isotropic turbulence which relates the second- and third-order velocity structure functions. This equation is interesting physically as it is an evolution equation for $\langle\delta u_r^2\rangle_E(r,t)$. This quantity represents, roughly speaking, the energy contained in eddies of characteristic size r or less (see Townsend (1976); Frisch (1995); Davidson and Pearson (2005)). Moving from left to right in (1.3), the first term is an unsteadiness term, the second term is an interscale transfer term, the third term is a scale space viscous diffusion term and the final term is viscous dissipation.

The seminal contribution Kolmogorov (1941a) starts from the KH equation written in the form (1.3). It can be argued from the idea of an energy cascade that $\langle\delta u_r^2\rangle_E$ regardless of r evolves on a time scale similar to the overall turbulent kinetic energy evolution ($\sim L/u$, where u and L are large-scale turbulent velocity and length scales) (see e.g. chapter 6 of Batchelor (1953)). If the local time scale of the energy evolution at scales $r \ll L$ is much smaller than the time scale of the overall turbulent kinetic energy evolution, the local turbulence can be viewed as in approximate local equilibrium

$$\frac{1}{3r^4}\frac{\partial}{\partial r}\big(r^4\langle\delta u_r^3\rangle_E\big) \approx \frac{2\nu}{r^4}\frac{\partial}{\partial r}\big(r^4\frac{\partial\langle\delta u_r^2\rangle_E}{\partial r}\big) - \frac{4}{3}\langle\epsilon\rangle_E, \tag{1.6}$$

This local equilibrium assumption is an approximation which becomes increasingly accurate at smaller scales r with decreasing local time scales. If we imagine a flow at a very high Reynolds number with a range of scales with scales small enough for local equilibrium to be valid while large enough for the viscous diffusion term in (1.6) to be negligible (denoted the inertial range of scales), we obtain in this range of scales

$$\frac{1}{3r^4}\frac{\partial}{\partial r}\big(r^4\langle\delta u_r^3\rangle_E\big) \approx -\frac{4}{3}\langle\epsilon\rangle_E. \tag{1.7}$$

If we multiply this equation with r^4 and integrate across separations from 0 to r, we attain the so-called Kolmogorov "4/5-law"

$$\frac{\langle\delta u_r^3\rangle_E(r)}{r} \approx -\frac{4}{5}\langle\epsilon\rangle_E. \tag{1.8}$$

This equation can be interpreted in terms of a self-similar equilibrium cascade at an intermediate range of scales, where there is an average energy cascade from larger to smaller scales which is proportional to the average viscous dissipation rate.

Kolmogorov (1941a) combined (1.8) with an assumption of a Reynolds number independent δu_r skewness factor $\langle \delta u_r^3 \rangle_E / \langle \delta u_r^2 \rangle_E^{3/2}$ at inertial scales such that

$$\langle \delta u_r^2 \rangle_E(r) = C_K \langle \epsilon \rangle_E^{2/3} r^{2/3}, \tag{1.9}$$

which is denoted the Kolmogorov "2/3-law" and C_K is the Kolmogorov constant, a universal constant of order unity. This relation describes a self-similar manner in which energy is distributed at intermediate scales r. Note that the earlier Kolmogorov paper Kolmogorov (1941c) arrived at a $r^{2/3}$-scaling of $\langle \delta u_r^2 \rangle_E(r)$ for more general conditions than statistical homogeneity and isotropy (i.e. local homogeneity and local isotropy) with no assumption of δu_r constant skewness. However, this result is strictly from dimensional considerations and not the Navier-Stokes equations. As a final ingredient to the K41 theory, we note that Kolmogorov (1941b) assumed that (1.9) can be extended to scales $r \sim L$ such that

$$\langle \epsilon \rangle_E \sim \frac{u^3}{L}. \tag{1.10}$$

The scaling (1.10) was first introduced by Taylor (1935) from dimensional arguments. This scaling can also be derived by extending the 4/5-law (1.8) to scales $r \sim L$, but this is problematic as it hypothesises local equilibrium at scales where unsteadiness is presumably important. The above developments can also be performed in Fourier space in terms of the Lin equation (Lin, 1949) with a resulting balance between interscale energy transfer and dissipation and a $k^{-5/3}$ scaling of the $\boldsymbol{u}$ power spectrum at intermediate wavenumbers k (Obukhov, 1941) (i.e. the Fourier space analogue to the 2/3-law).

Modern developments have relaxed the assumptions of homogeneity and isotropy required to arrive at the 4/5-law (1.8). These efforts culminated in the works of Hill (Hill, 1997, 2002) (see also Nie and Tanveer (1999)), who generalised the KH equation to arbitrary incompressible fluid flows in the form of the Kármán-Howarth-Monin-Hill (KHMH) equation (we introduce this equation in chapter 3). It can be derived from this equation in anisotropic and locally homogeneous flow regions at intermediate scales $\boldsymbol{r}$ the relation

$$\langle \delta u_j \frac{\partial \delta u_i \delta u_i}{\partial r_j} \rangle_E(\boldsymbol{r}) \approx -4 \langle \epsilon \rangle_E, \tag{1.11}$$

where $\delta u_i(\boldsymbol{x}, \boldsymbol{r}, t) = u_i(\boldsymbol{x} + 1/2\boldsymbol{r}, t) - u_i(\boldsymbol{x} - 1/2\boldsymbol{r}, t)$. As the LHS of (1.11) can be viewed as the average interscale transfer rate at scale $\boldsymbol{r}$, we have a self-similar balance between interscale transfer and viscous dissipation at an intermediate range of scales. Even though the homogeneity and isotropy assumptions have been relaxed in (1.11), it is still required to assume local equilibrium, i.e. the local rate of change of $\delta u_i \delta u_i = |\delta \boldsymbol{u}|^2$ moving with approximately u_i is negligibly small/evolves slowly compared to the local turbulence evolution (i.e. the interscale transfer and viscous dissipation terms) (Vassilicos, 2015)

$$\langle \frac{\partial |\delta \boldsymbol{u}|^2}{\partial t} + \overline{u}_i \frac{\partial |\delta \boldsymbol{u}|^2}{\partial x_i} \rangle_E(\boldsymbol{r}) \ll \langle \delta u_j \frac{\partial |\delta \boldsymbol{u}|^2}{\partial r_j} \rangle_E(\boldsymbol{r}). \tag{1.12}$$

1.2 Real Turbulence Compared to K41 Turbulence

The K41 theory has achieved an "embarrassment of success" (Kraichnan, 1974) with the $-5/3$ scaling of the energy spectrum observed in numerous flows, even where its assumptions are invalid (see Alves Portela et al. (2017) and references therein). This apparent success of the theory has made the K41 predictions implemented in widely used one-point (RANS) (Leschziner, 2016) and two-point (LES) (Sagaut, 2006) turbulent flow prediction methods.

Concerning the underlying assumptions of the K41 theory, the memory-losing property of the energy cascade in terms of local-in-scale energy transfers has largely been confirmed in direct numerical simulations (DNS) of homogeneous turbulence (Domaradzki and Carati, 2007; Goto et al., 2017; Doan et al., 2018). Energy at a scale r is typically cascaded to scales $r^{'}$, which are similar to and smaller than r, due to interactions at scales similar to r. However, the local equilibrium assumption has repeatedly been shown to be invalid in a wide range of scales in freely decaying and forced homogeneous/periodic turbulence and grid-generated turbulence with the unsteadiness term in the KH equation (1.3) non-negligible (Goto and Vassilicos, 2015, 2016a; Obligado and Vassilicos, 2019). It follows that we cannot have a Taylor dissipation scaling (1.10) for K41 reasons.

Some recent DNS investigations of forced homogeneous turbulence have investigated the unsteadiness of the turbulent energy cascade in detail. The Lin equation integrated from wavenumbers k to ∞ reads (Batchelor, 1953)

$$\frac{\partial K_{>}(k,t)}{\partial t} = \Pi(k,t) - \epsilon_{>}(k,t), \tag{1.13}$$

where the scale- and time-varying terms in the equation are defined in terms of the three-dimensional energy spectrum $E(k,t)$ (see equation 2.20 in the next chapter):

$$K_{>}(k,t) = \int_{k}^{\infty} E(k,t)dk, \tag{1.14a}$$

$$\epsilon_{>}(k,t) = \int_{k}^{\infty} k^2 E(k,t)dk, \tag{1.14b}$$

where $K_{>}(k,t)$ and $\epsilon_{>}(k,t)$ are the kinetic energy and energy dissipation at wavenumbers larger than k (and we have only considered wavenumbers k larger than those affected directly by the large-scale forcing). $\Pi(k,t)$ is the interscale transfer rate of kinetic energy from wavenumbers smaller than k to wavenumbers larger than k. This equation governs the evolution of turbulent kinetic energy across scales k^{-1} and time t. In DNSs of forced homogeneous turbulence the unsteadiness term in (1.13) is (instantaneously) non-negligible at scales k^{-1} similar to the integral length scale L (Goto and Vassilicos, 2015, 2016a). Moreover, there is a significant time-lag between the interscale transfer rate $\Pi(k,t)$ and the dissipation rate $\epsilon_{>}(k,t)$ at such wavenumbers, which decreases with decreasing scale k^{-1} (Goto and Vassilicos, 2016a). This behaviour is consistent with a step-by-step energy cascade where each cascade step takes some finite time. As this time-lag is significant relative to the time scale at which $\epsilon_{>}(k,t)$ evolves, there are imbalances between $\Pi(k,t)$ and $\epsilon_{>}(k,t)$ with resulting unsteadiness at such scales (i.e. non-K41 behaviour). Note that this time-lagged cascade behaviour emerges only when we lift the typical time-averaging operation $\langle \ldots \rangle_t$ applied to the integrated Lin equation (1.13) for forced homogeneous turbulence as $\langle \Pi \rangle_t(k) = -\langle \epsilon^{>} \rangle_t(k)$ from statistical stationarity.

Cascade theories based on the KH/Lin equations, with effects of unsteadiness included or neglected (e.g. K41), are limited by their mean-field description of the turbulent energy cascade. The K41 theory considers only the spatially-averaged energy cascade (i.e. the turbulence evolution across scales k^{-1} and time t). Turbulence exhibits significant spatial inhomogeneity instantaneously such that the 4/5-law (1.8), or similar predictions which take into account unsteadiness effects, might not be representative locally in space. This turbulence feature of spatial inhomogeneity/intermittency was first discovered in the grid turbulence experiments of Batchelor et al. (1949), which showed that the viscous dissipation rate is very intermittent. This discovery and Landau's objection to the universality of C_K (Landau and Lifshitz, 1987; Frisch, 1995) led to Kolmogorov's revised theory K62 (Kolmogorov, 1962). In K62 the velocity structure functions at scale r are hypothesised to be dependent on the local-in-space volume-averaged dissipation rate at scale r. K62 has since been eclipsed by the multifractal formalism (Parisi and Frisch, 1985; Frisch, 1995), but common for these phenomenological theories is a localisation in space of the 4/5-law (i.e. the interscale transfer and dissipation are hypothesised to be phenomenologically related *locally* in space and time). In contrast to the 4/5-law, these theories have not been derived from the NS equations and the multifractal formalism has a large set of parameters that can be fitted to experimental data (Gotoh and Kraichnan, 2004; Tsinober, 2009).

DNS evidence since the early 1990s has shown a limited tendency of the intermediate-scale interscale transfer and dissipation to balance locally (Piomelli et al., 1991; Aoyama et al., 2005; Yasuda and Vassilicos, 2018). The local (in time and space) interscale transfer rate exhibits violent fluctuations with interscale transfers from larger to smaller scales and interscale transfers from smaller to larger scales. A balance between interscale transfer and dissipation is unable to explain such inverse energy transfer events (i.e. $\epsilon \geq 0$). This begs the question: which physical processes balance with the interscale transfer rate locally? Beyond its importance in accurately characterising the turbulent energy cascade, this question is of practical relevance for LES modelling. To yield correct coherent structures and kinetic energy distributions in the resolved scales, LES models need to replicate the dynamics locally (Vela-Martín, 2022a). Local in space and time cascade dynamics are also of relevance at the smallest scales of turbulence. Kolmogorov deduced from phenomenological arguments that the smallest average length scale in turbulent flows equals $\eta = (\nu^3/\langle \epsilon \rangle_E)^{1/4}$ (i.e. the Kolmogorov scale) (Kolmogorov, 1941c). Frisch and Vergassola (1991) combines a local balance between viscous effects and interscale transfer and the multifractal formalism to derive an expression for the smallest length scales of turbulent flows (see also Dubrulle (2019)). These estimates are smaller than η and can be used to assess DNS/experiment resolution requirements. Similar scaling arguments based on Onsager's prediction of non-viscous dissipation (Onsager, 1949) in turbulent flows are also used to probe weak Euler solutions of the NS equations (see e.g. Eyink (2018)). A local balance between viscous effects and interscale transfer has been used to investigate potential singularities of the NS equations (Dubrulle and Gibbon, 2021). These predictions have limited experimental support. However, they suggest that an accurate description of the local small-scale dynamics can answer important questions on small-scale resolution requirements, NS non-viscous dissipation and NS singularities.

1.3 Thesis Objectives and Outline

The K41 theory and the 4/5-law only concern the *average* energy cascade at intermediate scales and do not necessarily hold locally in space and time across scales. Numerous studies have shown that this assumption is misguided with no or limited local balance (in space and time) between the interscale transfer rate and the dissipation rate. It remains to develop a thorough characterisation of the local cascade dynamics rather than representing it in terms of an inaccurate average cascade picture. The first part of this thesis studies the spatio-temporally varying energy cascade dynamics in forced statistically stationary homogeneous/periodic turbulence. We perform scale-by-scale analysis locally in space and time of DNSs of forced homogeneous/periodic turbulence to provide a more accurate description of the local cascade dynamics. Our investigations are facilitated by a subdivision of the cascade dynamics using Helmholtz decompositions of the dynamical equations (see Tsinober et al. (2001)). This topic is primarily interesting on a fundamental level, but we will also relate our findings to LES modelling and small-scale resolution requirements in DNS.

Having tentatively characterised the local (in space and time) turbulent energy cascade in the first part of the thesis, in the second and final part of the thesis we consider its spatially-averaged manifestation. We connect the local cascade dynamics, unsteady spatially-averaged cascade dynamics and the popular cascade time-lag concept (see e.g. Lumley (1992)) with the novel "formalised time-lag hypothesis". This hypothesis relates the spatially-averaged interscale transfer rate and the spatially-averaged viscous dissipation rate, where the former increasingly precedes the latter with increasing scale. We use the formalised time-lag hypothesis as a starting point to predict the energy cascade dynamics and energy scaling at scales where the local equilibrium hypothesis is inapplicable. We also use the phenomenology of a time-lagged energy cascade to motivate a new redistributive dissipation scaling law which is approximately identical to the successful non-equilibrium dissipation scaling (Goto and Vassilicos, 2015) for low to moderate Reynolds number DNSs of forced homogeneous/periodic turbulence.

All in all, the overarching thesis objective common for the two thesis parts is to contribute to uncovering the basic/conceptual physical mechanisms of the turbulent energy cascade. This is required to narrow the gap between turbulence theories (and their associated prediction methods) and experimental/DNS observations. We pursue this objective with a "bottom-up" approach going from the local to the average cascade behaviour rather than the more conventional "top-down" approach going from the average to the local cascade behaviour.

The numerical methodology used in this thesis is described in chapter 2. We detail the key parameters of the DNS datasets and how they relate to established criteria for appropriately resolved DNSs of forced homogeneous/periodic turbulence. We also detail and verify the DNS post-processing methodology. Chapter 3 studies the local energy cascade dynamics at intermediate and large scales with various Kármán-Howarth-Monin-Hill (KHMH) equations. We employ the Helmholtz decomposition to derive new KHMH equations to describe the local dynamics. This approach simplifies the dynamics considerably and allows for a novel characterisation of the local intermediate- and large-scale cascade dynamics. We extend this characterisation of the local cascade dynamics to small scales with KHMH analysis of a well-resolved DNS simulation in chapter 4. In chapter 5 we study the spatially-averaged energy cascade. We motivate and test our formalised time-lag hypothesis and develop and test corrections to local equilibrium under appropriate conditions at our Reynolds numbers. We use the phenomenology of a time-lagged energy cascade to justify a new dissipation scaling law applicable in low to moderate Reynolds number DNSs of forced homogeneous/periodic turbulence. In chapter 6 we conclude with the main results presented in the thesis and we suggest how they may be used in future studies of the turbulent energy cascade and turbulence modelling.

2. Numerical Methodology

Direct numerical simulations of the Navier-Stokes equations resolve all the scales of turbulent flows. This yields a wealth of detailed results which can be used to discover new turbulence phenomena and validate turbulence theories and models. This contrasts with coarse-grained approaches to turbulence (e.g. LES (Sagaut, 2006) or RANS methods (Leschziner, 2016)), where the solution is highly dependent on the various turbulence modelling assumptions.

DNSs of homogeneous/periodic turbulence obtain the highest Reynolds numbers achievable with DNS (Davidson, 2015) and thus the highest separation of length scales. This makes DNSs of homogeneous/periodic turbulence ideal to pursue the thesis objectives, and to investigate the turbulent energy cascade per se, without any further complicating physical processes (e.g. from interactions between a mean flow and the turbulent fluctuations). However, it can be argued that homogeneous turbulence is not found in nature and that it might be of limited aid in understanding naturally occurring turbulent flows (Moffatt, 2002). On the other hand, many features of DNSs of homogeneous turbulence are also found in naturally occurring flows (see e.g. the comparison of homogeneous turbulence and a field experiment in Gulitski et al. (2007)).

The numerical resolution in DNSs must be fine enough not to affect the solution, and in particular the flow statistics of interest. These resolution requirements limit DNSs to relatively low/moderate Reynolds numbers and simple flow configurations. The case of homogeneous/periodic turbulence, which is the focus of this thesis, is a particularly simple flow configuration. This problem allows for the use of efficient and highly accurate pseudospectral methods. These methods were pioneered in the 1970s (Patterson and Orszag, 1971, 1972) and are still the workhorses of DNSs of homogeneous/periodic turbulence.

Section 2.1 describes the methodology of the solver for our DNSs of homogeneous/periodic turbulence. This DNS code was originally developed by Prof. Susumu Goto of Osaka University and it has been used in numerous peer-reviewed articles on homogeneous/periodic turbulence (see e.g. Goto (2008); Yasuda et al. (2014); Goto and Vassilicos (2016b); Goto et al. (2017); Tsuruhashi et al. (2022)). We also detail the large-scale forcings, initial field generation and in-situ processing used for the DNS datasets. We motivate and describe the numerical setup of our DNSs in section 2.2 and our KHMH post-processing methodology in section 2.3.

2.1 Solver Description

We use a pseudospectral DNS code that solves the incompressible vorticity equations

$$\frac{\partial \boldsymbol{\omega}}{\partial t} = \nabla_{\boldsymbol{x}} \times (\boldsymbol{u} \times \boldsymbol{\omega}) + \nu \nabla^2_{\boldsymbol{x}} \boldsymbol{\omega} + \nabla_{\boldsymbol{x}} \times \boldsymbol{f}, \tag{2.1a}$$

$$\nabla_{\boldsymbol{x}} \cdot \boldsymbol{u} = 0, \tag{2.1b}$$

where $\boldsymbol{\omega}(\boldsymbol{x}, t) = \nabla_{\boldsymbol{x}} \times \boldsymbol{u}$ is the vorticity field and $\boldsymbol{f}(\boldsymbol{x}, t)$ is the body force. The computational domain is $[0, 2\pi]^3$ and the boundary conditions are triply periodic

$$\boldsymbol{u}(x_1, x_2, x_3) = \boldsymbol{u}(x_1 + 2\pi, x_2, x_3) = \boldsymbol{u}(x_1, x_2 + 2\pi, x_3) = \boldsymbol{u}(x_1, x_2, x_3 + 2\pi). \tag{2.2}$$

The code is written in FORTRAN 90 and the FFTW library (Frigo and Johnson, 2005) is used for fast Fourier transforms (FFTs).

2.1.1 A Pseudospectral Method for the Vorticity Equation

To compute the evolution of the vorticity field, we employ a Fourier decomposition similar to Canuto et al. (1987). Let the fields in (2.1) be defined on points of the discrete equidistant grid $N \times N \times N$ with positions $\boldsymbol{x} = 2\pi\boldsymbol{n}/N$ with $0 \leq n_j \leq N - 1$ for integer n_j and $j = 1, 2, 3$. The Fourier coefficients of the velocity $\widehat{\boldsymbol{u}}(\boldsymbol{k}, t)$, pressure $\widehat{p}(\boldsymbol{k}, t)$, forcing $\widehat{\boldsymbol{f}}(\boldsymbol{k}, t)$ and vorticity $\widehat{\boldsymbol{\omega}}(\boldsymbol{k}, t)$ fields are defined on the grid $-N/2 \leq k_j < N/2 - 1$. E.g. the Fourier transform pair of $\boldsymbol{\omega}$ reads (i is the imaginary unit)

$$\boldsymbol{\omega}(\boldsymbol{x}, t) = \sum_{\boldsymbol{k}} \widehat{\boldsymbol{\omega}}(\boldsymbol{k}, t) e^{i\boldsymbol{k}\cdot\boldsymbol{x}}, \tag{2.3a}$$

$$\widehat{\boldsymbol{\omega}}(\boldsymbol{k}, t) = \frac{1}{N^3} \sum_{\boldsymbol{x}} \boldsymbol{\omega}(\boldsymbol{x}, t) e^{-i\boldsymbol{k}\cdot\boldsymbol{x}}. \tag{2.3b}$$

To derive an evolution equation for the Fourier modes $\widehat{\boldsymbol{\omega}}(\boldsymbol{k}, t)$, one inserts the truncated Fourier series (2.3a) into the vorticity equation (2.1a), applies the discrete Fourier transform and uses the orthogonality relation between discrete Fourier modes (Canuto et al., 1987) to obtain a set of coupled ordinary differential equations: e.g. the time derivative term transformed to Fourier space reads

$$\langle \frac{\partial \boldsymbol{\omega}}{\partial t} \rangle_{\boldsymbol{k}} = \frac{1}{N^3} \sum_{\boldsymbol{x}} \frac{\partial \boldsymbol{\omega}}{\partial t} e^{-i\boldsymbol{k}\cdot\boldsymbol{x}}, \tag{2.4a}$$

$$= \frac{\partial}{\partial t} \sum_{\boldsymbol{k}'} \widehat{\boldsymbol{\omega}}(\boldsymbol{k}', t) \frac{1}{N^3} \sum_{\boldsymbol{x}} e^{i(-\boldsymbol{k}+\boldsymbol{k}')\cdot\boldsymbol{x}}, \tag{2.4b}$$

$$= \frac{d\widehat{\boldsymbol{\omega}}(\boldsymbol{k}, t)}{dt}, \tag{2.4c}$$

where we use the notation $\langle \phi \rangle_{\boldsymbol{k}} \equiv \widehat{\phi}(\boldsymbol{k})$. We move from (2.4a) to (2.4b) by inserting (2.3a) and (2.4c) follows from the orthogonality relation of the discrete Fourier modes (Canuto et al., 1987). We have for the other linear terms $\langle \nu \nabla^2_{\boldsymbol{x}} \boldsymbol{\omega} \rangle_{\boldsymbol{k}} = -\nu k^2 \widehat{\boldsymbol{\omega}}(\boldsymbol{k}, t)$ where $k = |\boldsymbol{k}|$ and $\langle \nabla_{\boldsymbol{x}} \times \boldsymbol{f} \rangle_{\boldsymbol{k}} = i\boldsymbol{k} \times \widehat{\boldsymbol{f}}(\boldsymbol{k}, t)$. This yields the following $\widehat{\boldsymbol{\omega}}(\boldsymbol{k}, t)$ evolution equations

$$\frac{d\widehat{\boldsymbol{\omega}}}{dt} = -\nu k^2 \widehat{\boldsymbol{\omega}} + i\boldsymbol{k} \times \widehat{\boldsymbol{f}} + \langle \nabla_{\boldsymbol{x}} \times (\boldsymbol{u} \times \boldsymbol{\omega}) \rangle_{\boldsymbol{k}}, \tag{2.5a}$$

$$\boldsymbol{k} \cdot \widehat{\boldsymbol{u}}(\boldsymbol{k}, t) = 0, \tag{2.5b}$$

where (2.5b) is the incompressibility condition in Fourier space.

The rightmost term on the RHS of (2.5a), the non-linear term, poses the largest difficulty in a spectral method. This term in physical space can be written as

$$[\nabla_{\boldsymbol{x}} \times (\boldsymbol{u} \times \boldsymbol{\omega})]_q(\boldsymbol{x}, t) = -\epsilon_{qjl} \frac{\partial^2}{\partial x_j \partial x_m}(u_m u_l), \tag{2.6}$$

where ϵ_{qjl} is the Levi-Civita tensor. Transforming this expression to Fourier space yields

$$[\langle \nabla_{\boldsymbol{x}} \times (\boldsymbol{u} \times \boldsymbol{\omega}) \rangle_{\boldsymbol{k}}]_q = \epsilon_{qjl} k_j k_m \langle u_m u_l \rangle_{\boldsymbol{k}}, \tag{2.7a}$$

$$= \epsilon_{qjl} k_j k_m \sum_{\boldsymbol{k} = \boldsymbol{k}' + \boldsymbol{k}''} \widehat{u}_m(\boldsymbol{k}') \widehat{u}_l(\boldsymbol{k}''). \tag{2.7b}$$

The term $\langle u_m u_l \rangle_{\boldsymbol{k}}$ takes the form of a convolution sum where all wavenumbers $\boldsymbol{k}' + \boldsymbol{k}'' = \boldsymbol{k}$ contribute to the evolution of $\widehat{\boldsymbol{\omega}}$ at wavenumber $\boldsymbol{k}$. These triadic interactions arising from the non-linear term couple the dynamics at different wavenumbers.

$\langle u_m u_l \rangle_{\boldsymbol{k}}$ evaluated directly has complexity $\mathcal{O}(N^6)$. To avoid this expensive computation, this term can be calculated in physical space and then transformed to Fourier space with efficient FFT algorithms with complexity $\mathcal{O}(N^3 \log_2 N)$ (i.e. a pseudospectral method) (Canuto et al., 1987). Let us consider a pseudospectral method where $\widehat{\boldsymbol{u}}$ is tranformed to physical space with an inverse FFT, the tensor $u_m u_l$ is calculated in physical space and then transformed back to Fourier space. This pseudospectral evaluation of $\langle u_m u_l \rangle_{\boldsymbol{k}}$ yields

$$\langle u_m u_l \rangle_{\boldsymbol{k}} = \frac{1}{N^3} \sum_{\boldsymbol{x}} u_m u_l e^{-i\boldsymbol{k}\cdot\boldsymbol{x}}, \tag{2.8a}$$

$$= \sum_{\boldsymbol{k}'} \sum_{\boldsymbol{k}''} \widehat{u}_m(\boldsymbol{k}') \widehat{u}_l(\boldsymbol{k}'') \frac{1}{N^3} \sum_{\boldsymbol{x}} e^{i(\boldsymbol{k}' + \boldsymbol{k}'' - \boldsymbol{k})\cdot\boldsymbol{x}}. \tag{2.8b}$$

Contributions to the rightmost sum in (2.8b) are non-zero when $k_j' + k_j'' - k_j = Ne_j$, where $e_j \in \{0, -1, 1\}$ (Canuto et al., 1987). Hence, $\langle u_m u_l \rangle_{\boldsymbol{k}}$ can be written as

$$\langle u_m u_l \rangle_{\boldsymbol{k}} = \sum_{\boldsymbol{k} = \boldsymbol{k}' + \boldsymbol{k}''} \widehat{u}_m(\boldsymbol{k}') \widehat{u}_l(\boldsymbol{k}'') + \sum_{\substack{\boldsymbol{e} \\ \boldsymbol{e} \neq (0,0,0) \\ e_j \in \{0,-1,1\}}} \sum_{\boldsymbol{k} + N\boldsymbol{e} = \boldsymbol{k}' + \boldsymbol{k}''} \widehat{u}_m(\boldsymbol{k}') \widehat{u}_l(\boldsymbol{k}''), \tag{2.9}$$

where the first term is the same as in (2.7b), while the second term consists of aliasing errors which arise due to the discreteness of the grid (Patterson and Orszag, 1971). Thus, a pseudospectral method can efficiently calculate the convolution sum but introduces aliasing errors. To remove the aliasing errors, the solver uses a combined phase-shift and truncation technique developed by Patterson and Orszag (1971). If we consider the velocity fields shifted to $\boldsymbol{x} + \pi\overline{\boldsymbol{e}}/N$ where $\overline{\boldsymbol{e}} = (1,1,1)$ and we denote the shifted velocity field as $\boldsymbol{v}$, we have

$$\boldsymbol{v}(\boldsymbol{x} + \pi\overline{\boldsymbol{e}}/N) = \sum_{\boldsymbol{k}} \widehat{\boldsymbol{u}}(\boldsymbol{k}) e^{i\boldsymbol{k}\cdot(\boldsymbol{x}+\pi\overline{\boldsymbol{e}}/N)}. \tag{2.10}$$

If we transform the tensor $v_l v_m$ to Fourier space, we obtain

$$\langle v_m v_l \rangle_{\boldsymbol{k}} = \sum_{\boldsymbol{k}=\boldsymbol{k}'+\boldsymbol{k}''} \widehat{u}_m(\boldsymbol{k}')\widehat{u}_l(\boldsymbol{k}'') + \sum_{\substack{\boldsymbol{e} \\ \boldsymbol{e}\neq(0,0,0) \\ e_l\in\{1,-1,0\}}} e^{i\pi\boldsymbol{e}\cdot\overline{\boldsymbol{e}}} \sum_{\boldsymbol{k}+N\boldsymbol{e}=\boldsymbol{k}'+\boldsymbol{k}''} \widehat{u}_m(\boldsymbol{k}')\widehat{u}_l(\boldsymbol{k}''). \tag{2.11}$$

The choice $\overline{\boldsymbol{e}} = (1,1,1)$ makes $e^{i\pi\boldsymbol{e}\cdot\overline{\boldsymbol{e}}} = -1$ for the singly and triply aliased contributions, i.e. the aliasing errors with one or three $\boldsymbol{e}$ non-zero components. Thus, by averaging $\langle u_m u_l \rangle_{\boldsymbol{k}}$ and $\langle v_m v_l \rangle_{\boldsymbol{k}}$, the singly and triply aliased contributions cancel with

$$\frac{1}{2}[\langle u_m u_l \rangle_{\boldsymbol{k}} + \langle v_m v_l \rangle_{\boldsymbol{k}}] = \sum_{\boldsymbol{k}=\boldsymbol{k}'+\boldsymbol{k}''} \widehat{u}_m(\boldsymbol{k}')\widehat{u}_l(\boldsymbol{k}'') + \sum_{\boldsymbol{e}'} \sum_{\boldsymbol{k}+N\boldsymbol{e}=\boldsymbol{k}'+\boldsymbol{k}''} \widehat{u}_m(\boldsymbol{k}')\widehat{u}_l(\boldsymbol{k}''), \tag{2.12}$$

where the summation over $\boldsymbol{e}'$ is over vectors $\boldsymbol{e}$ with two non-zero components. The remaining doubly aliased contributions are removed with spherical truncation with wavenumbers $k = |\boldsymbol{k}| > k_{\max} = \sqrt{2}/3N$ set equal to zero (i.e. the highest resolved wavenumber is $k_{\max}$) (Patterson and Orszag, 1971). This yields the final pseudospectral expression for the fully dealiased non-linear term in the vorticity equation

$$[\langle \nabla_{\boldsymbol{x}} \times (\boldsymbol{u} \times \boldsymbol{\omega}) \rangle_{\boldsymbol{k}}]_q = \begin{cases} \frac{1}{2}\epsilon_{qjl} k_j k_m [\langle u_m u_l \rangle_{\boldsymbol{k}} + \langle v_m v_l \rangle_{\boldsymbol{k}}], & k \leq \frac{\sqrt{2}}{3}N, \\ 0, & k > \frac{\sqrt{2}}{3}N. \end{cases} \tag{2.13}$$

The tensor $\langle u_m u_l \rangle_{\boldsymbol{k}}$ is symmetric and the solver exploits this to limit the computational expense and memory requirements in (2.13) (see Rogallo (1981)). Note that the pseudospectral treatment of the non-linear term in the vorticity equation is very similar to the pseudospectral treatment of the non-linear term in the NS equations (see e.g. Canuto et al. (1987)). However, by solving the vorticity equation rather than the NS equations there is no need to project the non-linear term onto its component orthogonal to $\boldsymbol{k}$ (i.e. its solenoidal part) as the terms in the vorticity equation are all solenoidal, yielding some cost reduction relative to the NS case.

The above dealiasing technique (2.13) with no aliasing errors is popular in DNSs of homogeneous/periodic turbulence (see e.g. Wan et al. (2010); Ishihara et al. (2016)). An alternative popular dealiasing technique introduced by Rogallo (1977) uses a random shifting technique and truncation to limit rather than eliminate aliasing errors (see e.g. Yeung et al. (2018)). If used in conjunction with a second-order Runge-Kutta method for time integration, the aliasing errors are of order $\mathcal{O}(\Delta t^2)$ where Δt is the time step. This method has the advantage of being less costly in terms of required operations than the full dealiasing technique (2.13) as the non-linear term is only calculated once rather than twice, but it does not eliminate aliasing errors. The choice of dealiasing technique is closely related to the choice of time integration method (see section 2.1.4).

The computational complexity of pseudospectral methods is comparable to that of finite difference methods with complexity $\mathcal{O}(N^3)$. In contrast to finite difference methods with algebraic order of convergence, the pseudospectral methods have faster than algebraic order of convergence (Hussaini and Zang, 1987; Canuto et al., 1987). This high spatial accuracy, combined with the complexity mentioned above, make pseudospectral methods the methods of choice for DNSs of homogeneous/periodic turbulence.

2.1.2 Large-scale Body Forcings

Turbulent flows are highly dissipative; unless energy is injected, they decay rapidly (Tennekes and Lumley, 1972). In DNSs of statistically steady forced homogeneous/periodic turbulence, the large scales are forced to keep the turbulence from decaying in a time-averaged sense. Only the large scales are forced with the intention that the memory-losing property of the cascade (see section 1.2) makes the behaviour at intermediate and small scales universal irrespective of the particular forcing. This insensitivity to the large-scale forcing has been confirmed in DNSs in terms of the energy spectrum with an approximate $k^{-5/3}$ scaling present at intermediate wavenumbers and an exponential decay at high wavenumbers with various forcings (Sagaut and Cambon, 2018). To assess the sensitivity of our results to the forcing, we have used two qualitatively different forcings.

The first forcing is a negative damping forcing (see Linkmann and Morozov (2015); McComb et al. (2015))

$$\widehat{\boldsymbol{f}}(\boldsymbol{k},t) = \begin{cases} (\epsilon_W/2K_f)\widehat{\boldsymbol{u}}(\boldsymbol{k},t), & 0 < |\boldsymbol{k}| < k_f, \\ 0, & \text{otherwise}, \end{cases} \tag{2.14}$$

where $\epsilon_W = const.$, k_f is the cutoff wavenumber and K_f is the total kinetic energy per unit mass contained in the forcing band $0 < |\boldsymbol{k}| < k_f$. This forcing yields a constant energy input rate per unit mass ϵ_W at scales $0 < |\boldsymbol{k}| < k_f$ (Yoffe, 2012)

$$\sum_{\boldsymbol{k}} \widehat{u}_i(-\boldsymbol{k},t)\widehat{f}_i(\boldsymbol{k},t) = \frac{\epsilon_W}{K_f} \sum_{\substack{\boldsymbol{k} \\ 0<|\boldsymbol{k}|<k_f}} \frac{1}{2}\widehat{u}_i(-\boldsymbol{k},t)\widehat{u}_i(\boldsymbol{k},t), \tag{2.15a}$$

$$= \frac{\epsilon_W}{K_f} \sum_{0<k<k_f} E(k,t), \tag{2.15b}$$

$$= \epsilon_W. \tag{2.15c}$$

Negative damping forcing is a standard type of forcing in DNS (see e.g. Machiels (1997); Kaneda and Ishihara (2006); Vela-Martín (2022b)). (2.14) does not prefer any particular direction and has a complicated, time-dependent spatial profile (McComb et al., 2015).

The second forcing is an ABC forcing (Podvigina and Pouquet, 1994; Linkmann, 2018)

$$\boldsymbol{f}(\boldsymbol{x}, k) = (A \sin kx_3 + C \cos kx_2, B \sin kx_1 + A \cos kx_3, C \sin kx_2 + B \cos kx_1). \tag{2.16}$$

This forcing is time-independent, deterministic and maximally helical as $\nabla_{\boldsymbol{x}} \times \boldsymbol{f}$ is parallel to $\boldsymbol{f}$ (Galanti and Tsinober, 2000). This forcing injects helicity $h = \boldsymbol{u} \cdot \boldsymbol{\omega}$, which limits the Lamb vector $\boldsymbol{\omega} \times \boldsymbol{u}$ and consequently non-linear interactions (Moffatt, 2014) (as $\boldsymbol{u} \cdot \nabla_{\boldsymbol{x}} \boldsymbol{u} = 1/2 \nabla_{\boldsymbol{x}} |\boldsymbol{u}|^2 - \boldsymbol{\omega} \times \boldsymbol{u}$ and $1/2 \nabla_{\boldsymbol{x}} |\boldsymbol{u}|^2$ can be absorbed in a modified pressure).

2.1.3 Initial Conditions

To integrate the vorticity equation forward in time, we need to set appropriate initial conditions. We choose realistic initial conditions (to be clarified below) such that we limit the computational effort to integrate the $\widehat{\boldsymbol{\omega}}$ field from this initial artificial configuration to homogeneous turbulence. This approach assumes that the turbulent flow after some initial transient $t > t_0$ loses its memory of the initial conditions in the sense that it has equal statistical behaviour across appropriate initial conditions for $t > t_0$ (this turbulence feature is denoted as "Loss of predictability" by Tsinober (2009)).

We use an algorithm from Yoffe (2012) to set the initial conditions for our DNSs. At each point in space, each velocity component is assigned a value according to a standard normal variable. This velocity field is transformed to Fourier space where it is made incompressible through the projection operator (see appendix B and equation (B.1)) and truncated for $k > k_{\max}$. The energy spectrum $E_c(k)$ is calculated from this velocity field $\widehat{\boldsymbol{u}}$ (see equation (2.20)). $\widehat{\boldsymbol{u}}$ is next scaled according to (':=' denotes computer assignment)

$$\widehat{\boldsymbol{u}}(\boldsymbol{k}, 0) := \widehat{\boldsymbol{u}}(\boldsymbol{k}, 0) \sqrt{\frac{E_m(k)}{E_c(k)}}, \tag{2.17}$$

where the model spectrum $E_m(k)$ is specified as

$$E_m(k) = 0.001702 k^4 e^{-2(k/5)^2}, \tag{2.18}$$

and it is plotted in figure 2.1. Equation (2.17) yields an initial velocity field which is random and solenoidal with kinetic energy similar to unity ($\int_0^\infty E_m(k) dk \sim 1$). At small wavenumbers $E_m(k) \sim k^4$, which mimics Batchelor turbulence (see Batchelor et al. (1956); Davidson (2015)). As k increases the local power-law exponent p in $E_m(k) \sim k^p$ decreases and p becomes negative. At large k, $E_m(k)$ decays exponentially (see Kraichnan (1959) and Pope (2000) on the exponential decay of E at dissipative k).

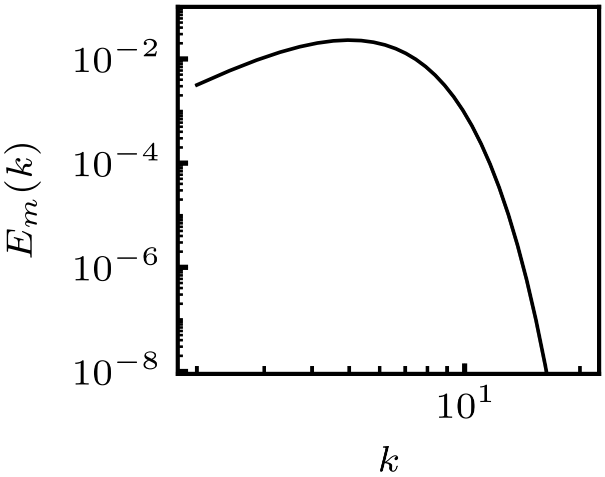

Figure 2.1: Yoffe's model spectrum (2.18) used to set DNS initial conditions.

2.1.4 Temporal Evolution

Having specified the various terms in the vorticity equation (2.5a) and initial conditions, we can numerically integrate (2.5a) forwards in time. We can write this equation in the semi-discretised form (the methods of lines) (Hirsch, 2007)

$$\frac{d\widehat{\boldsymbol{\omega}}(\boldsymbol{k},t)}{dt} = \boldsymbol{F}(\widehat{\boldsymbol{\omega}}), \tag{2.19}$$

where $\boldsymbol{F}(\widehat{\boldsymbol{\omega}})$ denotes the RHS of (2.5a). We integrate in time the ordinary differential equations (2.19) with the fourth-order low-storage Runge-Kutta-Gill (RKG) method (Gill, 1951). Algorithm 1 details the steps to integrate $\widehat{\boldsymbol{\omega}}$ one time step Δt forward.

The chosen spatial and temporal discretisations determine stability criteria arising from the viscous and convective terms. The viscous criterion reads $\nu k_{\mathrm{max}}^2 \Delta t \leq 2.79$ (Hirsch, 2007; Canuto et al., 1987). Note that the viscous term can alternatively be integrated exactly (see Rogallo (1977)). If c denotes a characteristic velocity scale, the convective term yields the stability criterion $k_{\mathrm{max}} c \Delta t \leq 2\sqrt{2}$ (Canuto et al., 1987). This critertion can be rewritten in terms of the CFL number $\beta = c\Delta t/\Delta x$ and reads $\beta \leq 3/\pi \approx 0.95$ (where Δx denotes the grid spacing $2\pi/N$).

The RKG method has truncation errors of order Δt^4 and tends to be used together with the dealiasing technique of Patterson and Orszag (1971) (see e.g. Ishihara et al. (2016)). This contrasts with the dealiasing technique of Rogallo (1977), where the reduction in aliasing errors is intimately linked to a second-order Runge-Kutta method. On one hand, the dealiasing and temporal integration method used in this thesis has a relatively high dealiasing cost but high temporal accuracy, allowing relatively large Δt. On the other hand, the dealiasing and temporal integration method of Rogallo (1977) has a lower dealiasing cost but lower temporal accuracy, allowing relatively small Δt (we discuss the issue of adequate temporal resolution in section 2.2.1).

Algorithm 1 Runge-Kutta-Gill method for the vorticity equation

```
$\boldsymbol{R} \coloneqq \boldsymbol{F}(\widehat{\boldsymbol{\omega}})\Delta t.$
$\widehat{\boldsymbol{\omega}} \coloneqq \widehat{\boldsymbol{\omega}} + 1/2\boldsymbol{R}.$
$\boldsymbol{Q} \coloneqq \boldsymbol{R}.$
$\boldsymbol{R} \coloneqq \boldsymbol{F}(\widehat{\boldsymbol{\omega}})\Delta t.$
$\widehat{\boldsymbol{\omega}} \coloneqq \widehat{\boldsymbol{\omega}} + (1 - 1/\sqrt{2})(\boldsymbol{R} - \boldsymbol{Q}).$
$\boldsymbol{Q} \coloneqq (-2 + 3/\sqrt{2})\boldsymbol{Q} + (2 - \sqrt{2})\boldsymbol{R}.$
$\boldsymbol{R} \coloneqq \boldsymbol{F}(\widehat{\boldsymbol{\omega}})\Delta t.$
$\widehat{\boldsymbol{\omega}} \coloneqq \widehat{\boldsymbol{\omega}} + (1 + 1/\sqrt{2})(\boldsymbol{R} - \boldsymbol{Q}).$
$\boldsymbol{Q} \coloneqq -(2 + 3/\sqrt{2})\boldsymbol{Q} + (2 + \sqrt{2})\boldsymbol{R}.$
$\boldsymbol{R} \coloneqq \boldsymbol{F}(\widehat{\boldsymbol{\omega}})\Delta t.$
$\widehat{\boldsymbol{\omega}} \coloneqq \widehat{\boldsymbol{\omega}} + 1/6(\boldsymbol{R} - 2\boldsymbol{Q}).$
```

2.1.5 In-situ Processing and Output

As the code numerically integrates the vorticity equation forwards in time, it calculates and outputs numerous quantities. These include:

Energy spectrum. The instantaneous three-dimensional energy spectrum is calculated from $\widehat{u}_i(\boldsymbol{k}, t)$ as

$$E(k,t) = \sum_{\substack{\boldsymbol{k} \\ k-1/2 \leq |\boldsymbol{k}| < k+1/2}} \frac{1}{2} \widehat{u}_i^*(\boldsymbol{k},t)\widehat{u}_i(\boldsymbol{k},t), \tag{2.20}$$

where the superscript '$*$' is the complex conjugate.

Turbulent kinetic energy. The spatially averaged turbulent kinetic energy $K(t)$ per unit mass is found by summing $E(k,t)$ across all wavenumbers k

$$K(t) = \sum_k E(k,t). \tag{2.21}$$

Integral length scale. A characteristic large-scale length scale, the integral length scale, is calculated as

$$L(t) = \frac{3\pi}{4} \sum_k k^{-1} E(k,t)/K(t) dk. \tag{2.22}$$

Viscous dissipation rate. The spatially averaged viscous dissipation rate ($\langle \ldots \rangle_{\boldsymbol{x}}$ denotes a spatial average over the computational domain) is calculated as

$$\langle \epsilon \rangle_{\boldsymbol{x}}(t) = 2\nu \sum_k k^2 E(k,t) dk. \tag{2.23}$$

Root-mean-square (r.m.s.) velocity. A large-scale velocity scale is found from $K(t)$. If one assumes isotropy, $\langle u_1^2 \rangle_{\boldsymbol{x}}(t) = \langle u_2^2 \rangle_{\boldsymbol{x}}(t) = \langle u_3^2 \rangle_{\boldsymbol{x}}(t) = u(t)^2$ and we get

$$u(t) = \sqrt{\frac{2}{3} K(t)}. \tag{2.24}$$

Dissipation coefficient. The dissipation rate can be normalised with large-scale quantities as

$$C_\epsilon(t) = \langle \epsilon \rangle_{\boldsymbol{x}}(t) \frac{L(t)}{u(t)^3}. \tag{2.25}$$

Small-scale resolution. The instantaneous Kolmogorov scale $\eta(t)$ is given as $\langle \epsilon \rangle_{\boldsymbol{x}}^{-1/4}(t) \nu^{3/4}$ (see section 1.2). The small-scale resolution can be measured in terms of the ratio of $\eta(t)$ to the highest resolved wavelength (see section 2.1.1)

$$k_{\max} \eta(t) = \frac{\sqrt{2}}{3} N \langle \epsilon \rangle_{\boldsymbol{x}}^{-1/4}(t) \nu^{3/4}. \tag{2.26}$$

Taylor scale. The Taylor scale $\lambda(t)$ is an intermediate length scale, i.e. $\eta(t) < \lambda(t) < L(t)$ (Pope, 2000). In homogeneous turbulence it is defined as (Taylor, 1935)

$$\lambda(t) = \Big(\frac{15 \nu u(t)^2}{\langle \epsilon \rangle_{\boldsymbol{x}}(t)}\Big)^{1/2}. \tag{2.27}$$

Reynolds number. In homogeneous turbulence the Reynolds number is typically specified in terms of the Taylor-scale Reynolds number

$$Re_\lambda(t) = \frac{u(t)\lambda(t)}{\nu}. \tag{2.28}$$

Courant-Friedrichs-Lewy (CFL) number. The CFL number characterises the ratio of the time step Δt to the smallest time scale of the numerical solution. The solver calculates at each time step the maximum CFL number across space and velocity components

$$\beta(t) = \max_i \Big[\max_{\boldsymbol{x}} \big(\frac{\Delta t}{\Delta x} u_i(\boldsymbol{x}, t) \big) \Big]. \tag{2.29}$$

Besides the above-listed quantities, the solver outputs $\boldsymbol{u}, p$ and $\boldsymbol{f}$ at regular time intervals (see section 2.2.2 and table 2.2).

2.2 Numerical Setup

2.2.1 Resolution Requirements and Large-scale Periodicity

A DNS needs to resolve all time and length scales of the flow. Otherwise, the results are resolution dependent and reminiscent of LES rather than DNS. We consider the spatial resolution in a DNS simulation with the quantity $k_{\max}\langle\eta\rangle_t$. This quantity is proportional to the ratio of the smallest turbulent length scale $\langle\eta\rangle_t$ to the smallest resolved length scale $(2\pi/k_{\max})$. As $k_{\max}\langle\eta\rangle_t$ increases, the spatial resolution improves. Traditionally, $k_{\max}\langle\eta\rangle_t$ has been set to about 1.50. This resolution is typically considered adequate for intermediate-scale quantities (Donzis et al., 2008). Intense small-scale quantities, e.g. higher-order moments of ϵ, require higher $k_{\max}\langle\eta\rangle_t$. The investigations of Yeung et al. (2018) suggest that the required $k_{\max}\langle\eta\rangle_t$ increases with $\langle Re_\lambda\rangle_t$ and that $k_{\max}\langle\eta\rangle_t \approx 5.5$ is adequate to capture the evolution of the maximum value of ϵ for $\langle Re_\lambda\rangle_t \leq 650$.

Regarding temporal resolution, accuracy is typically more restrictive than stability and typically requires $\langle\beta\rangle_t \lesssim 0.1$ for DNS simulations of homogeneous turbulence. Yeung et al. (2018) showed that $\langle\beta\rangle_t$ in the range $0.1-0.3$ for a spatially well-resolved simulation is adequate to resolve the time scales determining intense small-scale quantities. This study used a second-order temporal discretisation, such that the CFL range $0.1 - 0.3$ is a conservative range for a fourth-order temporal discretisation as used in this thesis.

Another quantity which can severely affect the numerical solution is the integral length scale $L(t)$ to box size (2π) ratio. If the ratio $2\pi/L(t)$ is too small, the largest scales of the flow will be affected by the imposed periodicity (Davidson, 2015). To avoid this scenario and have the turbulence mimic, say, turbulence in a wind tunnel, it is important that $L(t) \ll 2\pi$. However, if $L(t)$ is reduced, it limits the range of scales which can be resolved for a given resolution N. Typically, the compromise between achieving a high range of scales and limiting the effects of periodicity is selected in forced homogeneous turbulence as $2\pi/\langle L\rangle_t \approx 5$ (see e.g. Leung et al. (2012); Yeung et al. (2015); Iyer et al. (2020)).

2.2.2 DNS Data Description

We generated the DNS datasets in table 2.1 to pursue the thesis objectives outlined in section 1.3 within the resolution and large-scale periodicity restrictions of the previous section. We ensured that all datasets satisfy the "periodicity criterion" $2\pi/\langle L\rangle_t \gtrapprox 5$. All datasets have good temporal resolution with $\langle\beta\rangle_t \leq 0.20$ and $\beta(t) \leq 0.28$ at all times. This ensures that the convective stability criterion is satisfied and the viscous stability criterion is satisfied with $\nu k_{\max}^2\Delta t \leq 0.3 \ll 2.79$ across the datasets (see section 2.1.4).

Concerning the spatial resolution $k_{\max}\langle\eta\rangle_t$, there is a trade-off between resolution and the range of scales/Reynolds number. The dataset DNS1 is used in chapter 4 to study the small-scale dynamics, which requires a high spatial resolution $(k_{\max}\langle\eta\rangle_t = 5.5)$. The datasets DNS2-DNS3-DNS4 are used to study intermediate scale dynamics in chapters

	$\langle Re_\lambda \rangle_t$	N	ν	$k_{\max}\langle\eta\rangle_t$	$\langle\beta\rangle_t$	$2\pi/\langle L\rangle_t$	$\langle C_\epsilon\rangle_t$	Forcing
DNS1	81	512	0.003	5.5	0.19	5.8	0.50	ND
DNS2	111	256	0.0018	1.9	0.11	5.4	0.47	ABC
DNS3	112	256	0.0018	1.9	0.10	5.7	0.47	ND
DNS4	174	512	0.00072	1.9	0.20	5.4	0.45	ND

Table 2.1: DNS parameters and we used the acronym ND (negative damping).

3 and 5. This requires only moderately spatially resolved simulations ($k_{\max}\langle\eta\rangle_t = 1.9$), such that we can obtain higher Reynolds numbers for a given simulation size. The datasets DNS3-DNS4 with the same type of forcing allow us to investigate the Reynolds number effect on the dynamics. We use DNS2-DNS3 at the practically identical Reynolds number to consider the effect of the large-scale forcing on the dynamics. Note that the four datasets have $\langle C_\epsilon\rangle_t$ values consistent with the literature (Sreenivasan, 1998).

The datasets with the negative damping forcing all have the forcing parameters $k_f = 2.5$ and $\epsilon_W = 0.1$ (see section 2.1.2). We adopted these parameter values from previous studies (Linkmann and Morozov, 2015; Yasuda and Vassilicos, 2018). DNS2 is forced with the sum of two ABC forcings: one forcing with $A = B = C = 0.032$ at $k = 1$ and one forcing with $A = B = C = 0.095$ at $k = 2$. These parameters make DNS2-DNS3 have similar $\langle Re_\lambda\rangle_t$ and $2\pi/\langle L\rangle_t$ such that we can isolate the effect of the large-scale forcing.

There are initial transients in the simulations where the DNSs are affected in a statistical sense by the initial conditions (see section 2.1.3). We sample statistics from the datasets only after these initial transients. Figure 2.2 shows the temporal evolution of the turbulent kinetic energy $K(t)$ for the four datasets ($T \equiv \langle L\rangle_t/\langle u\rangle_t$ is the integral time scale). Initially, there are large variations in $K(t)$ before the variations become smaller in magnitude. $K(t)$ does not become constant after the initial transient but keeps varying due to cascade imbalances between the large-scale interscale transfer rate and the dissipation rate (Goto and Vassilicos, 2016a; Goto et al., 2017). Hence, the end of the initial transient is difficult to determine. The vertical lines in figure 2.2 show the times we start sampling the four DNSs as the $K(t)$ variations become similar to the variations at later times. We sample $\boldsymbol{u}$, p and $\boldsymbol{f}$ every $dT = 0.01T$ for the DNSs with $N = 256$ and every $dT = 0.1T$ for the DNSs with $N = 512$. $\boldsymbol{u}$ is also sampled Δt thereafter for every DNS so we can calculate time derivatives. dT, the sample starting time T_s, the sample end time T_e and the total sampling time $\Delta T = T_e - T_s$ are listed in table 2.2. The time-averaged statistics in table 2.1 and the KHMH terms (see section 2.3) are calculated over these time periods. Figure 2.3 shows the time-averaged three-dimensional energy spectra. An intermediate scale $-5/3$ scaling becomes increasingly apparent as $\langle Re_\lambda\rangle_t$ increases.

Note that our $\langle Re_\lambda\rangle_t$ are relatively limited due to the high computational cost of our KHMH Helmholtz-decomposed post-processing (which is typically at least one order of

	T_s/T	T_e/T	$\Delta T/T$	dT/T
DNS1	6.42	33.0	26.58	0.1
DNS2	11.68	31.31	19.63	0.01
DNS3	12.5	33.5	21	0.01
DNS4	8.63	35.5	26.87	0.1

Table 2.2: Sampling starting times T_s, sampling end times T_e, total sampling times ΔT and sampling intervals dT for fields $\boldsymbol{u}$, p and $\boldsymbol{f}$ in DNS1-DNS4.

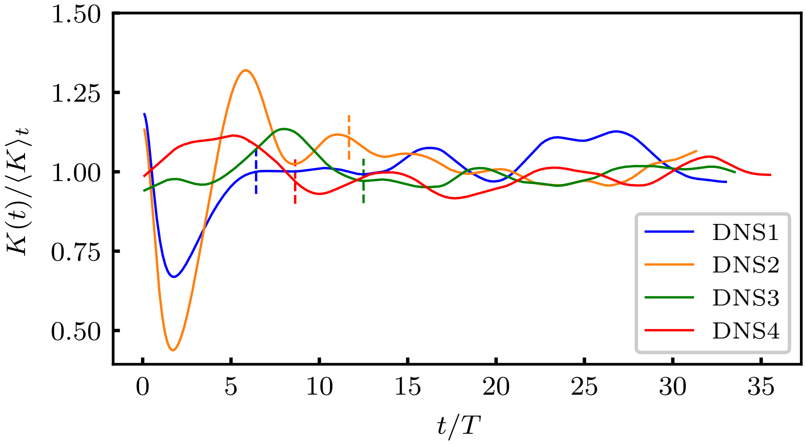

Figure 2.2: Temporal evolution of the turbulent kinetic energy $K(t)$ for the DNSs. The vertical dashed lines denote the time instances at which we start to sample data from the datasets after their initial transients.

magnitude more expensive than the DNSs themselves). We detail the computational expense of this particular aspect of the post-processing once the relevant terms have been introduced in section 3.1.3 (see also section 3.4 discussing an alternative evaluation method). The next section details the other aspects of our KHMH post-processing.

2.3 KHMH Post-processing

Having obtained appropriate DNSs datasets, we use $\boldsymbol{u}$, p and $\boldsymbol{f}$ to study the cascade dynamics in these simulations in terms of the KHMH equation and the spatially averaged KHMH equation (we introduce the KHMH equation (3.19) and an interpretation of its terms in the next chapter and we give its derivation in appendix A). This requires accurate calculations of the various KHMH terms, which we describe in this section (these calculations benefit from the Armadillo `C++` library (Sanderson and Curtin, 2016, 2018)).

A KHMH term $\mathcal{Q}$ at time t depends in general on its centroid $\boldsymbol{x}$ and its separation vector $\boldsymbol{r}$. In chapters 3-4 we calculate spatio-temporal KHMH statistics across scales (i.e. $\mathcal{Q}$ statistics over $\boldsymbol{x}$, $\boldsymbol{r}$ and t) and in chapter 5 we calculate temporal statistics across

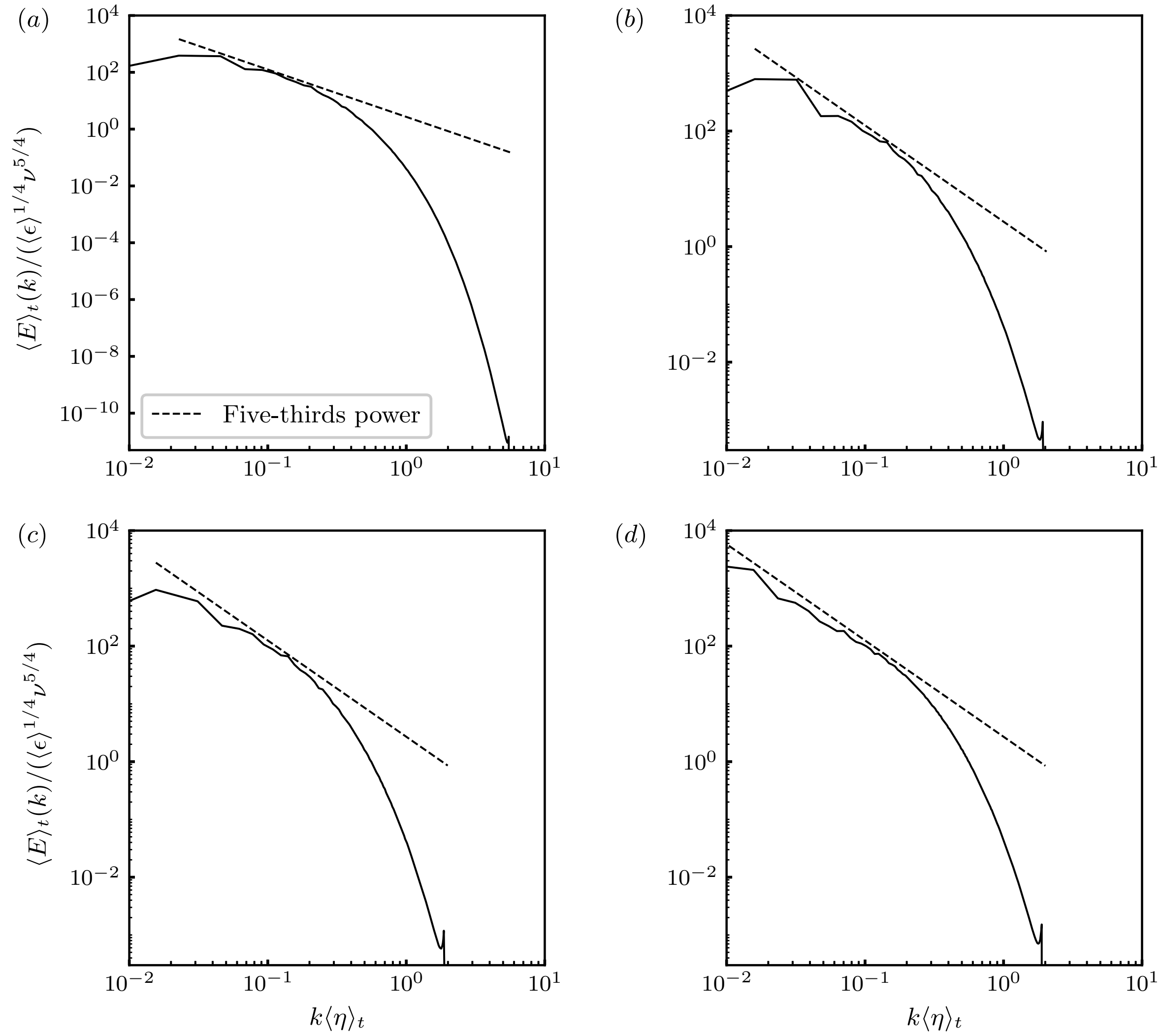

Figure 2.3: Time-averaged three-dimensional energy spectra $\langle E\rangle_t(k)$. $(a)-(d)$ correspond to the DNS datasets DNS1-DNS4. The energy spectra are normalised with K41 variables $\langle\epsilon\rangle$ and ν and $\langle\ldots\rangle$ denotes a space and time average.

scales of spatially averaged KHMH terms $\langle\mathcal{Q}\rangle_{\boldsymbol{x}} = \langle\mathcal{Q}\rangle_{\boldsymbol{x}}(\boldsymbol{r},t)$ (i.e. $\langle\mathcal{Q}\rangle_{\boldsymbol{x}}$ statistics over t and $\boldsymbol{r}$). The latter case of spatially averaged KHMH terms permits efficient and accurate evaluation methods which take advantage of Parseval's theorem; the KHMH terms can be rewritten in terms of sums of products of velocity/force components which can be evaluated in Fourier space. E.g. we can evaluate $\langle u_i(\boldsymbol{x}+\boldsymbol{r})u_j(\boldsymbol{x})\rangle_{\boldsymbol{x}}$ in Fourier space as

$$\langle u_i(\boldsymbol{x}+\boldsymbol{r})u_j(\boldsymbol{x})\rangle_{\boldsymbol{x}} = \langle\sum_{\boldsymbol{k}} \widehat{u}_i(\boldsymbol{k}) e^{i\boldsymbol{k}\cdot(\boldsymbol{x}+\boldsymbol{r})} \sum_{\boldsymbol{k}'} \widehat{u}_j(\boldsymbol{k}') e^{i\boldsymbol{k}'\cdot\boldsymbol{x}}\rangle_{\boldsymbol{x}}, \tag{2.30a}$$

$$= \sum_{\boldsymbol{k}} \widehat{u}_i(\boldsymbol{k}) \widehat{u}_j^{*}(\boldsymbol{k}) e^{i\boldsymbol{r}\cdot\boldsymbol{k}}, \tag{2.30b}$$

where the final line follows from the orthogonality of Fourier modes and $\widehat{u}_i$ conjugate symmetry. We derive expressions for the spatially averaged KHMH terms in terms of $\widehat{u}_i$ and $\widehat{f}_i$ in appendix C. This methodology was inspired by Gatti et al. (2019), who used this approach to calculate spatially averaged KHMH terms in the turbulent channel flow.

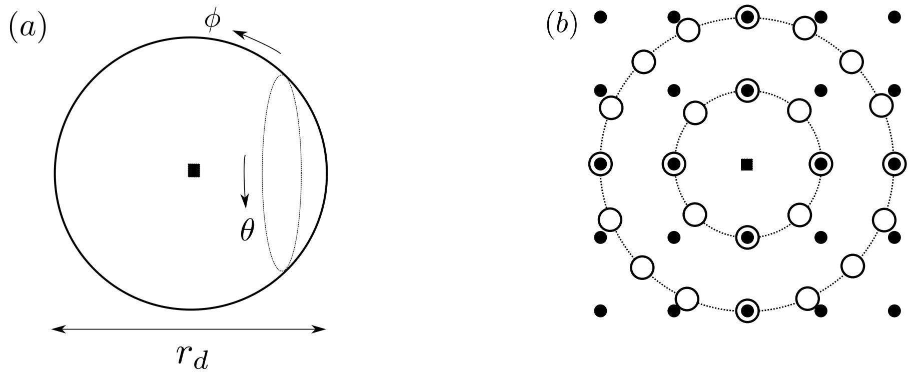

Figure 2.4: (*a*) The spherical coordinate system. The filled square denotes its centre. (*b*) The integration and grid points with radii $r = 1$ and $r = 2$. The filled circles are grid points and the open circles are integration points.

We calculate $\mathcal{Q}(\boldsymbol{x}, \boldsymbol{r}, t)$ spatio-temporal statistics in physical space. The KHMH terms can be rewritten in terms of combinations of terms involving $\boldsymbol{u}, \boldsymbol{f}, p$ and their derivatives at locations $\boldsymbol{x} \pm \boldsymbol{r}/2$ (see the end of appendix A for two examples). As the points $\boldsymbol{x} \pm \boldsymbol{r}/2$ do not necessarily coincide with grid points, we calculate the contributions to the KHMH terms with trilinear interpolation. We use sixth-order central differences for spatial derivatives and first-order forward differences for time derivatives (and we use the same time discretisation for time derivatives of the spatially averaged KHMH terms).

We typically consider statistics of KHMH terms $\mathcal{Q}$ (or quantities derived from KHMH terms such as $\mathcal{Q}^2$) in terms of their spherically averaged values across scales $r_d = |\boldsymbol{r}|$. If we let $\mathcal{Q}$ denote an arbitrary KHMH term or a derived KHMH quantity, the spherical averaging operation over a sphere of diameter r_d can be written as

$$\mathcal{Q}^a = \frac{1}{\pi r_d^2} \iint_{|\boldsymbol{r}|=r_d} \mathcal{Q} d\boldsymbol{r}, \tag{2.31a}$$

$$= \frac{1}{4\pi} \int_0^{\pi} \sin\phi \; d\phi \int_0^{2\pi} \mathcal{Q} \; d\theta, \tag{2.31b}$$

where θ and ϕ denote the polar and azimuthal angles (see figure 2.4(*a*)). We approximate (2.31) numerically by two repeated one-dimensional quadratures

$$\mathcal{Q}^a \approx \frac{1}{4\pi} \int_0^{\pi} \sin\phi \; d\phi \sum_{j=1}^{N_\theta(\phi)} w_j \mathcal{Q}(\phi, \theta_j) \Delta\theta, \tag{2.32a}$$

$$\approx \frac{1}{4\pi} \sum_{i=1}^{N_\phi(r)} \sum_{j=1}^{N_\theta(r,\phi)} w_i w_j \sin\phi_i \mathcal{Q}(\phi_i, \theta_j) \Delta\theta \Delta\phi, \tag{2.32b}$$

where w_i and w_j are integration weights, N_ϕ and N_θ are the number of grid points in azimuthal and polar directions, $\Delta\theta$ and $\Delta\phi$ are the spherically equidistant integration spacings and r denotes the integration radius in integer grid points. For a given r we have $N_\phi = 4r + 1$ and $N_\theta = 8r_\phi = 8r\sin\phi$ available grid points, where r_ϕ denotes the radius of the circle at the given ϕ (see figure 2.4). The grid spacings are given as $\Delta\phi = \pi/(N_\phi(r)-1)$

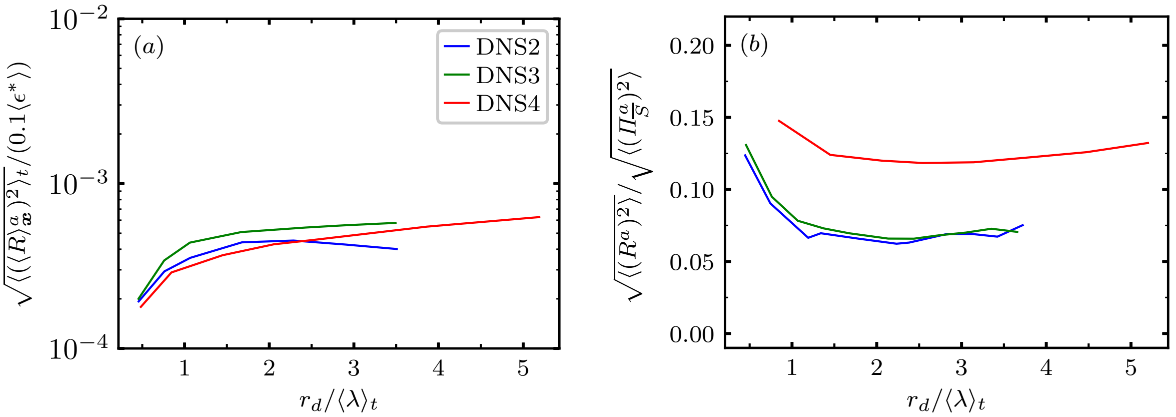

Figure 2.5: Relative KHMH residuals at intermediate and large scales for DNS datasets DNS2-DNS3-DNS4. (*a*) Relative average residual magnitudes of the spatially averaged KHMH equation. (*b*) Relative average residual magnitudes of the KHMH equation.

and $\Delta\theta = 2\pi/(N_\theta(r,\phi) - 1)$. We use Simpson's rule to set the weights w_i and w_j.

The equidistant integration approach limits the distance between grid points and integration points (see figure 2.4(*b*)) such that we limit the effect of interpolation errors in the computation of $\mathcal{Q}(\phi_i, \theta_j)$. This is important at small scales where the grid spacing and the scales of interest are of a similar order of magnitude. This contrasts with a Lebedev quadrature approach where interpolation errors from a discrete grid are not considered (Lebedev, 1975) (and as we generally do not calculate the entire $\mathcal{Q}$ field in $\boldsymbol{x}$-space, we cannot use the recent integration method of Iyer et al. (2017), which spectrally interpolates the field of interest to Lebedev integration points). The smallest integration sphere we employ is for DNS1 with the sphere $r = 1$ and $r_d \approx \langle\eta\rangle_t$. This results in rather coarse spherical averages $\mathcal{Q}^a$ (i.e. 26 integration points). The spherically averaged $\mathcal{Q}$ might not be converged in terms of the spherical integration, and one should be careful when comparing absolute statistics (such as e.g. $\langle\mathcal{Q}^2\rangle^a$ where $\langle\rangle$ denotes a spatio-temporal average) at small scales between studies using coarse surface integrations (we get a lower estimate of the integration error at $r = 1$ by integrating a constant over the sphere with a relative error of $3 * 10^{-3}$). In terms of relative magnitudes, the coarseness of the spherical averaging does not invalidate relative statements between KHMH terms $\mathcal{Q}_1^a$ and $\mathcal{Q}_2^a$ such as $\mathcal{Q}_1^a \gg \mathcal{Q}_2^a$. We see from (2.32b) that the local difference between KHMH terms $\mathcal{Q}_1^a$ and $\mathcal{Q}_2^a$ can only be considerable if $\mathcal{Q}_1 \gg \mathcal{Q}_2$ in an average sense over the considered separations $\boldsymbol{r}$.

We consider the accuracy of our KHMH post-processing methodology by calculating the residuals of the relevant KHMH equations (which will be introduced in the following chapters). We denote the local residual of the solenoidal KHMH equation (3.22a) as $R(\boldsymbol{x}, \boldsymbol{r}, t)$ such that the residual of the spatially and spherically averaged solenoidal KHMH equation equals $\langle R\rangle^a_{\boldsymbol{x}}(r_d, t)$. The effect of the residuals on the KHMH statistics of interest are negligible if the magnitudes of the residuals are negligible compared to the

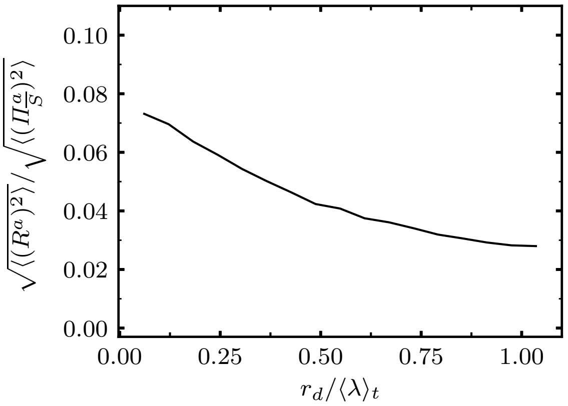

Figure 2.6: Relative KHMH residuals at small scales for dataset DNS1.

magnitudes of the dominant KHMH terms. That is, in chapter 5 we study the spatially averaged KHMH dynamics at intermediate and large scales. For our results from DNS datasets DNS2-DNS3-DNS4 to be appropriately accurate, we require that the magnitude of the average residual in the spatially averaged KHMH equation $\sqrt{\langle (\langle R\rangle^a_{\boldsymbol{x}})^2\rangle_t}$ to be negligible compared to the magnitude of the dominant spatially averaged KHMH terms (see figure 5.2). We show in this chapter that this latter quantity is of the order $0.1\langle\epsilon^*\rangle$, where ϵ^* is the two-point viscous pseudo-dissipation rate (see equation (3.20)). Figure 2.5(a) shows that indeed the residuals are negligible compared to the dominant spatially averaged KHMH terms at intermediate and large scales. These results confirm the evaluation methods of the spatially averaged KHMH terms developed in appendix C and show that the time-derivative evaluation and spherical integration methods are accurate (note that these two latter methods are also used in chapters 3-4).

Chapter 3 studies the spatio-temporally fluctuating cascade dynamics at intermediate and large scales. Our KHMH post-processing of DNS2-DNS3-DNS4 is appropriately accurate if the magnitudes of the spatio-temporal residuals $\sqrt{\langle (R^a)^2\rangle}$ are negligible compared to the spatio-temporal fluctuations of the dominant KHMH terms, which equals $\sqrt{\langle (\Pi^a_{\overline{S}})^2\rangle}$ where $\Pi_{\overline{S}}$ is the solenoidal interscale transfer rate (see chapter 3 and figure 3.9). Figure 2.5(b) shows that the residuals are an order of magnitude smaller than the dominant KHMH terms at intermediate and large scales for DNS2-DNS3-DNS4. The normalised residuals seem to increase with $\langle Re_\lambda\rangle_t$. As the spatial resolution is almost identical for these DNSs, it seems that the spatio-temporal KHMH dynamics become increasingly challenging to resolve/demanding finer spatial resolution as $\langle Re_\lambda\rangle_t$ increases.

Finally, chapter 4 studies the spatio-temporally fluctuating cascade dynamics at small scales. Our KHMH post-processing of DNS1 is appropriately accurate if the spatio-temporal residuals $\sqrt{\langle (R^a)^2\rangle}$ are negligible compared to $\sqrt{\langle (\Pi^a_{\overline{S}})^2\rangle}$ at small scales (see figure 4.2(c)). This is verified in figure 2.6 with the residuals being an order of magnitude smaller than the dominant KHMH terms. All in all, our KHMH post-processing methodology applied to our DNS datasets is adequately accurate to study the cascade dynamics as outlined in the thesis objectives (see section 1.3).

3. Interscale and Interspace Energy Transfer Dynamics in Homogeneous Turbulence

Turbulence has been known to be intermittent since the late 1940s (Batchelor et al., 1949), and this intermittency has mainly been taken into account as structure function exponent corrections to K41's average picture (see section 1.2). However, Yasuda and Vassilicos (2018) studied intermittent fluctuations without reference to structure function exponents which require high Reynolds numbers to be well defined and to be predicted from Kolmogorov's theory or various intermittency-accounting variants of this theory (see Frisch (1995) and references therein). They concentrated their attention on the actual fundamental basis of Kolmogorov's theory which is scale-by-scale equilibrium for statistically homogeneous and stationary turbulence, and not on the theory's structure function and energy spectrum scaling consequences. The scale-by-scale equilibrium implied by statistical homogeneity and stationarity is that the average interscale turbulence energy transfer rate is balanced by nothing more than average scale-by-scale viscous diffusion rate, average turbulence dissipation rate and average energy input rate by a stirring force, irrespective of Reynolds number (except that the Reynolds number needs to be large enough for the presence of random fluctuations). It is most natural for a study of intermittency to start with the fluctuations around this balance, which means that along with the fluctuations of interscale transfer, dissipation, diffusion and energy input, all other fluctuating turbulent energy change rates need to be taken into account as well even if their spatio-temporal averages equal zero.

The intermittency corrections to Kolmogorov's average cascade theory which have been developed since the 1960s (e.g. see Sreenivasan and Antonia (1997)) are most often based on the intermittent fluctuations of the local (in space and time) turbulence dissipation rate, yet Yasuda and Vassilicos (2018) demonstrated that these dissipation fluctuations are much less intense than the fluctuations of other turbulent energy change rates such as the non-linear interspace energy transfer rate (which is a scale-by-scale rate of turbulent transport in physical space), the fluctuating work resulting from the correlation of the fluctuating pressure gradient with the fluctuating velocity and the time-derivative of the scale-by-scale turbulent kinetic energy. These results showed that the fluctuations around the average scale-by-scale balance are significant at low to moderate Reynolds numbers ($\langle Re_\lambda \rangle_t$ ranging from 80 to 170), implying that the average scale-by-scale balance is not locally representative at such Reynolds numbers. Moreover the various energy exchange processes exhibit significant correlations: the fluctuating pressure-velocity term is correlated with the interscale energy transfer rate, and the time derivative of the turbulent kinetic energy below a certain two-point length r_d is correlated with the inter-space energy transport rate at the same length r_d. Yasuda and Vassilicos (2018) explained the former correlation as resulting from the link between non-linearity and pressure and the latter correlation as reflecting the passive sweeping of small turbulent eddies by large ones (Tennekes, 1975) (Baj et al. (2022) recently showed that these correlation results extend to higher Reynolds numbers forced homogeneous/periodic turbulence at $\langle Re_\lambda \rangle_t = 433$ and the von Kárman flow at $\langle Re_\lambda \rangle_t = 199$). This sweeping (also termed "random Taylor hypothesis") has been studied by reference to the one-point incompressible Navier-Stokes equation (e.g. Tennekes (1975), Tsinober et al. (2001)) rather than the two-point Kármán-Howarth-Monin-Hill (KHMH) equation, used by Yasuda and Vassilicos (2018) in their study of the fluctuating turbulence cascade. The KHMH equation is a scale-by-scale energy budget local in space and time, directly derived from the incompressible Navier-Stokes equations for the instantaneous velocity field (see Hill (2002)) without decomposition (e.g. Reynolds decomposition), without averages (e.g. Reynolds averages), and without any assumption made about the turbulent flow (e.g. isotropy).

The initial trigger of the present chapter is to substantiate the claim of Yasuda and Vassilicos (2018) concerning KHMH correlations being caused by random sweeping by translating the sweeping analysis of Tsinober et al. (2001) to the KHMH equation. In doing so we espouse the Helmholtz decomposition which Tsinober et al. (2001) introduced for the analysis of the acceleration field. We apply it to the two-point Navier-Stokes difference (NSD) equation (which is the equation governing the dynamics of two-point velocity differences) and the KHMH equation which derives from it. This decomposition into solenoidal and irrotational terms breaks the Navier-Stokes equation into two equations, one being the irrotational balance between non-linearity and pressure and the other being the solenoidal balance between local unsteadiness and advection which encapsulates the sweeping. With this decomposition we substantiate all the correlations observed by Yasuda and Vassilicos (2018) between different KHMH terms representing different energy change processes, not only the ones caused by sweeping. In fact, we educe the relation between interspace turbulence energy transfer/transport and two-point sweeping (i.e. the random Taylor hypothesis that we generalise to two-point statistics), and we extend the correlation study to solenoidal and irrotational sub-terms of the KHMH equation. This leads to even stronger correlations than those found by Yasuda and Vassilicos (2018) and deeper insights into the local cascade dynamics. We also study the recently introduced decomposition (Alves Portela et al., 2020) of the interscale transfer rate into a homogeneous and an inhomogeneous interscale transfer component. We analyse their fluctuations and the correlations of these fluctuations, both unconditionally and conditionally on relatively rare intense interscale transfer events. Finally, we derive solenoidal and irrotational KHMH equations for arbitrary boundary conditions.

Section 3.1.1 is a reminder of the application of the Helmholtz decomposition to the one-point Navier-Stokes equation by Tsinober et al. (2001). In this section we also validate our DNSs by retrieving the conclusions of Tsinober et al. (2001) on sweeping and by comparing our DNS results on one-point acceleration dynamics to theirs. In sections 3.1.2-3.1.3 we apply the Helmholtz decomposition to the two-point NSD equation for the case of homogeneous/periodic turbulence and in section 3.1.4 we derive from the Helmholtz decomposed Navier-Stokes difference equations corresponding KHMH equations. Section 3.1.4 formalises the connection between the NS and KHMH dynamics, clarifies under which conditions a link exists between NS and KHMH dynamics and provides results on scale and Reynolds number dependencies of the KHMH dynamics. By considering the NSD dynamics in terms of solenoidal and irrotational dynamics, we derive two new KHMH equations. In section 3.2 we use these two new KHMH equations to obtain new results on the fluctuating cascade dynamics across scales both unconditionally and conditionally on relatively rare intense interscale energy transfer events. In section 3.3 we analyse the inhomogeneous and homogeneous contributions to the interscale energy transfer rate (Alves Portela et al., 2020). Section 3.4 derives the irrotational and solenoidal KHMH equations for arbitrary boundary conditions (rather than periodic boundary conditions). Finally, section 3.5 summarises our results.

3.1 Helmholtz Decomposition of Two-point Navier-Stokes Dynamics and Corresponding Turbulent Energy Exchanges

We next show how we apply the Helmholtz decomposition to the KHMH equation for homogeneous/periodic turbulence. We start in 3.1.1 by applying this decomposition to the one-point Navier-Stokes equation following Tsinober et al. (2001). In this section we also validate DNS2-DNS3-DNS4 by retrieving the conclusions and results of Tsinober et al. (2001) on one-point acceleration dynamics. In sections 3.1.2 and 3.1.3 we apply the Helmholtz decomposition to the two-point Navier-Stokes difference equation for the case of homogeneous/periodic turbulence and in section 3.1.4 we derive from the Helmholtz-decomposed Navier-Stokes difference equations corresponding KHMH equations.

The converged spatio-temporal results are mainly from the datasets DNS3-DNS4 (with negative damping forcing and Taylor-scale Reynolds numbers 112 and 174), but we display some key results also for the dataset DNS2 (with ABC forcing and $\langle Re_\lambda \rangle_t = 111$). Unless otherwise stated, the results from the dataset with the ABC forcing are qualitatively equal to the results with the negative damping forcing with $\langle Re_\lambda \rangle_t = 112$.

3.1.1 Solenoidal and Irrotational Acceleration Fluctuations

The Helmholtz decomposition states that a twice continuously differentiable 3D vector field $\boldsymbol{q}(\boldsymbol{x},t)$ defined on a domain $V \subseteq \mathbb{R}^3$ can be expressed as the sum of an irrotational vector field $\boldsymbol{q}_I(\boldsymbol{x},t)$ and a solenoidal vector field $\boldsymbol{q}_S(\boldsymbol{x},t)$ (Helmholtz, 1867; Sprössig, 2010)

$$\boldsymbol{q}_I(\boldsymbol{x},t) = -\nabla_{\boldsymbol{x}}\phi(\boldsymbol{x},t), \quad \boldsymbol{q}_S(\boldsymbol{x},t) = \nabla_{\boldsymbol{x}} \times \boldsymbol{B}(\boldsymbol{x},t), \tag{3.1}$$

where $\phi(\boldsymbol{x},t)$ is a scalar potential and $\boldsymbol{B}(\boldsymbol{x},t)$ is a vector potential. Helmholtz's rationale in developing this decomposition was in the description of continuous fluid motion in $\mathbb{R}^3$. He considered the fluid motion consisting of: *i*) expansion or contraction in three orthogonal directions, *ii*) rotation about an instantaneous axis and *iii*) translation (Helmholtz, 1867). The expansion/contraction can be considered as a scalar potential as the corresponding motion is irrotational ($\nabla_{\boldsymbol{x}} \times \nabla_{\boldsymbol{x}} = 0$), and the second part can be considered as the curl of a vector potential as the corresponding motion is solenoidal/incompressible ($\nabla_{\boldsymbol{x}} \cdot \nabla_{\boldsymbol{x}} \times = 0$). The translation being both solenoidal and irrotational can be considered as either included in the vector potential or in the scalar potential (Bhatia et al., 2013). The Helmholtz decomposition and its interpretation can be applied to any vector field $\boldsymbol{q}(\boldsymbol{x},t)$ satisfying the above conditions, and Tsinober et al. (2001) applied it to fluid accelerations and the incompressible Navier-Stokes equation.

The solenoidal and irrotational Navier-Stokes equations in homogeneous/periodic turbulence can be derived from the incompressible Navier-Stokes equation in Fourier space. After transforming back to physical space, one obtains

$$\frac{\partial \boldsymbol{u}}{\partial t} + (\boldsymbol{u} \cdot \nabla_{\boldsymbol{x}}\boldsymbol{u})^T = \nu\nabla^2_{\boldsymbol{x}}\boldsymbol{u} + \boldsymbol{f}^T, \tag{3.2a}$$

$$(\boldsymbol{u} \cdot \nabla_{\boldsymbol{x}}\boldsymbol{u})^L = -\frac{1}{\rho}\nabla_{\boldsymbol{x}}p + \boldsymbol{f}^L, \tag{3.2b}$$

where superscripts L and T denote fields obtained from longitudinal and transverse parts of respective Fourier vector fields (see the first paragraph of appendix B for definitions). For a periodic vector field $\boldsymbol{q}$, $\boldsymbol{q}^L$ equals the irrotational field $\boldsymbol{q}_I$ and $\boldsymbol{q}^T$ equals the solenoidal field $\boldsymbol{q}_S$ (see appendix B). From (3.2a)-(3.2b), one arrives at (Tsinober et al., 2001)

$$\frac{\partial \boldsymbol{u}}{\partial t} + (\boldsymbol{u} \cdot \nabla_{\boldsymbol{x}}\boldsymbol{u})_S = \nu\nabla^2_{\boldsymbol{x}}\boldsymbol{u} + \boldsymbol{f}_S, \tag{3.3a}$$

$$(\boldsymbol{u} \cdot \nabla_{\boldsymbol{x}}\boldsymbol{u})_I = -\frac{1}{\rho}\nabla_{\boldsymbol{x}}p + \boldsymbol{f}_I, \tag{3.3b}$$

which we refer to as Tsinober equations. (3.3a) contains only solenoidal vector fields and (3.3b) contains only irrotational vector fields. Note that in the case of an incompressible periodic velocity field, the velocity field is solenoidal, i.e. $\boldsymbol{u} = \boldsymbol{u}_S$. This follows immediately from the scalar potential ϕ being the solution to $\nabla^2_{\boldsymbol{x}}\phi = 0$ with periodic boundary conditions for $\nabla_{\boldsymbol{x}}\phi$, yielding $\phi = const$.

	$\langle \boldsymbol{q}^2\rangle/(3\langle\epsilon\rangle^{3/2}\nu^{-1/2})$			$\langle \boldsymbol{q}^2\rangle/\langle \boldsymbol{a}_c^2\rangle$		
$\langle Re_\lambda\rangle_t$	111	112	174	111	112	174
$\boldsymbol{a}_c$	7.21	8.47	14.28	1	1	1
$\boldsymbol{a}_l$	4.92	5.87	11.21	0.68	0.69	0.78
$\boldsymbol{a}_{c_S}$	4.98	5.93	11.26	0.69	0.70	0.79
$\boldsymbol{a}_{c_I}$	2.23	2.55	3.03	0.31	0.30	0.21
$\boldsymbol{a}_p$	2.23	2.55	3.03	0.31	0.30	0.21
$\boldsymbol{a}$	2.38	2.60	3.09	0.32	0.31	0.22
$\boldsymbol{a}_\nu$	0.05	0.05	0.05	0.0069	0.0062	0.0038
$\boldsymbol{f}$	0.01	0.007	0.005	0.00020	0.00081	0.00032

Table 3.1: Normalised average magnitudes $\langle \boldsymbol{q}^2\rangle/(3\langle\epsilon\rangle^{3/2}\nu^{-1/2})$ and $\langle \boldsymbol{q}^2\rangle/\langle \boldsymbol{a}_c^2\rangle$ for Navier-Stokes accelerations and forces $\boldsymbol{q}$ for DNS2-DNS3-DNS4. The former normalisation and the notation $\boldsymbol{q}^2 \equiv q_i q_i$ follow from Tsinober et al. (2001).

In section 3.4 we show that (3.3a) is the integrated vorticity equation and that (3.3b) is the integrated Poisson equation for pressure. The procedure presented in section 3.4 for obtaining the Tsinober equations is also used in this same section to obtain generalised Tsinober equations for turbulence with arbitrary boundary conditions.

Following the notation of Tsinober et al. (2001), we define $\boldsymbol{a}_l \equiv \partial\boldsymbol{u}/\partial t$, $\boldsymbol{a}_c \equiv \boldsymbol{u}\cdot\nabla_{\boldsymbol{x}}\boldsymbol{u}$, $\boldsymbol{a} \equiv \boldsymbol{a}_l + \boldsymbol{a}_c$, $\boldsymbol{a}_p \equiv -1/\rho\nabla_{\boldsymbol{x}} p$ and $\boldsymbol{a}_\nu \equiv \nu\nabla^2_{\boldsymbol{x}}\boldsymbol{u}$. In such notation, equations (3.3a)-(3.3b) are $\boldsymbol{a}_l + \boldsymbol{a}_{c_S} = \boldsymbol{a}_\nu + \boldsymbol{f}_S$ and $\boldsymbol{a}_{c_I} = \boldsymbol{a}_p + \boldsymbol{f}_I$. Tsinober et al. (2001) in fact wrote these equations for statistically homogeneous/periodic Navier-Stokes turbulence without body forces, i.e. with $\boldsymbol{f} = 0$. In general, however, the body forcing can be considered, as in the present work, to be non-zero and typically incompressible, i.e. $\boldsymbol{f}_I = \boldsymbol{0}$ but $\boldsymbol{f}_s \not\equiv \boldsymbol{0}$, given that a compressible component of the forcing can be subsumed into the pressure field in incompressible turbulence. In body-forced statistically stationary homogeneous/periodic turbulence, the average forcing magnitude $\langle \boldsymbol{f}^2\rangle (\equiv \langle f_i f_i\rangle)$, where the brackets denote spatio-temporal averaging, tends to be small compared to $\langle \boldsymbol{a}_\nu^2\rangle$ when the forcing is applied only to the largest scales (Vedula and Yeung, 1999). Given that $\langle \boldsymbol{f}\cdot\boldsymbol{u}\rangle = \langle\epsilon\rangle$, where ϵ is the viscous (pseudo-)dissipation rate, $\boldsymbol{f}^2$ can be quite small if $\boldsymbol{f}$ is not close to orthogonal to the velocity field. This is indeed the case with the negative damping and ABC forcings used in this study. In cases where $\boldsymbol{f}$ is close to orthogonal to the velocity field, which is conceivable in electromagnetic situations (Lorentz force), $\boldsymbol{f}^2$ needs to be large enough for $\langle \boldsymbol{f}\cdot\boldsymbol{u}\rangle$ to balance $\langle\epsilon\rangle$. In this study we have not considered such forcings and some of our results might not apply to such situations. Our results for the forcings we used indicate that $\langle \boldsymbol{f}^2\rangle$ is indeed much smaller than $\langle \boldsymbol{a}_\nu^2\rangle$ (see results from our DNS in table 3.1) and the probability to find values of $\boldsymbol{f}^2$ large enough to be comparable to the other terms in the Tsinober equations is extremely small (see results from our DNS in figure 3.1 and table 3.2 where we see, in particular, that $|\boldsymbol{f}| > 0.1|\boldsymbol{a}_{c_S}|$ in 15.3% and 6.3% of the

α	0.001	0.01	0.1	1
Prob($\boldsymbol{a}_\nu^2 > \alpha \boldsymbol{a}_{c_S}^2$)	(0.893, 0.808)	(0.441, 0.308)	(0.068, 0.037)	(0.004, 0.002)
Prob($\boldsymbol{f}^2 > \alpha \boldsymbol{a}_{c_S}^2$)	(0.707, 0.476)	(0.155, 0.063)	(0.008, 0.003)	($3 * 10^{-4}$, $9 * 10^{-5}$)

Table 3.2: Probabilities of events $\boldsymbol{q}^2 > \alpha \boldsymbol{p}^2$ for NS terms $(\boldsymbol{q}, \boldsymbol{p})$ with α specified on the top row. The two probability values in the brackets for each $(\boldsymbol{q}, \boldsymbol{p}, \alpha)$ combination refer to $\langle Re_\lambda \rangle_t = 112$ and $\langle Re_\lambda \rangle_t = 174$ respectively.

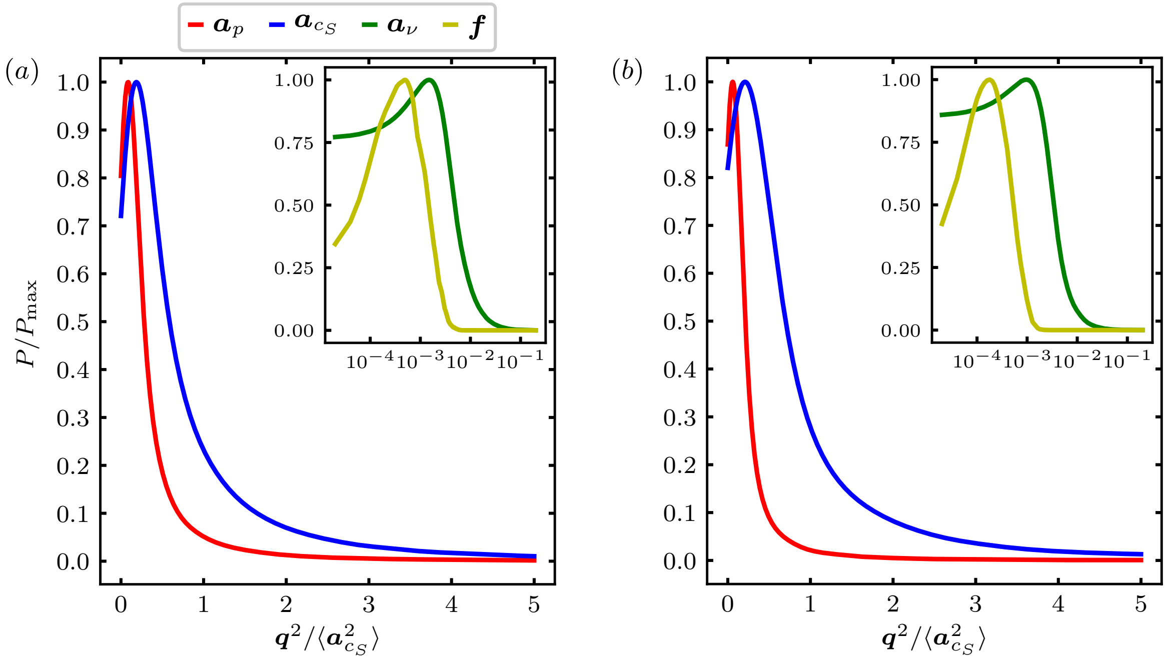

Figure 3.1: Probability density functions (PDFs) P of Navier-Stokes acceleration and force magnitudes $\boldsymbol{q}^2$ for terms $\boldsymbol{q}$ listed at the top of (a). $P_{\max}$ for the PDF of $\boldsymbol{q}^2$ denotes its maximum value. (a) $\langle Re_\lambda \rangle_t = 112$, (b) $\langle Re_\lambda \rangle_t = 174$.

spatio-temporal domain for the two Reynolds numbers respectively, the percentage being smaller for the higher Reynolds number. If we consider $|\boldsymbol{f}| > \sqrt{0.1}|\boldsymbol{a}_{c_S}| \approx 0.32|\boldsymbol{a}_{c_S}|$, we see that this is only satisfied in 0.8% and 0.3% of the spatio-temporal domain respectively. Furthermore, figure 3.1 and table 3.2 show that $\boldsymbol{f}$ is also typically much smaller than $\boldsymbol{a}_\nu$. We can therefore write $\boldsymbol{a}_l + \boldsymbol{a}_{c_S} \approx \boldsymbol{a}_\nu$, this being a good approximation in the majority of the flow for the majority of the time. With $\boldsymbol{a}_{c_I} = \boldsymbol{a}_p$ given that $\boldsymbol{f}_I = \boldsymbol{0}$, these two equations are very close to the way that Tsinober et al. (2001) originally wrote them ($\boldsymbol{a}_l + \boldsymbol{a}_{c_S} = \boldsymbol{a}_\nu$ and $\boldsymbol{a}_{c_I} = \boldsymbol{a}_p$ for $\boldsymbol{f} \equiv 0$) and we can therefore expect to retrieve the results and conclusions of Tsinober et al. (2001).

The DNS of Tsinober et al. (2001) showed that $\boldsymbol{a}_\nu$ is typically negligible (i.e. in a statistical sense, not everywhere at any time in the flow) compared to all the other acceleration terms in the Tsinober equations, namely $\boldsymbol{a}_l$, $\boldsymbol{a}_{c_S}$, $\boldsymbol{a}_{c_I}$ and $\boldsymbol{a}_p$. This is confirmed by our DNS results in tables 3.1-3.2 and in figure 3.1 which are for similar Reynolds numbers to those of Tsinober et al. (2001) and where we report magnitudes, and probabilities of

$\langle Re_\lambda \rangle_t$	$\langle \cos(\boldsymbol{a}_{c_I}, \boldsymbol{a}_p) \rangle$	$\langle \cos(\boldsymbol{a}, \boldsymbol{a}_p) \rangle$	$\langle \cos(\boldsymbol{a}_l, \boldsymbol{a}_{c_S}) \rangle$	$\langle \cos(\boldsymbol{a}_l, \boldsymbol{a}_c) \rangle$	$\langle \cos(\boldsymbol{a}_c, \boldsymbol{a}_p) \rangle$
111	0.9999	0.969	-0.976	-0.707	0.406
112	0.9999	0.972	-0.985	-0.726	0.388
174	0.9999	0.975	-0.990	-0.796	0.308

Table 3.3: NS average alignments $\langle \cos(\boldsymbol{q}, \boldsymbol{p}) \rangle$ for NS acceleration pairs $(\boldsymbol{q}, \boldsymbol{p})$.

various acceleration terms. It is worth noting that $\boldsymbol{a}_\nu$ is not everywhere always negligible, at these Reynolds numbers at least. For example, $|\boldsymbol{a}_\nu| > 0.1|\boldsymbol{a}_{c_S}|$ in 44.1% and 30.8% of the space-time domain for our lower and higher Reynolds number respectively; and if we consider $|\boldsymbol{a}_\nu| > 0.32|\boldsymbol{a}_{c_S}|$, this is satisfied in 6.8% and 3.7% of cases. Note that the DNS results of Tsinober et al. (2001) suggest that the viscous force *typically* decreases in magnitude compared to $\boldsymbol{a}_{c_S}$ as the Reynolds number increases and our results for our two Reynolds numbers agree with this trend. One may therefore expect the first of the two Tsinober equations for homogeneous/periodic turbulence with the kind of forcing we consider here to *typically* reduce to

$$\boldsymbol{a}_l + \boldsymbol{a}_{c_S} \approx 0, \tag{3.4}$$

at high enough Reynold numbers, the approximation being valid in the sense that the neglected terms are significantly smaller than the retained ones in the majority of the flow for the majority of the time. There exist, however, some relatively rare spatio-temporal events where the neglected viscous force and/or body force are significant (for example, as stated a few lines above, $|\boldsymbol{a}_\nu|$ is larger than $0.32|\boldsymbol{a}_{c_S}|$ in 6.8% and 3.7% of all spatio-temporal events for our lower and higher Reynolds numbers respectively) and where the right-hand side of (3.4) is therefore not zero. More generally, one cannot use equation (3.4) to derive statistics of small-scale quantities, as in Tang et al. (2022) for example.

The second of the two Tsinober equations, namely

$$\boldsymbol{a}_{c_I} = \boldsymbol{a}_p, \tag{3.5}$$

is exact everywhere and at any time and we keep it as it is.

Equations (3.4)-(3.5) suggest similar magnitudes and strong alignment between $\boldsymbol{a}_l$ and $-\boldsymbol{a}_{c_S}$ and equal magnitudes as well as perfect alignment between $\boldsymbol{a}_{c_I}$ and $\boldsymbol{a}_p$. Such magnitudes and alignments were observed in the DNS of Tsinober et al. (2001) and are also strongly confirmed by our own DNS in table 3.3 ($\boldsymbol{a}_{c_S}$ and $\boldsymbol{a}_{c_I}$ are calculated on the basis of equation (B.1) in appendix B and aliasing errors are removed by phase-shifting and truncation (Patterson and Orszag, 1971)). As suggested by previous DNS and experimental results (e.g. Tsinober et al. (2001); Chevillard et al. (2005); Yeung et al. (2006)), and as also supported by our own DNS results in tables 3.1 and 3.3, $\boldsymbol{a} \approx \boldsymbol{a}_p$ and

$\langle \boldsymbol{a}_l^2 \rangle / \langle \boldsymbol{a}^2 \rangle \sim \langle Re_\lambda \rangle_t^{1/2}$. In fact, the scaling $\langle \boldsymbol{a}_l^2 \rangle / \langle \boldsymbol{a}^2 \rangle \sim \langle Re_\lambda \rangle_t^{1/2}$ follows from the analysis of Tennekes (1975) who expressed the concept of passive sweeping by pointing out that "at high Reynolds number the dissipative eddies flow past an Eulerian observer in a time much shorter than the time scale which characterizes their own dynamics". It then follows from equations (3.4)-(3.5), from $\langle \boldsymbol{a}_l^2 \rangle / \langle \boldsymbol{a}^2 \rangle \sim \langle Re_\lambda \rangle_t^{1/2}$ and from $\langle \boldsymbol{a}_p^2 \rangle \approx \langle \boldsymbol{a}^2 \rangle$ that $\langle \boldsymbol{a}_{c_S}^2 \rangle / \langle \boldsymbol{a}_{c_I}^2 \rangle \sim \langle Re_\lambda \rangle_t^{1/2}$ with increasing $\langle Re_\lambda \rangle_t$, i.e. $\boldsymbol{a}_c$ becomes increasingly solenoidal with increasing $\langle Re_\lambda \rangle_t$. In this way, (3.4) leads to an increasing anti-alignment tendency between $\boldsymbol{a}_l$ and $\boldsymbol{a}_c$ with increasing Reynolds number, which is consistent with the notion of passive sweeping of small eddies by large ones, i.e. the random Taylor hypothesis of Tennekes (1975). These observations and conclusions were all made by Tsinober et al. (2001) and their DNS who showed, in particular, that the Taylor length-based Reynolds number does not need to be so large to make them, and are now confirmed by our DNS in table 3.1.

As a final point, it is a general property of periodic vector fields $\boldsymbol{q}$ that $\langle \boldsymbol{q}_I(\boldsymbol{x}, t) \cdot \boldsymbol{q}_S(\boldsymbol{x} + \boldsymbol{r}, t) \rangle_{\boldsymbol{x}} = 0$ for any $\boldsymbol{r}$ (including $\boldsymbol{r} = 0$), where $\langle \ldots \rangle_{\boldsymbol{x}}$ signifies a spatial average. This is readily shown by inserting the Fourier representation of $\boldsymbol{q}_I$ and $\boldsymbol{q}_S$ (see appendix B) and applying the orthogonality relation of the discrete Fourier modes (Canuto et al., 1987). Thus, $\langle \boldsymbol{a}_c^2 \rangle = \langle \boldsymbol{a}_{c_I}^2 \rangle + \langle \boldsymbol{a}_{c_S}^2 \rangle$. Both our DNS and the DNS of Tsinober et al. (2001) confirm this equality. From this equality and from (3.4), $\langle \boldsymbol{a}_{c_S}^2 \rangle / \langle \boldsymbol{a}_{c_I}^2 \rangle \sim \langle Re_\lambda \rangle_t^{1/2}$, (3.5), $\boldsymbol{a} \approx \boldsymbol{a}_p$ and $\langle \boldsymbol{a}^2 \rangle \gg \langle \boldsymbol{a}_\nu^2 \rangle \gg \langle \boldsymbol{f}^2 \rangle$, we have all in all

$$\langle \boldsymbol{a}_c^2 \rangle \geq \langle \boldsymbol{a}_{c_S}^2 \rangle \approx \langle \boldsymbol{a}_l^2 \rangle \gg \langle \boldsymbol{a}_{c_I}^2 \rangle = \langle \boldsymbol{a}_p^2 \rangle \approx \langle \boldsymbol{a}^2 \rangle \gg \langle \boldsymbol{a}_\nu^2 \rangle \gg \langle \boldsymbol{f}^2 \rangle, \tag{3.6}$$

for large enough $\langle Re_\lambda \rangle_t$. The average magnitude ordering in (3.6) is confirmed in our DNS (see table 3.1) and the DNS of Tsinober et al. (2001) even though the Reynolds numbers of these DNS are moderate and so the difference between $\langle \boldsymbol{a}_{c_I}^2 \rangle$ and $\langle \boldsymbol{a}_l^2 \rangle$ is not so large. Tsinober's way to formulate sweeping is encapsulated in $\langle \boldsymbol{a}_{c_S}^2 \rangle \approx \langle \boldsymbol{a}_l^2 \rangle \gg \langle \boldsymbol{a}_{c_I}^2 \rangle = \langle \boldsymbol{a}_p^2 \rangle \approx \langle \boldsymbol{a}^2 \rangle$ and in the alignments implied by equations (3.4)-(3.5) which are also statistically confirmed by our DNS in table 3.3.

The results with the ABC forcing ($\langle Re_\lambda \rangle_t = 111$) are similar to the results with the negative damping forcing ($\langle Re_\lambda \rangle_t = 112$) (see tables 3.1 and 3.3). One noticeable difference is the lower magnitudes $\langle \boldsymbol{q}^2 \rangle / (3 \langle \epsilon \rangle^{3/2} \nu^{-1/2})$ with the ABC forcing compared to the negative damping forcing. Possibly, the ABC forcing helicity input limits the NS non-linearity and consequently the related fluctuations of the other NS accelerations.

3.1.2 From One-point to Two-point Navier-Stokes Dynamics

The Navier-Stokes difference (NSD) equation at centroid $\boldsymbol{x}$ and separation vector $\boldsymbol{r}$ is derived by subtracting the Navier-Stokes (NS) equation at location $\boldsymbol{x}^+ = \boldsymbol{x} + \boldsymbol{r}/2$ from the NS equation at location $\boldsymbol{x}^- = \boldsymbol{x} - \boldsymbol{r}/2$ (see appendix A and figure 3.2). Defining $\delta \boldsymbol{q}(\boldsymbol{x}, \boldsymbol{r}, t) \equiv \boldsymbol{q}(\boldsymbol{x} + \boldsymbol{r}/2, t) - \boldsymbol{q}(\boldsymbol{x} - \boldsymbol{r}/2, t)$ for any NS term $\boldsymbol{q}(\boldsymbol{x}, t)$, the NSD equation

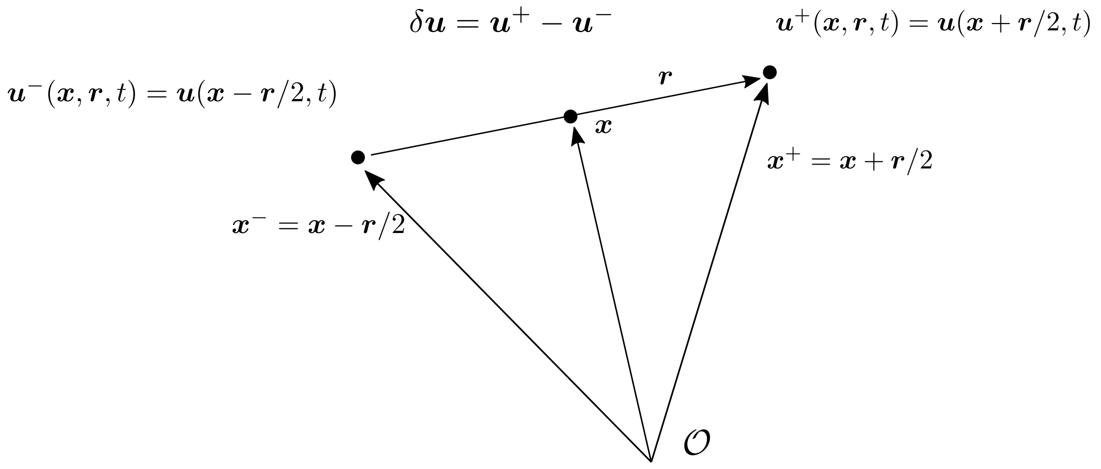
$\delta\boldsymbol{u} = \boldsymbol{u}^+ - \boldsymbol{u}^-$
$\boldsymbol{u}^+(\boldsymbol{x},\boldsymbol{r},t) = \boldsymbol{u}(\boldsymbol{x}+\boldsymbol{r}/2,t)$
$\boldsymbol{u}^-(\boldsymbol{x},\boldsymbol{r},t) = \boldsymbol{u}(\boldsymbol{x}-\boldsymbol{r}/2,t)$
$\boldsymbol{r}$
$\boldsymbol{x}$
$\boldsymbol{x}^+ = \boldsymbol{x}+\boldsymbol{r}/2$
$\boldsymbol{x}^- = \boldsymbol{x}-\boldsymbol{r}/2$
$\mathcal{O}$

Figure 3.2: Illustration of Navier-Stokes difference (NSD) centroid $\boldsymbol{x}$ and separation $\boldsymbol{r}$.

(Hill, 2002) reads

$$\frac{\partial \delta \boldsymbol{u}}{\partial t} + \delta \boldsymbol{a}_c = -\frac{1}{\rho}\nabla_{\boldsymbol{x}} \delta p + \delta \boldsymbol{a}_\nu + \delta \boldsymbol{f}, \tag{3.7}$$

The NSD equation governs the evolution of $\delta\boldsymbol{u}$, which can be thought of as approximately pertaining to the momentum at scales smaller or comparable to $|\boldsymbol{r}|$ (Townsend, 1976). We derive the solenoidal NSD equation by subtracting the solenoidal Tsinober equation (3.3a) at $\boldsymbol{x} - \boldsymbol{r}/2$ from the same equation at $\boldsymbol{x} + \boldsymbol{r}/2$. The same operation is used to derive the irrotational NSD equation. The resulting equations read (with $\delta \boldsymbol{f}_I = 0$)

$$\frac{\partial \delta \boldsymbol{u}}{\partial t} + \delta \boldsymbol{a}_{c_S} = \delta \boldsymbol{a}_\nu + \delta \boldsymbol{f}, \tag{3.8a}$$

$$\delta \boldsymbol{a}_{c_I} = -\frac{1}{\rho}\nabla_{\boldsymbol{x}} \delta p, \tag{3.8b}$$

where $\delta \boldsymbol{a}_{c_S}(\boldsymbol{x},\boldsymbol{r},t) \equiv \boldsymbol{a}_{c_S}(\boldsymbol{x}+\boldsymbol{r}/2,t) - \boldsymbol{a}_{c_S}(\boldsymbol{x}-\boldsymbol{r}/2,t)$ and $\delta \boldsymbol{a}_{c_I}(\boldsymbol{x},\boldsymbol{r},t) \equiv \boldsymbol{a}_{c_I}(\boldsymbol{x}+\boldsymbol{r}/2,t) - \boldsymbol{a}_{c_I}(\boldsymbol{x}-\boldsymbol{r}/2,t)$ and note that these terms refer to solenoidal and irrotational terms in $\boldsymbol{x}$-space rather than $\boldsymbol{r}$-space. The forcings we consider have no irrotational part and so $\delta \boldsymbol{f}_I = 0$. At the moderate $\langle Re_\lambda \rangle_t$ of our DNS, the approximate equation (3.4) is valid in the sense explained in the text which accompanies it in the previous sub-section, i.e. for a majority of spatio-temporal events. If the magnitude of the separation vector $\boldsymbol{r}$ is not too small for viscosity to matter directly nor too large for the forcing to be directly present, we may safely subtract equation (3.4) at $\boldsymbol{x} - \boldsymbol{r}/2$ from equation (3.4) at $\boldsymbol{x} + \boldsymbol{r}/2$ to obtain an approximation to (3.8a) for sufficiently high Reynolds number: this is the first of the two equations below where $\delta \boldsymbol{a}_l \equiv \partial \delta \boldsymbol{u}/\partial t$:

$$\delta \boldsymbol{a}_l + \delta \boldsymbol{a}_{c_S} \approx 0, \tag{3.9a}$$

$$\delta \boldsymbol{a}_{c_I} = -\frac{1}{\rho}\nabla_{\boldsymbol{x}} \delta p. \tag{3.9b}$$

The second equation, equation (3.9b), follows directly from (3.8b) without any restriction

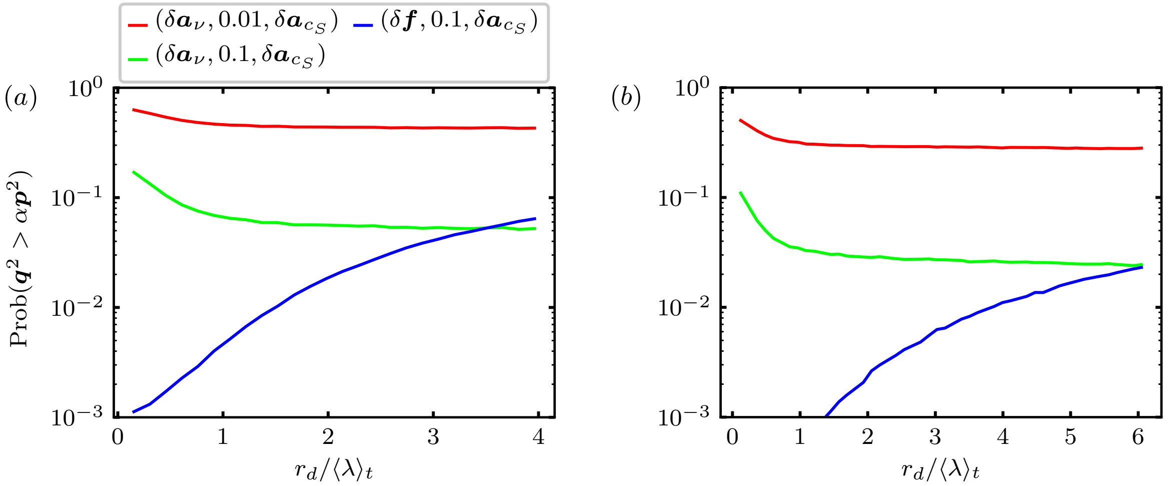

Figure 3.3: NSD exceedance probabilities $\mathrm{Prob}(\boldsymbol{q}^2 > \alpha\boldsymbol{p}^2)$ for the NSD terms on top of (a) as a function of separation length $r_d = |\boldsymbol{r}|$. The legend entries read $(\boldsymbol{q}, \alpha, \boldsymbol{p})$ for the NSD terms introduced in the first paragraph of 3.1.2.(a) $\langle Re_\lambda\rangle_t = 112$, $\langle L\rangle_t = 3.5\langle\lambda\rangle_t$. (b) $\langle Re_\lambda\rangle_t = 174$, $\langle L\rangle_t = 5.2\langle\lambda\rangle_t$. NSD magnitudes $\boldsymbol{q}^2$ and $\boldsymbol{p}^2$ are sampled at scale $r_d = |\boldsymbol{r}|$ at random orientations $\boldsymbol{r}$.

on either $\boldsymbol{r}$ or Reynolds number and is exact.

Like equation (3.4), (3.9a) can be expected to be valid broadly except where and when $\delta\boldsymbol{a}_\nu + \delta\boldsymbol{f}$ is large enough not to be negligible. Figure 3.3 shows statistically converged estimations of exceedance probabilities of NSD viscous and external force terms which suggest that (3.9a) is indeed a good approximation for most of space and time at the Reynolds numbers of our two DNS, at the very least for separation distances larger than $\langle\lambda\rangle_t$ and smaller than $\langle L\rangle_t$. With regards to the forcing, $\mathrm{Prob}(|\delta\boldsymbol{f}| > 0.32|\delta\boldsymbol{a}_{c_S}|)$ is typically of the order of 1%, in particular for our higher Reynolds number. With regards to the viscous force, $\mathrm{Prob}(|\delta\boldsymbol{a}_\nu| > 0.32|\delta\boldsymbol{a}_{c_S}|)$ is typically of the order of 5% for $r_d \geq \langle\lambda\rangle_t$ and even less for our higher Reynolds number.

The link between non-linearity and pressure invoked in the two-point analysis of Yasuda and Vassilicos (2018) has its root in equation (3.9b) which parallels (3.5) and states that $\delta\boldsymbol{a}_{c_I}$ and $\delta\boldsymbol{a}_p$ are perfectly aligned and have the same magnitudes. Furthermore, similarly to the way that equation (3.4) supports the concept of sweeping of small turbulent eddies by large ones in the usual one-point sense, (3.9a) suggests similar magnitudes for and strong alignment between $\delta\boldsymbol{a}_l$ and $-\delta\boldsymbol{a}_{c_S}$. A two-point concept of sweeping similar to the one of Tennekes (1975) which relies on alignment between $\delta\boldsymbol{a}_l$ and $-\delta\boldsymbol{a}_c$ should also require that $\delta\boldsymbol{a}_c$ tends towards $\delta\boldsymbol{a}_{c_s}$ with increasing Reynolds number, i.e. that $\delta\boldsymbol{a}_c$ becomes increasingly solenoidal. We therefore seek to obtain inequalities and approximate equalities similar to (3.6). Note that equations (3.9a)-(3.9b) immediately imply $\langle\delta\boldsymbol{a}_{c_S}^2\rangle \approx \langle\delta\boldsymbol{a}_l^2\rangle$, $\langle\delta\boldsymbol{a}_{c_I}^2\rangle = \langle\delta\boldsymbol{a}_p^2\rangle$ and $\langle\delta\boldsymbol{a}_p^2\rangle \approx \langle\delta\boldsymbol{a}^2\rangle$. It therefore remains to argue that $\langle\delta\boldsymbol{a}_c^2\rangle \geq \langle\delta\boldsymbol{a}_{c_S}^2\rangle \gg \langle\delta\boldsymbol{a}_{c_I}^2\rangle$ which is exactly what we need to arrive at a new concept of two-point sweeping.

We start from

$$\begin{aligned}\langle \delta \boldsymbol{q} \cdot \delta \boldsymbol{q} \rangle(\boldsymbol{r}) &= \langle \boldsymbol{q}^{+} \cdot \boldsymbol{q}^{+} \rangle - \langle \boldsymbol{q}^{+} \cdot \boldsymbol{q}^{-} \rangle + \langle \boldsymbol{q}^{-} \cdot \boldsymbol{q}^{-} \rangle - \langle \boldsymbol{q}^{-} \cdot \boldsymbol{q}^{+} \rangle, && (3.10a)\\ &= 2\big[\langle \boldsymbol{q} \cdot \boldsymbol{q} \rangle - \langle \boldsymbol{q}^{+} \cdot \boldsymbol{q}^{-} \rangle(\boldsymbol{r})\big], && (3.10b)\end{aligned}$$

where $\boldsymbol{q}^{+} \equiv \boldsymbol{q}(\boldsymbol{x} + \boldsymbol{r}/2)$ and $\boldsymbol{q}^{-} \equiv \boldsymbol{q}(\boldsymbol{x} - \boldsymbol{r}/2)$ and used $\langle \boldsymbol{q}^{+} \cdot \boldsymbol{q}^{+} \rangle = \langle \boldsymbol{q}^{-} \cdot \boldsymbol{q}^{-} \rangle = \langle \boldsymbol{q} \cdot \boldsymbol{q} \rangle$ because of statistical homogeneity/periodicity. Previous studies (Hill and Thoroddsen, 1997; Vedula and Yeung, 1999; Xu et al., 2007; Gulitski et al., 2007) demonstrated that fluid accelerations, pressure gradients and viscous forces have limited spatial correlations in terms of alignments at scales larger than $\langle \lambda \rangle_t$ for moderate and high $\langle Re_\lambda \rangle_t$. Thus, if we assume the two-point term to be negligible compared to the one-point term in equation (3.10b) for scales $|\boldsymbol{r}|$ larger than $\langle \lambda \rangle_t$, we have that $\langle \delta \boldsymbol{q} \cdot \delta \boldsymbol{q} \rangle(\boldsymbol{r})$ is approximately equal to $2\langle \boldsymbol{q} \cdot \boldsymbol{q} \rangle$ for $|\boldsymbol{r}|$ larger than $\langle \lambda \rangle_t$. From (3.6) we therefore obtain

$$\langle \delta \boldsymbol{a}_c^2 \rangle \geq \langle \delta \boldsymbol{a}_{c_S}^2 \rangle \approx \langle \delta \boldsymbol{a}_l^2 \rangle \gg \langle \delta \boldsymbol{a}_{c_I}^2 \rangle = \langle \delta \boldsymbol{a}_p^2 \rangle \approx \langle \delta \boldsymbol{a}^2 \rangle \gg \langle \delta \boldsymbol{a}_\nu^2 \rangle \gg \langle \delta \boldsymbol{f}^2 \rangle, \tag{3.11}$$

for $|\boldsymbol{r}|$ larger than $\langle \lambda \rangle_t$, but $\langle \delta \boldsymbol{a}_c^2 \rangle \geq \langle \delta \boldsymbol{a}_{c_S}^2 \rangle$ and $\langle \delta \boldsymbol{a}_{c_I}^2 \rangle = \langle \delta \boldsymbol{a}_p^2 \rangle$ are in fact valid for any $\boldsymbol{r}$. Inequality $\langle \delta \boldsymbol{a}_c^2 \rangle \geq \langle \delta \boldsymbol{a}_{c_S}^2 \rangle$ follows from $\langle \delta \boldsymbol{a}_c^2 \rangle = \langle \delta \boldsymbol{a}_{c_I}^2 \rangle + \langle \delta \boldsymbol{a}_{c_S}^2 \rangle$ which itself follows from $\langle \boldsymbol{a}_{c_I}(\boldsymbol{x}, t) \cdot \boldsymbol{a}_{c_S}(\boldsymbol{x} + \boldsymbol{r}, t) \rangle_{\boldsymbol{x}} = 0$ for any $\boldsymbol{r}$ for periodic turbulence (see section 3.1.1). Equality $\langle \delta \boldsymbol{a}_{c_I}^2 \rangle = \langle \delta \boldsymbol{a}_p^2 \rangle$ follows directly from (3.9b) which is exact and holds for any $\boldsymbol{r}$ and any Reynolds number. Of equalities/inequalities (3.11), the ones that we did not already directly derive from/with equations (3.9a)-(3.9b) are $\langle \delta \boldsymbol{a}_c^2 \rangle \geq \langle \delta \boldsymbol{a}_{c_S}^2 \rangle \gg \langle \delta \boldsymbol{a}_{c_I}^2 \rangle$ and $\langle \delta \boldsymbol{a}_\nu^2 \rangle \gg \langle \delta \boldsymbol{f}^2 \rangle$. The present way to formulate the new concept of two-point sweeping follows from Tsinober's way to formulate sweeping and is encapsulated $\langle \delta \boldsymbol{a}_{c_S}^2 \rangle \approx \langle \delta \boldsymbol{a}_l^2 \rangle \gg \langle \delta \boldsymbol{a}_{c_I}^2 \rangle = \langle \delta \boldsymbol{a}_p^2 \rangle \approx \langle \delta \boldsymbol{a}^2 \rangle$ and in the alignments implied by (3.9a)-(3.9b). We confirm equations (3.9a)-(3.9b)-(3.11) with our DNS in the remainder of this subsection.

To test (3.11) with our DNS data in a manageable way, we calculate spatio-temporal averages of $\boldsymbol{r}$-orientation-averaged quantities (see section 2.3 and equation (2.32))

$$(\delta \boldsymbol{q} \cdot \delta \boldsymbol{q})^a(\boldsymbol{x}, r_d, t) \equiv \frac{1}{\pi r_d^2} \iint_{|\boldsymbol{r}|=r_d} \delta \boldsymbol{q}(\boldsymbol{x}, \boldsymbol{r}, t) \cdot \delta \boldsymbol{q}(\boldsymbol{x}, \boldsymbol{r}, t),\ d\boldsymbol{r}, \tag{3.12}$$

which we plot in figure 3.4($a1$,$a2$) as ratios of such quantities versus r_d. In figure 3.4($a1$,$a2$) we plot spatio-temporal averages of $\boldsymbol{r}$-orientation-averaged quantities (3.12) for various NSD accelerations/forces. A comparison of relative magnitudes in the plots of figure 3.4($a1$,$a2$) with relative magnitudes in table 3.1 makes it clear that the results are consistent with (3.11) and $\langle \delta \boldsymbol{q} \cdot \delta \boldsymbol{q} \rangle(\boldsymbol{r})/\langle \boldsymbol{q} \cdot \boldsymbol{q} \rangle$ close to 2 for $r_d \geq \langle \lambda \rangle_t$ at both $\langle Re_\lambda \rangle_t$ to a good degree of accuracy ($\langle \delta \boldsymbol{q} \cdot \delta \boldsymbol{q} \rangle(\boldsymbol{r})/\langle \boldsymbol{q} \cdot \boldsymbol{q} \rangle$ increases from 1.8 to 2.0 as r_d grows from $\langle \lambda \rangle_t$ to $\langle L \rangle_t$). Note, in figure 3.4($a1$,$b1$) the average quantities corresponding to $\delta \boldsymbol{a}_l$ and $\delta \boldsymbol{a}_{c_S}$ overlap and those corresponding to $\delta \boldsymbol{a}_p$, $\delta \boldsymbol{a}$ and $\delta \boldsymbol{a}_{c_I}$ also overlap. At scales below $\langle \lambda \rangle_t$, the average relative magnitudes change slightly, but the NSD magnitude separations still abide by (3.11), the NSD analogue to (3.6), at all scales.

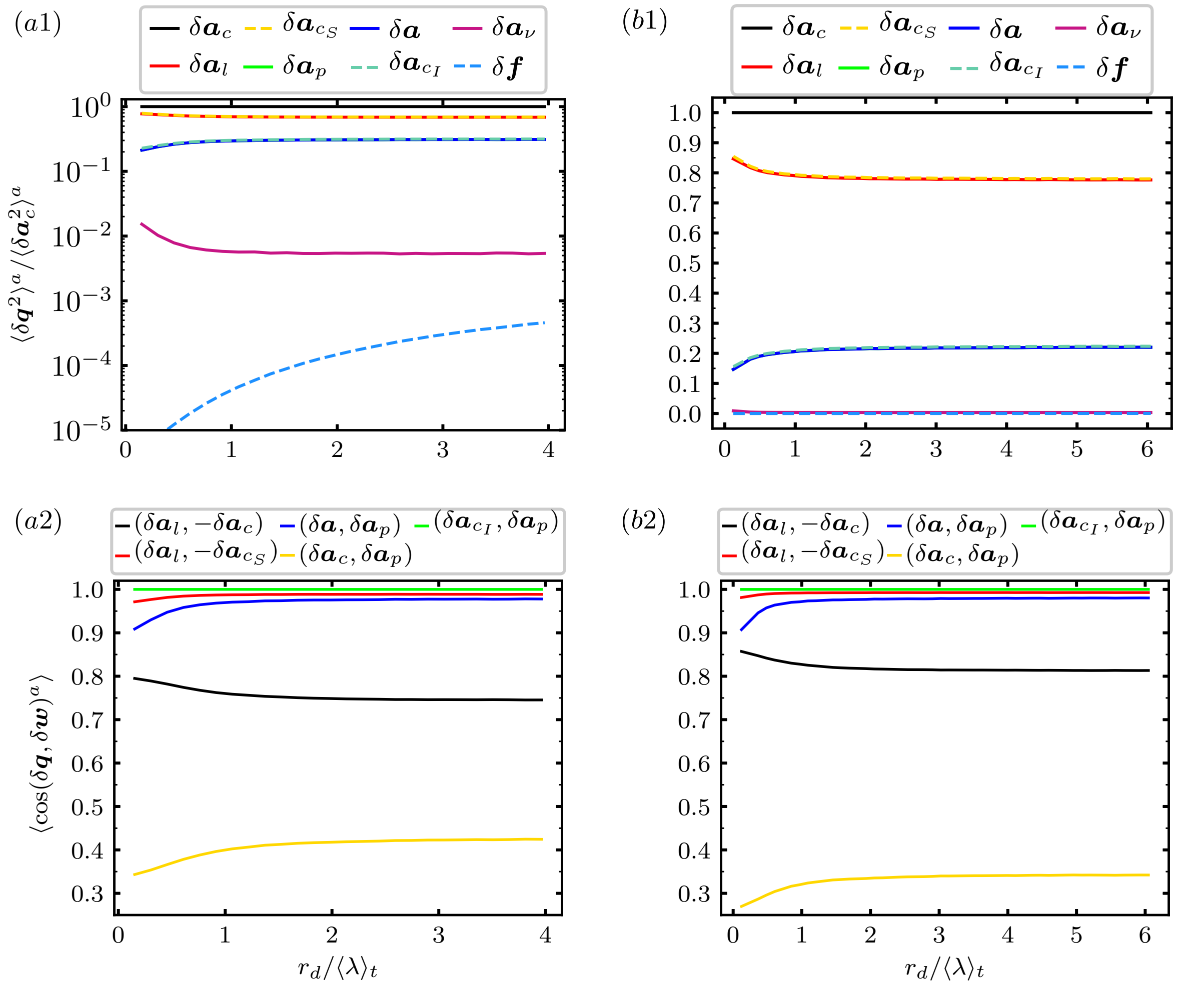

Figure 3.4: $(a1,\ b1)$ Spatio-temporal averages of spherically averaged NSD magnitudes $\langle\delta\boldsymbol{q}^2\rangle^a$ for NSD terms $\delta\boldsymbol{q}$ as a function of r_d: $(a1)$ $\langle Re_\lambda\rangle_t = 112$, $(b1)$ $\langle Re_\lambda\rangle_t = 174$. The magnitudes of the terms $(\delta\boldsymbol{a}_l, \delta\boldsymbol{a}_{c_S})$ overlap and the magnitudes of the terms $(\delta\boldsymbol{a}_p, \delta\boldsymbol{a}, \delta\boldsymbol{a}_{c_I})$ overlap. $(a2,\ b2)$ average NSD alignments between NSD terms $(\delta\boldsymbol{q}, \delta\boldsymbol{w})$ as a function of r_d: $(a2)$ $\langle Re_\lambda\rangle_t = 112$, $(b2)$ $\langle Re_\lambda\rangle_t = 174$.

In figure 3.4($b1$,$b2$) we use our DNS data to plot spatio-temporal averages of $\boldsymbol{r}$-orientation-averaged cosines of angles between various NSD terms $\delta\boldsymbol{q}$ and $\delta\boldsymbol{w}$ to test for average alignments as a function of r_d. These alignment results are of course in perfect agreement with (3.9b) but they are also in good agreement with (3.9a) and acceptable agreement with $\delta\boldsymbol{a} \approx \delta\boldsymbol{a}_p$ (the cosine of the angle between these two acceleration vectors is higher than 0.9 for all r_d). They also show that we should not expect $\delta\boldsymbol{a}_l$ to be extremely well aligned with $-\delta\boldsymbol{a}_c$ at our moderate Reynolds numbers. This demonstrates the pertinence of the solenoidal-irrotational decomposition which has revealed very good alignments at our moderate Reynolds numbers for which there are significantly weaker alignments without this decomposition.

In conclusion, figure 3.4 provides strong support for equations (3.9a)-(3.9b)-(3.11) which establish the two-point link between non-linearity and pressure, and also a concept of two-point sweeping.

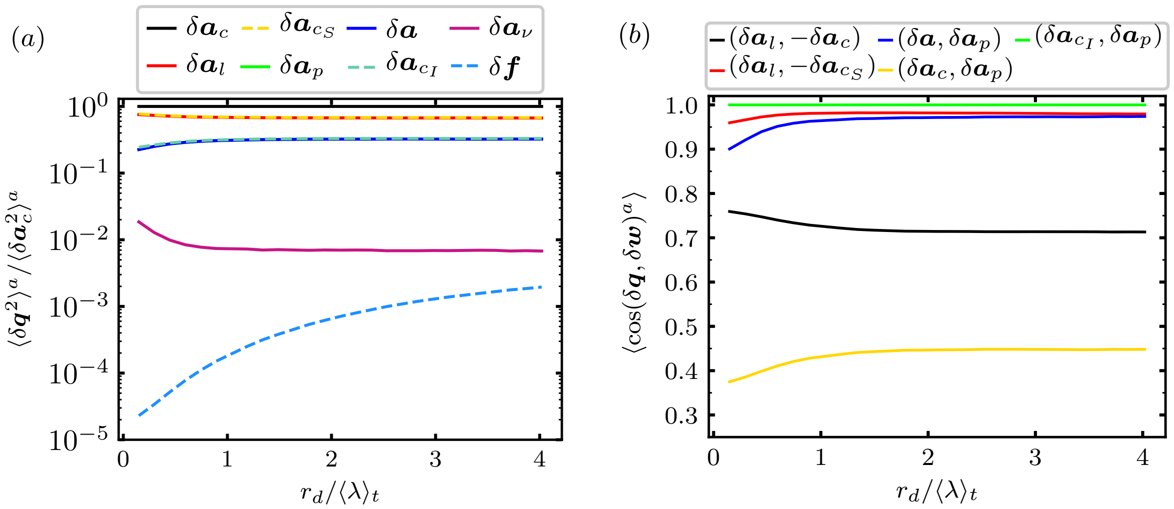

Figure 3.5: (a) Space-time-average NSD magnitudes $\langle \delta \boldsymbol{q}^2 \rangle^a$ as a function of r_d. The magnitudes of the terms $(\delta \boldsymbol{a}_l, \delta \boldsymbol{a}_{c_S})$ overlap and the magntiudes of the terms $(\delta \boldsymbol{a}_p, \delta \boldsymbol{a}, \delta \boldsymbol{a}_{c_I})$ overlap. (b) average NSD alignments between NSD terms $(\delta \boldsymbol{q}, \delta \boldsymbol{w})$ as a function of r_d. $\langle Re_\lambda \rangle_t = 111$ (ABC forcing).

Figure 3.5 shows the NSD average magnitudes and alignments results with the ABC forcing. We note that the results with the negative damping forcing (DNS3) extend to the DNS with ABC forcing (DNS2). The relative NSD magnitudes approximately equal the analogue NS magnitudes and the average alignments behave similarly to the negative damping forcing alignments (compare figures 3.4(a2) and 3.5(b)).

3.1.3 Interscale Transfer and Physical Space Transport Accelerations

The convective non-linearity is responsible for non-linear turbulence transport through space and non-linear transfer through scales. We want to separate these two effects and therefore decompose the two-point non-linear acceleration term $\delta \boldsymbol{a}_c$ into an interscale transfer acceleration $\boldsymbol{a}_\Pi$ and a physical space transport acceleration $\boldsymbol{a}_\mathcal{T}$ (see Hill (2002) and appendix A for more details), i.e $\delta \boldsymbol{a}_c = \boldsymbol{a}_\Pi + \boldsymbol{a}_\mathcal{T}$ with

$$\boldsymbol{a}_\mathcal{T}(\boldsymbol{x}, \boldsymbol{r}, t) = \frac{1}{2}(\boldsymbol{u}^+ + \boldsymbol{u}^-) \cdot \nabla_{\boldsymbol{x}} \delta \boldsymbol{u}, \quad \boldsymbol{a}_\Pi(\boldsymbol{x}, \boldsymbol{r}, t) = \delta \boldsymbol{u} \cdot \nabla_{\boldsymbol{r}} \delta \boldsymbol{u}. \tag{3.13}$$

With this decomposition of the non-linear term, the NSD equation (3.7) reads

$$\frac{\partial \delta \boldsymbol{u}}{\partial t} + \boldsymbol{a}_\Pi + \boldsymbol{a}_\mathcal{T} = -\frac{1}{\rho} \nabla_{\boldsymbol{x}} \delta p + \delta \boldsymbol{a}_\nu + \delta \boldsymbol{f}. \tag{3.14}$$

We note relations $\boldsymbol{a}_\Pi = 1/2(\delta \boldsymbol{a}_C + u_j^+ \partial \boldsymbol{u}^- / \partial x_j^- - u_j^- \partial \boldsymbol{u}^+ / \partial x_j^+)$ and $\boldsymbol{a}_\mathcal{T} = 1/2(\delta \boldsymbol{a}_C - u_j^+ \partial \boldsymbol{u}^- / \partial x_j^- + u_j^- \partial \boldsymbol{u}^+ / \partial x_j^+)$ which can be used to show that $\langle \boldsymbol{a}_\Pi^2 \rangle$ and $\langle \boldsymbol{a}_\mathcal{T}^2 \rangle$ tend towards each other as $|\boldsymbol{r}|$ grows above the integral length scale due to negligible average velocity alignments at such scales. We report DNS evidence of this tendency below in this section.

We want to consider the effects of the interscale transfer and interspace transport terms in the solenoidal and irrotational NSD dynamics and we therefore break down the NSD equation (3.14) into two equations, one irrotational and one solenoidal. We perform Helmholtz decompositions in centroid space $\boldsymbol{x}$ for a given separation $\boldsymbol{r}$ at time t

$$\delta \boldsymbol{q}(\boldsymbol{x},\boldsymbol{r},t) = \delta \boldsymbol{q}_{\overline{I}}(\boldsymbol{x},\boldsymbol{r},t) + \delta \boldsymbol{q}_{\overline{S}}(\boldsymbol{x},\boldsymbol{r},t) = -\nabla_{\boldsymbol{x}}\phi(\boldsymbol{x},\boldsymbol{r},t) + \nabla_{\boldsymbol{x}} \times \boldsymbol{B}(\boldsymbol{x},\boldsymbol{r},t), \tag{3.15}$$

where $\phi(\boldsymbol{x},\boldsymbol{r},t)$ is a scalar potential and $\boldsymbol{B}(\boldsymbol{x},\boldsymbol{r},t)$ is a vector potential. In periodic turbulence the Helmholtz decomposition in centroid space equals the difference of the Helmholtz decomposition in physical space $\delta \boldsymbol{q}_I = \delta \boldsymbol{q}_{\overline{I}}$ and $\delta \boldsymbol{q}_S = \delta \boldsymbol{q}_{\overline{S}}$ (see appendix B). From $\delta \boldsymbol{a}_c = \boldsymbol{a}_{\Pi} + \boldsymbol{a}_{\mathcal{T}}$ and the linearity of the Fourier transform follow $\delta \boldsymbol{a}_{c_S} = \delta \boldsymbol{a}_{c_{\overline{S}}} = \boldsymbol{a}_{\Pi_{\overline{S}}} + \boldsymbol{a}_{\mathcal{T}_{\overline{S}}}$ and $\delta \boldsymbol{a}_{c_I} = \delta \boldsymbol{a}_{c_{\overline{I}}} = \boldsymbol{a}_{\Pi_{\overline{I}}} + \boldsymbol{a}_{\mathcal{T}_{\overline{I}}}$. Thus, we can rewrite the NSD solenoidal and irrotational equations (3.8a)-(3.8b) in periodic/homogeneous turbulence as

$$\boldsymbol{a}_{\Pi_{\overline{I}}} + \boldsymbol{a}_{\mathcal{T}_{\overline{I}}} = \delta \boldsymbol{a}_p, \tag{3.16a}$$

$$\delta \boldsymbol{a}_l + \boldsymbol{a}_{\Pi_{\overline{S}}} + \boldsymbol{a}_{\mathcal{T}_{\overline{S}}} = \delta \boldsymbol{a}_\nu + \delta \boldsymbol{f}. \tag{3.16b}$$

We emphasize that the interscale transfer term $\boldsymbol{a}_{\Pi_{\overline{S}}}$ is related non-locally in space to two-point vortex stretching/compression and tilting terms governing the evolution of the vorticity difference $\delta\boldsymbol{\omega}$. This follows from the fact that, as for the Tsinober equations, the NSD solenoidal equation is an integrated vorticity difference equation. We provide mathematical detail on the connection between $\boldsymbol{a}_{\Pi_{\overline{S}}}$ and $\delta\boldsymbol{\omega}$ in section 3.4.

Equation (3.16a) can also be obtained by integrating the Poisson equation for δp in centroid space similarly to equation (3.16b) which, as already mentioned, can be obtained by integrating the vorticity difference equation in that same space. We use this approach in section 3.4 to derive these equations for periodic/homogeneous turbulence but also their generalised form for non-homogeneous turbulence. By deriving the exact equations for $\boldsymbol{a}_{\mathcal{T}_{\overline{I}}}(\boldsymbol{x},\boldsymbol{r},t)$ and $\boldsymbol{a}_{\Pi_{\overline{I}}}(\boldsymbol{x},\boldsymbol{r},t)$ in Fourier centroid space we show in appendix B that we have $\boldsymbol{a}_{\mathcal{T}_{\overline{I}}}(\boldsymbol{x},\boldsymbol{r},t) = \boldsymbol{a}_{\Pi_{\overline{I}}}(\boldsymbol{x},\boldsymbol{r},t)$ in periodic/homogeneous turbulence. This result combined with (3.16a) yields

$$\boldsymbol{a}_{\Pi_{\overline{I}}} = \boldsymbol{a}_{\mathcal{T}_{\overline{I}}} = \frac{1}{2}\delta \boldsymbol{a}_p = \frac{1}{2}\delta \boldsymbol{a}_{c_I}, \tag{3.17}$$

in periodic/homogeneous turbulence. In figure 3.6 we plot spatio-temporal averages of $\boldsymbol{r}$-orientation-averaged quantities (3.12) for various acceleration/force terms in the Helmholtz decomposed NSD equations and in figure 3.7 we plot spatio-temporal averages of $\boldsymbol{r}$-orientation-averaged cosines of angles between various two-point acceleration terms in these equations. The overlapping magnitudes in figure 3.6 and the average alignments in figure 3.7 confirm (3.17), or rather validate our DNS given that (3.17) is exact.

Note that the computational procedure to calculate the various $\boldsymbol{r}$-orientation-averaged terms in these figures is computationally expensive. To calculate the NSD irrotational and solenoidal parts of the interscale and interspace transport terms at a given time t and

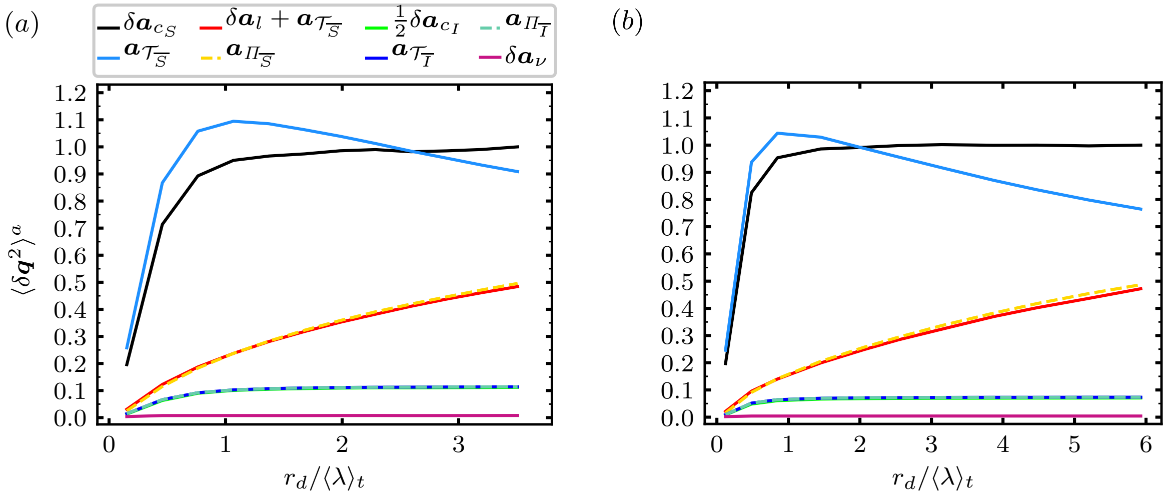

Figure 3.6: Average magnitudes $\langle \delta \boldsymbol{q}^2 \rangle^a$ of NSD terms present in the irrotational and solenoidal NSD equations (3.16b)-(3.17). All values have been normalised with $\langle \delta \boldsymbol{a}_{c_S}^2 \rangle^a$ at the largest considered separation r_d. The magnitudes of the terms $(\delta \boldsymbol{a}_l + \boldsymbol{a}_{\mathcal{T}_{\overline{S}}}, \boldsymbol{a}_{\Pi_{\overline{S}}})$ overlap and the magnitudes of the terms $(1/2\delta \boldsymbol{a}_{c_I}, \boldsymbol{a}_{\mathcal{T}_{\overline{I}}}, \boldsymbol{a}_{\Pi_{\overline{I}}})$ overlap. (*a*) $\langle Re_\lambda \rangle_t = 112$, (*b*) $\langle Re_\lambda \rangle_t = 174$.

separation $\boldsymbol{r}$, we use the pseudospectral algorithm of Patterson and Orszag (1971) with one phase-shift and spherical truncation. We apply this algorithm to δu_j and $\partial \delta u_i / \partial r_j$ for the interscale transfer and for $(u_j^+ + u_j^-)/2$ and $\partial \delta u_i / \partial x_j$ for the interspace transfer. Hence, we express these vectors/tensors in Fourier space (see equations (B.14a)-(B.14d) in appendix B) and apply the pseudospectral method of Patterson and Orszag (1971) to calculate $\widehat{\boldsymbol{a}_{\mathcal{T}}}(\boldsymbol{k}, \boldsymbol{r}, t)$ and $\widehat{\boldsymbol{a}_{\Pi}}(\boldsymbol{k}, \boldsymbol{r}, t)$ without aliasing errors. We next decompose these fields into irrotational and solenoidal fields with the projection operator and inverse these fields to physical space to obtain $\boldsymbol{a}_{\Pi_{\overline{S}}}(\boldsymbol{x}, \boldsymbol{r}, t)$, $\boldsymbol{a}_{\Pi_{\overline{I}}}(\boldsymbol{x}, \boldsymbol{r}, t)$, $\boldsymbol{a}_{\mathcal{T}_{\overline{S}}}(\boldsymbol{x}, \boldsymbol{r}, t)$ and $\boldsymbol{a}_{\mathcal{T}_{\overline{I}}}(\boldsymbol{x}, \boldsymbol{r}, t)$. These fields can then be sampled over $\boldsymbol{x}$ to calculate e.g. $\boldsymbol{a}^2_{\Pi_{\overline{S}}}(\boldsymbol{x}, \boldsymbol{r}, t)$ or KHMH terms such as $2\delta \boldsymbol{u} \cdot \boldsymbol{a}_{\Pi_{\overline{S}}}(\boldsymbol{x}, \boldsymbol{r}, t)$ (see section 3.1.4). If we assume that the cost of a DNS time step is similar to the cost of the pseudospectral method to calculate the NS non-linear term, the calculation of solenoidal and irrotational interspace and interscale transfers for one t and one $\boldsymbol{r}$ has similar cost to one DNS time step. The total cost of the pseudospectral post-processing method is proportional to the total number N_r of separation vectors $\boldsymbol{r}$ that we use in our spherical averaging across scales r_d and to the total number of samples in time $\Delta T / dT$ (see table 2.2). With a total number of separation vectors $N_r \sim 10^3 - 10^4$ and our $\Delta T / dT$ values, the total cost of the pseudospectral post-processing method in terms of DNS time steps is one order of magnitude larger than the cost of the DNS itself. This high post-processing cost limits the attainable $\langle Re_\lambda \rangle_t$ values.

The NSD solenoidal equation (3.16b) describes a balance between the time-derivative, solenoidal interscale transfer, solenoidal interspace transport, viscous and forcing terms. From the point we made in the sentence directly following equation (3.14), we expect $\langle \boldsymbol{a}^2_{\mathcal{T}_{\overline{S}}} \rangle$ and $\langle \boldsymbol{a}^2_{\Pi_{\overline{S}}} \rangle$ to tend to become equal to each other as the amplitude of $\boldsymbol{r}$ tends to values significantly larger than $\langle L \rangle_t$. Figure 3.6 confirms this trend. With decreasing

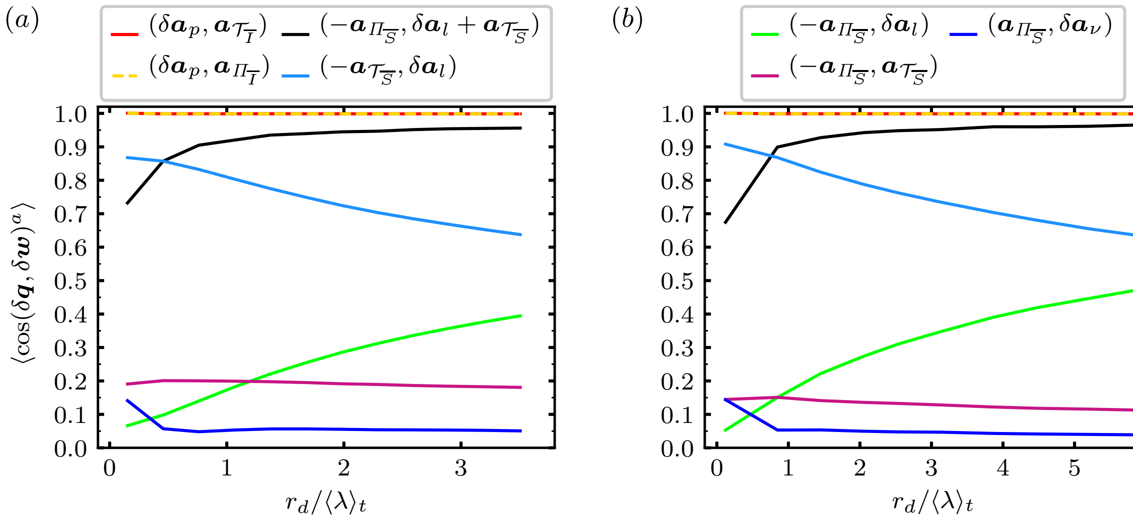

Figure 3.7: Average alignments of NSD terms $(\delta\boldsymbol{q}, \delta\boldsymbol{w})$ listed on top of (a) and (b). The average alignments of $(\delta\boldsymbol{a}_p, \boldsymbol{a}_{\mathcal{T}_{\overline{I}}})$ and $(\delta\boldsymbol{a}_p, \boldsymbol{a}_{\Pi_{\overline{I}}})$ overlap: (a) $\langle Re_\lambda\rangle_t = 112$, (b) $\langle Re_\lambda\rangle_t = 174$.

r_d, the magnitudes of $\boldsymbol{a}_{\Pi_{\overline{S}}}$ decrease relative to those of $\boldsymbol{a}_{\mathcal{T}_{\overline{S}}}$. At all scales $r_d \geq \langle\lambda\rangle_t$ the magnitudes of $\boldsymbol{a}_{\mathcal{T}_{\overline{S}}}$ and $\boldsymbol{a}_{\Pi_{\overline{S}}}$ are one order of magnitude larger than those of the viscous term $\delta\boldsymbol{a}_\nu$ and this separation is greater for the larger $\langle Re_\lambda\rangle_t$. The magnitudes of $\delta\boldsymbol{a}_\nu$ are themselves much larger than those of $\delta\boldsymbol{f}$ (not shown in figure 3.6 for not overloading the figure but see figure 3.4(a1)). These observations suggest that the solenoidal NSD equation (3.16b) reduces at scales $r_d \geq \langle\lambda\rangle_t$ to the approximate

$$\delta\boldsymbol{a}_l + \boldsymbol{a}_{\mathcal{T}_{\overline{S}}} \approx -\boldsymbol{a}_{\Pi_{\overline{S}}}, \tag{3.18}$$

where this equation is understood as accurate in most regions of the flow for the majority of the time (as for the NS dynamics, we do expect dynamically important regions localised in space and time where the dynamics differ from (3.18).) Figure 3.6 confirms equation (3.18) in this sense. An additional important observation to be made from figure 3.6 is that $\delta\boldsymbol{a}_{c_S}$ tends to become increasingly dominated by $\boldsymbol{a}_{\mathcal{T}_{\overline{S}}}$ rather than $\boldsymbol{a}_{\Pi_{\overline{S}}}$ as r_d decreases.

Equation (3.18) is the same as equation (3.9a), and similarly to figure 3.4 which provides support for equation (3.9a), figures 3.6 and 3.7 provide strong support for equation (3.18), in particular for $r_d \geq \langle\lambda\rangle_t$. It is interesting to note that the average alignment between the left and the right-hand side of equation (3.18) lies between 90% and 100% (typically 95%) for $r_d \geq \langle\lambda\rangle_t$. Whilst this is strong support for approximate equation (3.18), the fact that the alignment is not 100% is a reminder of the nature of the approximation, i.e. that relatively rare spatio-temporal events do exist where the viscous and/or driving forces are not negligible.

At length-scales $r_d \leq \langle\lambda\rangle_t$, the alignment between $\delta\boldsymbol{a}_l$ and $-\boldsymbol{a}_{\mathcal{T}_{\overline{S}}}$ improves while the alignment between $\delta\boldsymbol{a}_l + \boldsymbol{a}_{\mathcal{T}_{\overline{S}}}$ and $-\boldsymbol{a}_{\Pi_{\overline{S}}}$ worsens with decreasing r_d (see figure 3.7) presumably because of direct dissipation and diffusion effects, so that $\delta\boldsymbol{a}_l + \boldsymbol{a}_{\mathcal{T}_{\overline{S}}} \approx 0$ becomes a

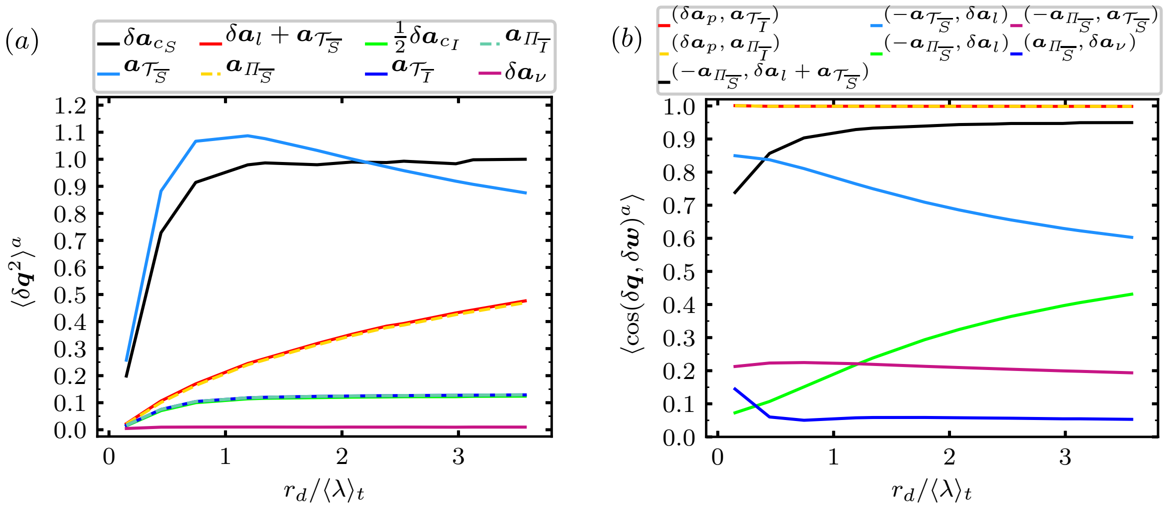

Figure 3.8: (a) $\langle \delta\boldsymbol{q}^2 \rangle^a$ normalised with $\langle \delta\boldsymbol{a}_{c_S}^2 \rangle^a$ at the largest considered r_d. The magnitudes of the terms $(\delta\boldsymbol{a}_l + \boldsymbol{a}_{\mathcal{T}_{\overline{S}}}, \boldsymbol{a}_{\Pi_{\overline{S}}})$ overlap and the magnitudes of the terms $(1/2\delta\boldsymbol{a}_{c_I}, \boldsymbol{a}_{\mathcal{T}_{\overline{I}}}, \boldsymbol{a}_{\Pi_{\overline{I}}})$ overlap. (b) NSD average alignments. The average alignments of $(\delta\boldsymbol{a}_p, \boldsymbol{a}_{\mathcal{T}_{\overline{I}}})$ and $(\delta\boldsymbol{a}_p, \boldsymbol{a}_{\Pi_{\overline{I}}})$ overlap. $\langle Re_\lambda \rangle_t = 111$ (ABC forcing).

better approximation than equation (3.18) at $r_d < 0.5\langle\lambda\rangle_t$. This observation is consistent with our parallel observation that the magnitude of $\boldsymbol{a}_{\mathcal{T}_{\overline{S}}}$ increases while the magnitude of $\boldsymbol{a}_{\Pi_{\overline{S}}}$ decreases with decreasing r_d.

On the other end of the spectrum, i.e. as the length scale r_d grows towards $\langle L \rangle_t$, the alignment between $\delta\boldsymbol{a}_l$ and $-\boldsymbol{a}_{\mathcal{T}_{\overline{S}}}$ worsens while the alignment between $\delta\boldsymbol{a}_l$ and $-\boldsymbol{a}_{\Pi_{\overline{S}}}$ improves (see figure 3.7), both reaching a comparable level of alignment/misalignment which contribute together to keep approximation (3.18) statistically well satisfied with 95% alignment between $\delta\boldsymbol{a}_l + \boldsymbol{a}_{\mathcal{T}_{\overline{S}}}$ and $-\boldsymbol{a}_{\Pi_{\overline{S}}}$.

The strong anti-alignment between $\boldsymbol{a}_{\mathcal{T}_{\overline{S}}}$ and $\delta\boldsymbol{a}_l$, increasingly so at smaller r_d (see figure 3.7) expresses the sweeping of the two-point momentum difference $\delta\boldsymbol{u}$ at scales r_d and smaller by the mainly large-scale velocity $(\boldsymbol{u}^+ + \boldsymbol{u}^-)/2$. Note that this two-point sweeping differs from anti-alignment between $\delta\boldsymbol{a}_l$ and $\delta\boldsymbol{a}_c$ for two reasons. Firstly, by using the Helmholtz decomposition we have removed the pressure effect embodied in the $\boldsymbol{a}_{c_I}$ contribution to $\boldsymbol{a}_c$ which balances the pressure gradient. This was first understood in Tsinober et al. (2001) in a one-point setting and is here extended to a two-point setting. Secondly, $\delta\boldsymbol{a}_{c_S}$ is the sum of an interspace transport $\boldsymbol{a}_{\mathcal{T}_{\overline{S}}}$ and an interscale transfer term $\boldsymbol{a}_{\Pi_{\overline{S}}}$ such that the interpretation of two-point sweeping as anti-alignment between $\boldsymbol{a}_{c_S}$ and $\boldsymbol{a}_l$ as sweeping cannot be exactly accurate. The advection of $\delta\boldsymbol{u}$ by the larger-scale velocity is attributable to $\boldsymbol{a}_{\mathcal{T}_{\overline{S}}}$, and figure 3.7 shows that the two-point sweeping anti-alignment between $\delta\boldsymbol{a}_l$ and $\boldsymbol{a}_{\mathcal{T}_{\overline{S}}}$ increases with decreasing r_d.

The sweeping anti-alignment between $\delta\boldsymbol{a}_l$ and $\boldsymbol{a}_{\mathcal{T}_{\overline{S}}}$ is by no means perfect even if it reaches about 90% accuracy at $r_d < \langle\lambda\rangle_t$, as is clear from the similar magnitudes and very strong alignment tendency between $\delta\boldsymbol{a}_l + \boldsymbol{a}_{\mathcal{T}_{\overline{S}}}$ and $-\boldsymbol{a}_{\Pi_{\overline{S}}}$ at scales $|\boldsymbol{r}| \geq \langle\lambda\rangle_t$ (see figures 3.6-3.7). (Note that the Lagrangian solenoidal acceleration $\delta\boldsymbol{a}_l + \boldsymbol{a}_{\mathcal{T}_{\overline{S}}}$ and $\boldsymbol{a}_{\Pi_{\overline{S}}}$ are both

Galilean invariant.) Equation (3.18) may be interpreted to mean that the Lagrangian acceleration of $\delta\boldsymbol{u}$ moving with the mainly large scale velocity $(\boldsymbol{u}^+ + \boldsymbol{u}^-)/2$, namely $\delta\boldsymbol{a}_l + \boldsymbol{a}_{\mathcal{T}_{\overline{S}}}$, is evolving in time and space in response to $-\boldsymbol{a}_{\mathit{\Pi}_{\overline{S}}}$: when there is an influx of momentum from larger scales there is an increase in $\delta\boldsymbol{a}_l + \boldsymbol{a}_{\mathcal{T}_{\overline{S}}}$ and $\delta\boldsymbol{u}$ and vice versa.

Figure 3.8 contains average NSD magnitudes and alignments for the DNS with ABC forcing. These quantities behave qualitatively identically for the two types of forcings.

3.1.4 From NSD Dynamics to KHMH Dynamics

The scale-by-scale evolution of $|\delta\boldsymbol{u}|^2$ locally in space and time is governed by a KHMH equation. This makes KHMH equations crucial tools for examining the turbulent energy cascade (see e.g. Marati et al. (2004); Thiesset et al. (2014); Cimarelli et al. (2016)). The original KHMH equation and the new solenoidal and irrotational KHMH equations that we derive below are simply projections of the corresponding NSD equations onto $2\delta\boldsymbol{u}$ (see appendix A for a detailed derivation of the KHMH equation). Hence, KHMH dynamics depend on NSD dynamics and the various NSD terms' alignment or non-alignment tendencies with $2\delta\boldsymbol{u}$. In this subsection we present four KHMH results all clearly demarcated and identified in *italics*.

By contracting the NSD equation (3.7) with $2\delta\boldsymbol{u}$, one obtains the KHMH equation (Hill, 2002; Yasuda and Vassilicos, 2018):

$$\begin{aligned}\frac{\partial}{\partial t}|\delta\boldsymbol{u}|^2 + \frac{u_k^+ + u_k^-}{2}\frac{\partial}{\partial x_k}|\delta\boldsymbol{u}|^2 + \frac{\partial}{\partial r_k}\big(\delta u_k|\delta\boldsymbol{u}|^2\big) &= -\frac{2}{\rho}\frac{\partial}{\partial x_k}\big(\delta u_k\delta p\big) + 2\nu\frac{\partial^2}{\partial r_k^2}|\delta\boldsymbol{u}|^2\\ &+ \frac{\nu}{2}\frac{\partial^2}{\partial x_k^2}|\delta\boldsymbol{u}|^2 - \left[2\nu\Big(\frac{\partial u_i^+}{\partial x_k^+}\Big)^2 + 2\nu\Big(\frac{\partial u_i^-}{\partial x_k^-}\Big)^2\right] + 2\delta u_k\delta f_k,\end{aligned} \tag{3.19}$$

where no fluid velocity decomposition nor averaging operations have been used. In line with the interpretation and naming convention of Yasuda and Vassilicos (2018), we associate the various terms with the following physical processes:

$$\mathcal{A}_t(\boldsymbol{x},\boldsymbol{r},t) \equiv \partial/\partial t(|\delta\boldsymbol{u}|^2) \text{ is the time-derivative term;} \tag{3.20a}$$

$$\mathcal{T}(\boldsymbol{x},\boldsymbol{r},t) \equiv \partial/\partial x_k((u_k^+ + u_k^-)|\delta\boldsymbol{u}|^2/2) \text{ is the turbulent transport term;} \tag{3.20b}$$

$$\mathit{\Pi}(\boldsymbol{x},\boldsymbol{r},t) \equiv \partial/\partial r_k(\delta u_k|\delta\boldsymbol{u}|^2) \text{ is the interscale energy transfer term;} \tag{3.20c}$$

$$\mathcal{T}_p(\boldsymbol{x},\boldsymbol{r},t) \equiv -(2/\rho)\partial/\partial x_k(\delta u_k\delta p) \text{ is the pressure-velocity term;} \tag{3.20d}$$

$$\mathcal{D}_{r,\nu}(\boldsymbol{x},\boldsymbol{r},t) \equiv 2\nu\partial^2/\partial r_k^2(|\delta\boldsymbol{u}|^2) \text{ is the viscous diffusion in } \boldsymbol{r}\text{-space;} \tag{3.20e}$$

$$\mathcal{D}_{x,\nu}(\boldsymbol{x},\boldsymbol{r},t) \equiv \nu\partial^2/\partial x_k^2(|\delta\boldsymbol{u}|^2/2) \text{ is the viscous diffusion in } \boldsymbol{x}\text{-space;} \tag{3.20f}$$

$$\mathcal{I}(\boldsymbol{x},\boldsymbol{r},t) \equiv 2\delta u_k\delta f_k \text{ is the energy input rate;} \tag{3.20g}$$

$$\epsilon^*(\boldsymbol{x},\boldsymbol{r},t) \equiv 2\nu[(\partial u_j^+/\partial x_k^+))^2 + (\partial u_j^-/\partial x_k^-))^2] \tag{3.20h}$$

is two times the sum of the pseudo-dissipation at $\boldsymbol{x}^+$ and $\boldsymbol{x}^-$.

With this notation (3.19) can be written

$$\mathcal{A}_t + \mathcal{T} + \mathit{\Pi} = \mathcal{T}_p + \mathcal{D}_{r,\nu} + \mathcal{D}_{x,\nu} - \epsilon^* + \mathcal{I}. \tag{3.21}$$

Preempting notation used further down in this chapter, $\mathcal{A}_c \equiv \mathcal{T} + \mathit{\Pi}$ and $\mathcal{D} \equiv \mathcal{D}_{r,\nu} + \mathcal{D}_{x,\nu} - \epsilon^*$ (see also table A.1 at the end of appendix A with a summary of the NS/NSD/KHMH notation sorted according to physical mechanism).

To examine the KHMH dynamics in terms of irrotational and solenoidal dynamics we contract the irrotational and solenoidal NSD equations with $2\delta\boldsymbol{u}$ to derive what we refer to as irrotational and solenoidal KHMH equations. Each of the KHMH terms can be subdivided into a contribution from the NSD irrotational part and a contribution from the NSD solenoidal part of the respective term in the NSD equation. A solenoidal KHMH term corresponding to a $\delta\boldsymbol{q}(\boldsymbol{x},\boldsymbol{r},t)$ or $\boldsymbol{q}(\boldsymbol{x},\boldsymbol{r},t)$ term in equation (3.16b) equals $\mathcal{Q}_{\overline{S}} = 2\delta\boldsymbol{u}\cdot\delta\boldsymbol{q}_{\overline{S}}$ or $\mathcal{Q}_{\overline{S}} = 2\delta\boldsymbol{u}\cdot\boldsymbol{q}_{\overline{S}}$, and an irrotational KHMH term corresponding to a $\delta\boldsymbol{q}(\boldsymbol{x},\boldsymbol{r},t)$ or $\boldsymbol{q}(\boldsymbol{x},\boldsymbol{r},t)$ term in equation (3.17) equals $\mathcal{Q}_{\overline{I}} = 2\delta\boldsymbol{u}\cdot\delta\boldsymbol{q}_{\overline{I}}$ or $\mathcal{Q}_{\overline{I}} = 2\delta\boldsymbol{u}\cdot\boldsymbol{q}_{\overline{I}}$. With $\mathcal{Q} = 2\delta\boldsymbol{u}\cdot\delta\boldsymbol{q}$ or $\mathcal{Q} = 2\delta\boldsymbol{u}\cdot\boldsymbol{q}$, we have $\mathcal{Q} = \mathcal{Q}_{\overline{I}} + \mathcal{Q}_{\overline{S}}$. The irrotational and solenoidal KHMH equations for periodic/homogeneous turbulence follow from contracting equations (3.16b) and (3.17) with $2\delta\boldsymbol{u}$ and read

$$\mathcal{A}_t + \mathcal{T}_{\overline{S}} + \mathit{\Pi}_{\overline{S}} = \mathcal{D}_{r,\nu} + \mathcal{D}_{x,\nu} - \epsilon^* + \mathcal{I}, \tag{3.22a}$$

$$\mathit{\Pi}_{\overline{I}} = \mathcal{T}_{\overline{I}} = \frac{1}{2}\mathcal{T}_p, \tag{3.22b}$$

where use has been made of the fact that the velocity and velocity difference fields are solenoidal. *These two equations are our first KHMH result.*

Space-local changes in time of $|\delta\boldsymbol{u}|^2$, expressed via $\mathcal{A}_t$, are only due to solenoidal KHMH dynamics in equation (3.22a) which include interspace transport, interscale transport, viscous and forcing effects. The irrotational KHMH equation (3.22b) formulates how the imposition of incompressibility by the pressure field affects interspace and interscale dynamics. Solenoidal and irrotational KHMH equations valid for arbitrary boundary conditions are given in section 3.4.

We first consider the spatio-temporal average of these equations in statistically steady forced periodic/homogeneous turbulence. As $\langle\mathcal{T}_p\rangle = 0$, we obtain from equation (3.22b), $\langle\mathit{\Pi}_{\overline{I}}\rangle = \langle\mathcal{T}_{\overline{I}}\rangle = 0$. It follows from $\langle\mathcal{T}_{\overline{S}}\rangle + \langle\mathcal{T}_{\overline{I}}\rangle = \langle\mathcal{T}\rangle = 0$ that $\langle\mathcal{T}_{\overline{S}}\rangle = 0$. Finally, as $\langle\mathcal{D}_{x,\nu}\rangle = 0$, the spatio-temporal average of (3.22a) reads

$$\langle\mathit{\Pi}\rangle = \langle\mathit{\Pi}_{\overline{S}}\rangle = \langle\mathcal{D}_{r,\nu}\rangle - \langle\epsilon^*\rangle + \langle\mathcal{I}\rangle. \tag{3.23}$$

If an intermediate inertial subrange of scales $|\boldsymbol{r}|$ can be defined where viscous diffusion and forcing are negligible, equation (3.23) reduces to $\langle\mathit{\Pi}_{\overline{S}}\rangle \approx -\langle\epsilon^*\rangle$ in that range. This theoretical conclusion (which is not part of our DNS study) is the backbone of the Kolmogorov (1941a,b,c) theory for high Reynolds number statistically homogeneous stationary small-scale turbulence with the additional information that *the part of the average interscale transfer rate involved in Kolmogorov's equilibrium balance is the solenoidal interscale transfer rate only. This is our second KHMH result.* On average, there is a cascade of kinetic energy from large to small scales where the rate of interscale transfer is dominated by two-point vortex stretching effects (see section 3.4 for the relation between $\boldsymbol{a}_{\Pi_{\overline{S}}}$ and vorticity difference dynamics) and is equal to $-\langle \epsilon^* \rangle$ independently of $|\boldsymbol{r}|$ over a range of scales where viscous diffusion and forcing effects are negligible.

In this chapter we concentrate on the fluctuations around the average picture described by the scale-by-scale equilibrium (3.23) for any Reynolds number. If we subtract the spatio-temporal average solenoidal KHMH equation (3.23) from the solenoidal KHMH equation (3.22a) and use the generic notation $\mathcal{Q}' \equiv \mathcal{Q} - \langle \mathcal{Q} \rangle$, we attain the fluctuating solenoidal KHMH equation

$$\mathcal{A}_t + \mathcal{T}_{\overline{S}} + \Pi'_{\overline{S}} = \mathcal{D}'_{r,\nu} + \mathcal{D}_{x,\nu} - \epsilon^{*'} + \mathcal{I}'. \tag{3.24}$$

This equation governs the fluctuations of the KHMH solenoidal dynamics around its spatio-temporal average. Clearly, if these non-equilibrium fluctuations are large relative to their average values, the average picture expressed by equation (3.23) is not characteristic of the interscale transfer dynamics. We now study the KHMH fluctuations in statistically stationary periodic/homogeneous turbulence on the basis of equations (3.22b) and (3.24). Concerning equation (3.22b), note that $\Pi'_{\overline{I}} = \Pi_{\overline{I}}$, $\mathcal{T}'_{\overline{I}} = \mathcal{T}_{\overline{I}}$ and $\mathcal{T}'_{p} = \mathcal{T}_{\overline{p}}$.

We start by determining the relative fluctuation magnitudes of the spatio-temporal fluctuations of each term in the KHMH equations (3.22b) and (3.24). These relative fluctuation magnitudes can emulate those of respective terms in the NSD equations under the following sufficient conditions: (i) the fluctuations are so intense that they dwarf averages, so that $\langle (\mathcal{Q}')^2 \rangle \approx \langle \mathcal{Q}^2 \rangle$; (ii) the mean square of any KHMH term $\mathcal{Q} = 2\delta\boldsymbol{u} \cdot \delta\boldsymbol{q}$ corresponding to a NSD term $\delta\boldsymbol{q}(\boldsymbol{x}, \boldsymbol{r}, t)$ (equivalently $\mathcal{Q} = 2\delta\boldsymbol{u} \cdot \boldsymbol{q}$ corresponding to $\boldsymbol{q}(\boldsymbol{x}, \boldsymbol{r}, t)$) can be approximated as

$$\langle \mathcal{Q}^2 \rangle(\boldsymbol{r}) \approx 4\langle |\delta\boldsymbol{u}|^2 \rangle \langle |\delta\boldsymbol{q}|^2 \rangle \langle \cos^2(\theta_q) \rangle, \tag{3.25}$$

where the approximate equality results from a degree of decorrelation and θ_q is the angle between $\delta\boldsymbol{q}(\boldsymbol{x}, \boldsymbol{r}, t)$ and $\delta\boldsymbol{u}(\boldsymbol{x}, \boldsymbol{r}, t)$; (iii) $\langle \cos^2(\theta_q) \rangle$ is not very sensitive to the choice of NSD term $\delta\boldsymbol{q}$ (or $\boldsymbol{q}$). For NSD terms $\delta\boldsymbol{q}$ and $\delta\boldsymbol{w}$ satisfying these conditions, we get

$$\frac{\langle (2\delta\boldsymbol{u} \cdot \delta\boldsymbol{q})^2 \rangle(\boldsymbol{r})}{\langle (2\delta\boldsymbol{u} \cdot \delta\boldsymbol{w})^2 \rangle(\boldsymbol{r})} \approx \frac{\langle |\delta\boldsymbol{u}|^2 \rangle \langle |\delta\boldsymbol{q}|^2 \rangle \langle \cos^2(\theta_q) \rangle(\boldsymbol{r})}{\langle |\delta\boldsymbol{u}|^2 \rangle \langle |\delta\boldsymbol{w}|^2 \rangle \langle \cos^2(\theta_w) \rangle(\boldsymbol{r})} \approx \frac{\langle |\delta\boldsymbol{q}|^2 \rangle(\boldsymbol{r})}{\langle |\delta\boldsymbol{w}|^2 \rangle(\boldsymbol{r})}, \tag{3.26}$$

which means that KHMH relative fluctuation magnitudes and NSD relative fluctuation magnitudes are approximately identical. The first approximate equality in (3.26) follows directly from (3.25) and the second approximate equality follows from hypothesis (iii) that $\cos^2(\theta_q)$ and $\cos^2(\theta_w)$ are about equal.

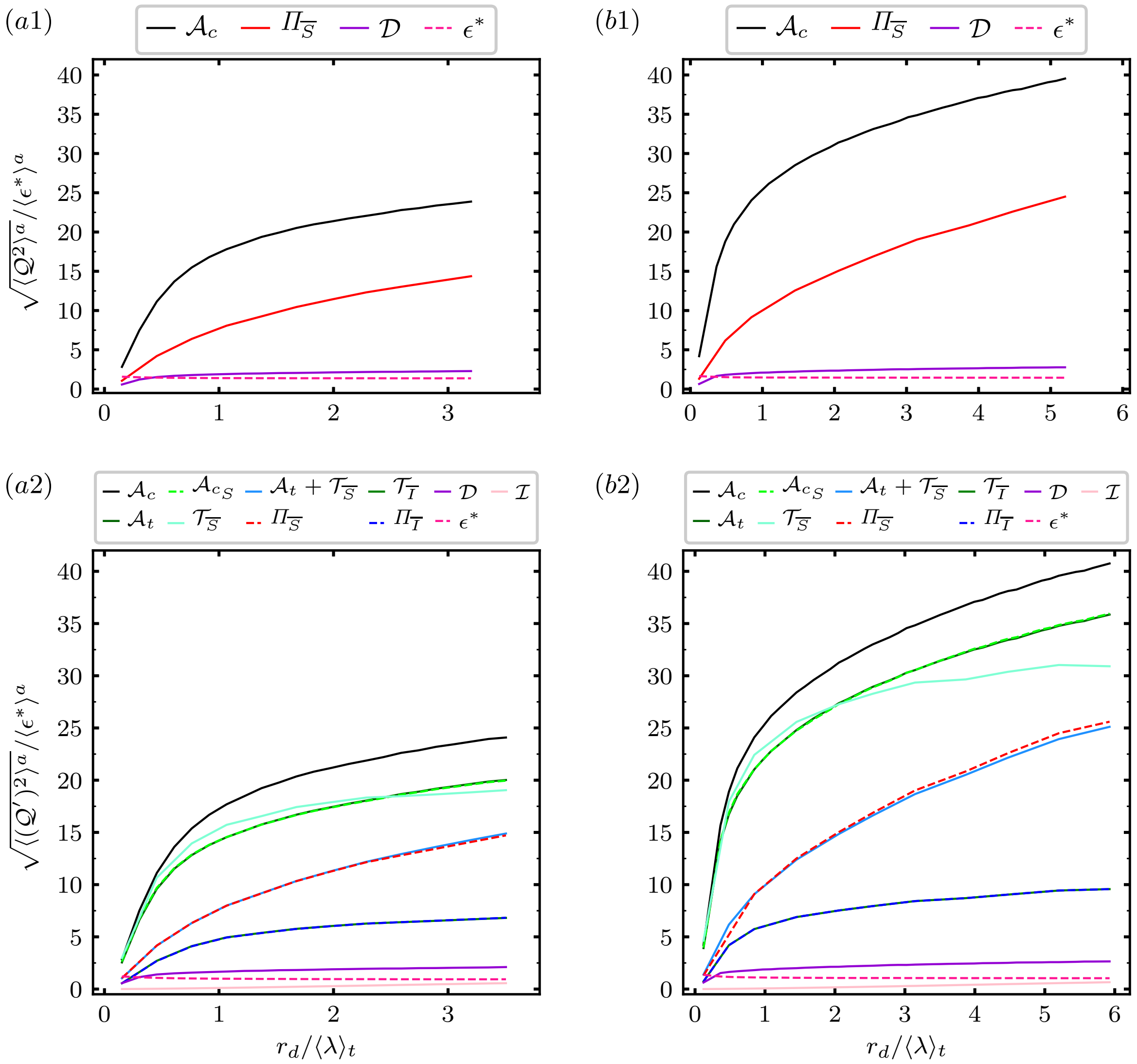

Figure 3.9: ($a1$, $b1$) KHMH average square magnitudes $\langle \mathcal{Q}\rangle^a$ and ($a2$, $b2$) KHMH average square fluctuating magnitudes $\langle \mathcal{Q}'\rangle^a$, where $\mathcal{Q}' = \mathcal{Q} - \langle \mathcal{Q}\rangle$, for the KHMH terms $\mathcal{Q}$ listed above the figures. The following pairs of KHMH terms have overlapping magnitudes in ($a2, b2$): ($\mathcal{A}_t, \mathcal{A}_{c_S}$), ($\mathcal{A}_t + \mathcal{T}_{\overline{S}}, \Pi_{\overline{S}}$) and ($\mathcal{T}_{\overline{I}}, \Pi_{\overline{I}}$). ($a1$, $a2$) $\langle Re_\lambda\rangle_t = 112$, ($b1$,$b2$) $\langle Re_\lambda\rangle_t = 174$.

We test hypothesis (i) by comparing the plots in figure 3.9($a1$, $b1$) with those in figure 3.9($a2$, $b2$). Figure 3.9($a1$, $b1$) shows average magnitudes of KHMH spatio-temporal fluctuations for terms with non-zero spatio-temporal averages. Comparing with figure 3.9($a2$, $b2$), we find $\langle (\mathcal{Q}')^2\rangle^a \approx \langle \mathcal{Q}^2\rangle^a$, i.e. hypothesis (i), for $\mathcal{A}_c$ and $\Pi_{\overline{S}}$, but not for $\mathcal{D}$.

We test hypothesis (ii) by testing the validity of (3.25) and hypothesis (iii) concerning approximately similar $\cos^2(\theta_q)$ behaviour for different KHMH terms. In figure 3.10($a1$, $b1$) we plot ratios of right-hand sides to left-hand sides of equation (3.25) and see that (3.25) is not valid, but it is nevertheless about 50% to 98% accurate for $r_d \geq \langle\lambda\rangle_t$. Note that (3.25) might be sufficient but that it is by no means necessary for the left-most and the right-most sides of (3.26) to approximately balance. In those cases where the variations between the ratios plotted in figure 3.10($a1$, $b1$) are not too large and the assumption of

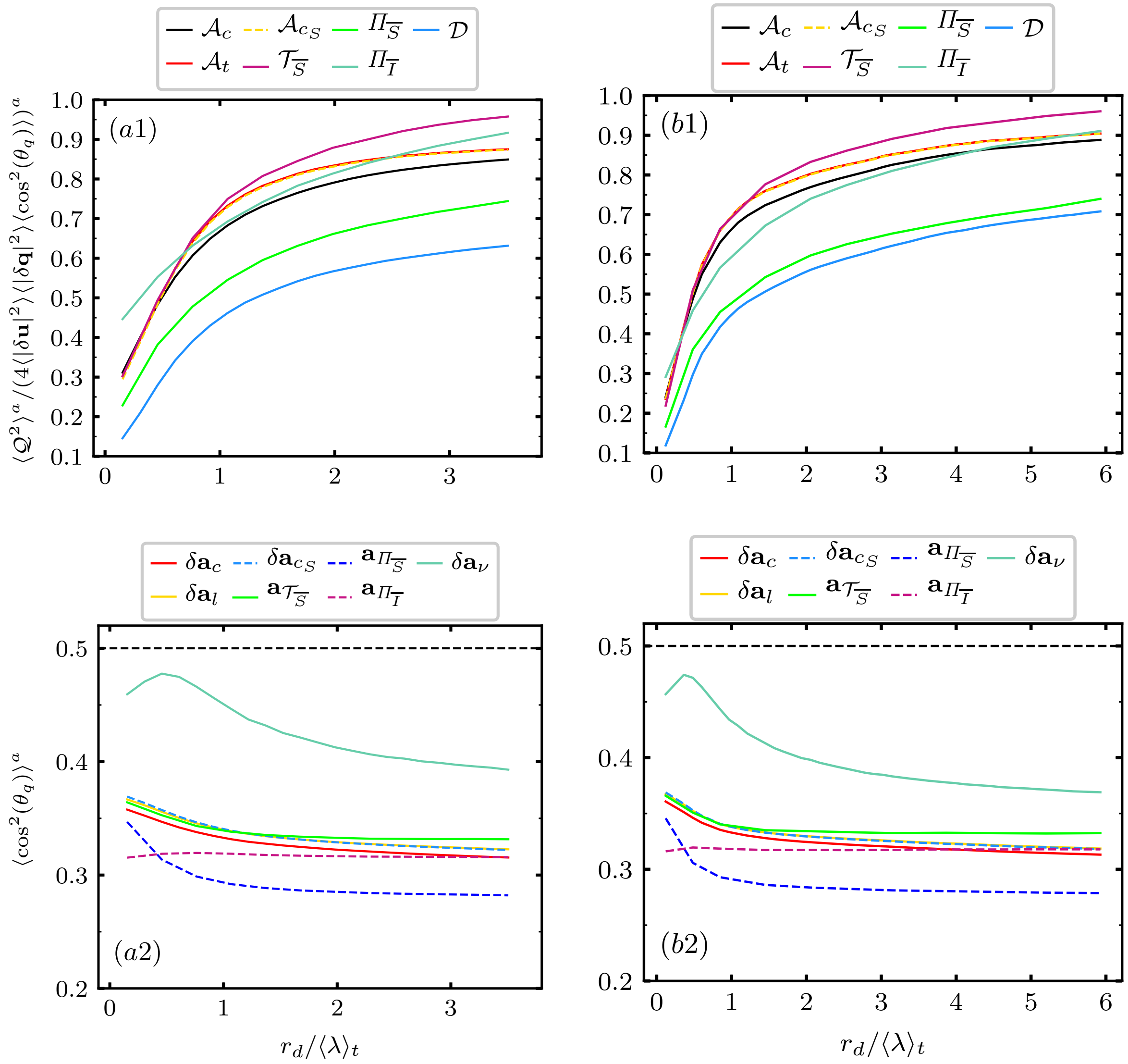

Figure 3.10: Test of the assumptions (ii)-(iii) related to relations (3.25)-(3.26) connecting NSD and KHMH relative magnitudes. ($a1$,$b1$) Test of assumption (ii) by taking the ratio of the left-hand and right-hand sides of (3.25) for the KHMH terms listed above the figures. ($a2$,$b2$) test of assumption (iii) used in (3.26) by comparing the behaviour of $\langle\cos^2(\theta_q)\rangle^a$ for the NSD terms listed above the figures. The horizontal line 0.5 corresponds to the value of $\langle\cos^2(\theta_q)\rangle$ if θ_q is uniformly distributed. $(a1, a2)$ $\langle Re_\lambda\rangle_t = 112$, $(b1, b2)$ $\langle Re_\lambda\rangle_t = 174$.

approximately similar $\cos^2(\theta_q)$ for different KHMH terms more or less holds, the left-most and the right-most sides of (3.26) can approximately balance.

Incidentally, figure 3.10($a2$, $b2$) also shows that the angles θ_q are not random but that they are more likely to be small rather than large in an approximately similar way for all important NSD terms: $\cos^2(\theta_q)$ ranges between about 0.28 and 0.36 for all NSD terms (except the viscous acceleration difference and the force difference) at all scales r_d. These values are much smaller than 0.5, the value that $\cos^2(\theta_q)$ would have taken if the angles θ_q were random. There is therefore an alignment tendency between $\delta\boldsymbol{u}$ and NSD terms which is similar for all the important NSD terms, thereby allowing the balance between

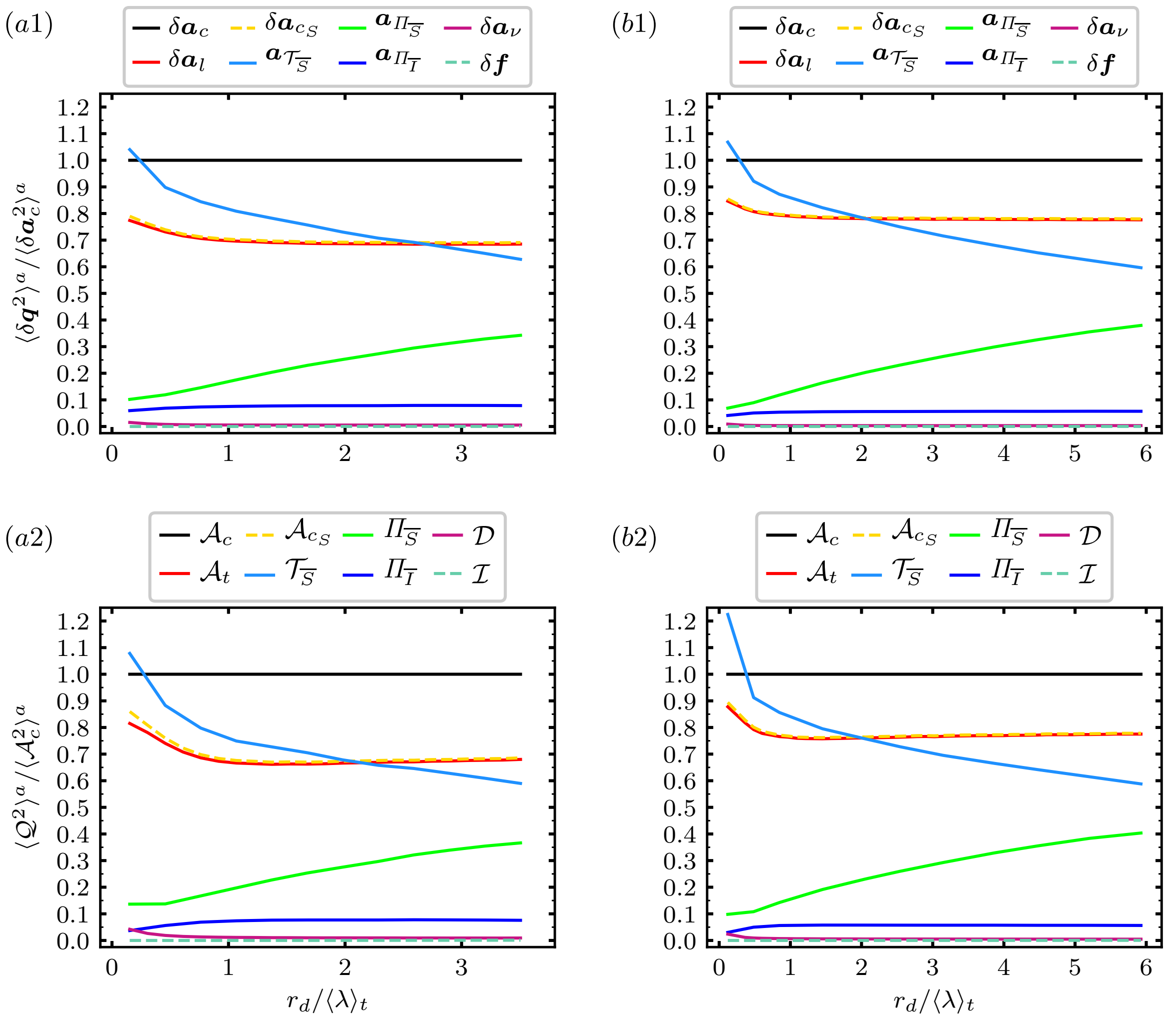

Figure 3.11: NSD and KHMH relative average square magnitudes (which should be similar based on (3.26)) for the terms listed above the figures: $(a1)$ NSD and $(a2)$ KHMH for $\langle Re_\lambda\rangle_t = 112$, $(b1)$ NSD and $(b2)$ KHMH for $\langle Re_\lambda\rangle_t = 174$.

the left-most (ratio of KHMH terms) and the right-most (ratio of NSD terms) sides of (3.26) to approximately hold as seen by comparing the plots $(a1)$-$(b1)$ (mean square NSD terms) with the plots $(a2)$-$(b2)$ (mean square KHMH terms) in figure 3.11. Note that the viscous term is bounded from above, $\langle \mathcal{D}^2\rangle(\boldsymbol{r}) \leq 4\langle|\delta\boldsymbol{u}|^2|\delta\boldsymbol{a}_\nu|^2\rangle$, which indicates limited magnitudes compared to the irrotational and the dominant solenoidal terms because of the limited magnitude of $\langle\delta\boldsymbol{a}_\nu^2\rangle$. The limited fluctuations of the viscous terms are clearly seen in figure 3.9 (hypotheses (i)-(iii), and subsequently equation (3.26), hold for the same KHMH terms with the ABC forcing as with the negative damping forcing, i.e. all terms except the viscous term $\mathcal{D}$ and the forcing term $\mathcal{I}$ (not shown)).

Figure 3.11 does confirm the NSD-KHMH correspondence (3.26) which is a step further from the NS-NSD correspondence reported earlier in this chapter. Consistent with this NSD-KHMH correspondence (3.26), figure 3.9 makes it clear that the magnitudes of the fluctuations of all KHMH terms (solenoidal and irrotational) are much higher than those of the turbulence dissipation at all scales $r_d > 0.5\langle\lambda\rangle_t$, and more so for the higher of the

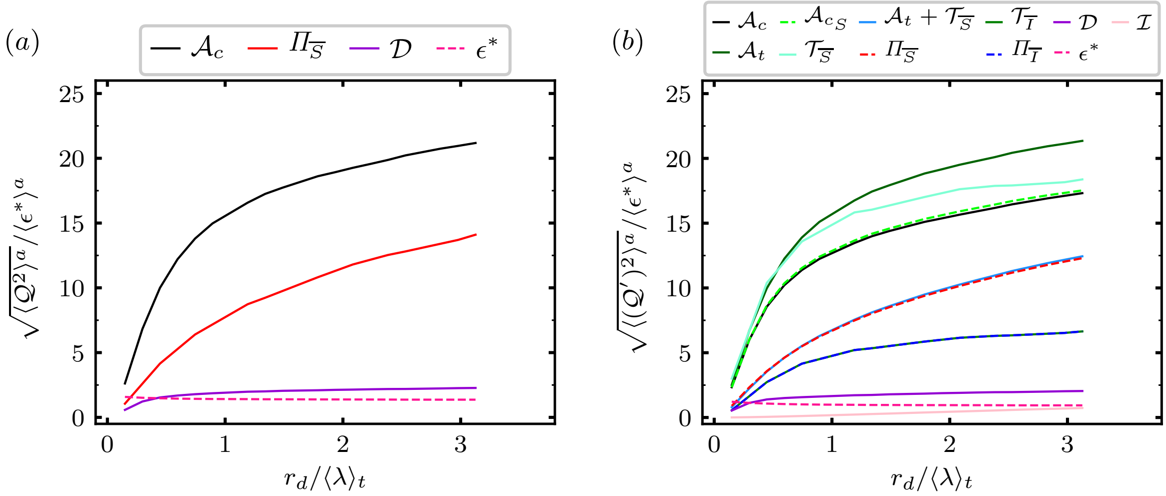

Figure 3.12: (a) KHMH average square magnitudes $\langle \mathcal{Q}^2\rangle^a$ and (b) KHMH average square fluctuating magnitudes $\langle(\mathcal{Q}^{'})^2\rangle^a$. In (b) the KHMH pairs $(\mathcal{A}_t, \mathcal{A}_{c_S})$, $(\mathcal{A}_t + \mathcal{T}_{\overline{S}}, \varPi_{\overline{S}})$ and $(\mathcal{T}_{\overline{I}}, \varPi_{\overline{I}})$ have overlapping magnitudes. $\langle Re_\lambda\rangle_t = 111$.

two Reynolds numbers. As these KHMH fluctuations $\sqrt{\langle(\mathcal{Q}')^2\rangle^a}$ are large relative to their spatio-temporal averages $\langle\mathcal{Q}\rangle^a$, an average description of the KHMH dynamics cannot, therefore, be accurate locally. Attention must be directed at most if not all KHMH terms to characterise the local KHMH dynamics at such scales. Figure 3.9 shows that for scales $r_d \geq \langle\lambda\rangle_t$, the largest average fluctuating magnitudes are those of $\mathcal{A}_c^{'}$, followed closely by $\mathcal{A}_t$ and $\mathcal{T}_{\overline{S}}$. Next come the very similar magnitudes of $\varPi_{\overline{S}}^{'}$ and $\mathcal{A}_t + \mathcal{T}_{\overline{S}}$. Thereafter follow the irrotational terms $\varPi_{\overline{I}} = \mathcal{T}_{\overline{I}}$ $(= 0.5\mathcal{T}_p)$ and finally the viscous, dissipative and forcing terms $\mathcal{D}^{'}$, $\epsilon^{*'}$ and $\mathcal{I}^{'}$ in that order. That is, for scales $r_d \geq \langle\lambda\rangle_t$, consistent with the NSD-KHMH correspondence (3.26) and the NSD magnitude hierarchy (3.11), we have

$$\langle\mathcal{A}_t^2\rangle \approx \langle\mathcal{A}_{c_S}^2\rangle \gg \langle\mathcal{T}_p^2\rangle = 4\langle\varPi_{\overline{I}}^2\rangle = 4\langle\mathcal{T}_{\overline{I}}^2\rangle = \langle\mathcal{A}_{c_I}^2\rangle \gg \langle\mathcal{D}^2\rangle \gg \langle\mathcal{I}^2\rangle. \tag{3.27}$$

Moreover, figure 3.11 shows for decreasing r_d for $r_d \geq \langle\lambda\rangle_t$ that the relative fluctuation magnitude of $\mathcal{A}_{c_S} = \mathcal{T}_{\overline{S}} + \varPi_{\overline{S}}$ remains about constant but that of $\mathcal{T}_{\overline{S}}$ increases while that of $\varPi_{\overline{S}}$ decreases. The convective non-linearity is increasingly of the spatial transport type and diminishingly of the interscale transfer type as the two-point separation length decreases. *This order of fluctuations is our third KHMH result.* (Figure 3.12 reiterates this hierarchy of KHMH fluctuation magnitudes for the DNS with an ABC forcing.)

These KHMH fluctuations suggest that the solenoidal KHMH equation reduces to:

$$\mathcal{A}_t + \mathcal{T}_{\overline{S}} + \varPi_{\overline{S}}^{'} \approx 0, \tag{3.28}$$

understood in the sense that it holds in the majority of the domain for the majority of time. *The approximate equation $\mathcal{A}_t + \mathcal{T}_{\overline{S}} + \varPi_{\overline{S}}^{'} \approx 0$ is our fourth KHMH result.*

We next consider correlations between different intermediate and large scale fluctuating KHMH terms in light of their fluctuation magnitudes and equations (3.22b)-(3.28).

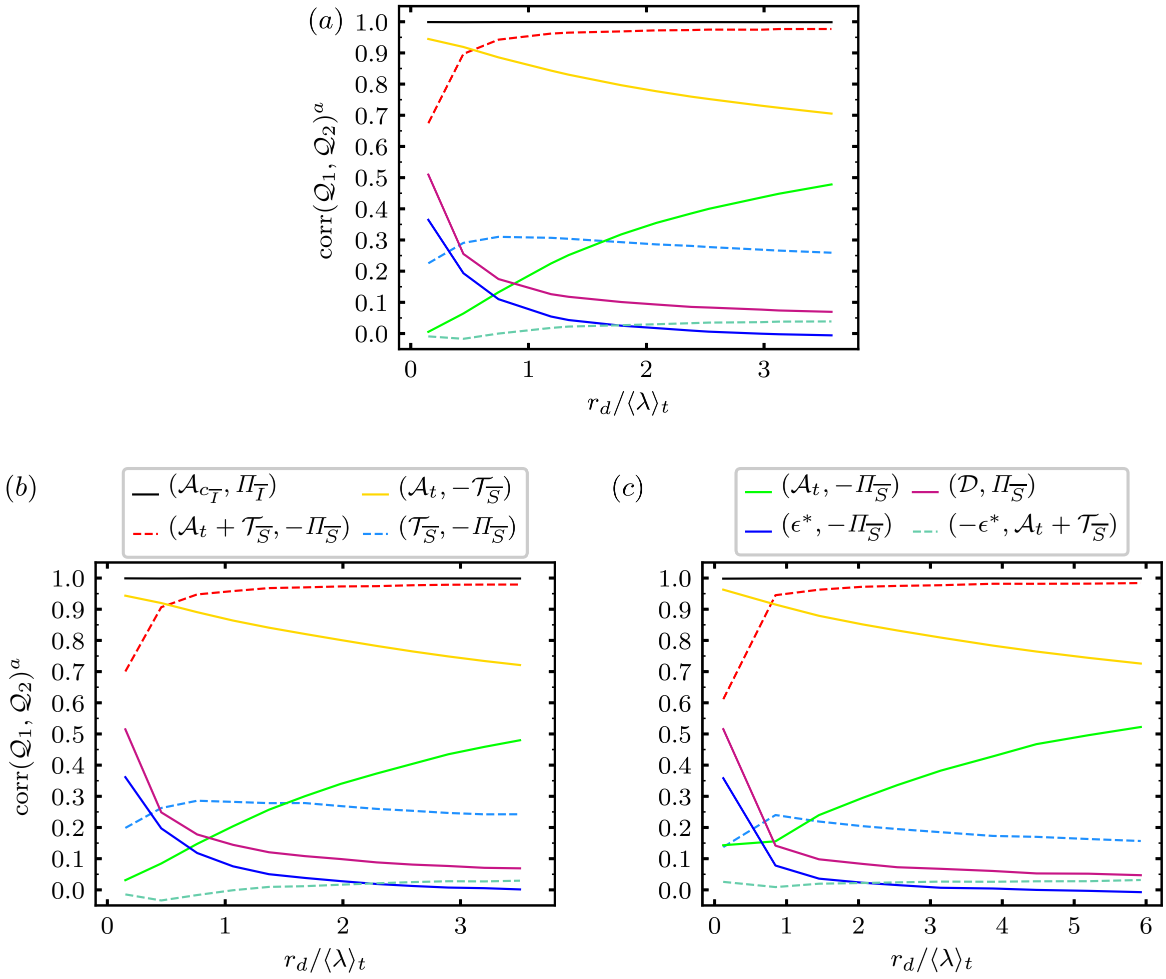

Figure 3.13: Spherically averaged correlation coefficients between KHMH terms listed on top of (b) and (c) as a function of scale r_d. (a) $\langle Re_\lambda\rangle_t = 111$, (b) $\langle Re_\lambda\rangle_t = 112$, (c) $\langle Re_\lambda\rangle_t = 174$.

3.2 Fluctuating KHMH Dynamics

3.2.1 Correlations between Different KHMH Terms

We start this section by assessing the existence/non-existence of local (in space and time) equilibrium between interscale transfer and dissipation at some intermediate scales. In figure 3.13 we plot correlations between various KHMH terms. In particular, this figure shows that the correlation coefficient between $\Pi'_{\overline{S}}$ and $-\epsilon^{*'}$ lies well below 0.2 for all scales $r_d \geq \langle\lambda\rangle_t$. The scatter plots of these quantities in figure 3.14 confirm the absence of a local relation between interscale transfer and dissipation. For example, for a given local dissipation fluctuation, the corresponding local interscale transfer rate fluctuation can be close to equally positive or negative. There is no local equilibrium between these quantities as they fluctuate at scales $r_d \geq \langle\lambda\rangle_t$. Such a correlation should of course not necessarily be expected. Our results show that the very weak correlation between these two quantities at these scales is even lower for the higher $\langle Re_\lambda\rangle_t$. However, as r_d

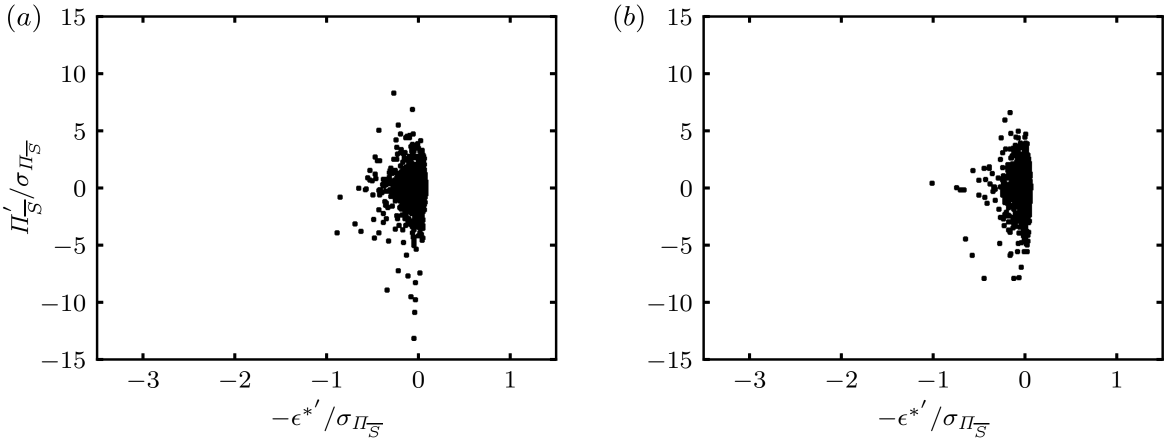

Figure 3.14: Scatter plots of $\Pi'_{\overline{S}}$ and $\epsilon^{*\prime}$ at random orientations $\boldsymbol{r}$ with $r_d/\langle\lambda\rangle_t = (1.45, 3.1)$ for (a, b), $\sigma_{\Pi_{\overline{S}}}$ is the standard deviation of $\Pi_{\overline{S}}$ and $\langle Re_\lambda\rangle_t = 174$.

decreases below $\langle\lambda\rangle_t$, the correlations between $\Pi'_{\overline{S}}$ and either $-\epsilon^{*\prime}$ or $\mathcal{D}'$ increase up to values between about 0.3 and about 0.5. This increased correlation may suggest a feeble tendency towards local equilibrium between interscale transfer rate and dissipation rate at scales $r_d < \langle\lambda\rangle_t$. However, these scales are strongly affected by direct viscous processes and can therefore not be inertial range scales.

Following the question of local equilibrium, we now look for local sweeping. Figure 3.13 shows strong anti-correlation between $\mathcal{A}_t$ and $\mathcal{T}_{\overline{S}}$, increasingly so as r_d decreases from larger to smaller scales. As $\mathcal{A}_t + \mathcal{T}_{\overline{S}} + \Pi_{\overline{S}} \approx 0$, this behaviour requires an increasing magnitude separation between the terms $(\mathcal{A}_t, \mathcal{T}_{\overline{S}})$ and $(\mathcal{A}_t + \mathcal{T}_{\overline{S}}, \Pi_{\overline{S}})$ as r_d decreases as observed in the previous section. In other words, the local Eulerian sweeping accelerations of $|\delta\boldsymbol{u}|^2$ by the mainly large-scale advection velocity $(\boldsymbol{u}^+ + \boldsymbol{u}^-)/2$ become increasingly strong relative to the local Lagrangian acceleration of $|\delta\boldsymbol{u}|^2$ moving in the $(\boldsymbol{u}^+ + \boldsymbol{u}^-)/2$ frame. This behaviour is clearly analogous to the behaviour pictured by Tennekes (1975). The scatter plots of $\mathcal{A}_t$ and $\mathcal{T}_{\overline{S}}$ in figure 3.15 make the two-point sweeping tendency with decreasing r_d very evident. As r_d decreases, $\Pi_{\overline{S}}$ causes decreasing deviations from two-point sweeping relative to the $(\mathcal{A}_t, \mathcal{T}_{\overline{S}})$ magnitudes.

The correlation coefficients in figure 3.13 and scatter plots in figure 3.16 show that it is only in relatively rare circumstances that $\mathcal{A}_t + \mathcal{T}_{\overline{S}} + \Pi_{\overline{S}} \approx 0$ is significantly inaccurate for scales $r_d \geq \langle\lambda\rangle_t$. Similarly to NSD dynamics, as more than average $|\delta\boldsymbol{u}|^2$ is cascaded from larger to smaller scales at a particular location $(\Pi'_{\overline{S}} < 0)$, $\mathcal{A}_t + \mathcal{T}_{\overline{S}}$ increases; and as more than average $|\delta\boldsymbol{u}|^2$ is inverse cascaded from smaller to larger scales $(\Pi'_{\overline{S}} > 0)$, $\mathcal{A}_t + \mathcal{T}_{\overline{S}}$ decreases. This behaviour differs from the analogue NS one-point behaviour in Tennekes (1975) and Tsinober et al. (2001); the Lagrangian two-point accelerations $\mathcal{A}_t + \mathcal{T}_{\overline{S}}$ balance mainly with solenoidal interscale transfers rather than with viscosity as in the one-point approximate balance $(\boldsymbol{a}_l + \boldsymbol{a}_{c_S} \approx \boldsymbol{a}_\nu)$. This dual role of non-linearity in terms of physical and interscale transport is unavailable in a one-point setting. Note that $\Pi'_{\overline{S}}$ is to a large extent determined by $\boldsymbol{a}_{\Pi_{\overline{S}}}$ which, as we show in section 3.4, is a non-local function in

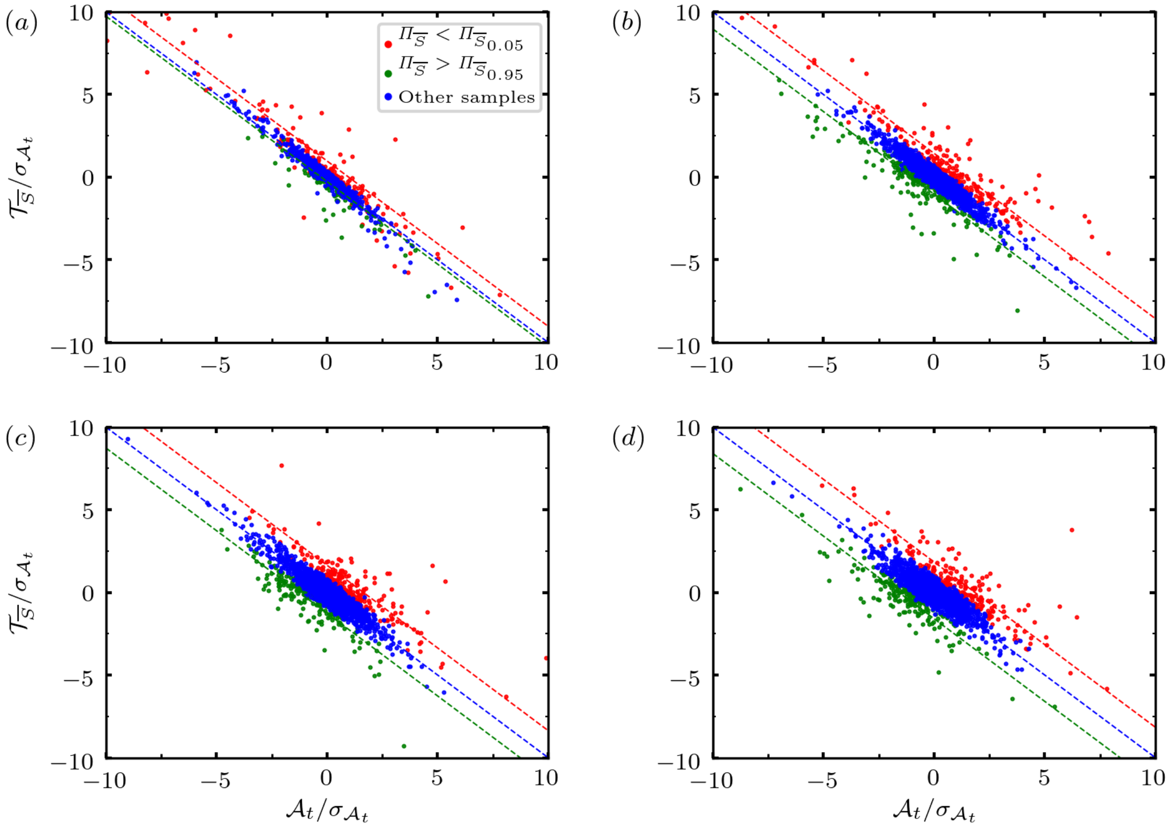

Figure 3.15: Scatter plots of $\mathcal{A}_t$ and $\mathcal{T}_{\overline{S}}$ at random orientations $\boldsymbol{r}$ normalised by $\sigma_{\mathcal{A}_t}$ and $\sigma_{\mathcal{T}_{\overline{S}}}$, their respective standard deviations. $\Pi_{\overline{S}_{0.05}}$ is the value of $\Pi_{\overline{S}}$ at the respective r_d for which 5% of the samples are more negative than $\Pi_{\overline{S}_{0.05}}$ and $\Pi_{\overline{S}_{0.95}}$ is the value of $\Pi_{\overline{S}}$ for which 95% of the samples are more positive than $\Pi_{\overline{S}_{0.95}}$. The events $\Pi_{\overline{S}} < \Pi_{\overline{S}_{0.05}}$ and $\Pi_{\overline{S}} > \Pi_{\overline{S}_{0.95}}$ are marked in red and green respectively, while the remaining events are marked in blue. The red line marks $\mathcal{A}_t = -\mathcal{T}_{\overline{S}} - \langle \Pi_{\overline{S}} | \Pi_{\overline{S}} < \Pi_{\overline{S}_{0.05}} \rangle$, where $\langle \Pi_{\overline{S}} | \Pi_{\overline{S}} < \Pi_{\overline{S}_{0.05}} \rangle$ is the average value of $\Pi_{\overline{S}}$ conditioned on $\Pi_{\overline{S}} < \Pi_{\overline{S}_{0.05}}$. The green line marks $\mathcal{A}_t = -\mathcal{T}_{\overline{S}} - \langle \Pi_{\overline{S}} | \Pi_{\overline{S}} > \Pi_{\overline{S}_{0.95}} \rangle$ and the blue line marks $\mathcal{A}_t = -\mathcal{T}_{\overline{S}}$ (with all terms appropriately normalised with $\sigma_{\mathcal{A}_t}$ and $\sigma_{\mathcal{T}_{\overline{S}}}$). $r_d/\langle \lambda \rangle_t = (0.12, 1.45, 3.1, 5.2)$ for (a, b, c, d) and $\langle Re_\lambda \rangle_t = 174$.

space of the vortex stretching/compression and tilting dynamics determining the two-point vorticity difference $\delta\boldsymbol{\omega}$ evolution (see the similar KHMH correlation coefficients with the ABC forcing in figure 3.13(a)).

A fairly complete way to summarise the balance $\mathcal{A}_t + \mathcal{T}_{\overline{S}} + \Pi_{\overline{S}} \approx 0$ at scales $r_d \geq \langle \lambda \rangle_t$ is by noting that as r_d decreases two-point sweeping makes the fluctuation magnitudes of $\mathcal{T}_{\overline{S}}$ tend to become comparable to those of $\mathcal{A}_t$ (i.e. local Eulerian accelerations) while those of $\mathcal{A}_t + \mathcal{T}_{\overline{S}}$ (i.e. local Lagrangian accelerations) decrease by comparison. As viscous effects are negligible at most locations at most times, $\mathcal{A}_t + \mathcal{T}_{\overline{S}} \approx -\Pi_{\overline{S}}$ is accurate with the interscale transfer rate (arising from the vortex stretching/compression dynamics of its spatial vicinity), making $|\delta \boldsymbol{u}|^2$ evolve in the frame moving with larger scales.

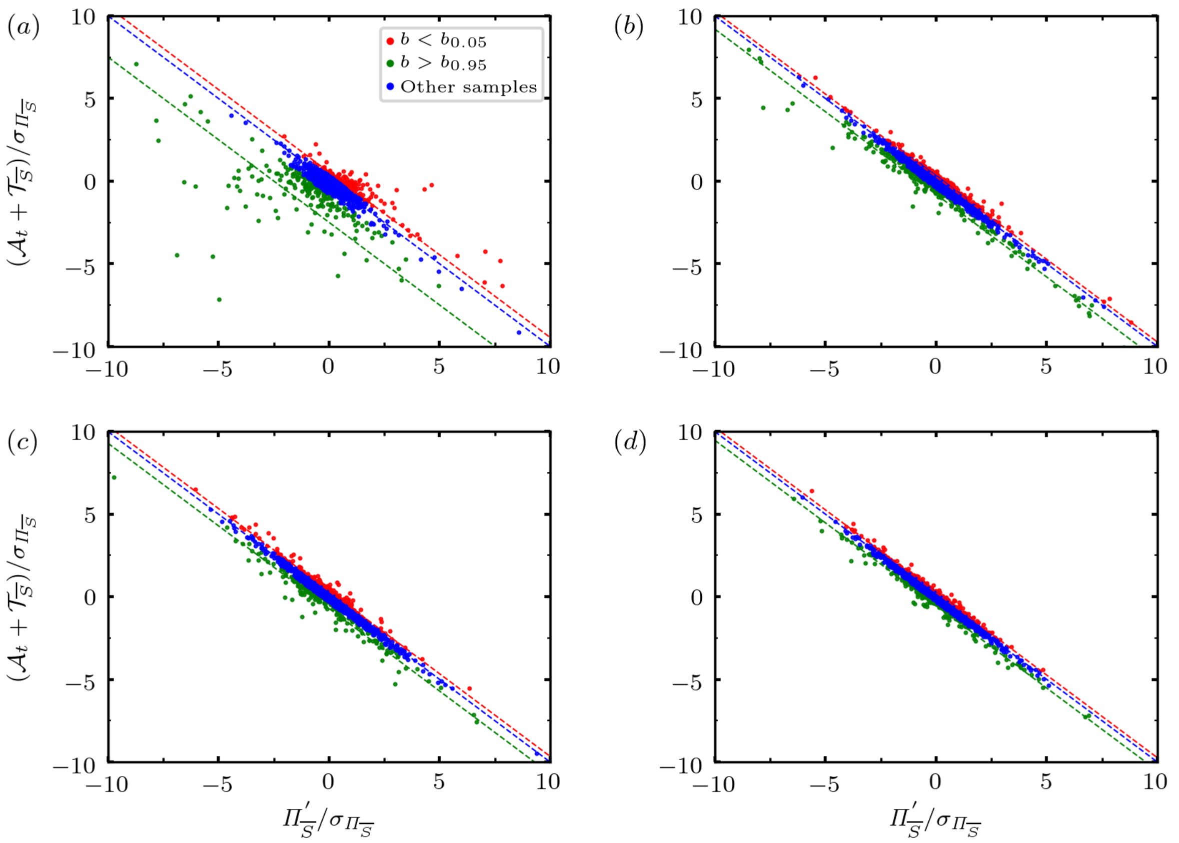

Figure 3.16: Scatter plots of $\mathcal{A}_t + \mathcal{T}_{\overline{S}}$ and $\Pi'_{\overline{S}}$ at random orientations $\boldsymbol{r}$. The residual $-b \equiv \mathcal{A}_t + \mathcal{T}_{\overline{S}} + \Pi'_{\overline{S}}$ and the values $b_{0.05}$ and $b_{0.95}$ are defined analogously as for $\Pi_{\overline{S}_{0.05}}$ and $\Pi_{\overline{S}_{0.95}}$ in the previous figure. The events $b < b_{0.05}$ and $b > b_{0.95}$ are marked in red and green respectively, while the remaining events are marked in blue. The red line marks $\mathcal{A}_t + \mathcal{T}_{\overline{S}} = -\Pi'_{\overline{S}} - \langle b | b < b_{0.05} \rangle$, the green line $\mathcal{A}_t + \mathcal{T}_{\overline{S}} = -\Pi'_{\overline{S}} - \langle b | b > b_{0.95} \rangle$ and the blue line $\mathcal{A}_t + \mathcal{T}_{\overline{S}} = -\Pi'_{\overline{S}}$ (with all terms appropriately normalised with $\sigma_{\Pi_{\overline{S}}}$). $r_d / \langle \lambda \rangle_t = (0.12, 1.45, 3.1, 5.2)$ for (a, b, c, d) and $\langle Re_\lambda \rangle_t = 174$.

3.2.2 Conditional KHMH Statistics

At scales r_d below $\langle \lambda \rangle_t$, the relation $\mathcal{A}_t + \mathcal{T}_{\overline{S}} + \Pi_{\overline{S}} \approx 0$ becomes less accurate as the correlation coefficient between $\mathcal{A}_t + \mathcal{T}_{\overline{S}}$ and $-\Pi_{\overline{S}}$ drops from 0.95 to 0.7 with decreasing r_d (see figure 3.13), reflecting the increase of correlation between ϵ^* and $-\Pi_{\overline{S}}$ and the even higher increase towards values close to 0.5 of the correlation coefficient between $\mathcal{D}$ and $\Pi_{\overline{S}}$. This increase of correlation appears to reflect the impact of relatively rare yet intense local/instantaneous occurrences of interscale transfer rate as shown in figure 3.17 where we plot correlations conditional on relatively rare interscale events where the magnitudes of the spherically averaged interscale transfer rates are higher than 95% of all interscale transfer rates of the same sign (positive for backward and negative for forward transfer) in our overall spatio-temporal sample. This impact is highest at scales smaller than $\langle \lambda \rangle_t$ where the correlation coefficient conditioned on intense forward or backward interscale transfer rate events of $\pm\Pi_{\overline{S}}$ and either ϵ^* or $\mathcal{D}$ can be as high as 0.7 ($+\Pi_{\overline{S}}$ in the

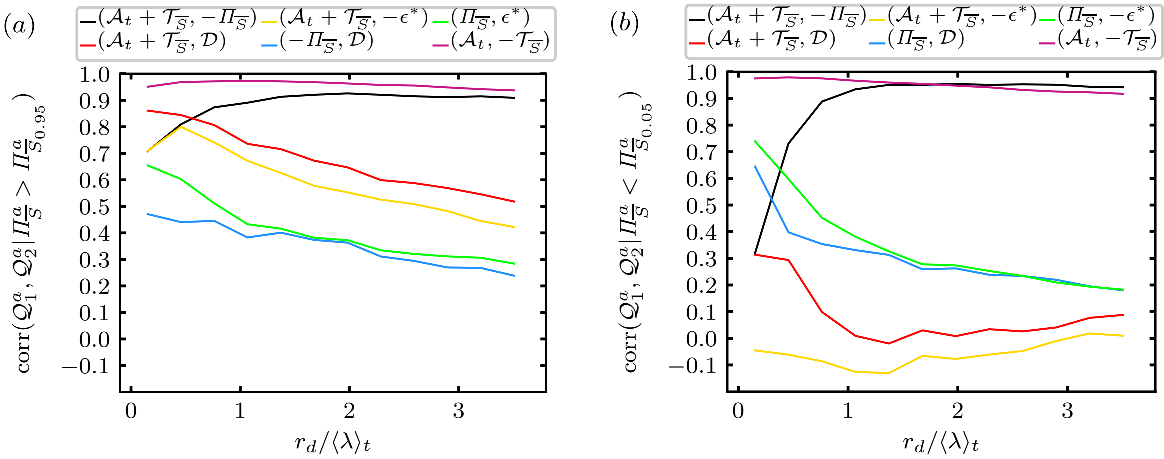

Figure 3.17: (*a*) KHMH correlation coefficients among the 5% strongest spherically averaged backward interscale transfer events $\Pi_{\overline{S}}^a > \Pi_{\overline{S}_{0.95}}^a$. (*b*) KHMH correlation coefficients among the 5% strongest spherically averaged forward interscale transfer events $\Pi_{\overline{S}}^a < \Pi_{\overline{S}_{0.05}}^a$. $\langle Re_\lambda \rangle_t = 112$ (corresponding plots for $\langle Re_\lambda \rangle_t = 174$ are omitted because they are very similar).

case of backward events and $-\Pi_{\overline{S}}$ in the case of forward events which causes significantly higher correlations between $\mathcal{A}_t + \mathcal{T}_{\overline{S}}$ and either $-\epsilon^*$ or $\mathcal{D}$ in the case of backward events than in the case of forward events as seen in figure 3.17). However, the impact of such relatively rare events is also manifest at scales larger than $\langle\lambda\rangle_t$ (see figure 3.17) where the conditioned correlation coefficient is significantly higher than the unconditioned one in figure 3.13. Interestingly, conditioning on these relatively rare events does not change the correlation coefficients of $\mathcal{A}_t + \mathcal{T}_{\overline{S}}$ with $-\Pi_{\overline{S}}^{'}$ except at scales r_d smaller than $\langle\lambda\rangle_t$ where, consistently with the increased conditioned correlations between $-\Pi_{\overline{S}}$ and $\mathcal{D}$, they are smaller than the unconditional correlation correlation coefficients of $\mathcal{A}_t + \mathcal{T}_{\overline{S}}$ with $-\Pi_{\overline{S}}^{'}$, particularly at relatively rare forward interscale events where this conditional correlation drops to values close to 0.3 at scales well below $\langle\lambda\rangle_t$.

Given our relatively rare intense interscale transfer rates can be the seat of some correlation between $\Pi_{\overline{S}}$ and either $-\epsilon^*$ or $\mathcal{D}$ particularly for $r_d < \langle\lambda\rangle_t$, and given that $\mathcal{A}_t + \mathcal{T}_{\overline{S}} \approx 0$ is a good approximation at scales smaller than $\langle\lambda\rangle_t$, do we have approximate two-point sweeping and approximate equilibrium $\Pi_{\overline{S}} \approx \mathcal{D}$ if we condition on relatively rare forward or backward interscale transfer rate events? In fact the conditional correlations between $\mathcal{A}_t$ and $-\mathcal{T}_{\overline{S}}$ are very high (close to and above 0.95) at all scales (see figure 3.17), higher than the corresponding unconditional correlations. However, the conditional averages of $\mathcal{A}_t$ and $-\mathcal{T}_{\overline{S}}$ shown in figure 3.18 are also significantly different at all scales, implying that these strong conditional correlations do not actually amount to two-point sweeping at relatively rare forward and backward events. Furthermore, if we condition on high negative/positive values of $\Pi_{\overline{S}}$, the averages of both $\mathcal{A}_t$ and $\mathcal{T}_{\overline{S}}$ are positive/negative (figure 3.18), even though these conditional averages do tend to 0 as r_d tends to 0. This implies that, even though $\mathcal{A}_t$ and $-\mathcal{T}_{\overline{S}}$ are very well correlated at these relatively

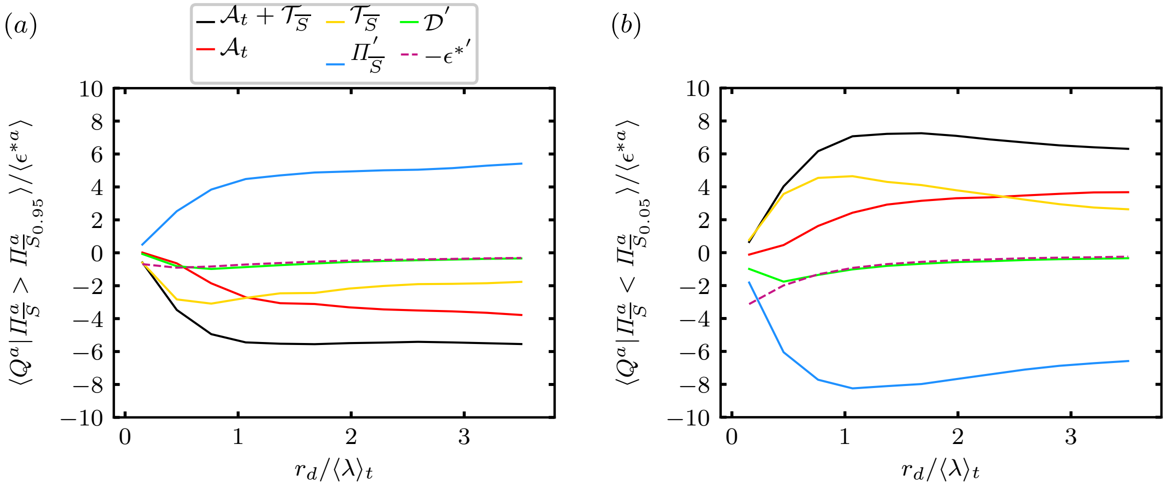

Figure 3.18: (a) Spatio-temporal averages of KHMH terms $\mathcal{Q}^a$ conditioned on the 5% strongest spherically averaged backward (a) and forward (b) interscale transfer events. $\langle Re_\lambda \rangle_t = 112$ (corresponding plots for $\langle Re_\lambda \rangle_t = 174$ are omitted because they are very similar).

rare events, $\mathcal{A}_t + \mathcal{T}_{\overline{S}}$ fluctuates around a constant C where $C > 0$ if we condition the fluctuations on relatively rare negative $\Pi_{\overline{S}}$ but $C < 0$ if we condition them on relatively rare positive $\Pi_{\overline{S}}$ ($C = 0$ if we do not condition). This amounts to a systematic deviation on average from two-point sweeping even though the strong correlation between the high magnitude fluctuations of $\mathcal{A}_t$ and $-\mathcal{T}_{\overline{S}}$ points at a tendency towards sweeping which is frustrated by the presence of the comparatively low non-zero local $\Pi_{\overline{S}}$. Given equation (3.24), the presence of this non-zero constant C (clearly non-zero for all scales, and non-zero but tending towards zero as r_d tends to 0 well below $\langle \lambda \rangle_t$) means that the equilibrium $\Pi_{\overline{S}} \approx \mathcal{D}$ for scales smaller than $\langle \lambda \rangle_t$ seems to not hold either, even at scales smaller than $\langle \lambda \rangle_t$ where the conditional correlation between $\Pi_{\overline{S}}$ and $\mathcal{D}$ is significant. In fact, figure 3.18 shows that the conditional averages of $\Pi'_{\overline{S}}$ are much larger than those of both $\mathcal{D}'$ and $-\epsilon^{*\prime}$; they are much closer to those of $\mathcal{A}_t + \mathcal{T}_{\overline{S}}$. Viscous effects $\mathcal{D}$ or ϵ^* are more important locally at intense interscale transfers than at average interscale transfer events, but this does not entail negligible Lagrangian transport $\mathcal{A}_t + \mathcal{T}_{\overline{S}}$. We provide a more in-depth characterisation of the KHMH dynamics at dissipative scales in the next chapter with KHMH analysis of our well-resolved DNS (DNS1).

In conclusion, $-\Pi_{\overline{S}}$ balances primarily with $\mathcal{A}_t + \mathcal{T}_{\overline{S}}$, in particular at scales larger than $\langle \lambda \rangle_t$. At scales $r_d \leq \langle \lambda \rangle_t$ viscous effects $\mathcal{D}$ become increasingly important in the fluctuating dynamics with decreasing r_d. At all scales the viscous effects $\mathcal{D}$ are more important at relatively rare intense interscale transfer events than at average interscale transfer events, but Lagrangian transport $\mathcal{A}_t + \mathcal{T}_{\overline{S}}$ is always non-negligible in the dynamics with no local equilibrium between $\Pi_{\overline{S}}$ and $\mathcal{D}$ in our DNS2-DNS3-DNS4.

3.3 Homogeneity and Inhomogeneity Contributions to Interscale Transfers

The decomposition $\Pi = \Pi_{\overline{I}} + \Pi_{\overline{S}}$ helped us distinguish between the solenoidal vortex stretching/tilting and the pressure-related aspects of the interscale transfer. As recently shown by Alves Portela et al. (2020), the interscale transfer rate Π can also be decomposed in a way which brings out the fact that it has a direct inhomogeneity contribution to it. We next examine the decomposition introduced by Alves Portela et al. (2020) which is $\Pi = \Pi_I + \Pi_H$ where

$$\Pi_I = \frac{1}{2}\delta u_i \frac{\partial}{\partial x_i}(u_k^+ u_k^+ - u_k^- u_k^-), \tag{3.29a}$$

$$\Pi_H = -2\delta u_i \frac{\partial}{\partial r_i}(u_k^- u_k^+). \tag{3.29b}$$

Π_I can be locally/instantaneously non-zero only in the presence of a local/instantaneous inhomogeneity. However, it averages to zero, i.e. $\langle \Pi_I \rangle = 0$, in homogeneous turbulence.

An equivalent expression for Π_I immediately reveals where the decomposition $\Pi = \Pi_I + \Pi_H$ comes from: $\Pi_I = \delta u_i \partial / \partial r_i (u_k^+ u_k^+ + u_k^- u_k^-)$. Given that the total interscale transfer rate is $\Pi = \delta u_i \partial / \partial r_i (\delta u_k \delta u_k)$, the Π_I part of the interscale transfer concerns the transferred energy differences coming mostly from differences between velocity amplitudes, i.e. local/instantaneous inhomogeneities of "turbulence intensity" in the flow; the Π_H part of the interscale transfer concerns transferred energy differences coming mostly from differences between velocity orientations. Consistently with its link to local/instantaneous non-homogeneity, Π_I can be written in the form (3.29a) making it clear that Π_I is zero only where and when fluctuating velocity magnitudes are locally uniform.

In comparing the decompositions $\Pi = \Pi_{\overline{S}} + \Pi_{\overline{I}}$ and $\Pi = \Pi_I + \Pi_H$, it is worth noting that $\Pi_I = \Pi_{I_{\overline{I}}}$ given that $\Pi_{I_{\overline{S}}} = 0$ from its centroid gradient form (see equation (3.29a) and the second paragraph of appendix B). It therefore follows that

$$\Pi_{\overline{S}} = \Pi_{H_{\overline{S}}}, \tag{3.30a}$$

$$\Pi_{\overline{I}} = \Pi_I + \Pi_{H_{\overline{I}}}. \tag{3.30b}$$

The inhomogeneity-based interscale transfer rate influences only the irrotational part of the total interscale transfer rate whereas Π_H influences both the irrotational and the solenoidal parts. As $\langle \Pi_I \rangle = 0$ and $\langle \Pi_{\overline{I}} \rangle = 0$, it follows that $\langle \Pi_{H_{\overline{I}}} \rangle = 0$. More to the point, $\langle \Pi_{\overline{S}} \rangle$ equals $\langle \Pi_{H_{\overline{S}}} \rangle$ and so equation (3.23) can be written as

$$\langle \Pi \rangle = \langle \Pi_{H_{\overline{S}}} \rangle = \langle \mathcal{D}_{r,\nu} \rangle - \langle \epsilon^* \rangle + \langle \mathcal{I} \rangle. \tag{3.31}$$

The part of Π present in the average interscale transfer/cascade dynamics is $\Pi_{\overline{S}} = \Pi_{H_{\overline{S}}}$.

Given that the average interscale transfer is controlled by $\Pi_{H_{\overline{S}}} = \Pi_{\overline{S}}$, it is worth

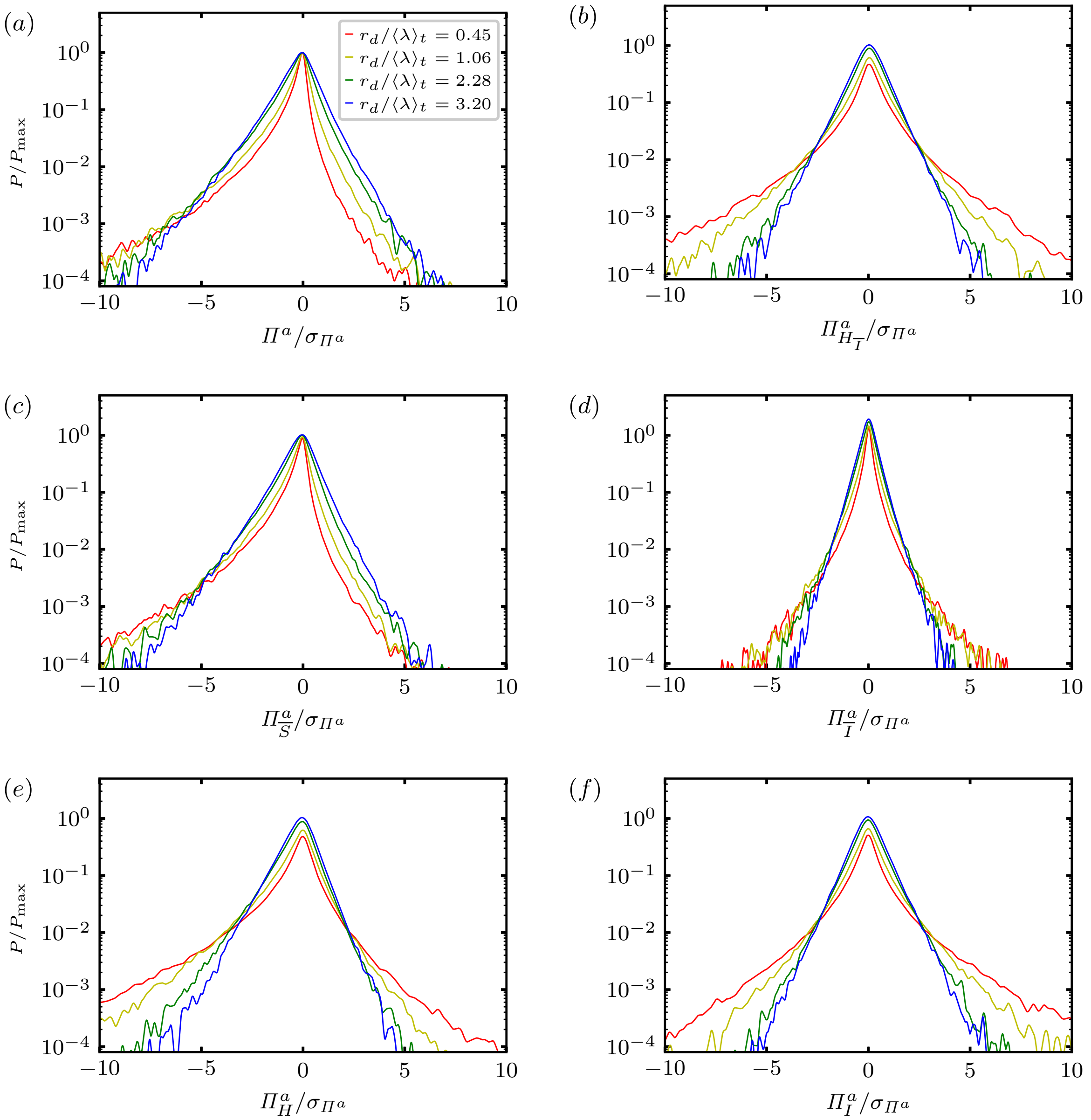

Figure 3.19: (a, b, c, d, e, f) PDFs of spherically averaged Π decompositions $(\Pi^a, \Pi^a_{H_{\overline{I}}}, \Pi^a_{\overline{S}}, \Pi^a_{\overline{I}}, \Pi^a_H, \Pi^a_I)$ at $\langle Re_\lambda\rangle_t = 112$. σ_{Π^a} is the standard deviation of Π^a and $P_{\max}$ is the maximum value of the PDF of Π^a.

asking whether the well-known negative skewness of the PDF of Π^a (e.g. see Yasuda and Vassilicos (2018) and references therein) is also present in the PDF of $\Pi^a_{\overline{S}}$ or/and whether it is spread across different terms of our two interscale transfer rate decompositions. In figure 3.19 we plot the PDFs of Π^a and of the different $\boldsymbol{r}$-orientation-averaged terms in the decompositions of Π that we use. It is clear that the PDFs of Π and $\Pi_{\overline{S}}$ are nearly identical whilst the PDFs of Π_H are different though also negatively skewed. The PDFs of $\Pi_{H_{\overline{I}}}$, $\Pi_{\overline{I}}$ and Π_I are not significantly skewed. In figure 3.20 we plot the skewness factors of the various interscale transfer terms as well as some other KHMH terms. The inhomogeneity interscale transfer Π_I has close to zero skewness across scales. Both $\Pi_{\overline{S}}$ and Π_H are negatively skewed, the former more so than the latter. Given equations

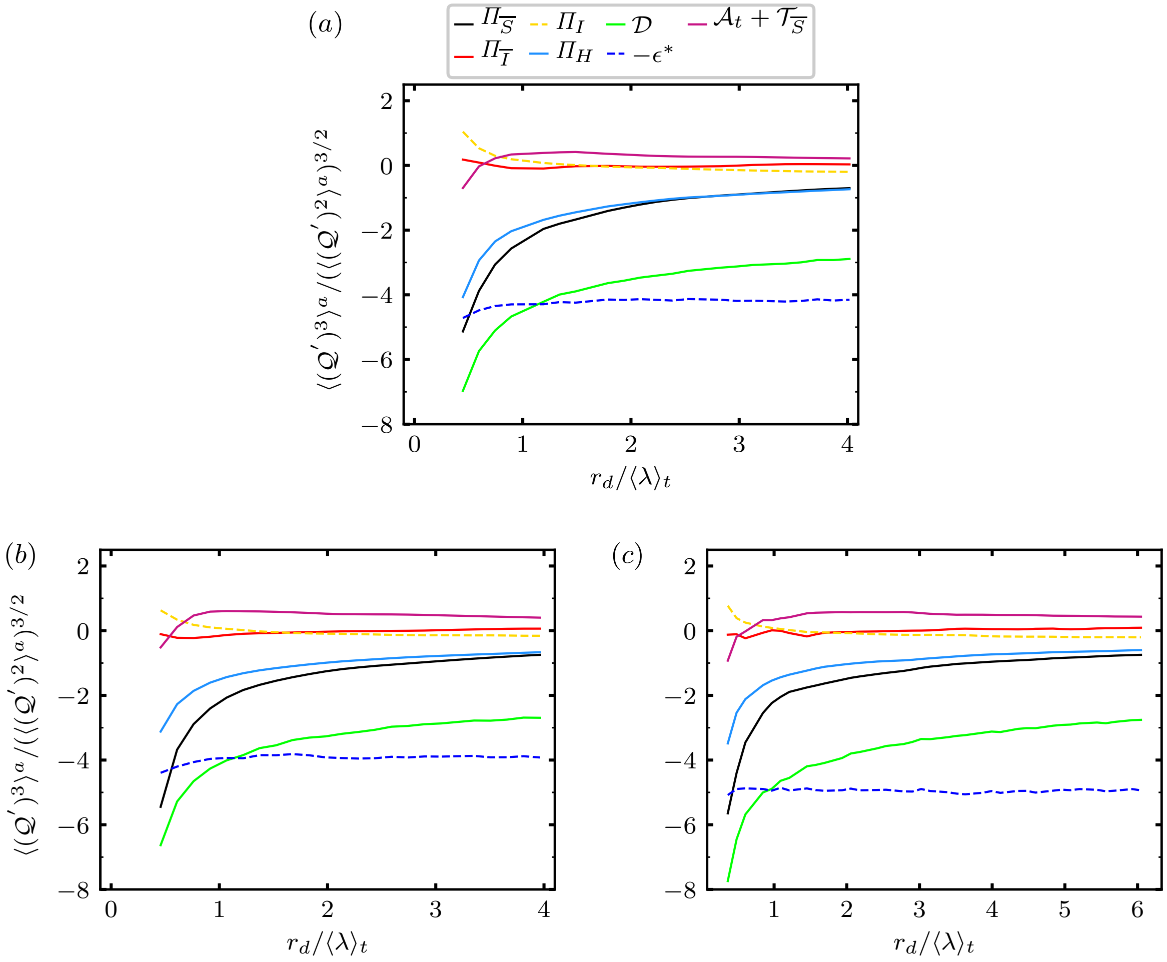

Figure 3.20: Skewness factors for KHMH terms $\mathcal{Q}$. (a, b, c) $\langle Re_\lambda\rangle_t = (111, 112, 174)$.

(3.30a)-(3.30b) and $\Pi_H = \Pi_{\overline{S}} + \Pi_{H_{\overline{I}}}$, this difference in skewness factors is due to the irrotational part of Π_H which is not significantly skewed and reduces the skewness of Π_H relative to that of $\Pi_{\overline{S}}$. All in all, the skewness towards forward rather than inverse interscale transfers is present in its homogeneous and solenoidal components but is absent in its non-homogeneous and irrotational parts.

Figure 3.20 also shows that $\mathcal{A}_t + \mathcal{T}_{\overline{S}}$ is slightly positively skewed with skewness factors of approximately 0.5 at scales $r_d \geq \langle\lambda\rangle_t$ and close to 0 or below at scales below $\langle\lambda\rangle_t$. The skewness factor of $-\Pi_{\overline{S}}$ with which $\mathcal{A}_t + \mathcal{T}_{\overline{S}}$ is very well correlated (as we have seen in the previous section) is about the same at scales close to the integral scale but steadily increases to values well above 0.5 as r_d decreases, reaching nearly 6.0 at scales close to $0.5\langle\lambda\rangle_t$. This is a concrete illustration of the fact already mentioned earlier in this chapter that $\mathcal{A}_t + \mathcal{T}_{\overline{S}} \approx -\Pi_{\overline{S}}$ is a very good approximation for most locations and most times but not all. Given the very significantly increased correlation/anti-correlation of $\Pi_{\overline{S}}$ with both $\mathcal{D}$ and ϵ^* at relatively intense forward/inverse interscale transfer events and with decreasing scale r_d, it is natural to expect the skewness factor of $\Pi_{\overline{S}}$ to veer towards the skewness factors of $\mathcal{D}$ and $-\epsilon^*$ which, as can be seen in figure 3.20, are highly negative with values between -3.0 and -7.0. Note the very similar skewness behaviour with the

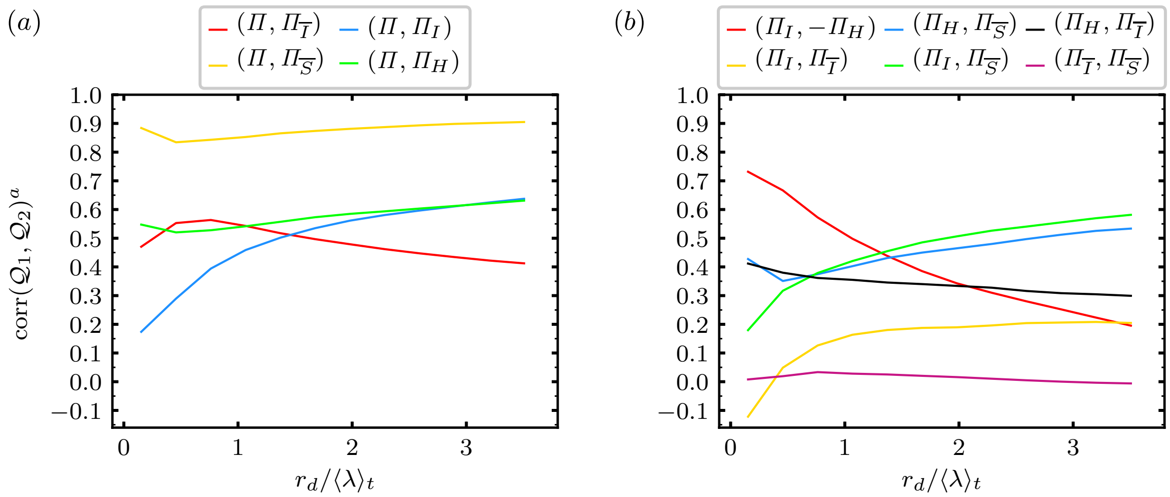

Figure 3.21: Correlation coefficients between various Π decompositions at $\langle Re_\lambda \rangle_t = 112$ (corresponding plots for $\langle Re_\lambda \rangle_t = 174$ are omitted because they are very similar).

ABC forcing and with the negative damping forcing.

We now consider the local/instantaneous relations between the various interscale transfer terms in terms of correlation coefficients plotted in figure 3.21(*a*). First, note the very strong correlation between Π and $\Pi_{\overline{S}}$ and the moderate correlation between Π and $\Pi_{\overline{I}}$. There is no correlation between $\Pi_{\overline{S}}$ and $\Pi_{\overline{I}}$ (see figure 3.21(*b*)), and so Π correlates with both $\Pi_{\overline{S}}$ (strongly) and $\Pi_{\overline{I}}$ (moderately) for different uncorrelated reasons. Π feels the influence of solenoidal vortex stretching/compression via $\Pi_{\overline{S}}$ and the influence of pressure fluctuations via $\Pi_{\overline{I}}$, the former influencing Π more than the latter. Figure 3.21(*a*) also shows significantly smaller correlations between Π and Π_H than between Π and $\Pi_{\overline{S}}$. This must be due to a decorrelating effect of $\Pi_{H_{\overline{I}}}$ as $\Pi_H = \Pi_{\overline{S}} + \Pi_{H_{\overline{I}}}$. The correlations between Π and Π_I are even smaller at the smaller scales but at integral size scales these correlations are equal to those between Π and Π_H (figure 3.21(*a*)).

Figure 3.21(*b*) reveals a strong anti-correlation between Π_I and Π_H at the small scales and a weak one at the large scales. As the scales decrease, the interscale transfers of fluctuating velocity differences caused by local/instantaneous non-homogeneities and the interscale transfers of fluctuating velocity differences caused by orientation differences get progressively more anti-correlated. This anti-correlation tendency results in Π_H and Π_I having larger fluctuation magnitudes than Π at smaller scales, in particular scales smaller than $\langle\lambda\rangle_t$ (verified with our DNS data but not shown here for economy of space).

The other significant correlations revealed in figure 3.21(*b*) are those between Π_H and $\Pi_{\overline{S}}$ and those between Π_I and $\Pi_{\overline{S}}$, particularly as r_d increases from around/below $\langle\lambda\rangle_t$ to the integral length scale. These correlations relate to the very strong correlations between Π and $\Pi_{\overline{S}}$ but are weaker. One can imagine that $\Pi_{\overline{S}}$ correlates with Π_H sometimes and with Π_I some other times, but not too often with both given that Π_I and Π_H tend to be anti-correlated, and that this happens in a way subjected to a continuously strong

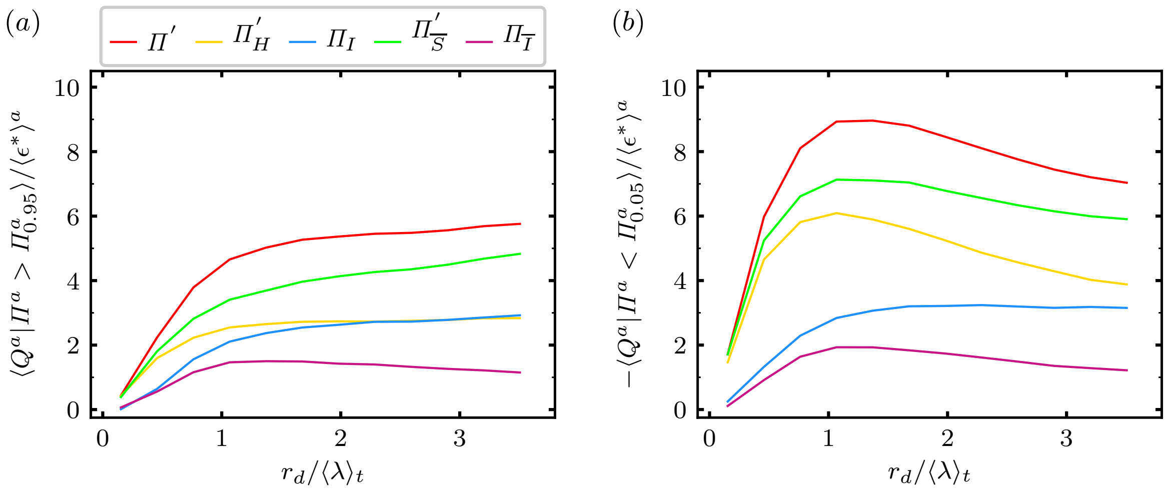

Figure 3.22: Average values of Π decompositions conditioned on (a) intense backward events, (b) intense forward events at $\langle Re_\lambda \rangle_t = 112$ (corresponding plots for $\langle Re_\lambda \rangle_t = 174$ are omitted because they are very similar).

correlation between $\Pi = \Pi_H + \Pi_I$ and $\Pi_{\overline{S}}$.

We finally consider in figure 3.22 the average values of the various Π-decompositions conditional on relatively rare intense Π-events. We calculate averages conditioned on 5% most negative (forward transfer) Π events (values of Π for which the probability that Π is smaller than a negative value $\Pi_{0.05}$ is 0.05) and on 5% most positive Π (inverse transfer) events (values of Π for which the probability that Π is larger than a positive value $\Pi_{0.95}$ is also 0.05). All these averages tend to 0 as r_d tends to 0 below $\langle \lambda \rangle_t$. The largest such conditional averages are those of Π' followed by those of $\Pi'_{\overline{S}}$. The weakest such conditional averages are those of $\Pi_{\overline{I}}$ for all r_d at both forward and inverse intense interscale transfer events. This is consistent with our observation in section 3.1.4 that the unconditional fluctuation magnitude of $\Pi_{\overline{I}}$ is smaller than the unconditional fluctuation magnitudes of Π followed by those of $\Pi_{\overline{S}}$. Figure 3.22 also shows a clear difference between conditional averages of Π'_H and Π_I when conditioned on intense forward or intense inverse interscale transfer events. Whilst the conditional averages of these two quantities are similar at intense inverse events, they differ substantially at forward transfer events where $-\Pi'_H$ is substantially higher than $-\Pi_I$ except close to the integral length scale. This behaviour, and the more intense forward rather than backward Π and $\Pi_{\overline{S}}$ events, are consistent with the negative skewness of Π_H, $\Pi_{\overline{S}}$ and Π and the non-skewed Π_I.

3.4 General Irrotational and Solenoidal KHMH Equations

We end this chapter by generalising the irrotational and solenoidal KHMH equations (3.22a)-(3.22b) to incompressible Newtonian flows with very general boundary conditions (Sprössig, 2010). Consider the twice continuously differentiable vector field $\boldsymbol{q}(\boldsymbol{x}, t)$ defined on a domain $V \subseteq \mathbb{R}^3$ with the bounding surface S. This field can be uniquely decomposed into the irrotational and solenoidal vector fields

$$\boldsymbol{q}(\boldsymbol{x},t) = \boldsymbol{q}_I(\boldsymbol{x},t) + \boldsymbol{q}_S(\boldsymbol{x},t) = -\nabla_{\boldsymbol{x}}\phi(\boldsymbol{x},t) + \nabla_{\boldsymbol{x}} \times \boldsymbol{B}(\boldsymbol{x},t), \tag{3.32}$$

The solution to this problem is $\boldsymbol{q}_I = \boldsymbol{q}_{IV} + \boldsymbol{q}_{IB}$ and $\boldsymbol{q}_S = \boldsymbol{q}_{SV} + \boldsymbol{q}_{SB}$, where the solenoidal and irrotational volume and boundary terms are given as (Sprössig, 2010)

$$\begin{aligned}
\boldsymbol{q}_{IV}(\boldsymbol{x},t) &= \frac{1}{4\pi}\int_V d\boldsymbol{y}\frac{\boldsymbol{x}-\boldsymbol{y}}{|\boldsymbol{x}-\boldsymbol{y}|^3}[\nabla_{\boldsymbol{y}} \cdot \boldsymbol{q}(\boldsymbol{y},t)], && (3.33a)\\
\boldsymbol{q}_{IB}(\boldsymbol{x},t) &= -\frac{1}{4\pi}\int_S dS_{\boldsymbol{y}}\frac{\boldsymbol{x}-\boldsymbol{y}}{|\boldsymbol{x}-\boldsymbol{y}|^3}[\widehat{\boldsymbol{n}}_{\boldsymbol{y}} \cdot \boldsymbol{q}(\boldsymbol{y},t)], && (3.33b)\\
\boldsymbol{q}_{SV}(\boldsymbol{x},t) &= -\frac{1}{4\pi}\int_V d\boldsymbol{y}\frac{\boldsymbol{x}-\boldsymbol{y}}{|\boldsymbol{x}-\boldsymbol{y}|^3} \times [\nabla_{\boldsymbol{y}} \times \boldsymbol{q}(\boldsymbol{y},t)], && (3.33c)\\
\boldsymbol{q}_{SB}(\boldsymbol{x},t) &= \frac{1}{4\pi}\int_S dS_{\boldsymbol{y}}\frac{\boldsymbol{x}-\boldsymbol{y}}{|\boldsymbol{x}-\boldsymbol{y}|^3} \times [\widehat{\boldsymbol{n}}_{\boldsymbol{y}} \times \boldsymbol{q}(\boldsymbol{y},t)]. && (3.33d)
\end{aligned}$$

Consider an incompressible fluid that satisfies the incompressible vorticity equation

$$\nabla_{\boldsymbol{y}} \times \big(\frac{\partial \boldsymbol{u}}{\partial t} + \boldsymbol{u}\cdot\nabla_{\boldsymbol{y}}\boldsymbol{u} - \nu\nabla^2_{\boldsymbol{y}}\boldsymbol{u} - \boldsymbol{f}\big) = 0. \tag{3.34}$$

By comparing this equation with (3.33c), it is clear that the vorticity equation can be used to derive an evolution equation for the solenoidal volume parts of the NS terms. We can apply the following operator to this equation

$$-\frac{1}{4\pi}\int_V d\boldsymbol{y}\frac{\boldsymbol{x}-\boldsymbol{y}}{|\boldsymbol{x}-\boldsymbol{y}|^3} \times \Big[\nabla_{\boldsymbol{y}} \times \big(\frac{\partial \boldsymbol{u}}{\partial t} + (\boldsymbol{u}\cdot\nabla_{\boldsymbol{y}})\boldsymbol{u} - \nu\nabla^2_{\boldsymbol{y}}\boldsymbol{u} - \boldsymbol{f}\big)\Big] = 0, \tag{3.35}$$

and use (3.33c) to rewrite this equation as

$$(\frac{\partial \boldsymbol{u}}{\partial t})_{SV} + (\boldsymbol{u}\cdot\nabla_{\boldsymbol{x}}\boldsymbol{u})_{SV} = (\nu\nabla^2_{\boldsymbol{x}}\boldsymbol{u})_{SV} + \boldsymbol{f}_{SV}. \tag{3.36}$$

We can in a similar manner obtain the evolution equation for the irrotational volume NS terms from the Poisson equation for pressure

$$\frac{1}{4\pi}\int_V d\boldsymbol{y}\frac{\boldsymbol{x}-\boldsymbol{y}}{|\boldsymbol{x}-\boldsymbol{y}|^3}\Big[\nabla_{\boldsymbol{y}} \cdot \big(\boldsymbol{u}\cdot\nabla_{\boldsymbol{y}}\boldsymbol{u} + \frac{1}{\rho}\nabla_{\boldsymbol{y}}p - \boldsymbol{f}\big)\Big] = 0, \tag{3.37}$$

which yields

$$(\boldsymbol{u}\cdot\nabla_{\boldsymbol{x}}\boldsymbol{u})_{IV} = (-\frac{1}{\rho}\nabla_{\boldsymbol{x}}p)_{IV} + \boldsymbol{f}_{IV}. \tag{3.38}$$

The equations (3.36) and (3.38) state that in all incompressible turbulent flows the solenoidal accelerations from volume contributions balance with solenoidal forces from volume contributions and irrotational accelerations from volume contributions balance with irrotational forces from volume contributions. The former can be viewed as an integrated vorticity equation which dictates a part of the solenoidal NS dynamics, while the latter equation as an integrated pressure Poisson equation which dictates a part of the irrotational NS dynamics. Due to the non-local character of the solenoidal and irrotational volume terms, we reformulate these equations in terms of full NS term minus boundary terms. E.g., for the time-derivative $(\partial \boldsymbol{u}/\partial t)_{SV} = \partial \boldsymbol{u}/\partial t - (\partial \boldsymbol{u}/\partial t)_{IB} - (\partial \boldsymbol{u}/\partial t)_{SB}$. The irrotational volume component (see (3.33a)) involves an integral of the divergence of the respective term $(\nabla_{\boldsymbol{y}} \cdot \boldsymbol{q}(\boldsymbol{y}))$. Thus, due to incompressibility, the time derivative and viscous terms have zero volume irrotational components, $(\partial \boldsymbol{u}/\partial t)_{IV} = (\nu \nabla^2_{\boldsymbol{x}} \boldsymbol{u})_{IV} = 0$. The solenoidal volume component (see (3.33c)) involves an integral of the curl of the respective term, and as the curl of the pressure gradient equals zero, this term will have a zero solenoidal volume component, $(-1/\rho \nabla_{\boldsymbol{x}} p)_{SV} = 0$. We rewrite the solenoidal volume terms in equation (3.36) with combinations of full terms and boundary terms to obtain

$$\begin{aligned} &\frac{\partial \boldsymbol{u}}{\partial t} + ((\boldsymbol{u} \cdot \nabla_{\boldsymbol{x}})\boldsymbol{u})_S = \nu \nabla^2_{\boldsymbol{x}} \boldsymbol{u} + \boldsymbol{f}_S + \\ &\qquad (\frac{\partial \boldsymbol{u}}{\partial t})_{IB} - (\nu \nabla^2_{\boldsymbol{x}} \boldsymbol{u})_{IB} + (\frac{\partial \boldsymbol{u}}{\partial t})_{SB} + ((\boldsymbol{u} \cdot \nabla_{\boldsymbol{x}})\boldsymbol{u})_{SB} - (\nu \nabla^2_{\boldsymbol{x}} \boldsymbol{u})_{SB} - \boldsymbol{f}_{SB} \ , \end{aligned} \tag{3.39}$$

where the sum of the four rightmost terms on the RHS equals $(-1/\rho \nabla_{\boldsymbol{x}} p)_{SB}$ as the NS equations are satisfied at the boundary. By using this simplification and writing out all the boundary terms, we arrive at

$$\begin{aligned} &\frac{\partial \boldsymbol{u}}{\partial t} + ((\boldsymbol{u} \cdot \nabla_{\boldsymbol{x}})\boldsymbol{u})_S = \nu \nabla^2_{\boldsymbol{x}} \boldsymbol{u} + \boldsymbol{f}_S \\ &- \frac{1}{4\pi} \int_S dS_{\boldsymbol{y}} \frac{\boldsymbol{x} - \boldsymbol{y}}{|\boldsymbol{x} - \boldsymbol{y}|^3} [\widehat{\boldsymbol{n}}_{\boldsymbol{y}} \cdot (\frac{\partial \boldsymbol{u}}{\partial t} - \nu \nabla^2_{\boldsymbol{y}} \boldsymbol{u})] - \frac{1}{4\pi} \int_S dS_{\boldsymbol{y}} \frac{\boldsymbol{x} - \boldsymbol{y}}{|\boldsymbol{x} - \boldsymbol{y}|^3} \times [\widehat{\boldsymbol{n}}_{\boldsymbol{y}} \times \nabla_{\boldsymbol{y}} \frac{1}{\rho} p]. \end{aligned} \tag{3.40}$$

By rewriting the irrotational volume components in equation (3.38) in terms of the full terms and the boundary terms, we have

$$((\boldsymbol{u} \cdot \nabla_{\boldsymbol{x}})\boldsymbol{u})_I = -\frac{1}{\rho} \nabla_{\boldsymbol{x}} p + \boldsymbol{f}_I + ((\boldsymbol{u} \cdot \nabla_{\boldsymbol{x}})\boldsymbol{u})_{IB} - (-\frac{1}{\rho} \nabla_{\boldsymbol{x}} p)_{IB} - \boldsymbol{f}_{IB} - (-\frac{1}{\rho} \nabla_{\boldsymbol{x}} p)_{SB}, \tag{3.41}$$

where the sum of the irrotational boundary terms equals $-(\partial \boldsymbol{u}/\partial t)_{IB} + (\nu \nabla^2_{\boldsymbol{x}} \boldsymbol{u})_{IB}$ by the NS equations at the boundary. If we use this relation and write out all boundary terms, we arrive at

$$\begin{aligned} &((\boldsymbol{u} \cdot \nabla_{\boldsymbol{x}})\boldsymbol{u})_I = -\frac{1}{\rho} \nabla_{\boldsymbol{x}} p + \boldsymbol{f}_I \\ &+ \frac{1}{4\pi} \int_S dS_{\boldsymbol{y}} \frac{\boldsymbol{x} - \boldsymbol{y}}{|\boldsymbol{x} - \boldsymbol{y}|^3} [\widehat{\boldsymbol{n}}_{\boldsymbol{y}} \cdot (\frac{\partial \boldsymbol{u}}{\partial t} - \nu \nabla^2_{\boldsymbol{y}} \boldsymbol{u})] + \frac{1}{4\pi} \int_S dS_{\boldsymbol{y}} \frac{\boldsymbol{x} - \boldsymbol{y}}{|\boldsymbol{x} - \boldsymbol{y}|^3} \times [\widehat{\boldsymbol{n}}_{\boldsymbol{y}} \times \nabla_{\boldsymbol{y}} \frac{1}{\rho} p]. \end{aligned} \tag{3.42}$$

The equations (3.40) and (3.42) are generalisations of the equations (3.3a)-(3.3b) for homogeneous turbulence and these equations are valid in all incompressible flows. The difference to homogeneous turbulence is the collection of boundary terms

$$\boldsymbol{R}(\boldsymbol{x},t) \equiv \frac{1}{4\pi}\int_S dS_{\boldsymbol{y}} \frac{\boldsymbol{x}-\boldsymbol{y}}{|\boldsymbol{x}-\boldsymbol{y}|^3}[\boldsymbol{n}_{\boldsymbol{y}} \cdot (\frac{\partial \boldsymbol{u}}{\partial t} - \nu\nabla^2_{\boldsymbol{y}}\boldsymbol{u})] + \frac{1}{4\pi}\int_S dS_{\boldsymbol{y}} \frac{\boldsymbol{x}-\boldsymbol{y}}{|\boldsymbol{x}-\boldsymbol{y}|^3} \times [\boldsymbol{n}_{\boldsymbol{y}} \times \nabla_{\boldsymbol{y}}\frac{1}{\rho}p], \tag{3.43a}$$

$$= -(\boldsymbol{a}_l)_{IB} + (\boldsymbol{a}_\nu)_{IB} - (\boldsymbol{a}_p)_{SB}. \tag{3.43b}$$

We use this notation to express the general irrotational and solenoidal NS equations as

$$\frac{\partial \boldsymbol{u}}{\partial t} + ((\boldsymbol{u}\cdot\nabla_{\boldsymbol{x}})\boldsymbol{u})_S = \nu\nabla^2_{\boldsymbol{x}}\boldsymbol{u} + \boldsymbol{f}_S - \boldsymbol{R}(\boldsymbol{x},t), \tag{3.44a}$$

$$((\boldsymbol{u}\cdot\nabla_{\boldsymbol{x}})\boldsymbol{u})_I = -\frac{1}{\rho}\nabla_{\boldsymbol{x}}p + \boldsymbol{f}_I + \boldsymbol{R}(\boldsymbol{x},t). \tag{3.44b}$$

In homogeneous turbulence all the boundary terms in $\boldsymbol{R}(\boldsymbol{x},t)$ equal zero individually (see the second paragraph of appendix B), such that we recover equations (3.3a)-(3.3b). In general, the boundary terms will be non-zero and differ in different flows; e.g. at a solid wall the boundary term from the time-derivative will vanish because of no-slip and the NS equations at the wall can be used to rewrite the boundary terms as a non-local function of the pressure gradient only. Note that the above procedure, at least partially, separates the NS dynamics into solenoidal and irrotational dynamics. This differs from other studies which have used the Helmholtz decomposition to study the effect of the solenoidal and irrotational parts of a given field in the full NS equations (e.g. the Reynolds stresses (Wu et al., 1996; Perot and Moin, 1996) or the convective acceleration from the fluctuating velocity field (Rosenberg and McKeon, 2019)).

The NSD irrotational and solenoidal equations in general turbulent flows are obtained by subtracting the solenoidal and irrotational NS equations (3.44a)-(3.44b) at $\boldsymbol{x}-\boldsymbol{r}/2$ from the same equations at $\boldsymbol{x}+\boldsymbol{r}/2$ to give

$$\frac{\partial \delta\boldsymbol{u}}{\partial t} + \delta\boldsymbol{a}_{c_S} = \delta\boldsymbol{a}_\nu + \delta\boldsymbol{f}_S - \delta\boldsymbol{R}, \tag{3.45a}$$

$$\delta\boldsymbol{a}_{c_I} = -\frac{1}{\rho}\nabla_{\boldsymbol{x}}\delta p + \delta\boldsymbol{f}_I + \delta\boldsymbol{R}. \tag{3.45b}$$

The rephrasing of the irrotational and solenoidal NSD equations in terms of the interscale and interspace transport terms can also be performed for non-homogeneous turbulence. We derive the centroid irrotational and solenoidal NSD equations similarly as for the NS irrotational and solenoidal equations by starting with the NSD equation (3.7). This yields the equations

$$\delta\boldsymbol{a}_l + \boldsymbol{a}_{\mathcal{T}_{\overline{S}}} + \boldsymbol{a}_{\Pi_{\overline{S}}} = \delta\boldsymbol{a}_\nu + \delta\boldsymbol{f}_{\overline{S}} - \overline{\boldsymbol{R}}, \tag{3.46a}$$

$$\boldsymbol{a}_{\mathcal{T}_{\overline{I}}} + \boldsymbol{a}_{\Pi_{\overline{I}}} = \delta\boldsymbol{a}_p + \delta\boldsymbol{f}_{\overline{I}} + \overline{\boldsymbol{R}}, \tag{3.46b}$$

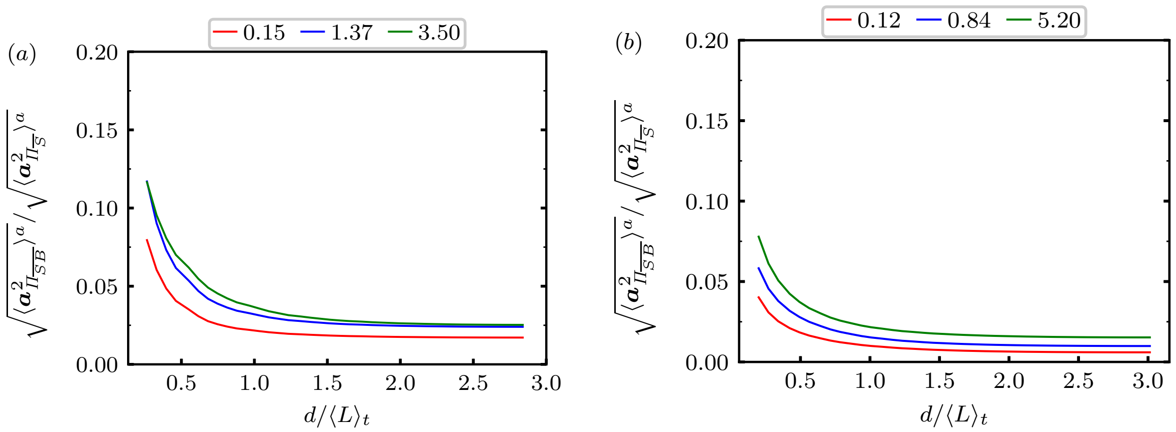

Figure 3.23: Average magnitudes of $\boldsymbol{a}_{\Pi_{\overline{SB}}}$ relative to the average magnitudes of $\boldsymbol{a}_{\Pi_{\overline{S}}}$ as a function of d: the Euclidian distance from the sampling location to the closest boundary. The legends denote $r_d/\langle\lambda\rangle_t$. (a) $\langle Re_\lambda\rangle_t = 112$, (b) $\langle Re_\lambda\rangle_t = 174$.

where

$$\overline{\boldsymbol{R}}(\boldsymbol{x},\boldsymbol{r},t) \equiv \frac{1}{4\pi}\int_S dS_{\boldsymbol{y}} \frac{\boldsymbol{x}-\boldsymbol{y}}{|\boldsymbol{x}-\boldsymbol{y}|^3}[\widehat{\boldsymbol{n}}_{\boldsymbol{y}}\cdot(\delta\boldsymbol{a}_l - \delta\boldsymbol{a}_\nu)] - \frac{1}{4\pi}\int_S dS_{\boldsymbol{y}} \frac{\boldsymbol{x}-\boldsymbol{y}}{|\boldsymbol{x}-\boldsymbol{y}|^3}\times[\widehat{\boldsymbol{n}}_{\boldsymbol{y}}\times\delta\boldsymbol{a}_p], \tag{3.47a}$$

$$= -(\delta\boldsymbol{a}_l)_{IB} + (\delta\boldsymbol{a}_\nu)_{IB} - (\delta\boldsymbol{a}_p)_{SB}. \tag{3.47b}$$

These boundary terms are individually equal to zero in homogeneous turbulence for the analogue reasons as in the NS dynamics. Regarding the irrotational dynamics, in general, $\boldsymbol{a}_{\mathcal{T}_{\overline{I}}} \neq \boldsymbol{a}_{\Pi_{\overline{I}}}$, but the irrotational volume terms are always equal, $(\boldsymbol{a}_{\mathcal{T}})_{\overline{IV}} = (\boldsymbol{a}_{\Pi})_{\overline{IV}}$ from equation (3.33a) and

$$\nabla_{\boldsymbol{x}}\cdot\boldsymbol{a}_\Pi = \nabla_{\boldsymbol{x}}\cdot\boldsymbol{a}_{\mathcal{T}} = \frac{1}{2}\Big(\frac{\partial u_k^+}{\partial x_i^+}\frac{\partial u_i^+}{\partial x_k^+} - \frac{\partial u_k^-}{\partial x_i^-}\frac{\partial u_i^-}{\partial x_k^-}\Big). \tag{3.48}$$

The solenoidal interscale transfer term $\boldsymbol{a}_{\Pi_{\overline{S}}}$ can be written as

$$\boldsymbol{a}_{\Pi_{\overline{S}}}(\boldsymbol{x},\boldsymbol{r},t) = -\frac{1}{4\pi}\int_V d\boldsymbol{y}\frac{\boldsymbol{x}-\boldsymbol{y}}{|\boldsymbol{x}-\boldsymbol{y}|^3}\times[\nabla_{\boldsymbol{y}}\times\boldsymbol{a}_\Pi(\boldsymbol{y},\boldsymbol{r},t)] + \\ \frac{1}{4\pi}\int_S dS_{\boldsymbol{y}}\frac{\boldsymbol{x}-\boldsymbol{y}}{|\boldsymbol{x}-\boldsymbol{y}|^3}\times[\widehat{\boldsymbol{n}}_{\boldsymbol{y}}\times\boldsymbol{a}_\Pi(\boldsymbol{y},\boldsymbol{r},t)], \tag{3.49}$$

where the surface integral is of smaller order of magnitude than the volume integral away from boundaries and increasingly so with increasing $\langle Re_\lambda\rangle_t$ in our DNSs (see figure 3.23). Hence, for an interpretation of $\boldsymbol{a}_{\Pi_{\overline{S}}}$, we consider $\boldsymbol{a}_{\Pi_{\overline{S}}} \approx \boldsymbol{a}_{\Pi_{\overline{SV}}}$ with

$$(\nabla_{\boldsymbol{x}}\times\boldsymbol{a}_\Pi)_i = \delta u_k\frac{\partial\delta\omega_i}{\partial r_k} - \frac{\delta\omega_k}{2}\frac{s_{ij}^+ + s_{ij}^-}{2} - \frac{\omega_k^+ + \omega_k^-}{4}\delta s_{ij} + \frac{\epsilon_{ijk}}{2}\Big[\frac{\partial u_l^+}{\partial x_j^+}\frac{\partial u_k^-}{\partial x_l^-} - \frac{\partial u_l^-}{\partial x_j^-}\frac{\partial u_k^+}{\partial x_l^+}\Big], \tag{3.50}$$

where s_{ij} is the strain-rate tensor and ϵ_{ijk} is the Levi-Civita tensor. This set of terms constitutes a part of the non-linear term in the evolution equation for the vorticity difference $\delta\boldsymbol{\omega}(\boldsymbol{x},\boldsymbol{r},t)$, i.e. vorticity at scales $|\boldsymbol{r}|$ and smaller, as $\nabla_{\boldsymbol{x}} \times \delta\boldsymbol{a}_c = \nabla_{\boldsymbol{x}} \times (\boldsymbol{a}_{\Pi} + \boldsymbol{a}_{\mathcal{T}})$. If one contracts (3.50) with $2\delta\boldsymbol{\omega}$, the RHS corresponds to non-linear terms which determine the evolution of the enstrophy $|\delta\boldsymbol{\omega}|^2$ at scales smaller or comparable to $|\boldsymbol{r}|$ (see Baj et al. (2022) for an investigation of the local $|\delta\boldsymbol{\omega}|^2$ dynamics in homogeneous turbulence). We interpret the first term on the RHS in (3.50) as vorticity interscale transfer. By the connection to $|\delta\boldsymbol{\omega}|^2$, we interpret the second and third terms as related to enstrophy production/destruction and vortex tilting (Tsinober, 2009) at scales smaller or comparable to $|\boldsymbol{r}|$ due to interactions between the vorticity and strain fields. These three terms justify the interpretation of $\boldsymbol{a}_{\Pi_{\overline{S}}}$ being related non-locally in space to the vortex stretching/compression and tilting dynamics of its spatial vicinity. The last term in (3.50) appears in $\nabla_{\boldsymbol{x}} \times \boldsymbol{a}_{\mathcal{T}_{\overline{SV}}}$ with a negative sign such that these terms cancel.

The exact solenoidal and irrotational KHMH equations follow from contracting equations (3.46a)-(3.46b) with $2\delta\boldsymbol{u}$

$$\mathcal{A}_t + \mathcal{T}_{\overline{S}} + \Pi_{\overline{S}} = \mathcal{D}_{r,\nu} + \mathcal{D}_{x,\nu} - \epsilon^* + \mathcal{I}_{\overline{S}} - 2\delta\boldsymbol{u}\cdot\overline{\boldsymbol{R}}, \tag{3.51a}$$

$$\mathcal{T}_{\overline{I}} + \Pi_{\overline{I}} = \mathcal{T}_p + \mathcal{I}_{\overline{I}} + 2\delta\boldsymbol{u}\cdot\overline{\boldsymbol{R}}, \tag{3.51b}$$

and $\mathcal{T}_{\overline{IV}} = \Pi_{\overline{IV}}$. This shows that the solenoidal and irrotational KHMH equations can be extended to non-homogeneous turbulence. In contrast to homogeneous turbulence, in general boundary terms couple the irrotational and solenoidal dynamics.

In the case of negligible boundary terms $2\delta\boldsymbol{u}\cdot\overline{\boldsymbol{R}}$, $\mathcal{T}_{\overline{IB}}$ and $\Pi_{\overline{IB}}$ and solenoidal forcing $\mathcal{I}_{\overline{I}} = 0$, we recover from (3.51) the solenoidal and irrotational KHMH equations in homogeneous turbulence (3.22). This would be very important in a practical sense as this would allow us to calculate the irrotational terms from $\mathcal{T}_{\overline{I}} = \Pi_{\overline{I}} = \mathcal{T}_p/2$ and subsequently the solenoidal terms from

$$\mathcal{T}_{\overline{S}} = \mathcal{T} - \mathcal{T}_{\overline{I}}, \tag{3.52a}$$

$$\Pi_{\overline{S}} = \Pi - \Pi_{\overline{I}}. \tag{3.52b}$$

Hence, in this case we would only require the pressure, forcing and velocity fields to calculate all the KHMH terms efficiently. This "indirect" evaluation of the irrotational and solenoidal terms contrasts with the computationally expensive evaluation of the integrals (3.33) for non-homogeneous turbulence and the pseudospectral method for homogeneous turbulence. We can use this indirect method in homogeneous turbulence whenever $\mathcal{I}_{\overline{I}} = 0$ as the above boundary terms equal zero. For non-homogeneous turbulence, we also need to assess that the boundary terms $2\delta\boldsymbol{u}\cdot\overline{\boldsymbol{R}}$, $\mathcal{T}_{\overline{IB}}$ and $\Pi_{\overline{IB}}$ are negligible. Note that this assessment requires the evaluation of surface integrals rather than the more computationally expensive evaluation of volume integrals.

In this chapter we used the direct evaluation of the centroid Helmholtz-decomposed

NSD and KHMH terms as described in section 3.1.3 for all but one statistic. We used the above indirect method to obtain sufficient samples to converge the skewness factors of the centroid Helmholtz-decomposed terms in figure 3.20. We checked that the direct and indirect evaluation methods yield identical results for lower-order statistics (i.e. average KHMH magnitudes and correlation coefficients).

3.5 Summary

The balance between space-time-averaged interscale energy transfer rate on the one hand and space-time-averaged viscous diffusion, turbulence dissipation rate and power input on the other does not represent in any way the actual energy transfer dynamics in statistically stationary homogeneous/periodic turbulence. In this chapter we have studied the fluctuations of one-point and two-point acceleration terms in the NS and NSD equations and their relation to the various terms of the KHMH equation and we now give a summary of the results.

The various corresponding terms in the NS and NSD equations behave similarly relative to each other at scales similar and larger than $\langle \lambda \rangle_t$ because of negligible effects of two-point acceleration alignments. The corresponding terms in the NSD and KHMH equations behave similarly relative to each other because the two-point velocity difference has a similar tendency of alignment with each one of the terms of the NSD equation.

The terms in the solenoidal KHMH equation which fluctuate with the highest magnitudes are the local (Eulerian) unsteadiness term $\mathcal{A}_t$ and the solenoidal interspace transfer rate $\mathcal{T}_{\overline{S}}$. The fluctuation intensity of the Lagrangian transport $\mathcal{A}_t + \mathcal{T}_{\overline{S}}$ is much reduced by comparison to both these terms as a consequence of two-point sweeping (and increasingly so as the scale decreases) and is comparable to the fluctuation intensity of the solenoidal interscale transfer rate $\mathit{\Pi}_{\overline{S}}$. In fact, for scales larger than $\langle \lambda \rangle_t$, the relation

$$\mathcal{A}_t + \mathcal{T}_{\overline{S}} + \mathit{\Pi}'_{\overline{S}} \approx 0, \tag{3.53}$$

is a good approximation for most times and most locations in the flow. $\mathcal{A}_t + \mathcal{T}_{\overline{S}}$ can be viewed as a Lagrangian time rate of change of $|\delta \boldsymbol{u}|^2$ moving with $(\boldsymbol{u}^+ + \boldsymbol{u}^-)/2$. As more than average $|\delta \boldsymbol{u}|^2$ is cascaded from larger to smaller scales at a particular location ($\mathit{\Pi}'_{\overline{S}} < 0$), $\mathcal{A}_t + \mathcal{T}_{\overline{S}}$ and $|\delta \boldsymbol{u}|^2$ increases; and as more than average $|\delta \boldsymbol{u}|^2$ is inverse cascaded from smaller to larger scales ($\mathit{\Pi}'_{\overline{S}} > 0$), $\mathcal{A}_t + \mathcal{T}_{\overline{S}}$ and $|\delta \boldsymbol{u}|^2$ decreases.

The solenoidal interscale transfer rate is negligibly correlated with viscous diffusion and/or turbulence dissipation at scales larger than $\langle \lambda \rangle_t$ and rather weakly correlated at scales smaller than $\langle \lambda \rangle_t$. Its fluctuation magnitude is also significantly larger than that of $\mathcal{D}$, $-\epsilon^*$ and $\mathcal{I}$ at all scales. That is, the solenoidal interscale transfer rate fluctuates almost exclusively with $\mathcal{A}_t + \mathcal{T}_{\overline{S}}$ with which it is extremely well correlated at length scales larger than $\langle \lambda \rangle_t$ and very significantly correlated at length scales smaller than $\langle \lambda \rangle_t$. The relatively rare space-time events which do not comply with (3.53) with non-negligible viscous effects are responsible for the different skewness factors of $\mathcal{A}_t + \mathcal{T}_{\overline{S}}$ (small, mostly positive, skewness factor) and of $\Pi'_{\overline{S}}$ (negative skewness factor, increasingly large negative values with decreasing scale). Among these rare events, there is no local equilibrium between interscale transfer and viscous effects with $\mathcal{A}_t + \mathcal{T}_{\overline{S}}$ typically non-negligible locally.

The irrotational part of the interscale transfer rate has zero spatio-temporal average but is exactly equal to the irrotational part of the interspace transfer rate and half the two-point pressure work term in the KHMH equation. In fact, the exact relation in homogeneous turbulence $\Pi_{\overline{I}} = \mathcal{T}_{\overline{I}} = \mathcal{T}_p/2$ explains the significant correlation between Π and $\mathcal{T}_p$ reported by Yasuda and Vassilicos (2018). The irrotational part of the interscale transfer rate derives from the integrated Poisson equation for two-point pressure fluctuations whereas the solenoidal part of the interscale transfer rate derives from the integrated two-point vorticity equation and includes non-local (in space) vortex stretching/compression and tilting effects of its spatial vicinity.

We have also considered the decomposition into homogeneous and inhomogeneous interscale transfer rates recently introduced by Alves Portela et al. (2020) and have studied their fluctuations in statistically stationary homogeneous turbulence. The PDFs of the homogeneous interscale transfer rate are skewed towards forward cascade events whereas the PDFs of the inhomogeneous interscale transfer rate are not significantly skewed. However, the skewness factors of the PDFs of the homogeneous interscale transfer rate are not as high as those of both the full and the solenoidal interscale transfer rates. Relating to this, Π is highly correlated with $\Pi_{\overline{S}}$ more than with $\Pi_{\overline{I}}$, Π_H and Π_I. There is an increasing correlation between Π_I and $-\Pi_H$ as the length scale decreases, in particular below $\langle\lambda\rangle_t$ where it reaches values above 0.6. The interscale transfer of $|\delta \boldsymbol{u}|^2$ caused by local inhomogeneities in fluctuating velocity magnitudes tends to cancel the interscale transfer of $|\delta \boldsymbol{u}|^2$ caused by misalignments between the two neighbouring fluctuating velocities, in particular at scales below $\langle\lambda\rangle_t$. As a result, the fluctuation magnitudes of Π are smaller than those of both Π_I and $-\Pi_H$.

Finally, we derived generalised irrotational and solenoidal KHMH equations which can be used to study the cascade dynamics in incompressible turbulent flows with very general boundary conditions. The equations are similar to their analogues in homogeneous turbulence, but in general boundary terms couple the irrotational and solenoidal dynamics. Our investigations of the non-zero boundary term $\boldsymbol{a}_{\Pi_{\overline{S}}}$ in homogeneous turbulence with our DNSs suggest that the boundary terms in the generalised irrotational and solenoidal KHMH equations might be negligible sufficiently far from boundaries, in particular at smaller scales and higher Reynolds numbers. Such a scenario would allow for efficient space-local (rather than non-local) calculations of all KHMH terms in the generalised solenoidal and irrotational KHMH equations, including centroid Helmholtz-decomposed non-linear terms.

4. Energy Transfer Dynamics at Small Scales

The evolution of turbulent kinetic energy in both physical and scale spaces is central to the understanding and prediction of turbulent flows. In the case of statistically homogeneous and stationary forced turbulence, we showed in chapter 3 that the average aspect of this evolution collapses into a simple balance between average (solenoidal) interscale turbulence transfer rate and average turbulence dissipation rate in an inertial range of scales bounded from below by the Taylor scale and from above by the integral length scale. Yasuda and Vassilicos (2018) and the previous chapter demonstrated how unrepresentative this average balance is of what actually happens in this range of scales.

In the range of scales below the Taylor scale, the average two-point turbulent kinetic energy balance does not involve only interscale transfer and dissipation but also viscous diffusion in scale space. Whilst the two-point turbulent energy evolution and balance in the inertial range is of paramount importance for reduced-order models and coarse-graining, it is essential in the dissipative range for determining the smallest, viscosity-affected or dominated, local length and time scales (Frisch and Vergassola, 1991; Dubrulle, 2019). In the present study we investigate how representative the average two-point turbulent kinetic energy balance is of what actually happens at length scales below the Taylor scale in statistically stationary forced periodic turbulence. To this end, we use the solenoidal KHMH equation of chapter 3 and a highly resolved Direct Numerical Simulation (DNS1) of forced homogeneous/periodic turbulence.

The following section describes the spatio-temporal average and fluctuating forms of the solenoidal KHMH equation for statistically homogeneous and stationary turbulence. We characterise the small-scale dynamics globally in terms of averages, standard deviations, skewnesses, flatness factors and correlation coefficients. In section 4.2 we focus on interscale transfer and viscous terms and their spatio-temporal coincidence/non-coincidence in low and high two-point kinetic energy $(|\delta \boldsymbol{u}|^2)^a$ regions. Section 4.3 investigates the non-coincidence of interscale transfer and viscous terms in terms of the solenoidal KHMH equation and KHMH statistics conditioned on various $(|\delta \boldsymbol{u}|^2)^a$ levels. We summarise our main findings in section 4.4.

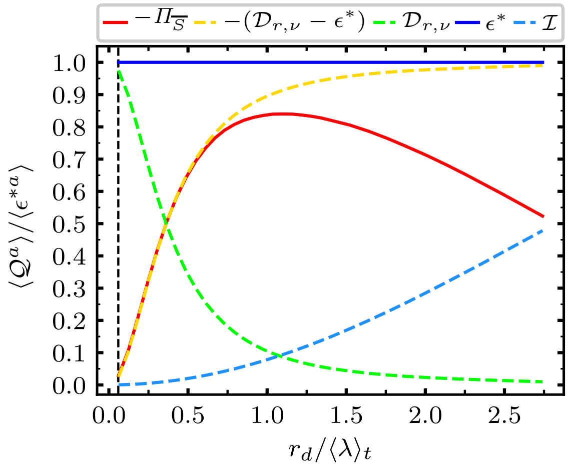

Figure 4.1: Spatio-temporal averages of surface-averaged terms of the solenoidal KHMH equation (4.1) as functions of $r_d/\langle\lambda\rangle_t$. The black vertical line marks $r_d=\langle\eta\rangle_t$.

4.1 Average and Fluctuating KHMH Dynamics

The KHMH equation governs the evolution of the velocity difference squared $|\delta\boldsymbol{u}|^2$ across scales, space and time. The solenoidal and irrotational KHMH equations, a decomposition of the KHMH equation, for statistically homogeneous/periodic turbulence derived in the previous chapter read

$$\mathcal{A}_t+\mathcal{T}_{\overline{S}}+\Pi_{\overline{S}}=\mathcal{D}_{x,\nu}+\mathcal{D}_{r,\nu}-\epsilon^*+\mathcal{I}, \tag{4.1}$$

$$\Pi_{\overline{I}}=\mathcal{T}_{\overline{I}}=\frac{1}{2}\mathcal{T}_p, \tag{4.2}$$

The spatio-temporal average of the solenoidal KHMH equation for statistically stationary and homogeneous turbulence at scales small enough for the large-scale ($|\delta\boldsymbol{u}|^2$) input rate $\langle\mathcal{I}\rangle$ to be negligible reads (see equation (3.23) in chapter 3)

$$\langle\Pi_{\overline{S}}\rangle\approx\langle\mathcal{D}_{r,\nu}\rangle-\langle\epsilon^*\rangle, \tag{4.3}$$

As proven by Valente and Vassilicos (2015) and confirmed by the DNS of Yasuda and Vassilicos (2018), $\langle\mathcal{D}_{r,\nu}\rangle$ is negligible at scales $|\boldsymbol{r}|$ larger than the Taylor scale. This average balance therefore simplifies to $\langle\Pi_{\overline{S}}\rangle\approx-\langle\epsilon^*\rangle$ at scales larger than the Taylor scale yet much smaller than the length scales where the large-scale forcing acts. Here we concentrate on scales below the Taylor scale and study how representative (4.3) is of what happens at these scales.

We calculated surface-averaged terms $\mathcal{Q}^a(\boldsymbol{x},r_d,t)=(\pi r_d^2)^{-1}\iint_{|\boldsymbol{r}|=r_d}\mathcal{Q}(\boldsymbol{x},\boldsymbol{r},t)d\boldsymbol{r}$ for every term $\mathcal{Q}$ in the solenoidal KHMH equation (4.1) for our well-resolved DNS (DNS1). Note that in this chapter we use the indirect evaluation method (see section 3.4) of the centroid Helmholtz-decomposed KHMH terms to efficiently sample these KHMH terms. In figure 4.1 we plot the non-zero spatio-temporal averages of surface-averaged terms. At scales $|\boldsymbol{r}| = r_d < 0.6\langle\lambda\rangle_t$, our DNS confirms (4.3) in the form

$$\langle \Pi_{\overline{S}}^{a} \rangle \approx \langle \mathcal{D}_{r,\nu}^{a} \rangle - \langle \epsilon^{*a} \rangle, \tag{4.4}$$

and also shows that both sides of the equation are negative and that they tend to zero monotonically with decreasing r_d. In fact, on average all terms in (4.1)-(4.2) equal or tend to zero as r_d tends to zero except for $\mathcal{D}_{r,\nu}$ and ϵ^*. Note, as clearly seen in figure 4.1, that $\langle \epsilon^{*a} \rangle$ is independent of r_d in statistically homogeneous/periodic turbulence and that $\lim_{r_d \to 0} \langle \mathcal{D}_{r,\nu}^{a} \rangle = \langle \epsilon^{*a} \rangle$ follows from a straightforward Taylor expansion of $\delta\boldsymbol{u}$ around $\boldsymbol{r} = 0$. Figure 4.1 confirms that $\langle \mathcal{D}_{r,\nu}^{a} \rangle$ tends to $\langle \epsilon^{*a} \rangle$ as r_d tends to zero and also shows that $\langle \mathcal{D}_{r,\nu}^{a} \rangle$ is a positive monotonically decreasing function of r_d.

The natural next step is to consider spatio-temporal fluctuations of the various terms in the KHMH equation around their average values. By subtracting the spatio-temporal average solenoidal KHMH equation from the solenoidal KHMH equation we obtain

$$\mathcal{A}_{t}^{a} + \mathcal{T}_{\overline{S}}^{a} + \Pi_{\overline{S}}^{a'} \approx \mathcal{D}_{x,\nu}^{a} + \mathcal{D}_{r,\nu}^{a'} - \epsilon^{*a'} \tag{4.5}$$

at scales r_d small enough for the large-scale $(|\delta\boldsymbol{u}|^2)^a$ input rate $\mathcal{I}$ to be negligibly small (and $\mathcal{Q}^{a'} = \mathcal{Q}^{a} - \langle \mathcal{Q}^{a} \rangle$). The focus of interest in this chapter is the extent in which the average balance (4.4) is representative locally, i.e. the extent of validity of a local balance $\Pi_{\overline{S}}^{a} \approx \mathcal{D}_{r,\nu}^{a} - \epsilon^{*a}$ at the smallest, dissipative, length scales ($r_d \lessapprox 0.5\langle\lambda\rangle_t$). The Reynolds number of our well-resolved DNS ($\langle Re_\lambda \rangle_t = 81$) may not be very high, but we are concerned with the dynamics at scales between $r_d = \langle\eta\rangle_t$ and $r_d = 0.5\langle\lambda\rangle_t$ which does not change much or change very slowly with increasing $\langle Re_\lambda \rangle_t$ (Pope, 2000).

A natural starting point for addressing our question is in terms of standard deviations of the various terms in the fluctuating solenoidal KHMH equation. In figure 4.2(a, b, c) we plot these terms versus $r_d/\langle\lambda\rangle_t$. To set the scene within a wider context, figure 4.2(a) shows how these standard deviations vary with $r_d/\langle\lambda\rangle_t$ over a range of scales r_d that is wider than our actual range of interest as it is from $\langle\eta\rangle_t$ to $\langle L \rangle_t = 2.6\langle\lambda\rangle_t$. These average fluctuations are similar to the results at higher Reynolds numbers, but they are smaller in magnitude (see figure 3.9 in chapter 3. This Reynolds number trend is consistent with the results in chapter 3). In figure 4.2(b) we concentrate attention on the range $\langle\eta\rangle_t \leq r_d \leq 0.5\langle\lambda\rangle_t$. It is clear that the standard deviations of all surface-averaged solenoidal KHMH terms except for $\mathcal{D}_{r,\nu}^{a}$ and ϵ^{*a} tend to zero monotonically as r_d decreases towards zero. The standard deviations of $\mathcal{D}_{r,\nu}^{a}$ and of ϵ^{*a} tend to the same non-zero value of about $1.2\langle \epsilon^{*a} \rangle$ as r_d decreases towards zero. Furthermore, the standard deviation of $\mathcal{D}_{r,\nu}^{a} - \epsilon^{*a}$ tends to zero in a way that is close to the way that the standard deviation of $\Pi_{\overline{S}}^{a}$ tends to zero as r_d tends to zero.

For a proper initial estimate of the importance of fluctuations in the cascade dynamics, we need to compare these standard deviations to an appropriate non-zero spatio-temporal average. In figure 4.2(c) we plot them normalised by the absolute value of the spatio-

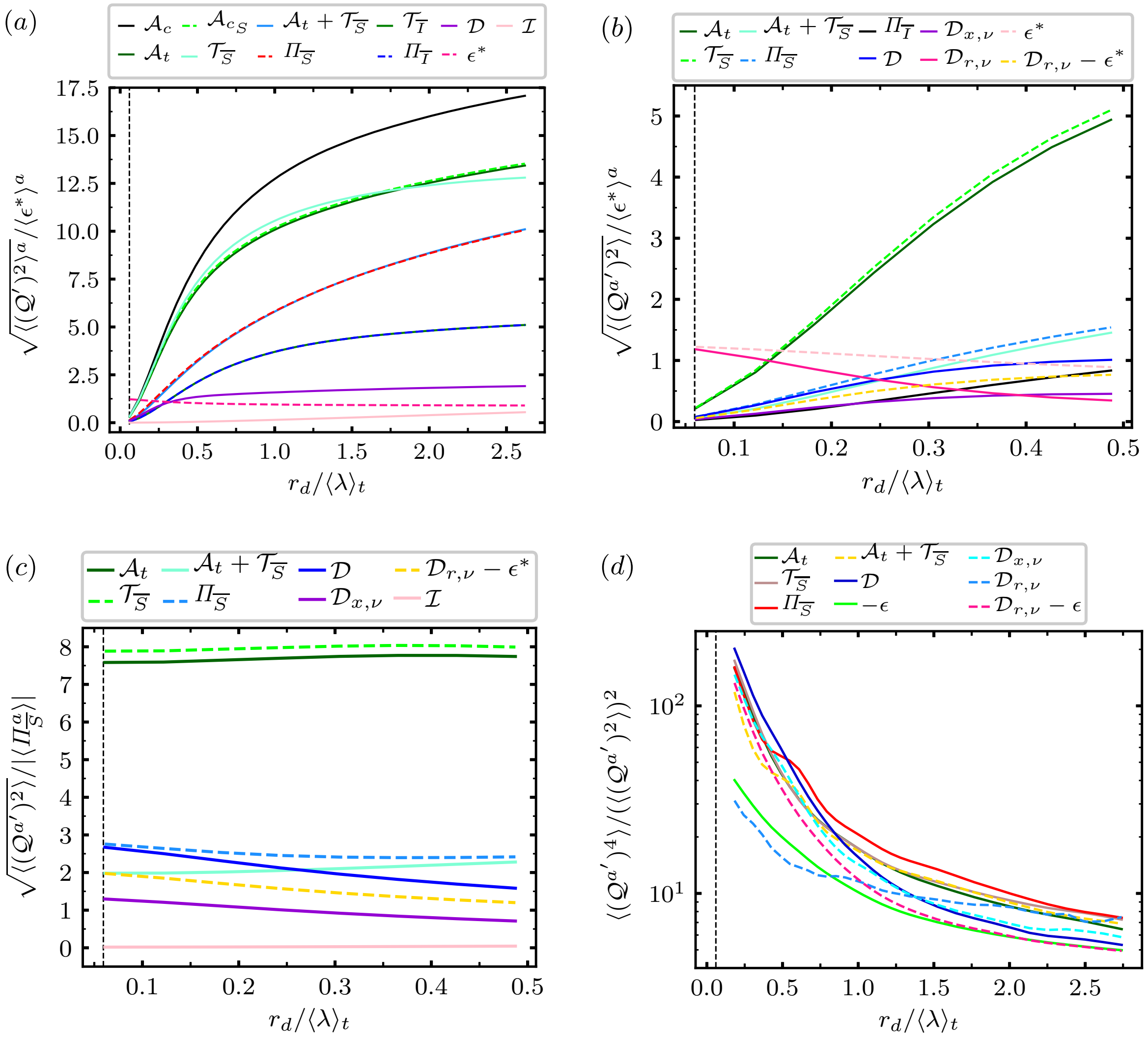

Figure 4.2: (a) Plot of $\sqrt{\langle(\mathcal{Q}')^2\rangle^a}$ with the same overlapping terms as in chapter 3: $(\mathcal{A}_t, \mathcal{A}_{c_S})$,$(\mathcal{A}_t + \mathcal{T}_{\overline{S}}, \Pi_{\overline{S}})$ and $(\mathcal{T}_{\overline{I}}, \Pi_{\overline{I}})$. (b, c) Plots of KHMH standard deviations of terms $\mathcal{Q}^a$; normalised by $\langle\epsilon^{*a}\rangle$ (which is independent of r_d) in (b) and normalised by $|\langle\Pi_{\overline{S}}^a\rangle|$ (which decreases with decreasing r_d) in (c). (d) Flatness factors of various spherically averaged KHMH terms.

temporal average of $\Pi_{\overline{S}}^a$, which also tends to zero as r_d tends to zero. The standard deviations of all the terms in the solenoidal KHMH equation which tend to zero as r_d tends to zero do so at a rate that is comparable to or even marginally slower than $|\langle\Pi_{\overline{S}}^a\rangle|$. In fact the standard deviation of $\Pi_{\overline{S}}^a$ is between 2.5 and 2.8 times larger than $|\langle\Pi_{\overline{S}}^a\rangle|$ for all r_d in the range $\langle\eta\rangle_t$ to $0.5\langle\lambda\rangle_t$ and the standard deviation of $\mathcal{D}_{r,\nu}^a - \epsilon^{*a}$ is between 1.2 and 2.0 times larger than $|\langle\Pi_{\overline{S}}^a\rangle|$ in that range. These fluctuations are clearly very significant compared to the average balance (4.4). Furthermore, whilst $\Pi_{\overline{S}}^a$ and $\mathcal{D}_{r,\nu}^a - \epsilon^{*a}$ are equal on average, the standard deviation of $\Pi_{\overline{S}}^a$ is at least 40% larger than the standard deviation of $\mathcal{D}_{r,\nu}^a - \epsilon^{*a}$ in this range of scales.

Figure 4.2(c) reveals that the largest fluctuations (except those of $\mathcal{D}_{r,\nu}^a$ and ϵ^{*a}) are by far those of $\mathcal{A}_t^a$ and $\mathcal{T}_{\overline{S}}^a$ at these viscous length scales but that they partially cancel by the sweeping effect (discussed in some detail in chapter 3) so that the fluctuations of

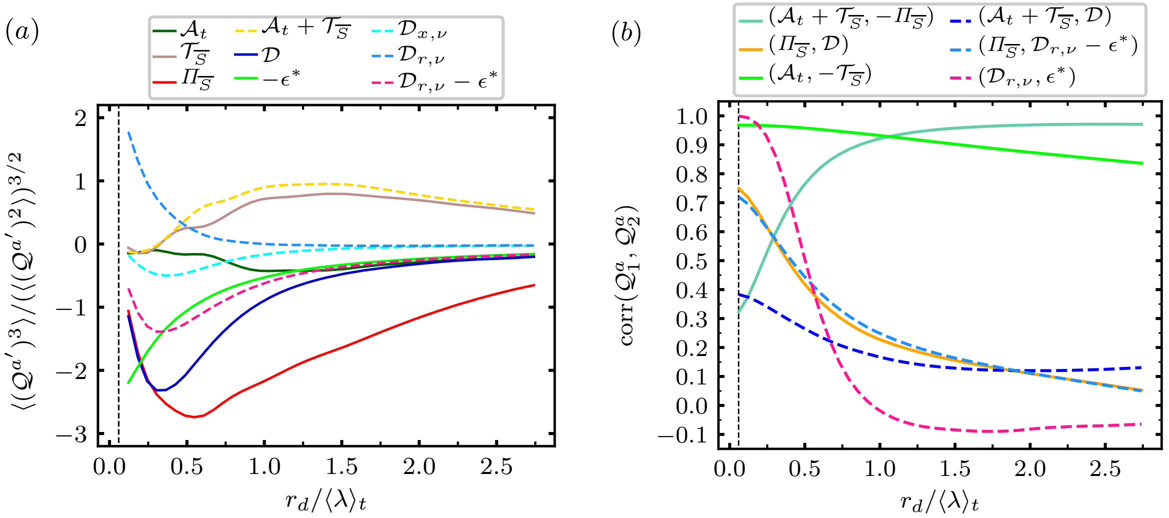

Figure 4.3: (a) Skewness factors and (b) correlation coefficients of terms in the solenoidal KHMH equation across normalised scales $r_d/\langle\lambda\rangle_t$.

$\mathcal{A}_t^a + \mathcal{T}_{\overline{S}}^a$ are between those of $\Pi_{\overline{S}}^a$ and $\mathcal{D}_{r,\nu}^a - \epsilon^{*a}$ in intensity. Except for the $(|\delta \boldsymbol{u}|^2)^a$ input rate $\mathcal{I}^a$ which is insignificant at the very small scales, the smallest standard deviations are those of $\mathcal{D}_{x,\nu}^a$, the viscous diffusion in physical space. Preempting observations made further down in this chapter concerning the importance of $\mathcal{D}_{x,\nu}^a$, we note that the standard deviations of $\Pi_{\overline{S}}^a$ and $\mathcal{D}^a \equiv \mathcal{D}_{x,\nu}^a + \mathcal{D}_{r,\nu}^a - \epsilon^{*a}$ tend to equal each other as r_d approaches $\langle\eta\rangle_t$ whereas the standard deviation of $\mathcal{D}_{r,\nu}^a - \epsilon^{*a}$ remains below that of $\Pi_{\overline{S}}^a$. That is, $\mathcal{D}_{x,\nu}^a$ seems to be non-negligible in the cascade dynamics at small scales.

The results of figure 4.2(a, b, c) are the first indications that the average balance (4.4) nor a local balance $\Pi_{\overline{S}}^a \approx \mathcal{D}_{r,\nu}^a - \epsilon^{*a}$ may be characteristic of reality. Not only are the standard deviations of $\Pi_{\overline{S}}^a$ and $\mathcal{D}_{r,\nu}^a - \epsilon^{*a}$ much larger than their average values at scales r_d under $0.5\langle\lambda\rangle_t$, they are also the result of extremely intermittent fluctuations as evidenced by their flatness factors which are well over 40 at these scales (see figure 4.2(d)). In fact, all the terms in the solenoidal KHMH equation are much more intermittent than ϵ^{*a} and $\mathcal{D}_{r,\nu}^a$ at these scales, even $\mathcal{D}_{r,\nu}^a - \epsilon^{*a}$. Furthermore, $\Pi_{\overline{S}}^a$ and $\mathcal{D}_{r,\nu}^a - \epsilon^{*a}$ have significantly different skewnesses as shown in figure 4.3(a). With very intermittent fluctuations which are different in terms of standard deviations and skewnesses, it is likely that $\Pi_{\overline{S}}^a$ and $\mathcal{D}_{r,\nu}^a - \epsilon^{*a}$ are not typically equal locally. In fact, it is interesting to note the role of the viscous diffusion in physical space once again as the skewness of $\mathcal{D}^a$ is equal to the skewness of $\Pi_{\overline{S}}^a$ at scales r_d between $\langle\eta\rangle_t$ and $0.25\langle\lambda\rangle_t$.

The fluctuations of $\Pi_{\overline{S}}^a$ and $\mathcal{D}_{r,\nu}^a - \epsilon^{*a}$ may be extremely intermittent and differ in magnitude, but be nevertheless correlated. The Pearson correlation coefficient of $\Pi_{\overline{S}}^a$ and $\mathcal{D}_{r,\nu}^a - \epsilon^{*a}$ is about 0.45 at $r_d = 0.5\langle\lambda\rangle_t$ and increases to about 0.72 at $r_d = \langle\eta\rangle_t$ (see figure 4.3(b)). This is a significant correlation but the correlation curve between $\Pi_{\overline{S}}^a$ and $\mathcal{D}^a$ in figure 4.3(b) is about the same. It is important to note that two signals can be well correlated yet be different in magnitude nearly everywhere/every time. Even so, the near-perfect correlation seen in figure 4.3(b) between $\mathcal{D}^a_{r,\nu}$ and ϵ^{*a} at scales close to $\langle\eta\rangle_t$ reflects very similar $\mathcal{D}^a_{r,\nu}$ and ϵ^{*a} spatio-temporal fields at r_d close to $\langle\eta\rangle_t$ (the standard deviation of $1-\mathcal{D}^a_{r,\nu}/\epsilon^{*a}$ at $r_d=\langle\eta\rangle_t$ is 0.025).

Given the high but far from perfect correlation between $\Pi^a_{\overline{S}}$ and $\mathcal{D}^a_{r,\nu}-\epsilon^{*a}$ at scales close to $\langle\eta\rangle_t$ it may still not be a priori inconceivable that the average balance (4.4) may be, to some degree, a fairly representative balance even though the two spatio-temporal fluctuations of $\Pi^a_{\overline{S}}$ and $\mathcal{D}^a_{r,\nu}-\epsilon^{*a}$ differ in fluctuation intensity and skewness. In the following section we investigate the degree of correspondence between $\Pi^a_{\overline{S}}$ and $\mathcal{D}^a_{r,\nu}-\epsilon^{*a}$ more closely by conditioning on low and high two-point energy $(|\delta\boldsymbol{u}|^2)^a$ regions. Given the results on $\Pi^a_{\overline{S}}$ and $\mathcal{D}^a$ in figures 4.2 and 4.3 (same standard deviation and skewness at scales close to $\langle\eta\rangle_t$, similar flatness factors, and correlations comparable to those of $\Pi^a_{\overline{S}}$ and $\mathcal{D}^a_{r,\nu}-\epsilon^{*a}$), we also investigate the relation between $\Pi^a_{\overline{S}}$ and $\mathcal{D}^a$.

4.2 Small-scale Interscale Transfer and Viscous Terms in Low and High Two-point Energy Regions

We define $\langle\mathcal{Q}|(|\delta\boldsymbol{u}|^2)^a\rangle$ to be the average value of $\mathcal{Q}$ conditionally on $(|\delta\boldsymbol{u}|^2)^a$ being within a certain range of $(|\delta\boldsymbol{u}|^2)^a$ values and we consider 20 such ranges of increasing values of $(|\delta\boldsymbol{u}|^2)^a$: the 5% smallest $(|\delta\boldsymbol{u}|^2)^a$ values, the 5% to 10% smallest $(|\delta\boldsymbol{u}|^2)^a$ values, and so on till the 95% to 100% smallest $(|\delta\boldsymbol{u}|^2)^a$ values which are actually the 5% highest values of $(|\delta\boldsymbol{u}|^2)^a$. In figure 4.4 we plot (a) $\langle\mathcal{D}^a|(|\delta\boldsymbol{u}|^2)^a\rangle$, ($b$) $\langle\mathcal{D}^a_{r,\nu}-\epsilon^{*a}|(|\delta\boldsymbol{u}|^2)^a\rangle$ and (c) $\langle\mathcal{D}^a_{x,\nu}|(|\delta\boldsymbol{u}|^2)^a\rangle$ versus $\langle\Pi^a_{\overline{S}}|(|\delta\boldsymbol{u}|^2)^a\rangle$ for increasing $(|\delta\boldsymbol{u}|^2)^a$ and for scales r_d between $\langle\eta\rangle_t$ and $\langle\lambda\rangle_t$. We checked that the results in this figure and figure 4.7 are insensitive to the number of $(|\delta\boldsymbol{u}|^2)^a$ ranges as we also tried 10 and 100 ranges with very similar results.

Figure 4.4 shows that as the $(|\delta\boldsymbol{u}|^2)^a$ values increase, the equality $\langle\Pi^a_{\overline{S}}|(|\delta\boldsymbol{u}|^2)^a\rangle\approx\langle\mathcal{D}^a|(|\delta\boldsymbol{u}|^2)^a\rangle$ appears clearly (see figure 4.4(a)) for all r_d in the range $\langle\eta\rangle_t\le r_d\le 0.6\langle\lambda\rangle_t$ whereas $\langle\Pi^a_{\overline{S}}|(|\delta\boldsymbol{u}|^2)^a\rangle\approx\langle\mathcal{D}^a_{r,\nu}-\epsilon^{*a}|(|\delta\boldsymbol{u}|^2)^a\rangle$ does not (see figure 4.4(b)). This behaviour has its root cause in the viscous diffusion in physical space which is non-zero in regions with high values of $(|\delta\boldsymbol{u}|^2)^a$. Interestingly, $\langle\mathcal{D}^a_{x,\nu}|(|\delta\boldsymbol{u}|^2)^a\rangle$ is increasingly negative as $(|\delta\boldsymbol{u}|^2)^a$ values increase (see figure 4.4(c)), which is also the case for all other three quantities plotted in figure 4.4. In fact both $\langle\mathcal{D}^a_{x,\nu}|(|\delta\boldsymbol{u}|^2)^a\rangle$ and $\langle\mathcal{D}^a_{r,\nu}-\epsilon^{*a}|(|\delta\boldsymbol{u}|^2)^a\rangle$ vary linearly with $\langle\Pi^a_{\overline{S}}|(|\delta\boldsymbol{u}|^2)^a\rangle$ if the $(|\delta\boldsymbol{u}|^2)^a$ values are not too small, and these two linear dependencies sum up to give $\langle\Pi^a_{\overline{S}}|(|\delta\boldsymbol{u}|^2)^a\rangle\approx\langle\mathcal{D}^a|(|\delta\boldsymbol{u}|^2)^a\rangle$.

We conclude that (i) with increasing $(|\delta\boldsymbol{u}|^2)^a$ values, the average balance (4.4) is increasingly not representative of the conditionally averaged transfer balance at viscosity affected/dominated length scales as (ii) the viscous diffusion in physical space cannot be neglected in regions of significant local inhomogeneity where $(|\delta\boldsymbol{u}|^2)^a$ is high. In such regions the viscous diffusion in physical space contributes to the loss of $(|\delta\boldsymbol{u}|^2)^a$, though, on average, less than $\mathcal{D}^a_{r,\nu}-\epsilon^{*a}$ which is also negative on average but with higher magnitudes (see figure 4.4(b,c)).

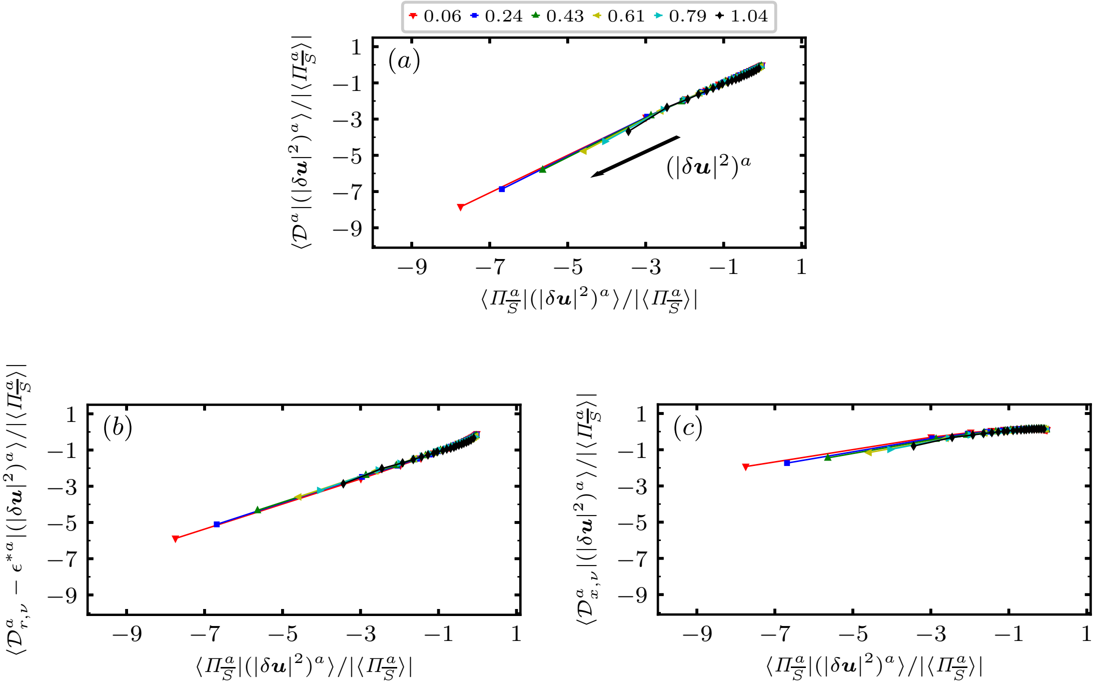

Figure 4.4: Plots of (a) $\langle \mathcal{D}^a|(|\delta \boldsymbol{u}|^2)^a\rangle$, (b) $\langle \mathcal{D}^a_{r,\nu} - \epsilon^{*a}|(|\delta \boldsymbol{u}|^2)^a\rangle$ and (c) $\langle \mathcal{D}^a_{x,\nu}|(|\delta \boldsymbol{u}|^2)^a\rangle$ versus $\langle \Pi^a_{\overline{S}}|(|\delta \boldsymbol{u}|^2)^a\rangle$ (see the definition of these conditional averages in the first paragraph of section 4.2). All plotted quantities are normalised by $|\langle \Pi^a_{\overline{S}}\rangle|$ and are plotted for different values of r_d. The legend at the top of (a) gives the values of $r_d/\langle\lambda\rangle_t$ which correspond to different coloured symbols (note $\langle\eta\rangle_t \approx 0.06\langle\lambda\rangle_t$). The average quantities plotted are conditional on 20 different ranges of $(|\delta \boldsymbol{u}|^2)^a$ values as described in the first paragraph of section 4.2 and ranges with increasing values of $(|\delta \boldsymbol{u}|^2)^a$ for each r_d are from right to left in (a)-(c) (see the arrow indicating increasing local two-point energy in (a)).

The third conclusion is quantitative, namely that

$$\langle \Pi^a_{\overline{S}}|(|\delta \boldsymbol{u}|^2)^a\rangle \approx \langle \mathcal{D}^a|(|\delta \boldsymbol{u}|^2)^a\rangle \tag{4.6}$$

holds for all ranges of high enough $(|\delta \boldsymbol{u}|^2)^a$ values in the range of scales $\langle\eta\rangle_t \leq r_d \leq 0.6\langle\lambda\rangle_t$ whereas $\langle \Pi^a_{\overline{S}}|(|\delta \boldsymbol{u}|^2)^a\rangle = \langle \mathcal{D}^a_{r,\nu} - \epsilon^{*a}|(|\delta \boldsymbol{u}|^2)^a\rangle$ does not. This raises the question whether $\Pi^a_{\overline{S}} \approx \mathcal{D}^a$ happens more often than $\Pi^a_{\overline{S}} \approx \mathcal{D}^a_{r,\nu} - \epsilon^{*a}$ at these very small scales.

To look more closely at the local cascade dynamics, including in the low two-point energy regions, we plot in figure 4.5 probability density functions (PDFs) of $\Pi^a_{\overline{S}} - \mathcal{D}^a$ and $\Pi^a_{\overline{S}} - (\mathcal{D}^a_{r,\nu} - \epsilon^{*a})$ conditional on $(|\delta \boldsymbol{u}|^2)^a$. The red curves are PDFs conditional on the 5% smallest values of $(|\delta \boldsymbol{u}|^2)^a$ whereas the blue and green curves are, respectively, PDFs conditional on the 5% and 0.5% highest values of $(|\delta \boldsymbol{u}|^2)^a$ for a given length scale r_d. The top plots (a) and (b) are for $r_d = \langle\eta\rangle_t$, the middle plots (c) and (d) are for $r_d = 0.24\langle\lambda\rangle_t$ and the bottom plots (e) and (f) are for $r_d = 0.48\langle\lambda\rangle_t$. The first observation to make is that, if normalised by their maximum PDF value $P_{\max}$ and the standard deviation of $\Pi^a_{\overline{S}}$ for high $(|\delta \boldsymbol{u}|^2)^a$ events, the high $(|\delta \boldsymbol{u}|^2)^a$ PDFs of $\Pi^a_{\overline{S}} - \mathcal{D}^a$ (blue and green curves in the left plots of figure 4.5) are approximately symmetric with respect to positive and

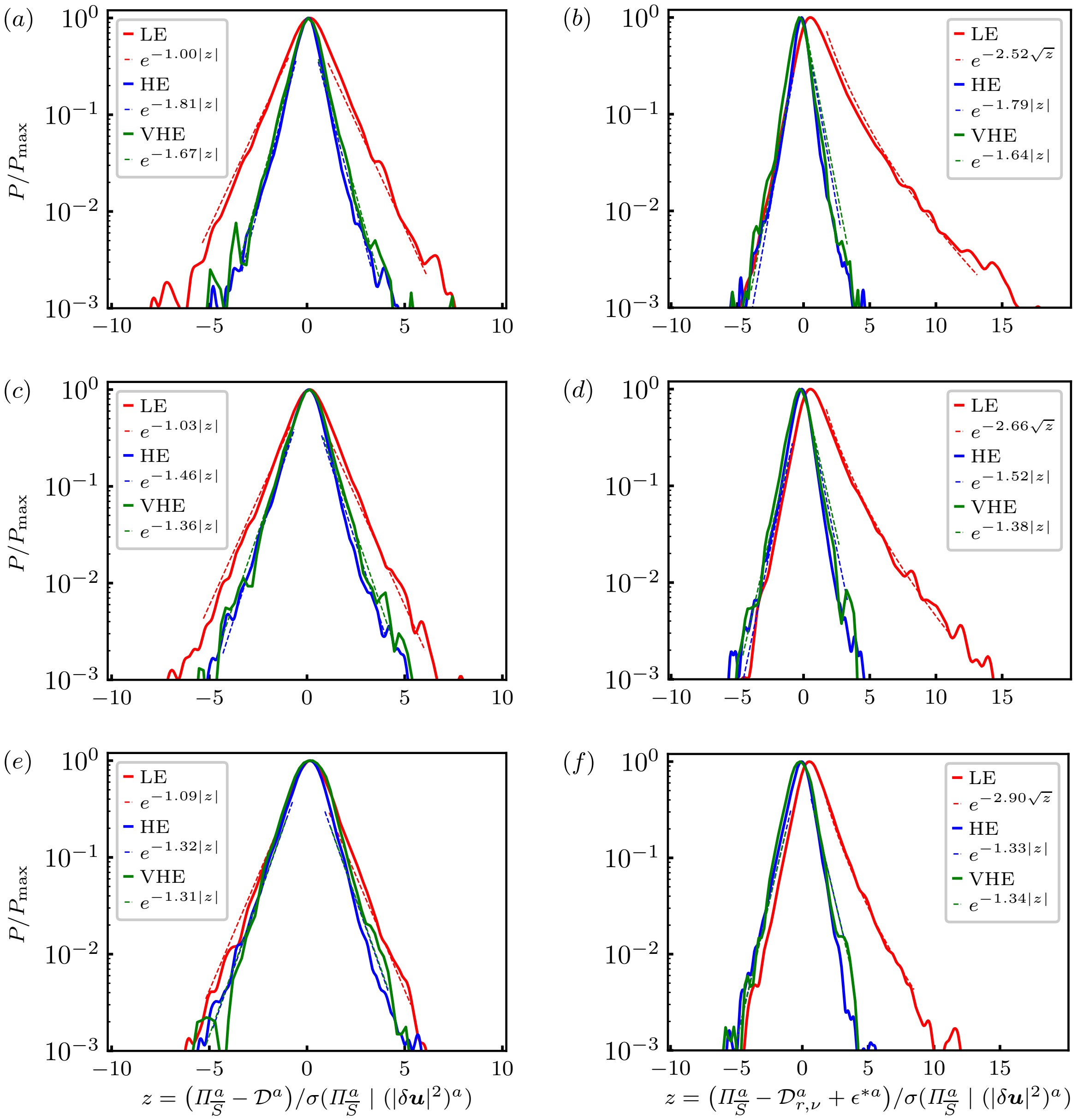

Figure 4.5: Probability density functions of $\Pi_{\frac{a}{S}} - \mathcal{D}^a$ (left) and $\Pi_{\frac{a}{S}} - \mathcal{D}^a_{r,\nu} + \epsilon^{*a}$ (right) conditional on low two-point energy $(|\delta \boldsymbol{u}|^2)^a$ (LE) events (the events with the 5% smallest $(|\delta \boldsymbol{u}|^2)^a$ values at scale r_d), high $(|\delta \boldsymbol{u}|^2)^a$ (HE) events (the events with the 5% highest $(|\delta \boldsymbol{u}|^2)^a$ values at scale r_d) and very high $(|\delta \boldsymbol{u}|^2)^a$ (VHE) events (the events with the 0.5% highest $(|\delta \boldsymbol{u}|^2)^a$ values at scale r_d): (a, b) $r_d = \langle \eta \rangle_t$, (c, d) $r_d = 0.24\langle \lambda \rangle_t$, (e, f) $r_d = 0.48\langle \lambda \rangle_t$). $P_{\max}$ and $\sigma(\Pi_{\frac{a}{S}} | (|\delta \boldsymbol{u}|^2)^a)$ denote, respectively, PDF maximum value and standard deviation of $\Pi_{\frac{a}{S}}$ conditional on the particular range of $(|\delta \boldsymbol{u}|^2)^a$ values considered. The dashed lines show exponential/stretched exponential fits of the PDFs calculated with least squares.

negative values and become decreasingly heavy-tailed with decreasing r_d. Irrespective of the value of r_d in the range $\langle \eta \rangle_t \leq r_d \leq 0.5\langle \lambda \rangle_t$, the most likely value of $\Pi_{\frac{a}{S}} - \mathcal{D}^a$ is zero at the 5% and 0.5% highest $(|\delta \boldsymbol{u}|^2)^a$ events. The most likely value of $\Pi_{\frac{a}{S}} - \mathcal{D}^a$ is also zero at the 5% lowest $(|\delta \boldsymbol{u}|^2)^a$ events. However, the PDF of $\Pi_{\frac{a}{S}} - \mathcal{D}^a$ conditional on these 5% lowest $(|\delta \boldsymbol{u}|^2)^a$ events and normalised by $P_{\max}$ and the standard deviation of $\Pi_{\frac{a}{S}}$ for these

$(\lvert\delta \boldsymbol{u}\rvert^2)^a$	-0.005	-0.05	-0.1	+0.1	+0.05	+0.005
$\langle\eta\rangle_t$	(9.7, 9.2)	(10.4, 12.7)	(10.9, 13.5)	(31.4, 25.3)	(34.2, 25.4)	(41.0, 24.3)
$0.24\langle\lambda\rangle_t$	(9.1, 10.4)	(10.1, 12.8)	(10.5, 13.7)	(27.5, 23.7)	(30.1, 24.4)	(37.9, 24.6)
$0.48\langle\lambda\rangle_t$	(8.9, 11.9)	(9.7, 13.5)	(10.0, 14.1)	(21.8, 19.5)	(23.6, 20.1)	(27.5, 20.9)

Table 4.1: Share of events (in %) with $\frac{2}{3}\mathcal{D}^a < \Pi^a_{\overline{S}} < \frac{4}{3}\mathcal{D}^a$ (left entries) and share of events with $\frac{2}{3}(\mathcal{D}^a_{r,\nu} - \epsilon^{*a}) < \Pi^a_{\overline{S}} < \frac{4}{3}(\mathcal{D}^a_{r,\nu} - \epsilon^{*a})$ (right entries) with various $(|\delta \boldsymbol{u}|^2)^a$ conditioning. Each row corresponds to one r_d given in the leftmost column and the top row denotes the $(|\delta \boldsymbol{u}|^2)^a$ conditioning. E. g. -0.05 denotes the 5% of the events with the lowest $(|\delta \boldsymbol{u}|^2)^a$ and +0.1 denotes the 10% of the events with the highest $(|\delta \boldsymbol{u}|^2)^a$.

events (red curves in the left plots of figure 4.5) becomes increasingly heavy-tailed with decreasing r_d in the range $\langle\eta\rangle_t \leq r_d \leq 0.5\langle\lambda\rangle_t$ (but remains approximately symmetric with respect to positive and negative values). We return to these tendencies when we discuss figure 4.7 in the next section.

The PDFs of $\Pi^a_{\overline{S}} - \mathcal{D}^a$ are plotted in log-lin axes to make it clear that their tails are exponential tails over a range of $\Pi^a_{\overline{S}} - \mathcal{D}^a$ values. Exponential tails are a sign of intermittency and mean that there is much more than a normal number of events in space and time with large and very large deviations from $\Pi^a_{\overline{S}} \approx \mathcal{D}^a$. The most likely occurrence remains $\Pi^a_{\overline{S}} - \mathcal{D}^a = 0$, but it is in fact not so likely. In table 4.1 we report the probability of finding $\frac{2}{3}\mathcal{D}^a < \Pi^a_{\overline{S}} < \frac{4}{3}\mathcal{D}^a$ which is a very generous upper bound on the probability to find $\Pi^a_{\overline{S}} \approx \mathcal{D}^a$: it increases as r_d decreases from $0.5\langle\lambda\rangle_t$ to $\langle\eta\rangle_t$ and it also increases as we condition on progressively higher $(|\delta \boldsymbol{u}|^2)^a$. This probability ranges from 8.9% if we condition on the 0.5% lowest $(|\delta \boldsymbol{u}|^2)^a$ and focus on $r_d = 0.48\langle\lambda\rangle_t$, to 41% if we condition on the 0.5% highest $(|\delta \boldsymbol{u}|^2)^a$ and focus on $r_d = \langle\eta\rangle_t$. It is therefore generally unlikely to find $\Pi^a_{\overline{S}} \approx \mathcal{D}^a$ in the turbulence except at the very highest $(|\delta \boldsymbol{u}|^2)^a$ with $r_d = \langle\eta\rangle_t$. Note that $\Pi^a_{\overline{S}} \approx \mathcal{D}^a$ is rather rare at $r_d = \langle\eta\rangle_t$ in low $(|\delta \boldsymbol{u}|^2)^a$ regions with e.g. a 10.4% probability among the 5% lowest $(|\delta \boldsymbol{u}|^2)^a$.

Unlike $\Pi^a_{\overline{S}} - \mathcal{D}^a$, the most likely value of $\Pi^a_{\overline{S}} - (\mathcal{D}^a_{r,\nu} - \epsilon^{*a})$ is not zero (see figure 4.5(b, d, f)). It is non-zero and positive if conditioned on the 5% lowest $(|\delta \boldsymbol{u}|^2)^a$ events, and non-zero and slightly negative if conditioned on either the 5% or the 0.5% highest $(|\delta \boldsymbol{u}|^2)^a$ events. Similarly to $\Pi^a_{\overline{S}} - \mathcal{D}^a$, the high $(|\delta \boldsymbol{u}|^2)^a$ PDFs of $\Pi^a_{\overline{S}} - (\mathcal{D}^a_{r,\nu} - \epsilon^{*a})$ (blue and green curves in the right plots of figure 4.5) normalised by their maximum PDF value $P_{\max}$ and the standard deviation of $\Pi^a_{\overline{S}}$ for high $(|\delta \boldsymbol{u}|^2)^a$ events, are decreasingly heavy-tailed (and exponential) for decreasing r_d. The PDF of $\Pi^a_{\overline{S}} - (\mathcal{D}^a_{r,\nu} - \epsilon^{*a})$ conditional on the 5% lowest $(|\delta \boldsymbol{u}|^2)^a$ events and normalised by $P_{\max}$ and the standard deviation of $\Pi^a_{\overline{S}}$ for these events (red curves in the right plots of figure 4.5) is different for different values of r_d in the range $\langle\eta\rangle_t \leq r_d \leq 0.5\langle\lambda\rangle_t$. It is very significantly asymmetric with a vast bias towards positive values and becomes increasingly heavy-tailed on its positive side as r_d decreases within this range, but not on both positive and negative sides as in the case

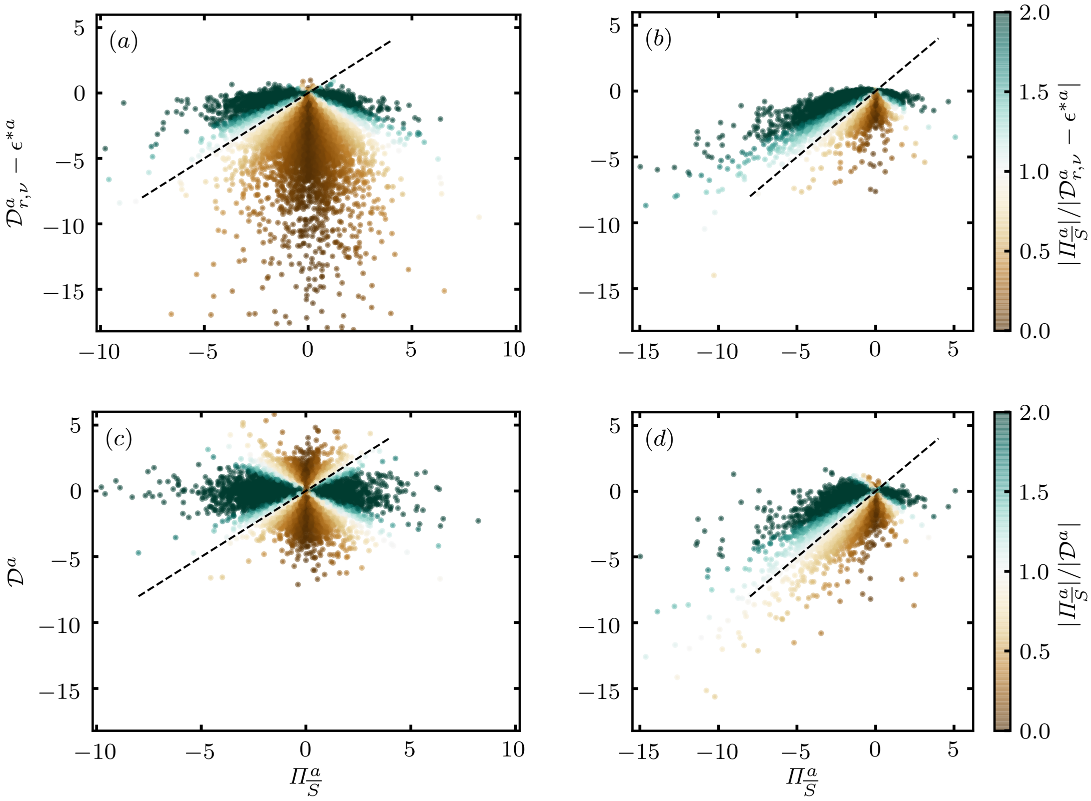

Figure 4.6: Scatter plots at $r_d = \langle \eta \rangle_t$ of (a,b) $(\mathcal{D}^a_{r,\nu} - \epsilon^{*a}, \varPi^a_{\tilde{S}})$ and (c,d) $(\mathcal{D}^a, \varPi^a_{\tilde{S}})$ conditioned on (a,c) the 5% lowest $(|\delta \boldsymbol{u}|^2)^a$ events and (b,d) the 5% highest $(|\delta \boldsymbol{u}|^2)^a$ events. The black dotted lines show (a,b) $\varPi^a_{\tilde{S}} = \mathcal{D}^a_{r,\nu} - \epsilon^{*a}$ and (c,d) $\varPi^a_{\tilde{S}} = \mathcal{D}^a$. All KHMH terms are normalised with the standard deviation of $\varPi^a_{\tilde{S}}$ conditioned on the 5% lowest (a,c) or 5% highest (b,d) $(|\delta \boldsymbol{u}|^2)^a$ events.

of $\varPi^a_{\tilde{S}} - \mathcal{D}^a$. On its negative side its tail is an exponential while its tail on the positive side is a stretched exponential. As the difference between $\mathcal{D}^a$ and $\mathcal{D}^a_{r,\nu} - \epsilon^{*a}$ equals $\mathcal{D}^a_{x,\nu}$, it follows from figure 4.5 that the strong bias towards positive $\varPi^a_{\tilde{S}} - (\mathcal{D}^a_{r,\nu} - \epsilon^{*a})$ events in low $(|\delta \boldsymbol{u}|^2)^a$ regions is balanced by $\mathcal{D}^a_{x,\nu} \gg 0$ events in such regions. Hence, as could be expected, physical space viscous diffusion $\mathcal{D}^a_{x,\nu}$ tends to transport $(|\delta \boldsymbol{u}|^2)^a$ from high $(|\delta \boldsymbol{u}|^2)^a$ regions to low $(|\delta \boldsymbol{u}|^2)^a$ regions (remember the behaviour of $\mathcal{D}^a_{x,\nu}$ in high $(|\delta \boldsymbol{u}|^2)^a$ regions in figure 4.4). However, it is less obvious that this physical mechanism is as non-negligible in the local KHMH dynamics at small scales as our results show.

The scatter plots in low and high $(|\delta \boldsymbol{u}|^2)^a$ regions in figure 4.6 shed more light on this behaviour. In low $(|\delta \boldsymbol{u}|^2)^a$ regions $\varPi^a_{\tilde{S}}$ is equally likely to be positive or negative, while $\mathcal{D}^a_{r,\nu} - \epsilon^a$ is heavily skewed towards negative values such that $\varPi^a_{\tilde{S}} - (\mathcal{D}^a_{r,\nu} - \epsilon^a)$ has a tendency of being positive. In low $(|\delta \boldsymbol{u}|^2)^a$ regions $\mathcal{D}^a$ is approximately symmetric with the events $\mathcal{D}^a_{r,\nu} - \epsilon^a \ll 0$ being balanced by events $\mathcal{D}^a_{x,\nu} \gg 0$ (compare figures 4.6(a,c)). In the high $(|\delta \boldsymbol{u}|^2)^a$ regions the behaviours of $\mathcal{D}^a_{r,\nu} - \epsilon^a$, $\mathcal{D}^a$ and $\varPi^a_{\tilde{S}}$ are all skewed towards negative values such that the high $(|\delta \boldsymbol{u}|^2)^a$ region PDFs in figure 4.5 are all approximately symmetric (the above scatter plots are qualitatively equal at $r_d/\langle \lambda \rangle_t = (0.24, 0.48)$).

As $\varPi^a_{\tilde{S}} \approx \mathcal{D}^a$ events are unlikely and physical space diffusion is non-negligible in a considerable set of events, it is not surprising that it is unlikely to find events $\Pi^a_{\overline{S}} \approx \mathcal{D}^a_{r,\nu} - \epsilon^{*a}$ (see table 4.1). It is significantly less likely finding such events than finding $\Pi^a_{\overline{S}} \approx \mathcal{D}^a$ events. The probability of finding $\frac{2}{3}(\mathcal{D}^a_{r,\nu} - \epsilon^{*a}) < \Pi^a_{\overline{S}} < \frac{4}{3}(\mathcal{D}^a_{r,\nu} - \epsilon^{*a})$ ranges from 9.2% to 25.4% whereas the probability of finding $\frac{2}{3}\mathcal{D}^a < \Pi^a_{\overline{S}} < \frac{4}{3}\mathcal{D}^a$ ranges from 8.9% to 41.0% (table 4.1). Unlike the latter which increases as we condition on progressively higher $(|\delta \boldsymbol{u}|^2)^a$, the probability of finding $\frac{2}{3}(\mathcal{D}^a_{r,\nu} - \epsilon^{*a}) < \Pi^a_{\overline{S}} < \frac{4}{3}(\mathcal{D}^a_{r,\nu} - \epsilon^{*a})$ levels off (see table 4.1). When we condition on increasing values of $(|\delta \boldsymbol{u}|^2)^a$ it becomes increasingly difficult to neglect the viscous diffusion in physical space.

We have therefore reached two conclusions in this section. First, physical space viscous diffusion is important in the local cascade dynamics in both low and high $(|\delta \boldsymbol{u}|^2)^a$ regions at small scales. That is, $\Pi^a_{\overline{S}} \approx \mathcal{D}^a$ is significantly more accurate than the local version of the average balance (4.4) $\Pi^a_{\overline{S}} \approx \mathcal{D}^a_{r,\nu} - \epsilon^{*a}$ in such regions. Second, the probability of finding events $\Pi^a_{\overline{S}} \approx \mathcal{D}^a$ is not overwhelming. The PDFs of $\Pi^a_{\overline{S}} - \mathcal{D}^a$ contain significant deviations from zero across $(|\delta \boldsymbol{u}|^2)^a$ levels with wide tails, especially in low $(|\delta \boldsymbol{u}|^2)^a$ regions and to a lesser extent in high $(|\delta \boldsymbol{u}|^2)^a$ regions. We next address the significant deviations of $\Pi^a_{\overline{S}} - \mathcal{D}^a$ from zero by considering the fluctuating solenoidal cascade dynamics for various $(|\delta \boldsymbol{u}|^2)^a$ conditionings at small scales.

4.3 Small-scale Dynamics across Two-point Energy Levels

Given that $\Pi^a_{\overline{S}} - \mathcal{D}^a$ is not so often zero at the small scales, is there a typical $(|\delta \boldsymbol{u}|^2)^a$ transfer balance at small dissipative length scales? To answer this question we return to the solenoidal KHMH equation (4.5) and plot in figure 4.7(a, c, e) standard deviations of various terms in this equation conditioned on various ranges of $(|\delta \boldsymbol{u}|^2)^a$ values. We consider the same 20 ranges of $(|\delta \boldsymbol{u}|^2)^a$ values that we considered for figure 4.4 (see the first paragraph of section 4.2), and in the horizontal axes of the two plots in figure 4.7 we mark each one of these ranges by its average $(|\delta \boldsymbol{u}|^2)^a$ value normalised by $(\langle|\delta \boldsymbol{u}|^2\rangle^a$. Figure 4.7($a$) shows that the standard deviations of $\Pi^a_{\overline{S}}$ and $\mathcal{D}^a$ are quite close to each other for all $(|\delta \boldsymbol{u}|^2)^a$ levels but that the standard deviation of $\Pi^a_{\overline{S}}$ is nevertheless consistently higher than that of $\mathcal{D}^a$. The only other term in $\mathcal{A}^a_t + \mathcal{T}^a_{\overline{S}} = -(\Pi^a_{\overline{S}} - \mathcal{D}^a)$ is $\mathcal{A}^a_t + \mathcal{T}^a_{\overline{S}}$, and the fluctuations of $\mathcal{A}^a_t + \mathcal{T}^a_{\overline{S}}$ are never negligible. Consistent with the wide tails in the PDFs of $(\Pi^a_{\overline{S}} - \mathcal{D}^a)$ normalised by the standard deviations of $\Pi^a_{\overline{S}}$ in figure 4.5(a, c, e), we see that in low $(|\delta \boldsymbol{u}|^2)^a$ regions the standard deviations of Lagrangian transport $\mathcal{A}^a_t + \mathcal{T}^a_{\overline{S}}$ to the standard deviations of interscale transfer increases with decreasing r_d as the PDF tails become wider. Similarly, in high $(|\delta \boldsymbol{u}|^2)^a$ regions the standard deviations of Lagrangian transport to the standard deviations of interscale transfer decrease with increasing r_d as the PDF tails become tighter. Hence, the deviations from $\Pi^a_{\overline{S}} - \mathcal{D}^a \approx 0$ seem intimately linked to Lagrangian transport and except perhaps at specific spatio-temporal instances, it is not possible to neglect this term in the cascade dynamics at these dissipative scales.

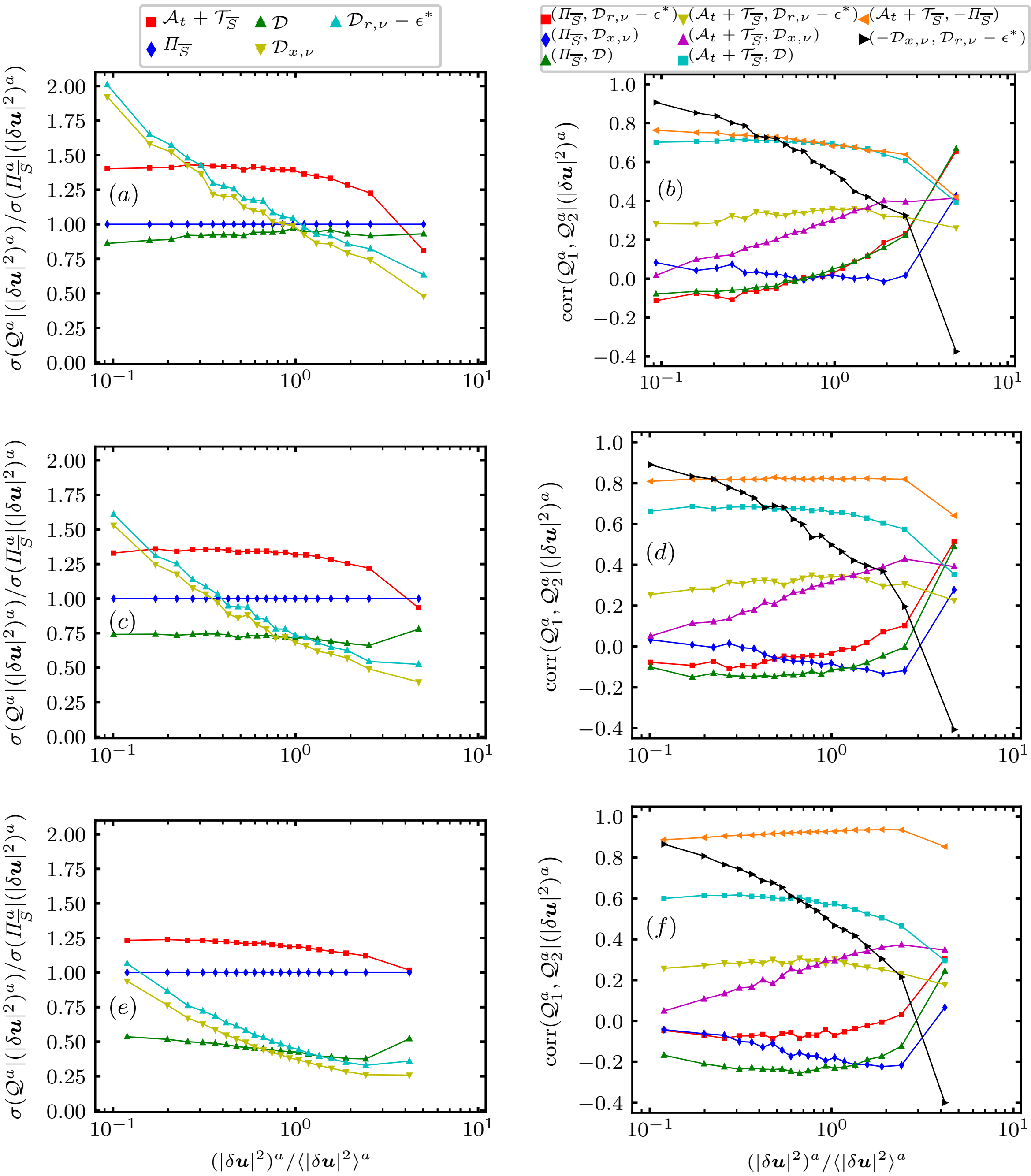

Figure 4.7: (a, c, e) Conditional standard deviations of various surface-averaged KHMH terms $\mathcal{Q}^a$ for $r_d = (\langle\eta\rangle_t, 0.24\langle\lambda\rangle_t, 0.48\langle\lambda\rangle_t)$ and (b, d, f) conditional Pearson correlation coefficients of pairs of surface-averaged KHMH terms $\mathcal{Q}_1^a$ and $\mathcal{Q}_2^a$ for $r_d = (\langle\eta\rangle_t, 0.24\langle\lambda\rangle_t, 0.48\langle\lambda\rangle_t)$. These standard deviations and correlation coefficients are calculated from spatio-temporal statistics conditioned on various ranges of $(|\delta \boldsymbol{u}|^2)^a$ at the r_d value of each corresponding plot. The conditioning is identical to that in figure 4.4: the horizontal axes display the average $(|\delta \boldsymbol{u}|^2)^a$ values within each $(|\delta \boldsymbol{u}|^2)^a$ range normalised by the spatio-temporally averaged $\langle|\delta \boldsymbol{u}|^2\rangle^a$. Increasing values of $(|\delta \boldsymbol{u}|^2)^a$ are therefore from left to right on the horizontal axes.

Figure 4.7(b, d, e) with correlation coefficients conditioned on $(|\delta \boldsymbol{u}|^2)^a$ provides further insights into the cascade dynamics. At the low to moderate $(|\delta \boldsymbol{u}|^2)^a$ levels at $r_d = \langle\eta\rangle_t$

there is a correlation of about 0.7 between $\mathcal{A}_t^a+\mathcal{T}_{\overline{S}}^a$ and $-\Pi_{\overline{S}}^a$ and also between $\mathcal{A}_t^a+\mathcal{T}_{\overline{S}}^a$ and $\mathcal{D}^a$. However, there is effectively no correlation at these $(|\delta \boldsymbol{u}|^2)^a$ levels between $\Pi_{\overline{S}}^a$ and any of the diffusion/dissipation terms $\mathcal{D}^a$, $\mathcal{D}_{x,\nu}^a$ and $\mathcal{D}_{r,\nu}^a-\epsilon^{*a}$. The significant correlations which exist between $\mathcal{A}_t^a+\mathcal{T}_{\overline{S}}^a$ and $-\Pi_{\overline{S}}^a$ on the one hand and between $\mathcal{A}_t^a+\mathcal{T}_{\overline{S}}^a$ and $\mathcal{D}^a$ on the other must therefore arise from different spatio-temporal instances given the absence of correlation between $\Pi_{\overline{S}}^a$ and $\mathcal{D}^a$. The picture suggested by $\mathcal{A}_t^a+\mathcal{T}_{\overline{S}}^a+\Pi_{\overline{S}}^a=\mathcal{D}^a$ and by these presences and absences of correlations conditioned on low to moderate $(|\delta \boldsymbol{u}|^2)^a$ levels is as follows: as $(|\delta \boldsymbol{u}|^2)^a$ at scale $r_d=\langle\eta\rangle_t$ is transported along a Lagrangian path, part of it may at one time be transferred to another scale and part of it may at another time be dissipated and diffused by viscosity, but very rarely will both significantly happen at the same time. There is indeed little spatio-temporal coincidence between interscale transfer rate and diffusion/dissipation at these $(|\delta \boldsymbol{u}|^2)^a$ levels. To complete the picture, viscous diffusion in space acts against viscous diffusion/dissipation $\mathcal{D}_{r,\nu}^a-\epsilon^{*a}$ at low to moderate $(|\delta \boldsymbol{u}|^2)^a$ levels: whilst $\mathcal{D}_{r,\nu}^a-\epsilon^{*a}$ most typically removes $(|\delta \boldsymbol{u}|^2)^a$, $\mathcal{D}_{x,\nu}^a$ counteracts by adding $(|\delta \boldsymbol{u}|^2)^a$ at that scale from neighbouring physical space. This picture is essentially true for all scales r_d between $\langle\eta\rangle_t$ and $0.5\langle\lambda\rangle_t$ (see figure 4.7(c,d,e,f)). With increasing r_d the standard deviations of $\mathcal{D}^a$, $\mathcal{D}_{x,\nu}^a$ and $\mathcal{D}_{r,\nu}^a-\epsilon^{*a}$ decrease relative to those of $\Pi_{\overline{S}}^a$ and $\mathcal{A}_t^a+\mathcal{T}_{\overline{S}}^a$. This leads to weaker correlations between $\mathcal{D}^a$ and $\Pi_{\overline{S}}^a$ and stronger correlations between $\mathcal{A}_t^a+\mathcal{T}_{\overline{S}}^a$ and $-\Pi_{\overline{S}}^a$, tending towards the KHMH dynamics in chapter 3.

This picture changes dramatically as we reach the 5% highest $(|\delta \boldsymbol{u}|^2)^a$ levels, i.e. levels between about 30 to 60 times $(\langle|\delta \boldsymbol{u}|^2\rangle^a$. Firstly, at such high $(|\delta \boldsymbol{u}|^2)^a$ levels, $\mathcal{D}_{r,\nu}^a-\epsilon^{*a}$ and $\mathcal{D}_{x,\nu}^a$ acquire some significant tendency to act together (correlation coefficient of about 0.4) to remove $(|\delta \boldsymbol{u}|^2)^a$ from scale $r_d=\langle\eta\rangle_t$. Secondly, the correlations of $\mathcal{A}_t^a+\mathcal{T}_{\overline{S}}^a$ with $-\Pi_{\overline{S}}^a$ and with $\mathcal{D}^a$ drop but remain significant (correlation coefficients of about 0.4) whilst $\Pi_{\overline{S}}^a$ acquires substantial correlation with the diffusion/dissipation terms: its correlation coefficients with $\mathcal{D}^a$ and with $\mathcal{D}_{r,\nu}^a-\epsilon^{*a}$ rise to about 0.7, and its correlation coefficient with $\mathcal{D}_{x,\nu}^a$ rises too but not so much (it reaches about 0.4). At these particularly high $(|\delta \boldsymbol{u}|^2)^a$ levels and very small scales $\langle\eta\rangle_t$, the strongest correlation is therefore the one between $\Pi_{\overline{S}}^a$ and $\mathcal{D}^a$ but it is not so strong that we may neglect the Lagrangian transport term $\mathcal{A}_t^a+\mathcal{T}_{\overline{S}}^a$, i.e. the remaining term in the full balance $\mathcal{A}_t^a+\mathcal{T}_{\overline{S}}^a+\Pi_{\overline{S}}^a=\mathcal{D}^a$, which is also significantly correlated with both $-\Pi_{\overline{S}}^a$ and $\mathcal{D}^a$. We chose to focus on the correlation between $\Pi_{\overline{S}}^a$ and $\mathcal{D}^a$ rather than between $\Pi_{\overline{S}}^a$ and $\mathcal{D}_{r,\nu}^a-\epsilon^{*a}$ even though they have the same correlation coefficients because we have seen that, unlike $\Pi_{\overline{S}}^a$ and $\mathcal{D}_{r,\nu}^a-\epsilon^{*a}$, $\Pi_{\overline{S}}^a$ and $\mathcal{D}^a$ have an increasing statistical tendency to get close to each other with increasing $(|\delta \boldsymbol{u}|^2)^a$ levels and decreasing length scale (see figure 4.4, table 4.1 and figure 4.7). However, this does not happen without some correlation with Lagrangian transport. As r_d increases, the standard deviations of viscous terms weaken relative to those of $\Pi_{\overline{S}}^a$ and $\mathcal{A}_t^a+\mathcal{T}_{\overline{S}}^a$ with the cascade dynamics tending towards the behaviour discussed in chapter 3. At $r_d=0.48\langle\lambda\rangle_t$, viscous terms correlate most strongly with interscale transfer at high rather than low $(|\delta \boldsymbol{u}|^2)^a$ levels.

4.4 Summary

In statistically stationary homogeneous/periodic turbulence the average relation $\langle \Pi^a_{\overline{S}} \rangle \approx \langle \mathcal{D}^a_{r,\nu} \rangle - \langle \epsilon^{*a} \rangle$ holds in the dissipation/diffusion-dominated range $r_d < 0.5\langle \lambda \rangle_t$, yet it does not represent reality locally. Events where $\Pi^a_{\overline{S}} \approx \mathcal{D}^a_{r,\nu} - \epsilon^{*a}$ can of course be found but they are few. What happens at these small scales cannot be described without Lagrangian transport $\mathcal{A}^a_t + \mathcal{T}^a_{\overline{S}}$ and physical space viscous diffusion $\mathcal{D}^a_{x,\nu}$.

In most of the flow for most of the time the levels of $(|\delta \boldsymbol{u}|^2)^a$ at these length scales are low to moderate and one finds significant correlations between $\mathcal{A}^a_t + \mathcal{T}^a_{\overline{S}}$ and $\Pi^a_{\overline{S}}$ on the one hand and between $\mathcal{A}^a_t + \mathcal{T}^a_{\overline{S}}$ and $\mathcal{D}^a = \mathcal{D}^a_{r,\nu} + \mathcal{D}^a_{x,\nu} - \epsilon^{*a}$ on the other. There are some spatio-temporal instances interscale transfer balance with Lagrangian transport and some other spatio-temporal instances viscous effects balance with Lagrangian transport, but rarely do viscous effects balance with interscale transfer. Also, viscous diffusion in space is typically positive and counteracts the $(|\delta \boldsymbol{u}|^2)^a$ -reducing action of $\mathcal{D}^a_{r,\nu} - \epsilon^{*a}$ which is typically negative.

As we focus on the highest levels of $(|\delta \boldsymbol{u}|^2)^a$ at these length scales the picture changes quite drastically but $\mathcal{A}^a_t + \mathcal{T}^a_{\overline{S}}$ maintains a presence even if weakened. The highest correlation is now between $\Pi^a_{\overline{S}}$ and $\mathcal{D}^a$. Even though this correlation is similar to that of $\Pi^a_{\overline{S}}$ and $\mathcal{D}^a_{r,\nu} - \epsilon^{*a}$, we have seen that there is much more of a tendency for $\Pi^a_{\overline{S}}$ and $\mathcal{D}^a$ to get close to each other than $\Pi^a_{\overline{S}}$ and $\mathcal{D}^a_{r,\nu} - \epsilon^{*a}$ as physical space viscous diffusion is non-negligible. In these regions the viscous diffusion in physical space acquires a tendency to cooperate/correlate with $\mathcal{D}^a_{r,\nu} - \epsilon^{*a}$ and enhance $(|\delta \boldsymbol{u}|^2)^a$ reduction. The balancing between $\Pi^a_{\overline{S}}$ and $\mathcal{D}^a$ does not happen perfectly though given that $\mathcal{A}^a_t + \mathcal{T}^a_{\overline{S}}$ retains some correlation with both $-\Pi^a_{\overline{S}}$ and $\mathcal{D}^a$, which means that all terms in $\mathcal{A}^a_t + \mathcal{T}^a_{\overline{S}} + \Pi^a_{\overline{S}} = \mathcal{D}^a$ can momentarily follow each other simultaneously at these high $(|\delta \boldsymbol{u}|^2)^a$ levels.

The cascade dynamics presented in this chapter, and the presence of Lagrangian transport and physical space viscous diffusion in particular, suggests limited validity of the assumption of a local balance between interscale transfer and viscous diffusion in scale space/dissipation (Frisch and Vergassola, 1991) at any $(|\delta \boldsymbol{u}|^2)^a$ level. At low and moderate $(|\delta \boldsymbol{u}|^2)^a$ levels, Lagrangian transport is very important in the cascade dynamics with a limited tendency of spatio-temporal coincidence of $\Pi^a_{\overline{S}}$ and $\mathcal{D}^a_{r,\nu} - \epsilon^{*a}$. The results at our higher $(|\delta \boldsymbol{u}|^2)^a$ levels show that physical space viscous diffusion is important in such regions. Moreover, the results suggest that $\mathcal{D}^a_{x,\nu}$ becomes increasingly important in the local small-scale cascade dynamics as one focuses on even higher $(|\delta \boldsymbol{u}|^2)^a$ levels than considered in this chapter.

5. Spatially Averaged Unsteady Energy Exchanges

The local cascade dynamics of chapters 3-4 fluctuates violently in space and time with strong departures from its average/equilibrium behaviour. The spatially averaged manifestation of the local cascade dynamics is highly unsteady at scales similar to the integral length scale and there is a time delay between large-scale turbulent kinetic energy or interscale transfer and small-scale dissipation (see section 1.2 and references therein). This large-to-small-scale time delay behaviour, which is consistent with a step-by-step energy cascade, is not restricted to homogeneous/periodic turbulence with similar behaviour also observed in e.g. homogeneous/periodic shear flow (Horiuti and Ozawa, 2011) and von Kárman flow (Pinton et al., 1999).

Starting with Yoshizawa (1994), several authors have considered corrections to the K41 inertial range behaviour at larger scales in homogeneous/periodic turbulence due to unsteadiness effects. Yoshizawa and others (see e.g. Woodruff and Rubinstein (2006)) have included unsteadiness effects (in Fourier space) by assuming small/slow perturbation(s) to the K41 equilibrium solution. This approach has been used to arrive at energy spectrum corrections with wavenumber dependence $k^{-7/3}$, new large-eddy simulation models (Horiuti and Tamaki, 2013) and turbulence dissipation scalings (Bos and Rubinstein, 2017). These predictions have been partly verified (see Horiuti and Tamaki (2013); Khurshid et al. (2021)). However, the physical basis and subsequent applicability/limitations of this perturbation approach remains unclear. That is, can the cascade dynamics at these larger scales simply be characterised as the K41 equilibrium solution and small/slow corrections or is the cascade dynamics at these scales fundamentally different from K41 behaviour?

This chapter considers the larger-scale unsteady cascade dynamics as generally being very different from K41 equilibrium behaviour. We characterise the cascade dynamics by formalising the well-known notion of a finite cascade time-lag (see e.g. (Lumley, 1992; Wan et al., 2010) in terms of a (physical space) hypothesis connecting the spatially averaged interscale transfer rate and the spatially averaged viscous dissipation rate, where the former increasingly precedes the latter with increasing scale separation (this hypothesis can be viewed as a generalisation of the earlier time-lag hypothesis of Bos et al. (2007)). From this physical basis, which accounts for generally non-negligible cascade unsteadiness, we develop and confirm with our DNSs that it is only under certain rather restrictive conditions the formalised time-lag hypothesis allow for a perturbation expansion around the K41 equilibrium solution. This limitation in scope of the non-equilibrium perturbation expansions is required to improve their accuracy. Moreover, by developing the physical basis of such a perturbation approach, it is argued that it can be more easily generalised to naturally occurring turbulent flows.

The next section considers the spatially averaged cascade dynamics in periodic/homogeneous turbulence. Our DNSs confirm the significant cascade unsteadiness in terms of physical space quantities. In section 5.2 we connect this cascade behaviour and earlier cascade time-lag ideas in terms of a (physical space) formalised time-lag hypothesis. We examine this hypothesis with our low to moderate Reynolds number DNSs before demonstrating in section 5.3 that this hypothesis can be used to decompose the low-frequency cascade dynamics and second-order structure function scaling into equilibrium and non-equilibrium contributions. Section 5.4 uses the phenomenology of a time-lagged energy cascade to motivate a new dissipation scaling law which is approximately identical to the non-equilibrium dissipation scaling (Goto and Vassilicos, 2015) for our DNSs of forced homogeneous/periodic turbulence. We provide a chapter summary in section 5.5.

5.1 Spatially Averaged KHMH Dynamics in Homogeneous Turbulence

We study the spatially averaged cascade dynamics in terms of the spatially averaged KHMH equation. This equation governs the evolution of $\langle|\delta\boldsymbol{u}|^2\rangle_{\boldsymbol{x}}(\boldsymbol{r},t)$ across scales $\boldsymbol{r}$ and time t and reads in homogeneous/periodic turbulence

$$\frac{\partial}{\partial t}\langle|\delta\boldsymbol{u}|^2\rangle_{\boldsymbol{x}} + \langle\delta u_k\frac{\partial|\delta\boldsymbol{u}|^2}{\partial r_k}\rangle_{\boldsymbol{x}} = 2\nu\frac{\partial^2}{\partial r_k^2}\langle|\delta\boldsymbol{u}|^2\rangle_{\boldsymbol{x}} - 2\nu\Big\langle\Big(\frac{\partial u_i^+}{\partial x_k^+}\Big)^2 + \Big(\frac{\partial u_i^-}{\partial x_k^-}\Big)^2\Big\rangle_{\boldsymbol{x}} + \langle 2\delta u_i\delta f_i\rangle_{\boldsymbol{x}} \tag{5.1}$$

or in terms of the notation introduced in equation (3.20) in chapter 3

$$\langle\mathcal{A}_t\rangle_{\boldsymbol{x}} + \langle\varPi\rangle_{\boldsymbol{x}} = \langle\mathcal{D}_{r,\nu}\rangle_{\boldsymbol{x}} - \langle\epsilon^*\rangle_{\boldsymbol{x}} + \langle\mathcal{I}\rangle_{\boldsymbol{x}}. \tag{5.2}$$

We have that $\langle\varPi_{\overline{S}}\rangle_{\boldsymbol{x}} = \langle\varPi\rangle_{\boldsymbol{x}}$ and $\langle\mathcal{T}_p\rangle_{\boldsymbol{x}} = \langle\mathcal{T}\rangle_{\boldsymbol{x}} = \langle\mathcal{D}_{x,\nu}\rangle_{\boldsymbol{x}} = 0$ from periodicity (see the non-averaged KHMH equation (3.21)) and note that the dissipation $\langle\epsilon^*\rangle_{\boldsymbol{x}} = 2\langle\epsilon^+\rangle_{\boldsymbol{x}}(t) + 2\langle\epsilon^-\rangle_{\boldsymbol{x}}(t) = 4\langle\epsilon\rangle_{\boldsymbol{x}}(t)$ does not depend on $\boldsymbol{r}$ (where $\epsilon = \nu(\partial u_i/\partial x_j)^2$).

We first consider the average cascade behaviour of forced and freely decaying homogeneous/periodic turbulence (treating these two cases together is useful in highlighting their similar cascade dynamics). We apply a time average to (5.2) in the case of forced homogeneous/periodic turbulence and an ensemble average to (5.2) in the case of freely decaying homogeneous/periodic turbulence. This operator is denoted $\langle\rangle_{t/E}$ and when applied to (5.2) it yields the equation

$$\langle \mathcal{A}_t \rangle_{\boldsymbol{x},t/E} + \langle \varPi \rangle_{\boldsymbol{x},t/E} = \langle \mathcal{D}_{r,\nu} \rangle_{\boldsymbol{x},t/E} - \langle \epsilon^* \rangle_{\boldsymbol{x},t/E} + \langle \mathcal{I} \rangle_{\boldsymbol{x},t/E}, \tag{5.3}$$

where $\langle \mathcal{A}_t \rangle_{\boldsymbol{x},t/E} = 0$ in forced homogeneous turbulence and $\mathcal{I} = 0$ in freely decaying homogeneous turbulence. If the forcing is not applied or only applied at the largest scales of the flow, and noting that $\langle \mathcal{D}_{r,\nu} \rangle_{\boldsymbol{x}} \ll \langle \epsilon^* \rangle_{\boldsymbol{x}}$ for $r_d > \lambda$ (see the kinematic upper bound in appendix B of Valente and Vassilicos (2015)), (5.3) reduces to

$$\langle \mathcal{A}_t \rangle_{\boldsymbol{x},t/E} + \langle \varPi \rangle_{\boldsymbol{x},t/E} \approx -\langle \epsilon^* \rangle_{\boldsymbol{x},t/E} \tag{5.4}$$

at scales $\lambda < r_d < L$. Hence, in an intermediate range of scales in forced and freely decaying homogeneous/periodic turbulence the KHMH spatio-temporal/ensemble average (5.3) reduces to approximately (5.4) which contains effects of unsteadiness, interscale transfer and dissipation and the interscale energy transfer is on average from larger to smaller scales $\langle \varPi \rangle_{\boldsymbol{x},t/E} < 0$ (Goto and Vassilicos, 2016b; Yasuda and Vassilicos, 2018).

The spatio-temporal/ensemble averaged cascade picture (5.3)-(5.4) only partially describes the spatially averaged energy cascade. Subtracting equation (5.3) from equation (5.2), yields the KHMH equation for temporal fluctuations around the space- and time/ensemble-averaged cascade behaviour

$$\mathcal{A}_t'' + \varPi'' = \mathcal{D}_{r,\nu}'' - \epsilon^{*''} + \mathcal{I}'', \tag{5.5}$$

where we used the generic notation $\mathcal{Q}'' \equiv \langle \mathcal{Q} \rangle_{\boldsymbol{x}} - \langle \mathcal{Q} \rangle_{\boldsymbol{x},t/E}$ for KHMH terms $\mathcal{Q}$. One might imagine that $\mathcal{D}_{r,\nu}''$ and $\mathcal{I}''$ can be neglected at scales $\lambda < r_d < L$ with

$$\mathcal{A}_t'' + \varPi'' \approx -\epsilon^{*''}. \tag{5.6}$$

In the case of both (5.4) and (5.6) being valid, the spatially averaged KHMH equation (5.2) in both forced and freely decaying homogeneous/periodic turbulence reduces at such scales to

$$\langle \mathcal{A}_t \rangle_{\boldsymbol{x}} + \langle \varPi \rangle_{\boldsymbol{x}} \approx -\langle \epsilon^* \rangle_{\boldsymbol{x}}, \tag{5.7}$$

where unsteadiness $\langle \mathcal{A}_t \rangle_{\boldsymbol{x}}$, interscale transfer $\langle \varPi \rangle_{\boldsymbol{x}}$ and the viscous dissipation $\langle \epsilon^* \rangle_{\boldsymbol{x}}$ are the cascade processes determining the spatially averaged energy cascade at such scales. Equation (5.7) is necessarily more general than K41 local equilibrium $\langle \varPi \rangle_{\boldsymbol{x}} \approx -\langle \epsilon^* \rangle_{\boldsymbol{x}}$.

The characterisation (5.7) of the spatially averaged cascade dynamics requires the spatial averaging scale L_a to be not much smaller or much bigger than the integral length scale L. In the case of forced homogeneous/periodic turbulence with typically $L_a/L \approx 5$ and $L_a = 2\pi$ (see section 2.2.1), the temporal fluctuations $\varPi''$ are small but non-negligible compared to its spatio-temporal/ensemble average value $\langle \varPi \rangle_{\boldsymbol{x},t/E}$ (Goto and Vassilicos, 2015). Hence, $\langle \varPi \rangle_{\boldsymbol{x}}$ is almost always negative across scales and $\langle \varPi \rangle_{\boldsymbol{x}} \not\approx \langle \varPi \rangle_{\boldsymbol{x},t/E}$. This

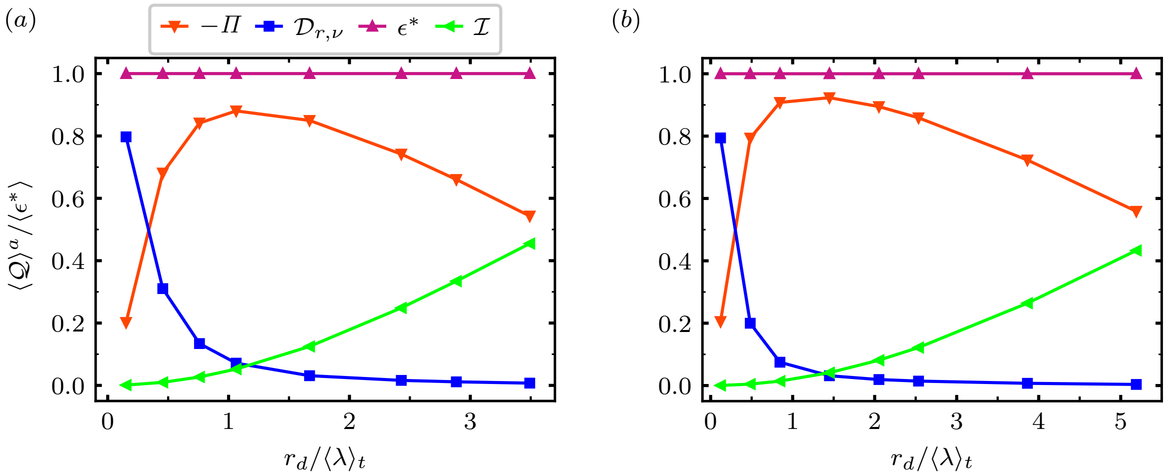

Figure 5.1: KHMH spatio-temporal averages. (a) $\langle Re_\lambda\rangle_t = 112$, (b) $\langle Re_\lambda\rangle_t = 174$.

contrasts on one end with an infinite averaging dimension $L_a/L \to \infty$, where the spatial averages converge to their spatio-temporal/ensemble averages (under periodic boundary conditions) with all unsteadiness effects concealed $\langle\varPi\rangle_{\boldsymbol{x}} = \langle\varPi\rangle_{\boldsymbol{x},t/E}$. On the other end, with the averaging dimension going to zero $L_a/L \to 0$ one obtains the original, non-averaged KHMH equation with the multitude of additional physical processes we considered in chapters 3-4 and a significant proportion of inverse cascade events ($\langle\varPi\rangle_{\boldsymbol{x}} > 0$) (Yasuda and Vassilicos, 2018). By considering the case of $5 \lesssim L_a/L \ll \infty$, we focus on an unsteady direct energy cascade ($\langle\varPi\rangle_{\boldsymbol{x}} < 0$) with periodic boundary conditions (these boundary conditions might limit the relevance of this chapter to naturally occurring turbulent flows where the spatially averaged fluid of size L_a^3 interacts with its surrounding fluid in a typically non-periodic manner).

Having broadly considered the spatially averaged KHMH dynamics in forced/freely decaying homogeneous/periodic turbulence, we analyse the spatially averaged KHMH dynamics in our DNSs of forced homogeneous/periodic turbulence with the efficient and accurate evaluation methods developed in appendix C. The majority of these results (and the results in the following sections) will be from the datasets DNS3-DNS4 with the negative damping forcing, but we will also report some key results with the dataset DNS2 with the ABC forcing. Unless otherwise stated, the results in DNS2 and DNS3 are qualitatively equal. Figure 5.1 shows the spatio-temporally and surface-averaged KHMH terms in datasets DNS3-DNS4, which satisfy $\langle\varPi^a\rangle = \langle\mathcal{D}^a_{r,\nu}\rangle - \langle\epsilon^*\rangle + \langle\mathcal{I}^a\rangle$ (where $\langle\rangle$ denotes a space-time average). The direct influence of the large-scale injection $\langle\mathcal{I}^a\rangle$ diminishes as r_d decreases below the integral length and approaches the Taylor scale, while the direct influence of scale space viscous diffusion $\langle\mathcal{D}^a_{r,\nu}\rangle$ is significant at scales similar and smaller than the Taylor scale.

These KHMH space-time-average values conceal temporal fluctuations which we characterise in terms of KHMH temporal standard deviations $\sqrt{\langle\mathcal{Q}''^2\rangle^a}$ in figure 5.2. The order of the largest of these temporal standard deviations is $0.1\langle\epsilon^*\rangle$ and belongs to $\langle\mathcal{A}_t\rangle_{\boldsymbol{x}}$, $\langle\varPi\rangle_{\boldsymbol{x}}$

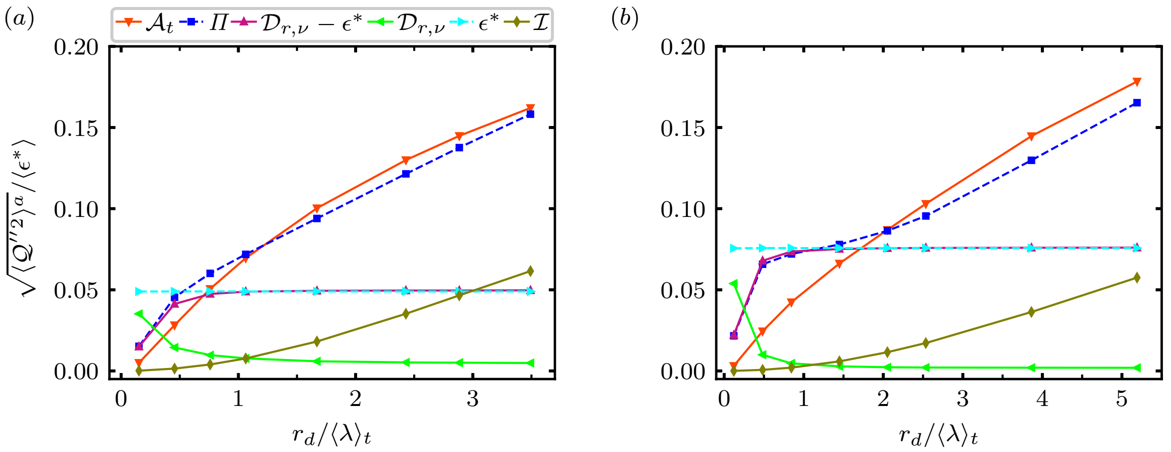

Figure 5.2: KHMH temporal standard deviations. (*a*) $\langle Re_\lambda\rangle_t = 112$, (*b*) $\langle Re_\lambda\rangle_t = 174$.

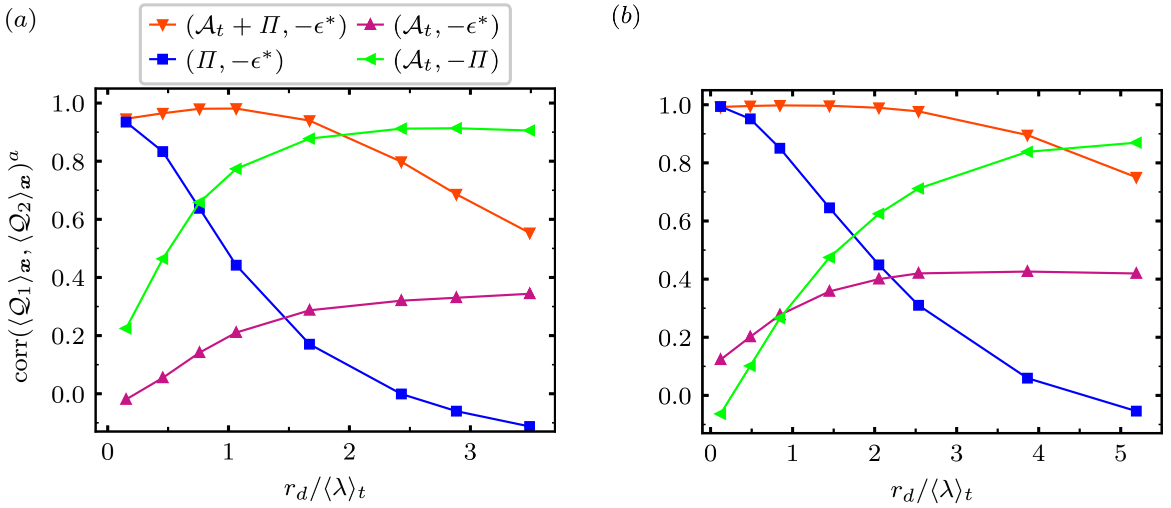

Figure 5.3: KHMH correlation coefficients. (*a*) $\langle Re_\lambda\rangle_t = 112$, (*b*) $\langle Re_\lambda\rangle_t = 174$.

and $\langle\epsilon^*\rangle_{\boldsymbol{x}}$. The injection temporal fluctuations $\mathcal{I}^{"}$ are only non-negligible compared to these three terms at scales r_d close to $\langle L\rangle_t$, while the viscous diffusion in scale space is non-negligible in terms of temporal fluctuations for scales $r_d < \langle\lambda\rangle_t$. We checked that the interscale transfer $\langle\varPi^a\rangle_{\boldsymbol{x}}(r_d,t)$ is always from larger to smaller scales at all times across scales and Reynolds number in our DNSs, i.e. $\langle\varPi^a\rangle_{\boldsymbol{x}}(r_d,t) < 0$ for all samples.

The KHMH temporal standard deviations translate into strong correlation coefficients between $\langle\mathcal{A}_t\rangle_{\boldsymbol{x}} + \langle\varPi\rangle_{\boldsymbol{x}}$ and $-\langle\epsilon^*\rangle_{\boldsymbol{x}}$ (see figure 5.3). These correlations peak at 0.981 and 0.997 at the lower and higher Reynolds number at the Taylor scale. They decrease slightly as r_d decreases below the Taylor scale due to scale space viscous diffusion and decrease more significantly as r_d increases towards the integral scale due to the effect of injection. These results, consistent with figure 5.2, suggest that both $\langle\mathcal{D}_{r.\nu}\rangle_{\boldsymbol{x}}^{"}$ and $\langle\mathcal{I}\rangle_{\boldsymbol{x}}^{"}$ have relatively limited influence in the temporally fluctuating cascade dynamics except at the very smallest and the very largest scales of the flow. This contrasts with the significance of these two processes in the space-time-average dynamics, where their direct influence

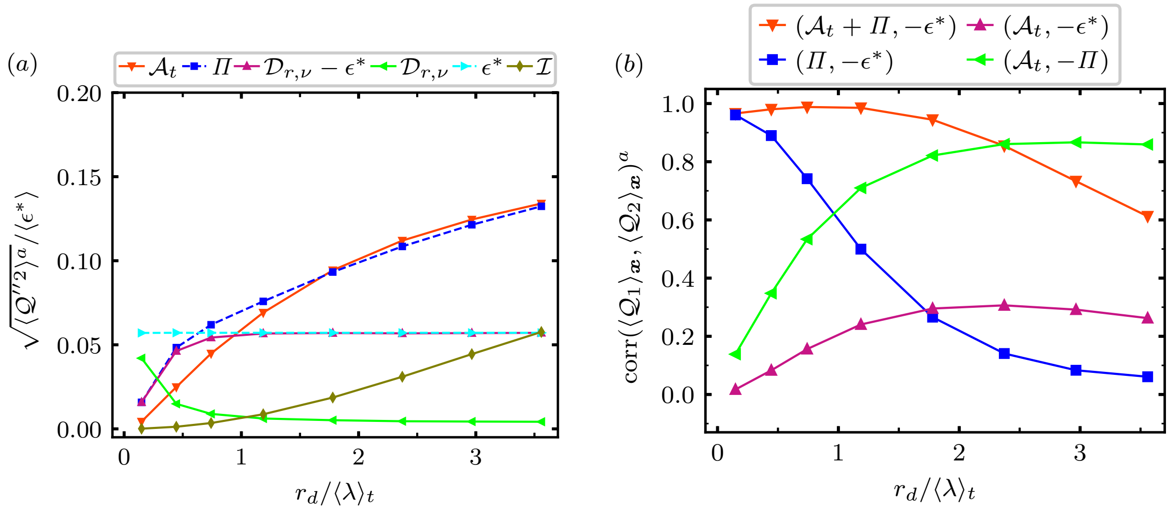

Figure 5.4: DNS2 KHMH (*a*) standard deviations and (*b*) correlation coefficients.

seems to be wider in scale (i.e. compare figure 5.1 with figures 5.2-5.3) (our results in the next section support this view on the temporally fluctuating cascade dynamics). It seems that the cascade dynamics can be viewed in terms of the sum of a background almost stationary cascade where both $\langle \mathcal{D}_{r.\nu}\rangle_{\boldsymbol{x}}$ and $\langle \mathcal{I}\rangle_{\boldsymbol{x}}$ are important and a temporally varying cascade where these two terms are less important. That is, equation (5.6) concerning the cascade temporal fluctuations seems satisfied in our DNSs at some intermediate scales and not the stronger equation (5.7) concerning both the cascade average and fluctuating behaviour. With regards to equation (5.6) and the temporally fluctuating cascade dynamics, it is worth mentioning the much higher correlation coefficients between $\langle \mathcal{A}_t\rangle_{\boldsymbol{x}} + \langle \varPi\rangle_{\boldsymbol{x}}$ and $-\langle \epsilon^*\rangle_{\boldsymbol{x}}$ than between $\langle \varPi\rangle_{\boldsymbol{x}}$ and $-\langle \epsilon^*\rangle_{\boldsymbol{x}}$, except at the very smallest scales. Neither $\langle \varPi\rangle_{\boldsymbol{x}}$ nor $\langle \mathcal{A}_t\rangle_{\boldsymbol{x}}$ correlates strongly with $-\langle \epsilon^*\rangle_{\boldsymbol{x}}$ at scales above the Taylor scale as there is a significant cancellation tendency between $\langle \varPi\rangle_{\boldsymbol{x}}$ and $\langle \mathcal{A}_t\rangle_{\boldsymbol{x}}$ (this might be interpreted in terms of advection in scale space/cascading from larger to smaller scales).

The KHMH temporal standard deviations and correlation coefficients with the ABC forcing (DNS2) (see figure 5.4) are very similar to those with the negative damping forcing (DNS3). This suggests that the temporally fluctuating cascade dynamics is relatively insensitive to the large-scale forcing. The KHMH spatio-temporal averages are also very similar (not shown).

It is important to note that the considerations in this section are not restricted to low Reynolds numbers. With increasing Reynolds number/range of scales one can expect an intermediate range of scales which might approximately be in K41 equilibrium, but one would still have larger scales similar to the integral length scale where unsteadiness is important in the cascade dynamics (Goto and Vassilicos, 2016b). Having validated our DNSs and KHMH physical space approach, we next delve further into the cascade dynamics by proposing and examining with our DNSs a formalised time-lag hypothesis partially motivated by the above spatially averaged cascade dynamics.

5.2 A Formalised Time-lag Hypothesis for Homogeneous Turbulence

A common concept to study the turbulent energy cascade is a time characterising the finite time larger-scale energy uses to cascade to dissipative scales. Typically, this time-lag is discussed informally (Lumley, 1992; Goto and Vassilicos, 2016a) or it is determined as the time-lag which optimises a (often high) correlation coefficient between a large- and a small-scale quantity (Wan et al., 2010; Cardesa et al., 2015; Ballouz et al., 2020; Vela-Martín, 2022b). With the notable exception of Bos et al. (2007), it is rarely used to predict the turbulence cascade dynamics. Bos et al. (2007) assumes in freely decaying homogeneous turbulence a time-lag between the large-scale spatio-ensemble averaged interscale transfer rate $\langle \mathit{\Pi} \rangle^{a}_{\boldsymbol{x},E}$ and the spatio-ensemble averaged dissipation rate $\langle \epsilon^{*} \rangle_{\boldsymbol{x},E}$ and uses this as a starting point to predict the dissipation coefficient in freely decaying homogeneous turbulence. This example shows how a formalisation of the popular time-lag idea can lead to non-trivial results. We next argue that the time-lag hypothesis of Bos et al. (2007) can be generalised to a wider range of scales in both forced and freely decaying homogeneous/periodic turbulence in an instantaneous spatially averaged sense.

The previous section corroborated that in homogeneous/periodic turbulence with $5 \lesssim L_a/L \ll \infty$ in a wide range of scales at low to moderate Re_λ:

i. $\langle \mathit{\Pi} \rangle^{a}_{\boldsymbol{x}} < 0$ almost always in time;

ii. $\mathcal{A}_t'' + \mathit{\Pi}'' \approx -\epsilon^{*''}$ almost always in time,

where condition (ii) is not applicable at the largest and smallest scales of the flow. This behaviour (i)-(ii) can be connected to time-lagged cascades by the argument of Lumley (1992). If the dissipation fluctuations in (ii) only directly affect scales $r_d < \lambda$, energy fluctuations at scales $\lambda < r_d < L$ are not directly affected by production, dissipation or diffusion. Hence, one might expect from (ii) that an energy fluctuation at scales $\lambda < r_d < L$ is conserved and simply cascaded from larger to smaller scales (i) in a finite time. Similarly, an interscale transfer fluctuation at such scales could be expected to cause a temporal fluctuation in the future dissipation rate. Such cascade behaviour is consistent with the relatively limited correlations between the interscale transfer and dissipation at scales $\langle \lambda \rangle_t < r_d < \langle L \rangle_t$ in figure 5.3 and the limited local importance of ϵ^{*} in the cascade dynamics at such scales (see chapter 3). That is, the above *fluctuating* cascade picture can be characterised as *unsteady*, *unidirectional* (from larger to smaller scales) and *inertial*, i.e. energy fluctuations are not directly affected by production, dissipation or diffusion.

Before formalising the above cascade picture, we highlight one additional topic pertinent to the time-lagged cascade dynamics. Figure 5.5 displays time series from our DNSs of the KHMH terms in condition (ii). Firstly, there is a time-lag between $\mathit{\Pi}''$ and $\epsilon^{*''}$ which tends to decrease with r_d (we quantify this time-lag below). Secondly, as discussed and demonstrated in the study of spectral energy transfers in Khurshid et al. (2021), it is

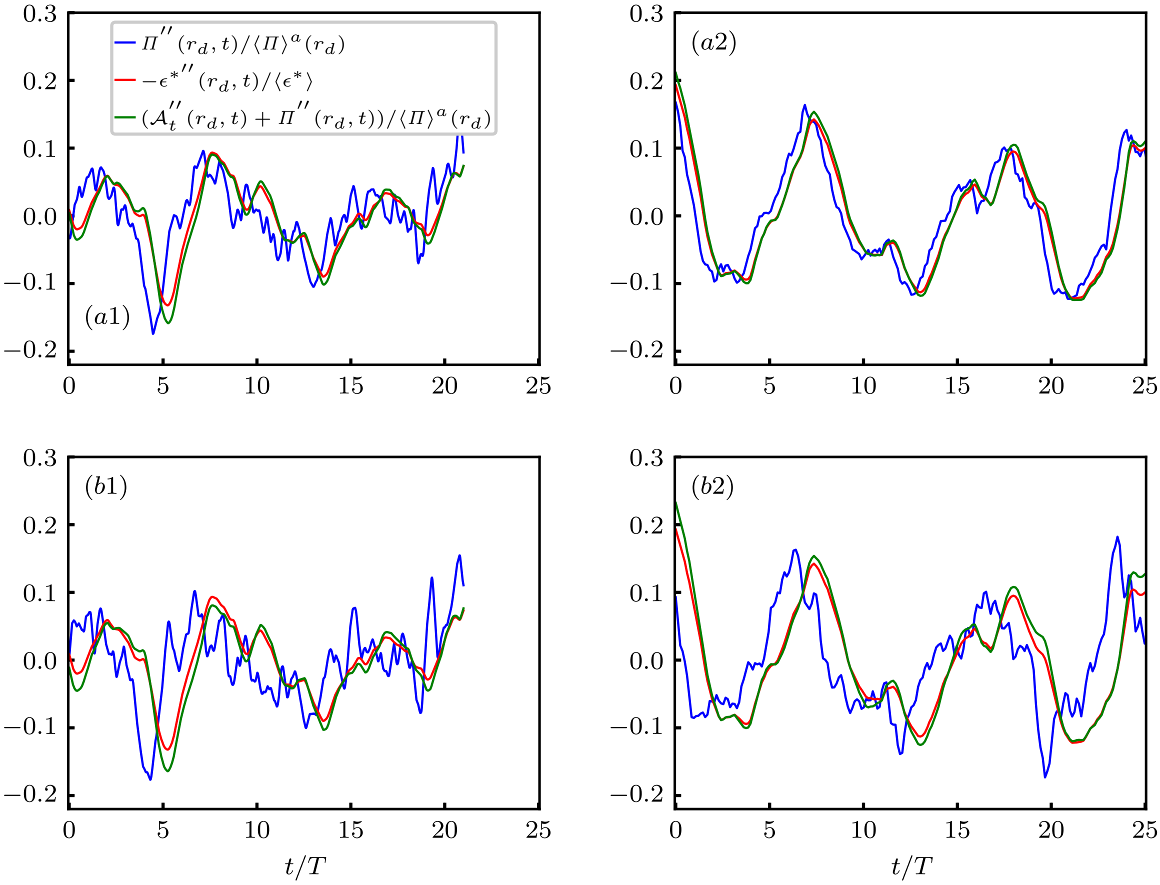

Figure 5.5: Time series of $\mathit{\Pi}''(r_d,t)$, $\epsilon^{*''}(t)$ and $(\mathcal{A}_t''(r_d,t)+\mathit{\Pi}''(r_d,t))$. $(a1,a2)$ $r_d=\langle\lambda\rangle_t$, $(b1,b2)$ $r_d=\langle L\rangle_t/2$. $(a1,b1)$ $\langle Re_\lambda\rangle_t=112$, $(a2,b2)$ $\langle Re_\lambda\rangle_t=174$.

only the *slow/low-frequency* part of the interscale transfer that is cascaded to the dissipative scales (Goto et al. (2017) discusses the slow/quasiperiodic turbulence evolution in forced homogeneous/periodic turbulence at length). The fast/high-frequency interscale transfers might not be transmitted through the scales as they are too fast to markedly affect $\langle|\delta\boldsymbol{u}|^2\rangle^a_{\boldsymbol{x}}$ (Khurshid et al., 2021) (there is a differential relation between interscale transfer and $\langle|\delta\boldsymbol{u}|^2\rangle^a_{\boldsymbol{x}}$ (5.1) such that both a significant interscale transfer amplitude and duration is required to significantly affect $\langle|\delta\boldsymbol{u}|^2\rangle^a_{\boldsymbol{x}}$). The high-frequency interscale transfers seem to decrease in amplitude at smaller r_d with a closer resemblance between $\mathit{\Pi}''$ and subsequent $\epsilon^{*''}$. This behaviour is consistent with the ratio L_a/r_d increasing as r_d decreases such that intermittent high-frequency interscale transfers are increasingly averaged out, leaving only the slow/quasiperiodic turbulence evolution affecting $\mathit{\Pi}''$. It follows that one should expect a causal relation between the present interscale transfer and the future dissipation to be more accurate at the lower rather than the higher end of $\lambda < r_d < L$.

Given the above deliberations, we propose the following formalisation of the unsteady cascade behaviour in homogeneous/periodic turbulence denoted the "formalised time-lag hypothesis":

$$\langle\mathit{\Pi}\rangle^a_{\boldsymbol{x}}(r_d,t) \approx -C_{\mathit{\Pi}}\langle\epsilon^*\rangle_{\boldsymbol{x}}(t+\tau), \tag{5.8}$$

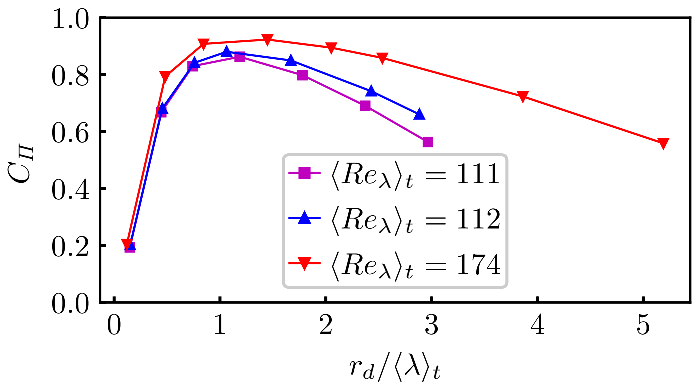

Figure 5.6: Formalised time-lag prefactor $C_\Pi = 1 - (\langle \mathcal{I}^a\rangle_{\boldsymbol{x},t} + \langle \mathcal{D}^a_{r,\nu}\rangle_{\boldsymbol{x},t})/\langle \epsilon^*\rangle_{\boldsymbol{x},t}$.

where $\tau > 0$ is the (single) time delay between subsequent variations in interscale transfer and dissipation, which is monotonically increasing with r_d. The prefactor C_Π is required to ensure consistency with the time/ensemble-averaged KHMH equation (5.3) and reads

$$C_\Pi = 1 - \frac{\langle \mathcal{I}^a\rangle_{\boldsymbol{x},t/E} + \langle \mathcal{D}^a_{r,\nu}\rangle_{\boldsymbol{x},t/E}}{\langle \epsilon^*\rangle_{\boldsymbol{x},t/E}}. \tag{5.9}$$

We use the remainder of this section to test the formalised time-lag hypothesis. We start by showing consistency between (5.8) and the average KHMH behaviour (5.3). In forced homogeneous turbulence, by virtue of the spatio-temporally averaged KHMH equation, the prefactor can be re-written $C_\Pi(r_d) = \langle \Pi\rangle^a_{\boldsymbol{x},t}(r_d)/\langle \epsilon^*\rangle_{\boldsymbol{x},t}$. If we insert this expression for $C_\Pi(r_d)$ into (5.8) and apply a time average, we obtain

$$\langle \Pi\rangle^a_{\boldsymbol{x},t}(r_d) \approx -C_\Pi(r_d)\langle\langle \epsilon^*\rangle_{\boldsymbol{x}}(t+\tau)\rangle_t = \langle \Pi\rangle^a_{\boldsymbol{x},t}(r_d) \tag{5.10}$$

under the condition that $\langle\langle \epsilon^*\rangle_{\boldsymbol{x}}(t+\tau)\rangle_t = \langle \epsilon^*\rangle_{\boldsymbol{x},t}$. This condition concerns the delay τ and is satisfied by e.g. a delay which only depends on r_d (see $\overline{\tau}$ below). The $C_\Pi(r_d)$-values in our DNSs are displayed in figure 5.6. One can imagine that $C_\Pi(r_d)$ tends to unity at the lower end of $\langle\lambda\rangle_t < r_d < \langle L\rangle_t$ as the Reynolds number increases with limited injection and viscous diffusion in scale space.

In freely decaying homogeneous turbulence, the spatio-ensemble averaged KHMH equation at scales $r_d > \lambda$ reads $\langle \mathcal{A}_t\rangle^a_{\boldsymbol{x},E} \approx -\langle \Pi\rangle^a_{\boldsymbol{x},E} - \langle \epsilon^*\rangle_{\boldsymbol{x},E}$ with $\langle \mathcal{A}_t\rangle^a_{\boldsymbol{x},E} < 0$ (see Goto and Vassilicos (2016b)). This behaviour is consistent with the ensemble-averaged (5.8) ($C_\Pi \approx 1$ with $\mathcal{I} = 0$ and $\langle \mathcal{D}^a_{r,\nu}\rangle_{\boldsymbol{x},E} \approx 0$)

$$-\langle \Pi\rangle^a_{\boldsymbol{x},E}(r_d,t) \approx \langle \epsilon^*\rangle_{\boldsymbol{x},E}(t+\tau) \tag{5.11}$$

as long as $-\langle \Pi\rangle^a_{\boldsymbol{x},E}(r_d,t)$ and $\langle \epsilon^*\rangle_{\boldsymbol{x},E}(t)$ are decaying in tandem with a delay such that the viscous dissipation is always corresponding to the more negative interscale transfer rate of the past. This corresponds to a decreasing $-\langle \Pi\rangle^a_{\boldsymbol{x},E}(r_d,t)/\langle \epsilon^*\rangle_{\boldsymbol{x},E}(t)$ ratio with increasing r_d, in agreement with the results and argument in Goto and Vassilicos (2016b).

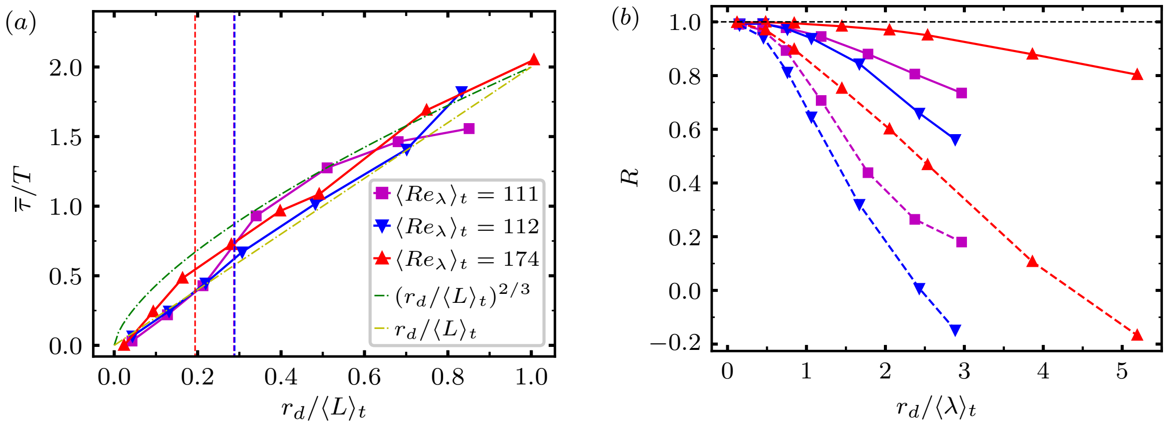

Figure 5.7: (*a*) Optimal time delays $\overline{\tau}/T$ and the vertical lines denote $\langle\lambda\rangle_t/\langle L\rangle_t$. We have inserted a linear and a 2/3 r_d-scaling. (*b*) Correlations at optimal time delays $R_{\overline{\tau}}(r_d)$ (solid lines) and at no time delay $R_0(r_d)$ (dashed lines). The black horizontal line equals 1.0.

We next use our DNSs of forced homogeneous/periodic turbulence to test the formalised time-lag hypothesis instantaneously. For now we assume that τ is a function of r_d only $\tau = \overline{\tau}(r_d)$ and calculate the delay as $\overline{\tau}(r_d) = \operatorname{argmax}_{\tau'} R(r_d, \tau')$, where $R(r_d, \tau')$ is the correlation function between $\langle \Pi\rangle^a_{\boldsymbol{x}}(r_d, t)$ and $-\langle\epsilon^*\rangle_{\boldsymbol{x}}(t)$ with time-lag τ'. We also consider the correlations with optimal time-lag $R_{\overline{\tau}}(r_d) = R(r_d, \overline{\tau}(r_d))$ and no time-lag $R_0(r_d) = R(r_d, 0)$ to compare the formalised time-lag hypothesis and no time-lag across scales r_d. Figure 5.7(*a*) displays the time-lags $\overline{\tau}(r_d)$, while figure 5.7(*b*) shows the $R_{\overline{\tau}}(r_d)$ and $R_0(r_d)$ values at the three DNSs. If we first focus on the larger scales, we see that $\overline{\tau}(\langle L\rangle_t) \approx 2.0T$ with correlations $R_{\overline{\tau}} = (0.7, 0.6, 0.8)$ with increasing Reynolds number. The Reynolds number difference might be due to the injection being less important in the dynamics at the highest Reynolds number (see figures 5.1-5.4). These $R_{\overline{\tau}}$ correlation values contrast with the no time-lag correlations $R_0 = (0.2, -0.2, -0.2)$. As we move to smaller r_d, the delays $\overline{\tau}$ decrease and the correlations increase. There is still a significant difference between no time-lag and the formalised time-lag hypothesis at $r_d \approx \langle\lambda\rangle_t$ with $\overline{\tau}(\langle\lambda\rangle_t) \approx 0.5T$ and time-lagged correlations $(0.95, 0.94, 0.99)$ and no time-lag correlations $(0.70, 0.65, 0.90)$ (displayed in increasing Reynolds number). This difference between $\overline{\tau}$ and $\tau = 0$ is consistent with the significant presence of unsteadiness in the cascade dynamics at the Taylor scale (see figures 5.2-5.4). At scales below $\langle\lambda\rangle_t$ the delay tends to zero with correlations close to unity for the formalised time-lag hypothesis and no time-lag (the $\overline{\tau}$-values are similar to those of Khurshid et al. (2021) in their figure 5(*c*)).

The large time-lag at the close to viscous $r_d \approx \langle\lambda\rangle_t$ is an interesting result. Conventionally, and as we introduced τ above, the delay τ is thought of as the time it takes larger-scale energy to cascade to viscous scales. However, τ in the formalised time-lag hypothesis is the delay between interscale transfer and viscous dissipation. Hence, τ includes both the inertial cascading time from larger scales to viscous scales and the time it takes this energy at viscous scales to be dissipated. That this latter time seems to

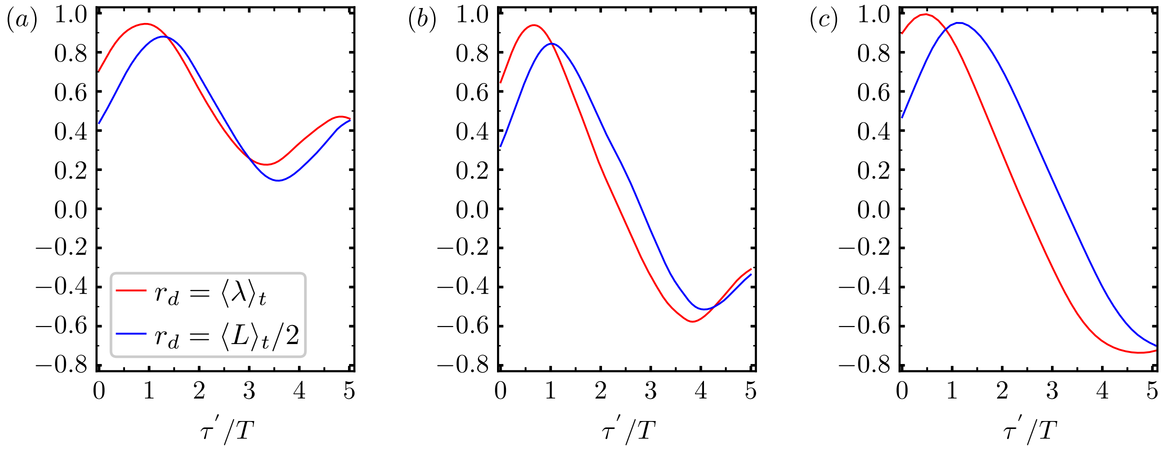

Figure 5.8: Correlation functions $R(r_d, \tau^{'})$ between $\langle \mathit{\Pi}\rangle^a_{\boldsymbol{x}}$ and $-\langle\epsilon^*\rangle_{\boldsymbol{x}}$ at scale r_d with time delay $\tau^{'}$. (a, b, c) for (DNS2,DNS3,DNS4).

be non-zero is consistent with our results in chapter 4 with only a limited tendency of a direct balance between interscale transfer and viscous effects at small scales. This latter small-scale time scale might be similar to the physical space viscous diffusion time scale, which at $\langle\lambda\rangle_t$ is given as $t_\nu \sim \langle\lambda\rangle_t^2/\nu \sim T$ (where we used the definition of the Taylor scale and the Taylor dissipation scaling (Sreenivasan, 1998)). Note that our above justification of the formalised time-lag hypothesis leaves the possibility of a τ diffusive component open. We merely hypothesise that there exists a $\tau > 0$ which increases with r_d such that $\langle \mathit{\Pi}\rangle^a_{\boldsymbol{x}}(r_d, t) \approx -C_{\mathit{\Pi}}(r_d)\langle\epsilon^*\rangle_{\boldsymbol{x}}(t + \tau)$, not that $\tau = 0$ at the doorstep to the viscous scales.

We can probe the time-lag between interscale transfer and dissipation more closely with their correlation functions at $r_d = \langle\lambda\rangle_t$ and $r_d = \langle L\rangle_t/2$ in figure 5.8. We see as expected that the maximum correlation shifts to the right and decreases as we consider larger scales and that the maximum correlations also increase with the Reynolds number. The correlation functions with DNS3-DNS4 (figure 5.8(b, c)) decrease to zero at approximately $2T$ after $\overline{\tau}$ and reach their most negative value approximately $4T$ after $\overline{\tau}$. This behaviour can be explained by the quasiperiodic behaviour of the interscale transfer and dissipation rates in our simulations (see figure 5.5), which has an approximate period $\overline{T} \sim 8T$ (and this type of behaviour is usual in DNSs of forced homogeneous turbulence across Reynolds numbers and forcings (Goto and Vassilicos, 2015; Goto et al., 2017)). It is readily shown that two sine functions with period $\overline{T}$ and time-lag $\overline{\tau}$ have correlation function $R(\tau^{'}) = \cos[2\pi(\tau^{'} - \overline{\tau})/\overline{T}]$. Hence, the time-lag in the formalised time-lag hypothesis seems to first and foremost capture this low-frequency, quasiperiodic behaviour. It follows that predicted time delays must be sufficiently accurate to capture this behaviour, i.e. deviations in predicted time delays relative to an optimal time delay $\tau^{'} - \overline{\tau}$ must be an order of magnitude less than $\overline{T}$, which approximately equals $0.8T$ in our DNSs (the behaviour with the ABC forcing is slightly different with less clear quasiperiodic behaviour with $R(r_d, \tau^{'}) > 0$ for all $\tau^{'}$).

So far we have considered time-lags which only depend on scale r_d. However, locally

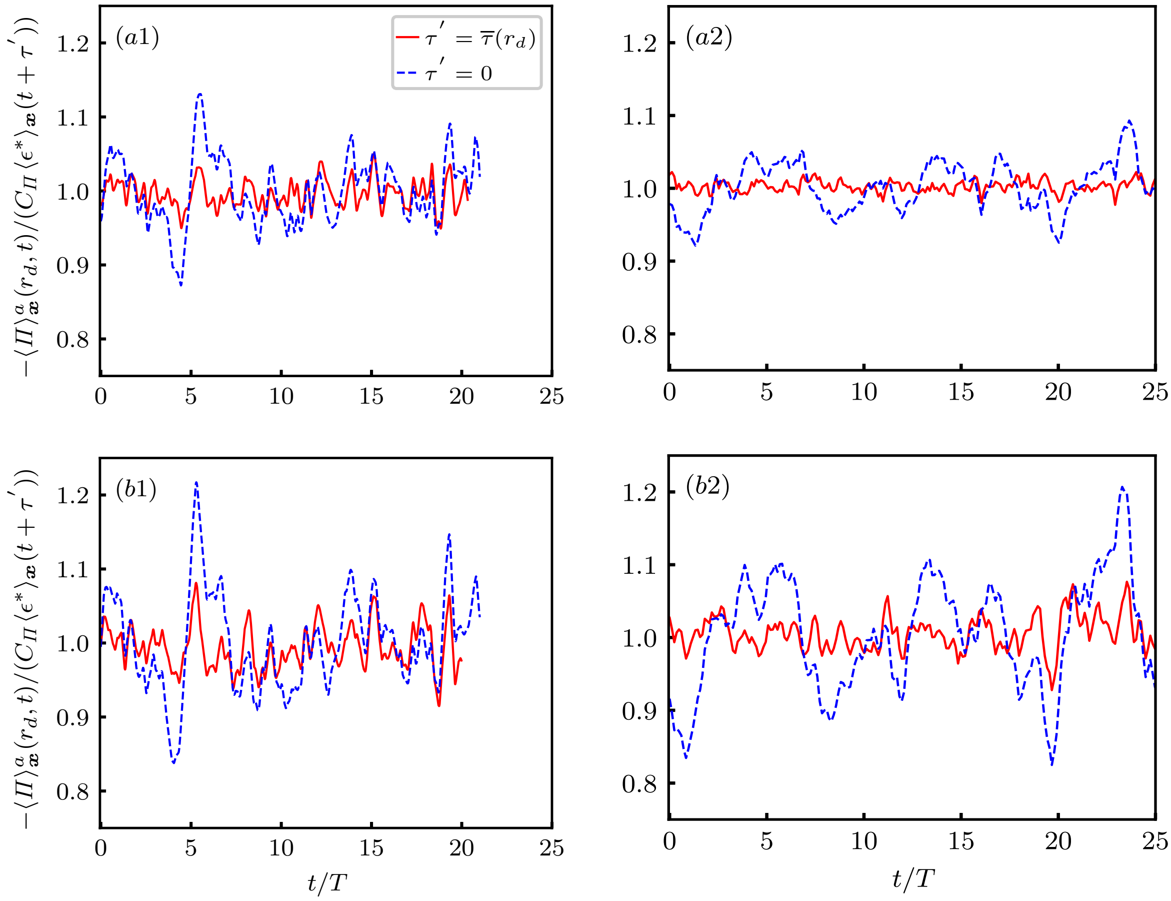

Figure 5.9: Ratio $-\langle \Pi \rangle^a_{\boldsymbol{x}}(r_d,t)/C_\Pi(r_d)\langle \epsilon^* \rangle_{\boldsymbol{x}}(t+\tau^{'})$ with $\tau^{'} = \overline{\tau}(r_d)$ and $\tau^{'} = 0$. $(a1, a2)$ $r_d = \langle \lambda \rangle_t$, $(b1, b2)$ $r_d = \langle L \rangle_t/2$. $(a1, b1)$ $\langle Re_\lambda \rangle_t = 112$, $(a2, b2)$ $\langle Re_\lambda \rangle_t = 174$.

in space and time, separate cascade chains will cascade energy to smaller scales more quickly or less quickly than $\overline{\tau}(r_d)$ (see e.g. Lumley (1992); Vela-Martín (2021, 2022b)). When considering the spatially averaged manifestation of this behaviour, one suspects at a given scale r_d a distribution of time delays τ between the spatially averaged interscale transfer and dissipation. In the case of our DNSs, where τ in the formalised time-lag hypothesis seems to mainly capture the low-frequency quasiperiodic cascade imbalances, we have that a time-invariant $\overline{\tau}(r_d)$ captures the time-lagged cascade behaviour as long as the temporal variations in the delay τ are order $0.1\overline{T}$ or less (i.e. $0.8T$ in our simulations). That is, a single time-lag approximation of the time-lagged cascade behaviour with time scale $\overline{T}$ is accurate when the typical variations of $\tau - \overline{\tau}$ are less than or order $0.1\overline{T}$. The good results in figure 5.7(b) suggest that the temporal variations in the delay are limited in this sense, in particular at scales $r_d \lesssim \langle \lambda \rangle_t$. This is supported by the results in Vela-Martín (2022b), where the difference in time-lag between large scales and average enstrophy $\omega_i\omega_i$ compared to intense or weak enstrophy equals roughly $0.5T$ (see their figure 6(b). Enstrophy is a small-scale quantity). It seems that only a crude/approximate scale-dependent time-lag estimate is needed to capture the quasiperiodic behaviour as it is evolving slowly and the temporal variations in local time delays are limited in comparison.

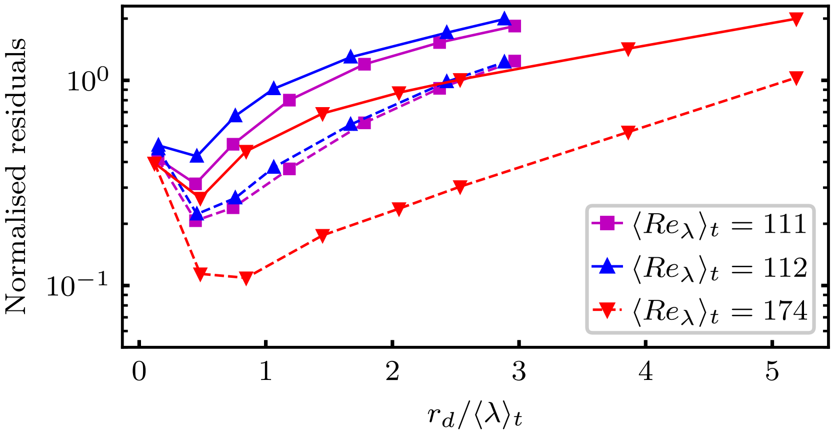

Figure 5.10: RMS(ϕ) denotes the root-mean-square $\sqrt{\langle\phi^2\rangle_t}$ and $\sigma(\phi)$ denotes the (temporal) standard deviation of $\phi = \phi(t)$. (solid lines) No time-lag RMS$(\langle\Pi^a\rangle_{\boldsymbol{x}}(r_d,t) + C_\Pi(r_d)\langle\epsilon^*\rangle_{\boldsymbol{x}}(r_d,t))$ and (dashed lines) time-lag RMS$(\langle\Pi^a\rangle_{\boldsymbol{x}}(r_d,t) + C_\Pi(r_d)\langle\epsilon^*\rangle_{\boldsymbol{x}}(r_d,t+\overline{\tau}(r_d)))$, both normalised by $\sigma(C_\Pi(r_d)\langle\epsilon^*\rangle_{\boldsymbol{x}}(t))$.

We end this section by testing whether the LHS and RHS of the formalised time-lag hypothesis have equal magnitudes. We first consider the ratio $-\langle\Pi\rangle^a_{\boldsymbol{x}}(r_d,t)/(C_\Pi(r_d)\langle\epsilon^*\rangle_{\boldsymbol{x}}(t+\overline{\tau}(r_d)))$. The time series of these ratios at scales $r_d = \langle\lambda\rangle_t$ and $r_d = \langle L\rangle_t/2$ are given in figure 5.9 with $\overline{\tau}(r_d)$ values from figure 5.7(a) and the no time-lag value $\tau = 0$. First note that the ratios oscillate around unity as the formalised time-lag hypothesis is accurate in a time-averaged sense with $\tau = \overline{\tau}(r_d)$ or with $\tau = 0$. Figure 5.9 also shows that the interscale transfer rate is better at predicting the future rather than the present dissipation rate. E.g. the ratio of the temporal standard deviation of $-\langle\Pi\rangle^a_{\boldsymbol{x}}(r_d,t)/(C_\Pi(r_d)\langle\epsilon^*\rangle_{\boldsymbol{x}}(t+\tau^{'}))$ to its time-average value at $\langle Re_\lambda\rangle_t = 174$ with $r_d = \langle L\rangle_t/2$ equals 2.3% for $\tau^{'} = \overline{\tau}(r_d)$ and 7.6% for $\tau^{'} = 0$. At $r_d = \langle\lambda\rangle_t$ these values reduce to 0.8% and 3.3% for $\tau^{'} = \overline{\tau}(r_d)$ and $\tau^{'} = 0$ respectively.

The accuracy of the formalised time-lag hypothesis can be checked more carefully with figure 5.10. We plot the root-mean-square $\sqrt{\langle\phi^2\rangle_t}$ of the residual ϕ of the formalised time-lag hypothesis (i.e. the difference between its RHS and LHS). This error measure captures errors due to time-averaged non-zero errors and fluctuating errors as $\langle\phi^2\rangle_t = \langle\phi\rangle_t^2 + \langle(\phi^{"})^2\rangle_t$ where $\phi^{"}(t) = \phi(t) - \langle\phi\rangle_t$. It is clear from this figure that the formalised time-lag hypothesis has the best performance at approximately $r_d \approx \langle\lambda\rangle_t$ with approximately 80% and 90% of the future dissipation rate fluctuations predicted by the present interscale transfer rate at the lower and highest $\langle Re_\lambda\rangle_t$. At the very smallest scales the performance deteriorates due to the effect of viscous diffusion in the fluctuating dynamics. At the largest scales the precision of the formalised time-lag hypothesis is also poor, presumably from the effects of the fluctuating injection and high-frequency interscale transfers. Note the significant improvements over local equilibrium at the lower end of $\langle\lambda\rangle < r_d < \langle L\rangle_t$. E.g. for $\langle Re_\lambda\rangle_t = 174$ for $\langle\lambda\rangle < r_d < 3\langle\lambda\rangle$ the normalised time-lag RMS ranges from 10% to 30% while the normalised local equilibrium RMS ranges from 40% to 100%.

In this section we predicted the unsteady cascade behaviour in homogeneous/periodic turbulence in terms of the formalised time-lag hypothesis. The hypothesis is consistent with the average cascade behaviour and it relatively accurately predicts the dissipation rate in our DNSs of forced homogeneous/periodic turbulence at the lower end of $\langle \lambda \rangle_t < r_d < \langle L \rangle_t$. It is important to emphasize that this hypothesis yields non-trivial predictions at as low Reynolds numbers as $\langle Re_\lambda \rangle_t \sim 100$ where unsteadiness/non-equilibrium is ubiquitous. This result and the similar behaviour with different large-scale forcings are consistent with the relatively limited importance of the injection fluctuations $\mathcal{I}''$ in the fluctuating cascade dynamics (see figures 5.2-5.4). That is, the formalised time-lag hypothesis seems relatively insensitive to the large-scale forcing. The time-lag τ seems to primarily capture the low-frequency, quasiperiodic turbulence evolution, making it relatively easy to develop time-lag estimates which are sufficiently accurate to capture the unsteady turbulence evolution. It is also worth mentioning that one can expect the formalised time-lag hypothesis also to apply at larger scales at higher Reynolds number (this is suggested by the interscale transfer and dissipation time series in figure 9 of Goto and Vassilicos (2016a) at $\langle Re_\lambda \rangle_t = 490$). In sum, one can suspect the formalised time-lag hypothesis to be broadly applicable to predict the spatially averaged dissipation rate in homogeneous/periodic turbulence. Future investigations with DNSs of forced and freely decaying homogeneous/periodic turbulence are required to verify this conjecture.

We focus our attention on the practical utility of this dissipation prediction in the two next sections in terms of corrections to the K41 equilibrium behaviour and a new dissipation scaling. By having a clear physical basis for these predictions, it is relatively straightforward to establish their inherent limitations. This physical justification is also useful for potential later generalisations of non-equilibrium predictions to naturally occurring flows. E.g. if the spatially averaged $(|\delta \boldsymbol{u}|^2)^a$ at intermediate scales is moving in space as it is cascading, it will not only be a time-lag between interscale transfers and dissipation, but also a spatial separation:

$$\langle \Pi \rangle^a_{\boldsymbol{x}}(\boldsymbol{x}, r_d, t) \approx -C_\Pi \langle \epsilon^* \rangle_{\boldsymbol{x}}(\boldsymbol{x} + \boldsymbol{x}_\tau, t + \tau) \tag{5.12}$$

with the spatial separation $\boldsymbol{x}_\tau$ given

$$\boldsymbol{x}_\tau(\boldsymbol{x}, r_d, t) = \int_t^{t+\tau} \boldsymbol{u}(\overline{\boldsymbol{x}}(\boldsymbol{x}, t), t^{'}) dt', \tag{5.13}$$

where $\overline{x}(\boldsymbol{x}, t)$ is the Lagrangian trajectory following $\boldsymbol{u}$ from $(\boldsymbol{x}, t)$ and $\tau > 0$ is monotonically increasing with r_d (see Wan et al. (2010); Ballouz et al. (2020) for Lagrangian investigations of large-to-small-scale time-lags). Equations (5.12)-(5.13) should not be taken too literally. They are only intended to show how simply the (physical space) formalised time-lag hypothesis might be generalised to accommodate spatial transport effects. From this or an analogue starting point, one can develop non-equilibrium predictions similarly as we do next for the simpler case of homogeneous/periodic turbulence.

5.3 Time-lag Corrections to Local Equilibrium

The local equilibrium hypothesis $\langle \Pi \rangle^a_{\boldsymbol{x}}(r_d, t) \approx -\langle \epsilon^* \rangle_{\boldsymbol{x}}(t)$ predicts $\langle \mathcal{A}_t \rangle^a_{\boldsymbol{x}}(r_d, t) \approx 0$ at sufficiently small inviscid scales. It can be used to motivate a $r_d^{2/3}$-scaling of the second-order structure function (see Kolmogorov (1941a) and section 1.1). The previous section demonstrated that the formalised time-lag hypothesis $\langle \Pi \rangle^a_{\boldsymbol{x}}(r_d, t) \approx -C_\Pi(r_d)\langle \epsilon^* \rangle_{\boldsymbol{x}}(t+\tau)$ is more accurate with $\tau = \overline{\tau}(r_d)$ than local equilibrium $\tau = 0$ in our low to moderate Reynolds number DNSs of forced homogeneous/periodic turbulence. In this section we use the formalised time-lag hypothesis to develop corrections to the K41 cascade dynamics and second-order structure function scaling. We verify these expressions with our DNSs and compare them with previous works on non-equilibrium/unsteadiness corrections to K41 (Yoshizawa, 1994; Woodruff and Rubinstein, 2006; Bos and Rubinstein, 2017).

5.3.1 Non-equilibrium Dynamics from Time-lag Corrections

We first develop non-equilibrium corrections to the K41 cascade dynamics from the formalised time-lag hypothesis. This equilibrium/non-equilibrium decomposition of the cascade dynamics supposes that it is meaningful to write $\langle \Pi \rangle^a_{\boldsymbol{x}}(r_d, t) = \overline{\Pi}(r_d, t) + \widetilde{\Pi}(r_d, t)$, where $\overline{\Pi}(r_d, t) = -C_\Pi(r_d)\langle \epsilon^* \rangle_{\boldsymbol{x}}(t)$ is the equilibrium interscale transfer and $\widetilde{\Pi}(r_d, t)$ is the non-equilibrium interscale transfer. If we combine this decomposition with the formalised time-lag hypothesis, the non-equilibrium interscale transfer can be written as

$$\widetilde{\Pi}(r_d, t) = \langle \Pi \rangle^a_{\boldsymbol{x}}(r_d, t) - \overline{\Pi}(r_d, t), \tag{5.14a}$$

$$= -C_\Pi(r_d)\langle \epsilon^* \rangle_{\boldsymbol{x}}(t+\tau) + C_\Pi(r_d)\langle \epsilon^* \rangle_{\boldsymbol{x}}(t), \tag{5.14b}$$

$$= -C_\Pi(r_d)\Big[\tau \frac{d\langle \epsilon^* \rangle_{\boldsymbol{x}}(t)}{dt} + \frac{\tau^2}{2}\frac{d^2\langle \epsilon^* \rangle_{\boldsymbol{x}}(t)}{dt^2} + \mathcal{O}(\tau^3)\Big], \tag{5.14c}$$

$$= -C_\Pi(r_d)\langle \epsilon^* \rangle_{\boldsymbol{x}}(t)\Big[\tau \frac{1}{\langle \epsilon^* \rangle_{\boldsymbol{x}}(t)}\frac{d\langle \epsilon^* \rangle_{\boldsymbol{x}}(t)}{dt} + \frac{\tau^2}{4}\frac{1}{\langle \epsilon^* \rangle_{\boldsymbol{x}}(t)^2}\frac{d^2\langle \epsilon^* \rangle_{\boldsymbol{x}}(t)^2}{dt^2} + \mathcal{O}(\tau^3)\Big], \tag{5.14d}$$

where we used a Taylor expansion of $\langle \epsilon^* \rangle_{\boldsymbol{x}}(t+\tau)$ from time t to go from (5.14b) to (5.14c). We see from (5.14d) that the size of the terms in the $\widetilde{\Pi}(r_d, t)$ Taylor series relative to the size of the equilibrium part $\overline{\Pi}(r_d, t) = C_\Pi(r_d)\langle \epsilon^* \rangle_{\boldsymbol{x}}(t)$ is dependent on the ratio of the delay τ to the time scale of change of the dissipation rate $T_\epsilon \geq 0$, where

$$\frac{1}{s_t(t)T_\epsilon(t)} = \frac{1}{\langle \epsilon^* \rangle_{\boldsymbol{x}}(t)}\frac{d\langle \epsilon^* \rangle_{\boldsymbol{x}}(t)}{dt}, \tag{5.15}$$

and $s_t(t)$ is the sign function of $d\langle \epsilon^* \rangle_{\boldsymbol{x}}(t)/dt$. Only when typically $\tau/T_\epsilon \ll 1$ can the RHS in (5.14d) be accurately characterised by a truncated Taylor series. We plot the time series of the first-order F and second-order S interscale transfer non-equilibrium corrections relative to the equilibrium interscale transfer in figure 5.11 with $\tau = \overline{\tau}$ and

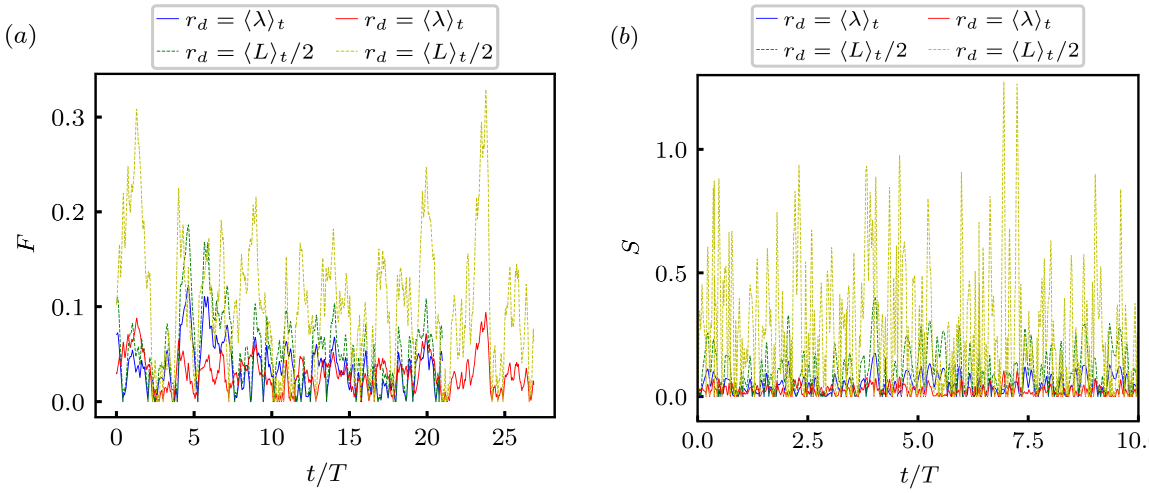

Figure 5.11: Time series of non-equilibrium (a) first-order terms F and (b) second-order terms S. Blue and green $\langle Re_\lambda\rangle_t = 112$, red and yellow $\langle Re_\lambda\rangle_t = 174$.

$$F(r_d, t) = \frac{\overline{\tau}(r_d)}{\langle\epsilon^*\rangle_{\boldsymbol{x}}(t)}\left|\frac{d\langle\epsilon^*\rangle_{\boldsymbol{x}}(t)}{dt}\right|, \tag{5.16a}$$

$$S(r_d, t) = \frac{\overline{\tau}(r_d)^2}{2\langle\epsilon^*\rangle_{\boldsymbol{x}}(t)}\left|\frac{d^2\langle\epsilon^*\rangle_{\boldsymbol{x}}(t)}{dt^2}\right|. \tag{5.16b}$$

Figure 5.11(a) shows that at scales $r_d \approx \langle L\rangle_t/2$, the second-order correction S takes on high values, of order unity and seems to be typically larger than the first-order correction F. At scales $r_d \approx \langle\lambda\rangle_t$, the first- and second-order corrections seem similar in magnitude $S \sim F$. The time-average values of F and S in figure 5.12(a) agree with these observations. At scales $r_d \geq 0.5\langle\lambda\rangle_t$, S is on average similar or larger than F. Hence, at no scale $r_d \geq 0.5\langle\lambda\rangle_t$ is there a magnitude separation $F \gg S$ in our low to moderate Reynolds number DNSs. This suggests that $\tau/T_\epsilon \not\ll 1$ such that (5.14) cannot be expressed as a truncated Taylor series in our DNSs. At even higher $\langle Re_\lambda\rangle_t$ there might exist a limited range of intermediate scales where τ is sufficiently small such that $\tau/T_\epsilon \ll 1$, but this scenario would not yield non-equilibrium corrections at larger scales similar to L (assuming similar T_ϵ values in homogeneous/periodic turbulence). It appears that the above Taylor expansion of the non-equilibrium interscale transfer has limited applicability in studying the non-equilibrium cascade dynamics. The Taylor series cannot be truncated at larger scales as the spatially averaged dissipation rate is evolving too quickly compared to the time-lag τ (i.e. the degree of non-equilibrium is too severe to allow such a truncation).

The previous section showed that the formalised time-lag hypothesis mainly captures low frequencies, not high frequencies (see also Khurshid et al. (2021)). The causal relation between larger-scale interscale transfer and dissipation seems restricted to slow, quasiperiodic cascade imbalances. Rather than developing non-equilibrium corrections to the full interscale transfer, we need to restrict ourselves to its lower frequencies. To develop low-frequency non-equilibrium corrections, we apply a low-pass filtering, denoted with superscript $<$ (and defined in detail below), to the expression for the non-equilibrium

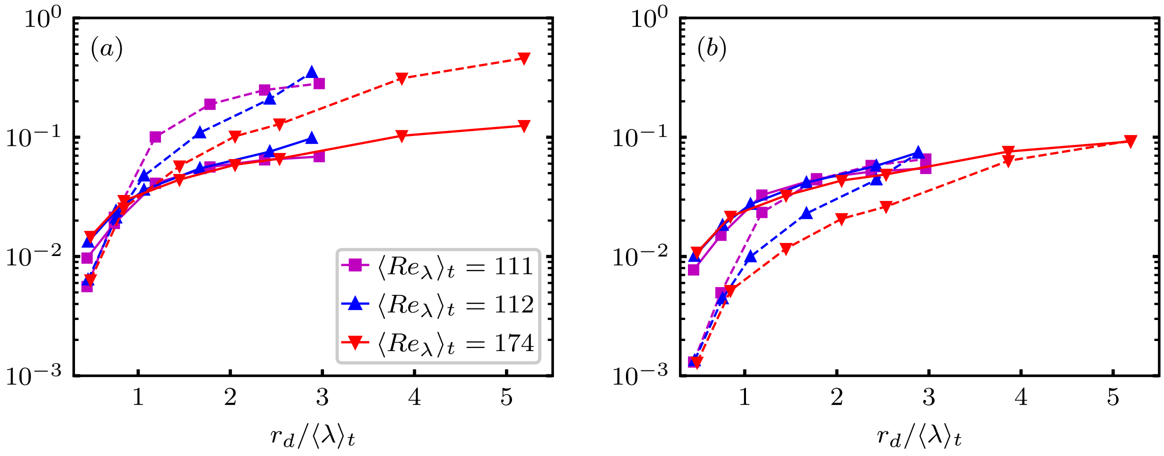

Figure 5.12: (*a*) Average size of non-equilibrium first-order corrections $\langle F\rangle_t(r_d)$ (solid lines) and second-order corrections $\langle S\rangle_t(r_d)$ (dashed lines). (*b*) Average size of low-pass non-equilibrium first-order corrections $\langle F_L\rangle_t(r_d)$ (solid lines) and second-order corrections $\langle S_L\rangle_t(r_d)$ (dashed lines).

interscale transfer (5.14)

$$\widetilde{\Pi}^<(r_d,t) = \langle \Pi^a\rangle^<_{\boldsymbol{x}}(r_d,t) - \overline{\Pi}^<(r_d,t) \tag{5.17a}$$

$$= -C_\Pi(r_d)\Big[\Big(\tau\frac{d\langle\epsilon^*\rangle_{\boldsymbol{x}}(t)}{dt}\Big)^< + \Big(\frac{\tau^2}{2}\frac{d^2\langle\epsilon^*\rangle_{\boldsymbol{x}}(t)}{dt^2}\Big)^< + \mathcal{O}(\tau^3)\Big], \tag{5.17b}$$

$$= -C_\Pi(r_d)\langle\epsilon^*\rangle^<_{\boldsymbol{x}}(t)\Big[\frac{1}{\langle\epsilon^*\rangle^<_{\boldsymbol{x}}(t)}\Big(\tau\frac{d\langle\epsilon^*\rangle_{\boldsymbol{x}}(t)}{dt})\Big)^< + \frac{1}{\langle\epsilon^*\rangle^<_{\boldsymbol{x}}(t)}\Big(\frac{\tau^2}{2}\frac{d^2\langle\epsilon^*\rangle_{\boldsymbol{x}}(t)}{dt^2}\Big)^< + \mathcal{O}(\tau^3)\Big]. \tag{5.17c}$$

We define associated non-equilibrium to equilibrium first- and second-order corrections

$$F_L(r_d,t) = \frac{\overline{\tau}(r_d)}{\langle\epsilon^*\rangle^<_{\boldsymbol{x}}(t)}\Big|\Big(\frac{d\langle\epsilon^*\rangle_{\boldsymbol{x}}(t)}{dt}\Big)^<\Big|, \tag{5.18a}$$

$$S_L(r_d,t) = \frac{\overline{\tau}(r_d)^2}{2\langle\epsilon^*\rangle^<_{\boldsymbol{x}}(t)}\Big|\Big(\frac{d^2\langle\epsilon^*\rangle_{\boldsymbol{x}}(t)}{dt^2}\Big)^<\Big|, \tag{5.18b}$$

and the time scale of change of the low-pass filtered dissipation rate $T_{\epsilon^<}$ as

$$\frac{1}{s_t(t)T_{\epsilon^<}(t)} = \frac{1}{\langle\epsilon^*\rangle^<_{\boldsymbol{x}}(t)}\Big(\frac{d\langle\epsilon^*\rangle_{\boldsymbol{x}}(t)}{dt}\Big)^<, \tag{5.19}$$

where $s_t(t)$ is the sign function of $(d\langle\epsilon^*\rangle_{\boldsymbol{x}}(t)/dt)^<$. By restricting ourselves to low frequencies rather than all frequencies, a truncated Taylor series of the low-pass non-equilibrium interscale transfer requires $\tau/T_{\epsilon^<} \ll 1$ rather than the more restrictive $\tau/T_\epsilon \ll 1$ (the low-pass filtering tends to make $T_{\epsilon^<} > T_\epsilon$). We next specify the low-pass filtering methodology before assessing if $\tau/T_{\epsilon^<} \ll 1$ in terms of F_L and S_L in our DNSs of forced homogeneous/periodic turbulence.

For a quantity $q(m)$ sampled at discrete times $0 \leq m \leq M-1$, we limit frequency leakage effects with a Hamming window (Blackman and Tukey, 1958; Prabhu, 2018)

$$h(m) = 0.54 - 0.46\cos\big(\frac{2\pi m}{M-1}\big), \tag{5.20}$$

i.e. we calculate the windowed signal $q_w(m) = h(m)q(m)$. We calculate the FFT of $q_w(m)$, denoted $\widehat{q}_w(f)$, where f denotes frequency. We apply a low-pass filter

$$g(f) = \begin{cases} 1.0, & |f| \leq 1/(2T), \\ 0.0, & |f| > 1/(2T) \end{cases} \tag{5.21}$$

to $\widehat{q}_w(f)$ to obtain $\widehat{q}^<_w(f) = g(f)\widetilde{q}_w(f)$. Finally, we apply an inverse FFT to $\widehat{q}^<_w(f)$ to obtain the low-pass filtered $q(m)$ with cut-off frequency $1/(2T)$, denoted $q^<$. This cut-off frequency approximately retains the quasiperiodic cascade imbalances (if one low-pass filters the formalised time-lag hypothesis (5.8) with this low-pass filtering methodology, we obtain behaviour very similar to the formalised time-lag hypothesis in terms of time-lags $\overline{\tau}$, correlation coefficients and residuals (not shown)).

Figure 5.12(b) shows the average low-pass first- and second-order corrections F_L and S_L. The second-order contribution becomes smaller than the first-order contribution at scales below $\langle L\rangle_t$ and at $r_d \approx \langle\lambda\rangle_t$ there is an approximate order of magnitude difference. Hence, at the lower end of $\langle\lambda\rangle_t < r_d < \langle L\rangle_t$, $\overline{\tau}$ seems to be typically smaller than the time scale of change of the low-pass filtered dissipation rate $T_{\epsilon^<}$. It follows that we indeed can express the low-pass non-equilibrium interscale transfer rate in terms of the first and second terms in the Taylor expansion (5.17b)

$$\widetilde{\varPi}^<(r_d,t) \approx -C_{\varPi}(r_d)\Big[\big(\tau\frac{d\langle\epsilon^*\rangle_{\boldsymbol{x}}(t)}{dt}\big)^< + \big(\frac{\tau^2}{2}\frac{d^2\langle\epsilon^*\rangle_{\boldsymbol{x}}(t)}{dt^2}\big)^<\Big]. \tag{5.22}$$

We test the validity of (5.22) by calculating the residuals and correlations between its LHS and RHS (and we calculate the LHS as $\widetilde{\varPi}^<(r_d,t) = \langle\varPi^a\rangle^<_{\boldsymbol{x}}(r_d,t) + C_{\varPi}(r_d)\langle\epsilon^*\rangle^<_{\boldsymbol{x}}(t)$). We denote the first- and second-order terms in (5.22) as $F_{\varPi} = C_{\varPi}(r_d)\overline{\tau}(r_d)(d\langle\epsilon^*\rangle_{\boldsymbol{x}}(t)/dt)^<$ and $S_{\varPi} = C_{\varPi}(r_d)\overline{\tau}^2/2(d^2\langle\epsilon^*\rangle_{\boldsymbol{x}}(t)/dt^2)^<$. Figure 5.13($a,b$) shows that the first- and first-plus second-order terms are best at predicting $\widetilde{\varPi}^<(r_d,t)$ close to the lower end of $\langle\lambda\rangle_t < r_d < \langle L\rangle_t$, where approximately 80% of its fluctuations are predicted. The residuals increase as r_d increases towards the integral length scale and at scales below the Taylor scale. Figure 5.13(c,d) with time series of $\widetilde{\varPi}^<$, $-F_{\varPi}$ and $-F_{\varPi} - S_{\varPi}$ makes the different behaviour of the LHS and RHS in the $\widetilde{\varPi}^<$ prediction clearer. At $\langle\lambda\rangle_t$ the majority of the $\widetilde{\varPi}^<$ fluctuations are captured by $-F_{\varPi}$ with some limited improvement in accuracy with the inclusion of $-S_{\varPi}$. At $\langle L\rangle_t$ the phase of $\widetilde{\varPi}^<$ is approximately captured by $-F_{\varPi} - S_{\varPi}$, but it overpredicts its amplitude as important higher-order terms in the Taylor expansion are neglected. This is consistent with the relatively high correlations and residuals in figure 5.13(a,b) at scales close to $\langle L\rangle_t$. The time series are similar for DNS2 and DNS4.

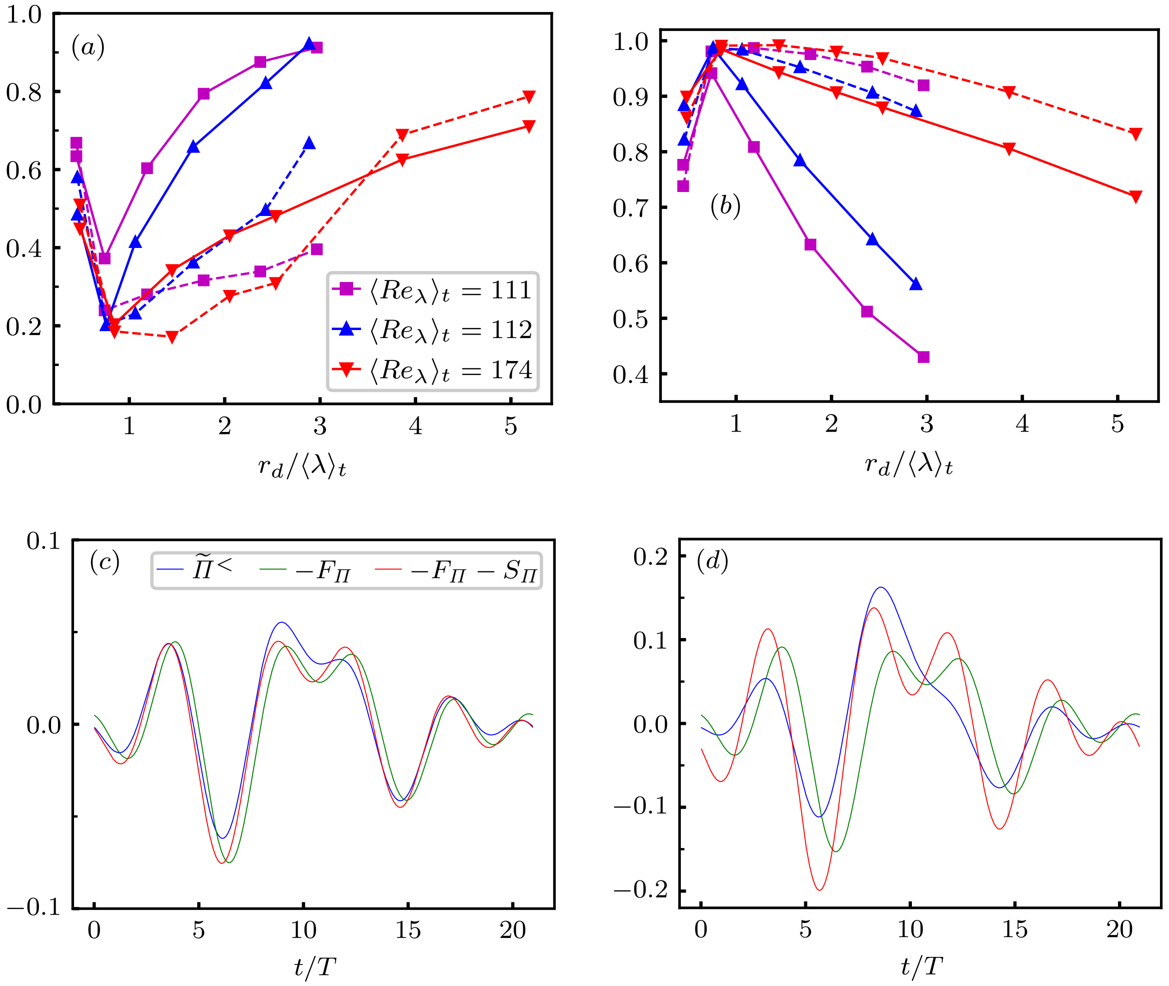

Figure 5.13: (a) First- and second-order residuals RMS($\widetilde{\Pi}^<+F_\Pi$)/RMS($\widetilde{\Pi}^<$) (solid lines) and RMS($\widetilde{\Pi}^< + F_\Pi + S_\Pi$)/RMS($\widetilde{\Pi}^<$) (dashed lines). ($b$) First- and second-order correlations corr($\widetilde{\Pi}^<, -F_\Pi$) (solid lines) and corr($\widetilde{\Pi}^<, -F_\Pi - S_\Pi$) (dashed lines).($c, d$) Time series of $\widetilde{\Pi}^<$, $-F_\Pi$ and $-F_\Pi - S_\Pi$ (normalised by $\langle\epsilon^*\rangle$) at $r_d = \langle\lambda\rangle_t$ and $r_d = \langle L\rangle_t$. $\langle Re_\lambda\rangle_t = 112$.

The truncated Taylor series (5.22) can also be used to predict the low-pass filtered time derivative term. If we combine the equilibrium/non-equilibrium decomposition of $\langle\Pi^a\rangle^<_{\boldsymbol{x}}(r_d, t)$ with the low-pass filtered spatially averaged KHMH equation, we obtain

$$\langle\mathcal{A}^a_t\rangle^<_{\boldsymbol{x}} + \widetilde{\Pi}^< = -(1 - C_\Pi)\langle\epsilon^*\rangle^<_{\boldsymbol{x}} + \langle\mathcal{D}^a_{r,\nu}\rangle^<_{\boldsymbol{x}} + \langle\mathcal{I}^a\rangle^<_{\boldsymbol{x}}. \tag{5.23}$$

If the temporal fluctuations of the RHS of this equation are typically small relative to the temporal fluctuations of its LHS, one might approximate $\langle\mathcal{A}^a_t\rangle^<_{\boldsymbol{x}} + \widetilde{\Pi}^< \approx 0$. This approximation seems most accurate at scales close to the Taylor scale with C_Π close to unity and limited temporal fluctuations of the viscous diffusion in scale space and injection. Assuming $\langle\mathcal{A}^a_t\rangle^<_{\boldsymbol{x}} + \widetilde{\Pi}^< \approx 0$, we obtain

$$\langle\mathcal{A}^a_t\rangle^<_{\boldsymbol{x}}(r_d, t) \approx -\widetilde{\Pi}^<(r_d, t) \approx C_\Pi(r_d)\Big[\Big(\tau\frac{d\langle\epsilon^*\rangle_{\boldsymbol{x}}(t)}{dt})\Big)^< + \Big(\frac{\tau^2}{2}\frac{d^2\langle\epsilon^*\rangle^<_{\boldsymbol{x}}(t)}{dt^2}\Big)^<\Big]. \tag{5.24}$$

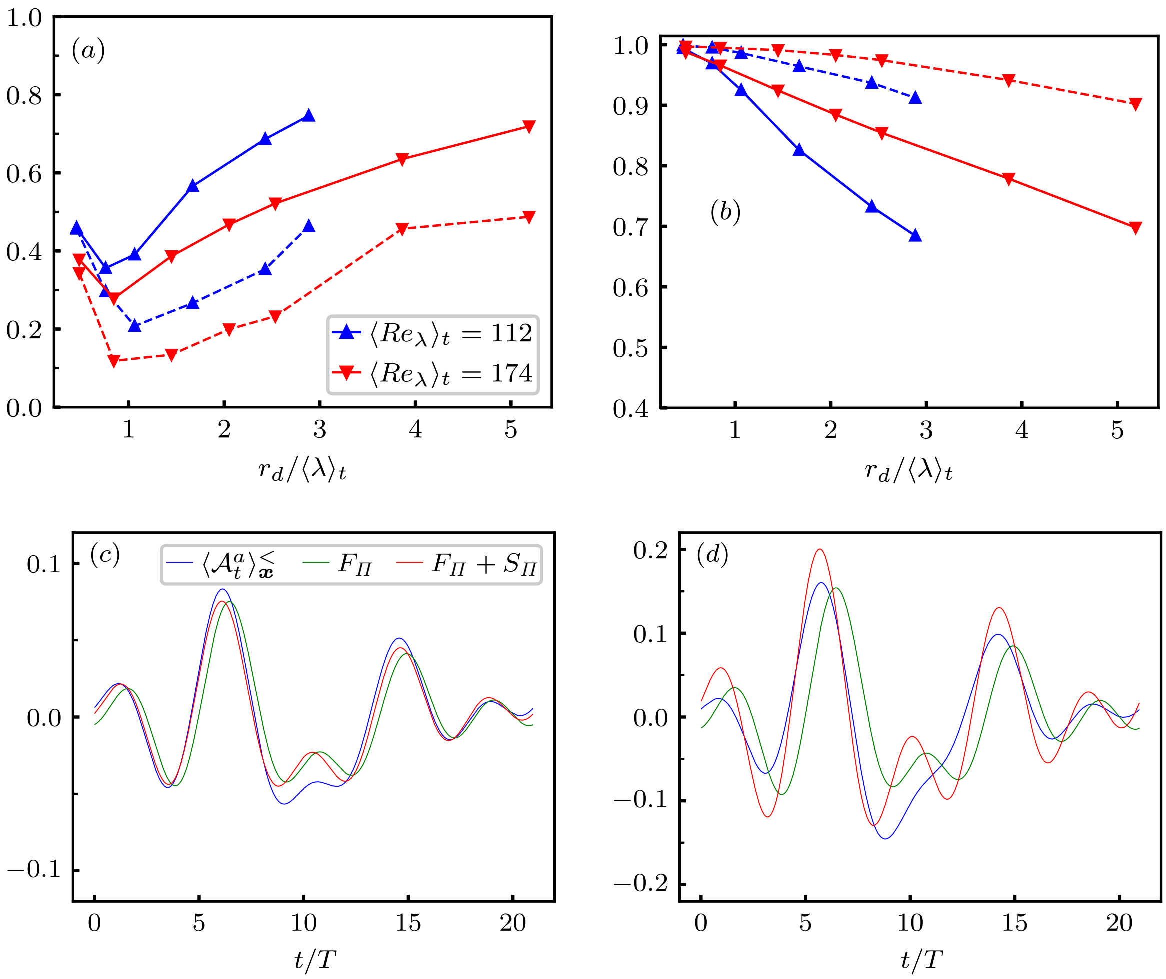

Figure 5.14: First- and second-order residuals (a) and correlations (b) as defined in figure 5.13 with $\langle \mathcal{A}_t^a \rangle_{\boldsymbol{x}}^<$ switched with $\widetilde{\Pi}^<$. (c, d) Time series of $\widetilde{\Pi}^<$, F_Π and $F_\Pi + S_\Pi$ (normalised by $\langle \epsilon^* \rangle$) at $r_d = \langle \lambda \rangle_t$ and $r_d = \langle L \rangle_t$. $\langle Re_\lambda \rangle_t = 112$.

We test (5.24) with DNS3-DNS4 in figure 5.14 similarly as we tested the $\widetilde{\Pi}^<(r_d, t)$ prediction in figure 5.13. In terms of residuals and correlations (figure 5.14(a, b)), the $\langle \mathcal{A}_t^a \rangle_{\boldsymbol{x}}^<(r_d, t)$ predictions have residuals and correlations very similar to the $\widetilde{\Pi}^<(r_d, t)$ predictions, consistent with $\langle \mathcal{A}_t^a \rangle_{\boldsymbol{x}}^< + \widetilde{\Pi}^< \approx 0$. The time series in figure 5.14(c, d) are approximately identical to the time series in figure 5.13(c, d) (except a minus sign as $\langle \mathcal{A}_t^a \rangle_{\boldsymbol{x}}^<(r_d, t) \approx -\widetilde{\Pi}^<(r_d, t)$) with similar behaviour for DNS2 and DNS4.

Figures 5.12(b)-5.13-5.14 show that at low to moderate Reynolds numbers the formalised time-lag hypothesis can be used to decompose the low-pass filtered cascade dynamics into equilibrium and non-equilibrium parts, where the non-equilibrium part equals the truncated series (5.24). This approach is most accurate at the lower end of $\langle \lambda \rangle_t < r_d < \langle L \rangle_t$ in our DNSs of forced homogeneous turbulence (where $\langle L \rangle_t = 3\langle \lambda \rangle_t - 5\langle \lambda \rangle_t$ in our DNSs). These predictions capture approximately $70 - 90\%$ of the fluctuations of the non-equilibrium dynamics in our DNSs at these scales smaller than and similar to the integral length scale. At these scales the non-equilibrium corrections are modest $\tau/T_{\epsilon^<} \ll 1$, allowing the truncation of the full non-equilibrium series (5.17b). Towards the upper end of $\langle\lambda\rangle_t < r_d < \langle L\rangle_t$ and at scales $r_d < \langle\lambda\rangle_t$ the predictions of the non-equilibrium dynamics are less accurate as the formalised time-lag hypothesis (and the truncated Taylor expansion at larger scales) is less accurate. One can susupect that (5.24) is also accurate at higher Reynolds numbers at inviscid scales $r_d \lesssim L$ with decreasing magnitude relative to the equilibrium dynamics as r_d and $\tau/T_{\epsilon^<}$ decrease.

The non-equilibrium dynamics (5.24) can be used to study the time/ensemble-averaged non-equilibrium dynamics in homogeneous/periodic turbulence. Applying time-averages to (5.24) in forced/statistically stationary homogeneous/periodic turbulence, yields no average non-equilibrium effects. If we apply an ensemble-average $\langle\rangle_E$ to (5.24), we obtain

$$\langle\mathcal{A}_t^a\rangle_E \approx -\langle\widetilde{\Pi}\rangle_E \approx C_\Pi(r_d)\Big[\langle\tau\frac{d\langle\epsilon^*\rangle_{\boldsymbol{x}}(t)}{dt})\rangle_E + \langle\frac{\tau^2}{2}\frac{d^2\langle\epsilon^*\rangle_{\boldsymbol{x}}(t)}{dt^2}\rangle_E\Big], \tag{5.25}$$

where we assumed that the ensemble-averaged terms approximately only contain frequencies equal or below the cut-off frequency, i.e. $\langle q^<\rangle_E \approx \langle q\rangle_E$. (5.25) can be used to predict the ensemble-averaged non-equilibrium cascade dynamics in decaying homogeneous turbulence. (5.25) highlights how finite large-to-small scale time-lags can yield non-zero average effects and that these non-equilibrium corrections are most clearly identified in terms of spatially averaged cascade dynamics. If one would extend the above non-equilibrium predictions to flows with spatial transport, one could obtain expressions similar to (5.25) to estimate non-equilibrium corrections. Having established the applicability of the non-equilibrium dynamics (5.24), we next use it to arrive at low-pass non-equilibrium corrections to the $(\langle|\delta\boldsymbol{u}|^2\rangle_{\boldsymbol{x}}^a)^<(r_d,t)$ scaling behaviour in homogeneous/periodic turbulence.

5.3.2 Non-equilibrium Second-order Structure Function Scaling from Time-lag Corrections

We next develop non-equilibrium predictions for the $(\langle|\delta\boldsymbol{u}|^2\rangle_{\boldsymbol{x}}^a)^<(r_d,t)$ scaling behaviour. In the following we first relate $(\langle|\delta\boldsymbol{u}|^2\rangle_{\boldsymbol{x}}^a)^<(r_d,t)$ to the full low-pass interscale transfer rate $\langle\Pi^a\rangle_{\boldsymbol{x}}^<(r_d,t)$ before applying its equilibrium/non-equilibrium decomposition to arrive at the $(\langle|\delta\boldsymbol{u}|^2\rangle_{\boldsymbol{x}}^a)^<(r_d,t)$ equilibrium and non-equilibrium scaling behaviour.

We investigate two closures relating $\langle\Pi^a\rangle_{\boldsymbol{x}}^<(r_d,t)$ and $(\langle|\delta\boldsymbol{u}|^2\rangle_{\boldsymbol{x}}^a)^<(r_d,t)$ (see Monin and Yaglom (1975)). The first is a low-pass "weak" Kovasznay closure (Kovasznay, 1948)

$$\langle\Pi^a\rangle_{\boldsymbol{x}}^<(r_d,t) = -D_{\mathrm{Kov}}\frac{(\langle|\delta\boldsymbol{u}|^2\rangle_{\boldsymbol{x}}^a)^<(r_d,t)^{3/2}}{r_d}, \tag{5.26}$$

where we use the term weak to note that the prefactor D_{Kov} can depend on r_d in a non-dimensional manner (e.g. r_d/L), the type of forcing (including non-forcing $\mathcal{I}=0$) and/or the Reynolds number, but not time t explicitly. We assume that the temporal variations of $\langle\Pi^a\rangle_{\boldsymbol{x}}^<(r_d,t)$ are given approximately by $(\langle|\delta\boldsymbol{u}|^2\rangle_{\boldsymbol{x}}^a)^<(r_d,t)^{3/2}$ and vice versa and the r_d-dependence is essentially left undetermined. That is, we focus on the temporal variations around some r_d-dependent average behaviour (see e.g. Iyer et al. (2020)).

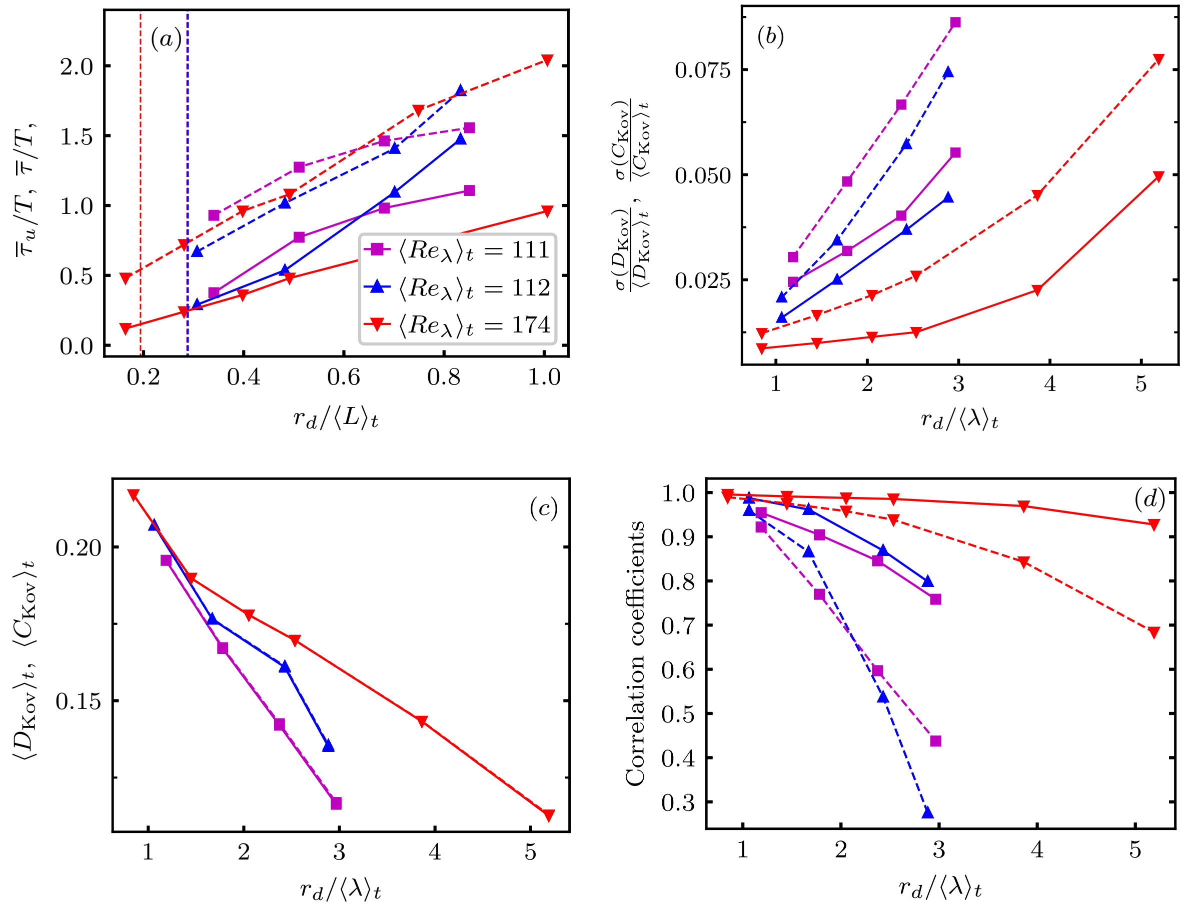

Figure 5.15: (*a*) Time-lags $\overline{\tau}_u(r_d)/T$ for the time-lagged closure (5.27) (solid lines) and time-lags $\overline{\tau}(r_d)/T$ from figure 5.7(*a*) (dashed lines). (*b*) Kovasznay prefactor normalised temporal standard deviations $\sigma(D_{\mathrm{Kov}})/\langle D_{\mathrm{Kov}}\rangle_t$ (dashed lines) and $\sigma(C_{\mathrm{Kov}})/\langle C_{\mathrm{Kov}}\rangle_t$ (solid lines). (*c*) Time-average Kovasznay prefactors $\langle D_{\mathrm{Kov}}\rangle_t$ (dashed lines) and $\langle C_{\mathrm{Kov}}\rangle_t$ (solid lines) calculated from equations (5.26)-(5.27)($\langle D_{\mathrm{Kov}}\rangle_t$ and $\langle C_{\mathrm{Kov}}\rangle_t$ overlap). (*d*) Correlation coefficients between the LHS and RHS of the closure with no time-lag (5.26) (dashed lines) and the LHS and RHS of the time-lagged closure (5.27) (solid lines).

The second closure we investigate is a time-lagged low-pass weak Kovasznay closure

$$\langle \Pi^a\rangle^<_{\boldsymbol{x}}(r_d,t) = -C_{\mathrm{Kov}}\frac{(\langle|\delta\boldsymbol{u}|^2\rangle^a_{\boldsymbol{x}})^<(r_d,t+\tau_u)^{3/2}}{r_d}, \tag{5.27}$$

where the delay $\tau_u > 0$ is increasing with r_d and C_{Kov} may have the same dependencies as we listed above for D_{Kov}. This closure is motivated by Khurshid et al. (2021) who found a significant delay between the low-pass spectral transfer and the low-pass energy spectrum at the same wavenumber (see their figure 6). There is a differential relation between $\langle \Pi^a\rangle^<_{\boldsymbol{x}}(r_d,t)$ and $(\langle|\delta\boldsymbol{u}|^2\rangle^a_{\boldsymbol{x}})^<(r_d,t)$, suggesting that a variation in $\langle \Pi^a\rangle^<_{\boldsymbol{x}}(r_d,t)$ will only lead to a variation in $(\langle|\delta\boldsymbol{u}|^2\rangle^a_{\boldsymbol{x}})^<(r_d,t)$ some time later (Khurshid et al., 2021) (see the third paragraph of section 5.2). We focus on these two closures because of their simplicity and as they allow us to compare our $(\langle|\delta\boldsymbol{u}|^2\rangle^a_{\boldsymbol{x}})^<(r_d,t)$ predictions with earlier studies which used the strong Kovasznay closure $D_{\mathrm{Kov}} = const.$ (see section 5.3.3).

Before testing these closures, we calculate the scale-dependent time-lags $\overline{\tau}_u(r_d)$ as in the previous section ($\overline{\tau}_u(r_d)$ is the delay which maximises the correlation between the LHS and RHS of (5.27) at scale r_d) and we display the results in figure 5.15(a). These $\overline{\tau}_u(r_d)$ values are significant relative to the time-lags between interscale transfer and dissipation $\overline{\tau}(r_d)$ and the quasiperiodic cascade imbalances $0.1\overline{T} \approx 0.8T$. Note that as $\overline{\tau}_u < \overline{\tau}$, the time-lag between $(\langle|\delta \boldsymbol{u}|^2\rangle_{\boldsymbol{x}}^a)^<$ at scale r_d and the dissipation rate is shorter than the time-lag between the interscale transfer at scale r_d and the dissipation rate.

We next test the two closures by calculating the Kovasznay prefactors D_{Kov} and C_{Kov} from (5.26) and (5.27) at every time instant and require that the closure(s) captures the temporal fluctuations, i.e. $\sigma(D_{\mathrm{Kov}}) \ll \langle D_{\mathrm{Kov}}\rangle_t$ or $\sigma(C_{\mathrm{Kov}}) \ll \langle C_{\mathrm{Kov}}\rangle_t$ (where $\sigma(q)$ denotes the temporal standard deviation of $q = q(t)$). Figure 5.15(b) shows that across the DNSs and scales r_d the time-lagged version of the low-pass Kovasznay closure better captures temporal variations than the non-time-lagged version of the low-pass Kovasznay closure. Figure 5.15(c) shows the similar average Kovasznay prefactors $\langle D_{\mathrm{Kov}}\rangle_t$ and $\langle C_{\mathrm{Kov}}\rangle_t$ across scales (their curves overlap). These prefactors vary considerably with r_d, implying that the $\langle \varPi^a\rangle_{\boldsymbol{x}}^<$ scale dependence is not captured by only $((\langle|\delta \boldsymbol{u}|^2\rangle_{\boldsymbol{x}}^a)^<)^{3/2}$ (a strong Kovasznay closure $D_{\mathrm{Kov}} = const.$ is not justified by our DNSs). Figure 5.15(d) shows the correlation coefficients between the LHS and RHS of (5.26) and (5.27). As could be expected, the time-lagged version of the low-pass Kovasznay closure outperforms the non-time-lagged version of the low-pass Kovasznay closure in terms of correlations. We conclude from figure 5.15 that the time-lagged low-pass weak Kovasznay closure provides a quite accurate relation between $\langle \varPi^a\rangle_{\boldsymbol{x}}^<$ and $(\langle|\delta \boldsymbol{u}|^2\rangle_{\boldsymbol{x}}^a)^<$ temporal variations in our DNSs at low to moderate $\langle Re_\lambda\rangle_t$, in particular at the lower end of $\langle\lambda\rangle_t < r_d < \langle L\rangle_t$.

The closure (5.27) and the earlier non-equilibrium dynamics can be used to develop the $(\langle|\delta \boldsymbol{u}|^2\rangle_{\boldsymbol{x}}^a)^<(r_d,t)$ scaling behaviour. We re-arrange (5.27) for $(\langle|\delta \boldsymbol{u}|^2\rangle_{\boldsymbol{x}}^a)^<(r_d,t)$ and use the formalised time-lag hypothesis to obtain

$$\begin{aligned}(\langle|\delta \boldsymbol{u}|^2\rangle_{\boldsymbol{x}}^a)^<(r_d,t) &= \Big[-r_d/C_{\mathrm{Kov}}(r_d)\langle \varPi^a\rangle_{\boldsymbol{x}}^<(r_d,t-\tau_u\Big]^{2/3}, &(5.28\mathrm{a})\\ &= \Big[r_d C_\varPi(r_d)/C_{\mathrm{Kov}}(r_d)\langle\epsilon^*\rangle_{\boldsymbol{x}}^<(t+\tau-\tau_u)\Big]^{2/3}. &(5.28\mathrm{b})\end{aligned}$$

As $\langle\epsilon^*\rangle_{\boldsymbol{x}}^<(t+\tau)$ can be approximated with a truncated Taylor series from t to $t+\tau$, we can similarly approximate $\langle\epsilon^*\rangle_{\boldsymbol{x}}^<(t+\tau-\tau_u)$ as $\tau-\tau_u<\tau$, which yields the expression

$$\begin{aligned}&(\langle|\delta \boldsymbol{u}|^2\rangle_{\boldsymbol{x}}^a)^<(r_d,t) \approx \Big[\frac{r_d C_\varPi(r_d)}{C_{\mathrm{Kov}}(r_d)}\big(\langle\epsilon^*\rangle_{\boldsymbol{x}}^<(t)+\\ &((\tau-\tau_u)\frac{d\langle\epsilon^*\rangle_{\boldsymbol{x}}(t)}{dt})^< + (\frac{(\tau-\tau_u)^2}{2}\frac{d^2\langle\epsilon^*\rangle_{\boldsymbol{x}}(t)}{dt^2})^<\big)\Big]^{2/3}, &(5.29\mathrm{a})\\ &\approx \big(\frac{r_d C_\varPi(r_d)}{C_{\mathrm{Kov}}(r_d)}\langle\epsilon^*\rangle_{\boldsymbol{x}}^<(t)\big)^{2/3}\Big[1+\frac{2}{3\langle\epsilon^*\rangle_{\boldsymbol{x}}^<(t)}((\tau-\tau_u)\frac{d\langle\epsilon^*\rangle_{\boldsymbol{x}}(t)}{dt})^< +\\ &\frac{1}{3\langle\epsilon^*\rangle_{\boldsymbol{x}}(t)}\Big(((\tau-\tau_u)^2\frac{d^2\langle\epsilon^*\rangle_{\boldsymbol{x}}(t)}{dt^2})^< - \frac{1}{3}\frac{1}{\langle\epsilon^*\rangle_{\boldsymbol{x}}^<(t)}\big((\tau-\tau_u)\frac{d\langle\epsilon^*\rangle_{\boldsymbol{x}}(t)}{dt}\big)^<)^2\Big)\Big], &(5.29\mathrm{b})\end{aligned}$$

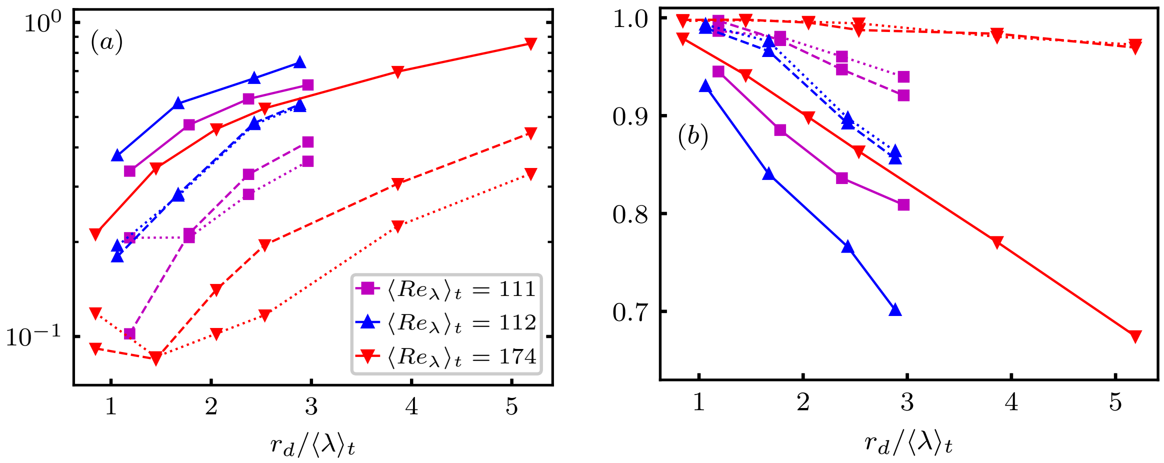

Figure 5.16: (*a*) RMSs between the LHS and RHS of (5.29b) with the zeroth-order term (solid lines), with the zeroth- and first-order term (proportional to $\tau - \tau_u$) (dashed lines) and with the full RHS of (5.29b) (dotted lines). RMSs are normalised with $\sigma(\langle|\delta \boldsymbol{u}|^2\rangle_{\boldsymbol{x}}^a)^<)$. (*b*) The same line-styling as (*a*) but it contains correlation coefficients.

where we moved from (5.29a) to (5.29b) by "pulling" $\langle\epsilon^*\rangle_{\boldsymbol{x}}^<(t)$ out from the parenthesis before assuming small non-equilibrium corrections relative to the equilibrium behaviour. The scaling (5.29b) contains three contributions: the zeroth order/equilibrium contribution independent of $\tau - \tau_u$, the first order non-equilibrium contribution proportional to $\tau - \tau_u$ and the second-order non-equilibrium contribution proportional to $(\tau - \tau_u)^2$. Note that this expansion parameter $\tau - \tau_u$ differs from the expansion parameter for the non-equilibrium dynamics τ due to finite time-lags between $\langle \Pi^a\rangle_{\boldsymbol{x}}^<$ and $(\langle|\delta \boldsymbol{u}|^2\rangle_{\boldsymbol{x}}^a)^<$.

We next test (5.29b) in terms of residuals and correlations in figure 5.16 and we investigate how the behaviour depends on the inclusion of the first-order and second-order non-equilibrium corrections (we use for the calculations $\tau - \tau_u = \overline{\tau}(r_d) - \overline{\tau}_u(r_d)$). There are significant decreases in residuals and increases in correlations by including the first-order non-equilibrium term in the scaling compared to only the zeroth-order term. This observation is valid across scales and DNSs. At the lower end of $\langle\lambda\rangle_t < r_d < \langle L\rangle_t$, the first-order non-equilibrium scaling captures $80\% - 90\%$ of the $\langle|\delta \boldsymbol{u}|^2\rangle_{\boldsymbol{x}}^a)^<$ fluctuations compared to $65\% - 80\%$ with the zeroth-order prediction. The largest improvements in accuracy are seen at the highest Reynolds number where the truncated series expansion of the non-equilibrium dynamics and the time-lagged low-pass weak Kovasznay closure are the most accurate. This might also explain the slight improvement in accuracy by including the second-order term at the highest Reynolds number, but this effect seems negligible at the lower Reynolds numbers.

The results in figures 5.15-5.16 show that the low-pass non-equilibrium dynamics along with an appropriate time-lagged relation between interscale transfer and $\langle|\delta \boldsymbol{u}|^2\rangle_{\boldsymbol{x}}^a)^<$ can be used to develop an accurate $\langle|\delta \boldsymbol{u}|^2\rangle_{\boldsymbol{x}}^a)^<$ non-equilibrium scaling. The scaling is applicable at our low to moderate Reynolds numbers and significantly outperforms the equilibrium

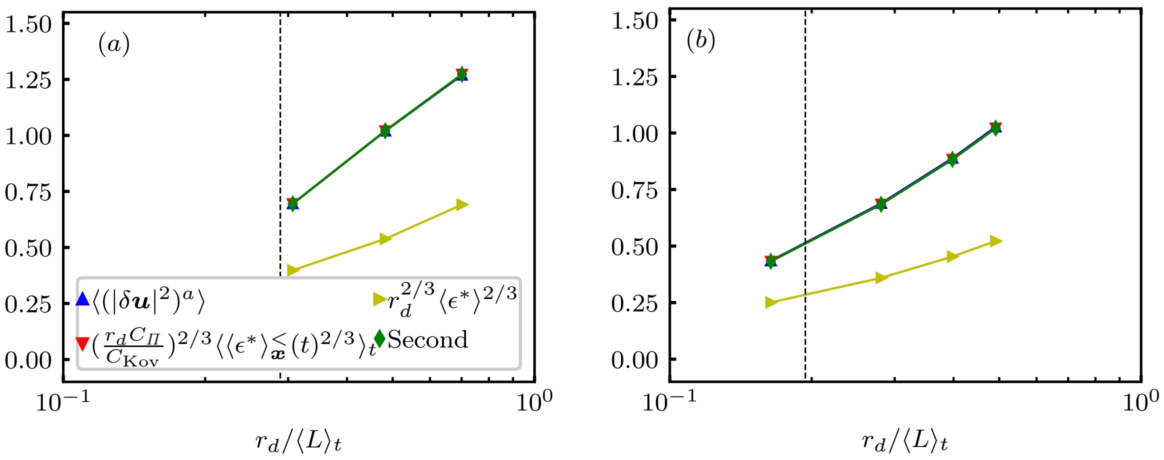

Figure 5.17: Time-averaged $\langle(|\delta \boldsymbol{u}|^2)^a\rangle$, zeroth-order time-averaged non-equilibrium scaling $(r_d C_\Pi(r_d)/C_{\mathrm{Kov}(r_d)})^{2/3}\langle\langle\epsilon^*\rangle_{\boldsymbol{x}}^{<}(t)^{2/3}\rangle_t$, the K41 scaling $r_d^{2/3}\langle\epsilon^*\rangle^{2/3}$ and the time-average of the RHS of (5.29b) ("Second"). The blue, red and green lines overlap and the black vertical lines denote $\langle\lambda\rangle_t/\langle L\rangle_t$. The y-axis unit is arbitrary. (a) $\langle Re_\lambda\rangle_t = 112$, (b) $\langle Re_\lambda\rangle_t = 174$. The behaviour is similar with the ABC forcing (DNS2).

scaling at scales $\langle\lambda\rangle_t < r_d < \langle L\rangle_t$. We remind the reader that the physical basis for the $\langle|\delta \boldsymbol{u}|^2\rangle_{\boldsymbol{x}}^a)^<$ scaling is time-lags between low-pass interscale transfers and subsequent low-pass $\langle|\delta \boldsymbol{u}|^2\rangle_{\boldsymbol{x}}^a)^<$ and dissipation temporal variations which are limited, yet significant enough to make $\langle|\delta \boldsymbol{u}|^2\rangle_{\boldsymbol{x}}^a)^<$ evolve in time according to (5.29b). This physical basis and the similar delay behaviour observed in Khurshid et al. (2021) at $\langle Re_\lambda\rangle_t \leq 390$ suggest that the non-equilibrium scaling (5.29b) might extend to and possibly improve at higher Reynolds numbers. Higher $\langle Re_\lambda\rangle_t$ DNSs are required to test the applicability of (5.29b).

In forced homogeneous turbulence $(\langle|\delta \boldsymbol{u}|^2\rangle_{\boldsymbol{x}}^a)^<$ evolves according to the quasiperiodic turbulence evolution and on average it is only the zeroth order term which is non-zero (see figure 5.17). If we consider an ensemble-average of (5.29b), we have at first order

$$\langle\langle|\delta \boldsymbol{u}|^2\rangle_{\boldsymbol{x}}^a(r_d)^<\rangle_E = \frac{(r_d C_\Pi(r_d)}{C_{\mathrm{Kov}}(r_d)}^{2/3}\Big[\langle(\langle\epsilon^*\rangle_{\boldsymbol{x}}^<)^{2/3}\rangle_E + \langle\frac{2}{3(\langle\epsilon^*\rangle_{\boldsymbol{x}}^<)^{1/3}}((\tau-\tau_u)\frac{d\langle\epsilon^*\rangle_{\boldsymbol{x}}}{dt})^<\rangle_E\Big]. \tag{5.30}$$

The dissipation rate decay in freely decaying periodic/homogeneous turbulence and the time-lag behaviour (5.29b) yield a non-zero (negative) average effect on the $\langle\langle|\delta \boldsymbol{u}|^2\rangle_{\boldsymbol{x}}^a(r_d)^<\rangle_E$ scaling. Hence, even though the average effect of the $(\langle|\delta \boldsymbol{u}|^2\rangle_{\boldsymbol{x}}^a)^<$ non-equilibrium corrections equal zero in forced homogeneous/periodic turbulence, these or analogue time-lag non-equilibrium corrections might be important in other flows. By extending the above framework to statistically stationary spatially decaying flows one can imagine similar non-zero average time-lag effects on the $\langle\langle|\delta \boldsymbol{u}|^2\rangle_{\boldsymbol{x}}^a(r_d)^<\rangle_t$ scaling behaviour.

We next verify a popular time-lag scaling with our DNSs, allowing us to compare our non-equilibrium predictions with similar predictions from other studies.

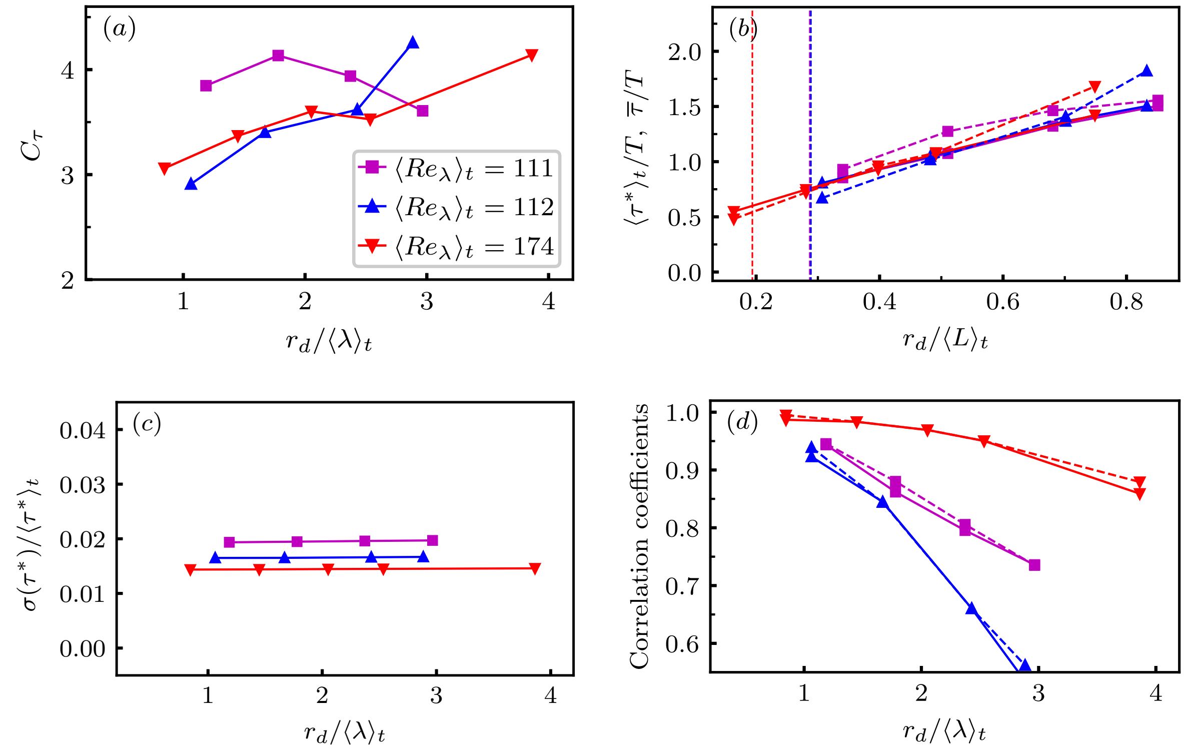

Figure 5.18: (*a*) Coefficient in (5.31) $C_\tau = \overline{\tau}(r_d)/(r_d^{2/3}(C_{\text{Kov}}/C_\Pi)^{1/3}\langle\langle\epsilon^*\rangle_{\boldsymbol{x}}^{<}(t)^{-1/3}\rangle_t)$. (*b*) Comparison of $\langle\tau^*\rangle_t$ (solid lines) and $\overline{\tau}$ (dashed lines). (*c*) Temporal standard deviations of τ^* relative to its time-averaged values across scales. Vertical lines denote $\langle\lambda\rangle_t/\langle L\rangle_t$. (*d*) Correlation coefficients between $\langle\Pi\rangle_{\boldsymbol{x}}^{a}(r_d,t)$ and $\langle\epsilon^*\rangle_{\boldsymbol{x}}(t+\tau^*(r_d,t))$ (solid lines) and $\langle\epsilon^*\rangle_{\boldsymbol{x}}(t+\overline{\tau}(r_d))$ (dashed lines).

5.3.3 Local Delay Scaling and Comparison with Similar Studies

A classical model for estimating the time-lag at some intermediate scale r_d to dissipative scales is the "loca"l scaling $\tau^*(r_d,t) \sim r_d/(\langle|\delta\boldsymbol{u}|^2\rangle_{\boldsymbol{x}}^{a})^{<}(r_d,t)^{1/2}$ (Lumley, 1992; Wan et al., 2010; Ballouz et al., 2020; Vela-Martín, 2022b). This scaling follows from dimensional necessity if one assumes that τ^* at scale r_d is only dependent on the local length and velocity scales. We can rephrase this local τ^*-estimate by use of the $(\langle|\delta\boldsymbol{u}|^2\rangle_{\boldsymbol{x}}^{a})^{<}(r_d,t)$ scaling (5.29b) at zeroth-order as

$$\tau^*(r_d,t) = C_\tau r_d^{2/3}\left(\frac{C_{\text{Kov}}(r_d)}{C_\Pi(r_d)}\right)^{1/3}\langle\epsilon^*\rangle_{\boldsymbol{x}}^{<}(t)^{-1/3}, \tag{5.31}$$

where $C_\tau = const. > 0$. We use only the zeroth-order $(\langle|\delta\boldsymbol{u}|^2\rangle_{\boldsymbol{x}}^{a})^{<}(r_d,t)$ scaling as this is sufficiently accurate to capture the time-lagged cascade behaviour (and it avoids a non-linear expression for τ^*). In contrast to the earlier $\overline{\tau}(r_d)$ time-lag estimate, $\tau^*(r_d,t)$ varies not only with scale r_d but also with time t.

Figure 5.18 tests the accuracy of the local delay scaling τ^* (5.31). We first calculate the proportionality coefficient C_τ in (5.31) by applying a time average to this relation and matching it with $\overline{\tau}(r_d)$ (see the caption of figure 5.18 and figure 5.18(*a*)). C_τ seems to approximately equal 3.5 for $\langle\lambda\rangle_t < r_d < \langle L\rangle_t$. We use this C_τ-value to calculate $\tau^*(r_d,t)$ with (5.31) at every time-instant and calculate the correlation coefficients between $\langle \varPi^a\rangle_{\boldsymbol{x}}(r_d,t)$ and $\langle\epsilon^*\rangle_{\boldsymbol{x}}(t+\tau^*(r_d,t))$. Having matched τ^* with $\overline{\tau}$ in a time-averaged sense, it is not surprising that their time-average values are very similar (see figure 5.18(b)). The results in figure 5.18(c) are less obvious and show that the temporal standard deviations of τ^* are tiny compared $\langle\tau^*\rangle_t$. If we consider $\tau^*(r_d=\langle\lambda\rangle_t)\approx 0.5T$ (see figure 5.18(c)), the typical τ^* variation is order $0.01-0.02T$ which is almost three orders of magnitude smaller than $\overline{T}=8T$. Hence, it is not surprising that the correlation coefficients between the interscale transfer and dissipation are close to identical with a $\overline{\tau}(r_d)$ time-lag or with a $\tau^*(r_d,t)$ time-lag (see figure 5.18(d)). Equation (5.31) provides a decent fit to $\overline{\tau}$ with negligible effect of $\tau^*(r_d,t)$ temporal variations. Note that the r_d-dependency of τ^* is given by $r_d^{2/3}(C_{\mathrm{Kov}}(r_d)/C_{\varPi}(r_d))^{1/3}$ which has approximately the same r_d-dependency as $\overline{\tau}(r_d)$. Figure 5.7(a) in section 5.2 suggests that $\overline{\tau}(r_d)$ follows a linear r_d-scaling rather than a $r_d^{2/3}$-scaling in our DNSs due to the r_d-dependencies of C_{Kov} and $C_{\varPi}$. Above we only used the local delay scaling to approximate the delay between interscale transfer and dissipation τ. Figure 5.15(a) suggests that $\overline{\tau}_u$ follows approximately the same local scaling with a proportionality coefficient $C_{\tau_u} < C_\tau$. Having verified the local delay scaling, we insert it into the first-order non-equilibrium dynamics (5.24)

$$\langle\mathcal{A}_t^a\rangle_{\boldsymbol{x}}^<(r_d,t) = C_\tau C_{\varPi}(r_d)^{2/3}C_{\mathrm{Kov}}(r_d)^{1/3}r_d^{2/3}\Big(\frac{1}{\langle\epsilon^*\rangle_{\boldsymbol{x}}^<(t)^{1/3}}\frac{d\langle\epsilon^*\rangle_{\boldsymbol{x}}(t)}{dt}\Big)^<, \tag{5.32}$$

and in the first-order non-equilibrium second-order structure function scaling (5.29b)

$$\begin{aligned}\langle(|\delta\boldsymbol{u}|^2)^a\rangle_{\boldsymbol{x}}^<(r_d,t) = \Big(\frac{C_{\varPi}(r_d)}{C_{\mathrm{Kov}}(r_d)}\Big)^{2/3}r_d^{2/3}\Big[\langle\epsilon^*\rangle_{\boldsymbol{x}}^<(t)^{2/3}\\ +\frac{2}{3}(C_\tau-C_{\tau_u})\Big(\frac{C_{\mathrm{Kov}}(r_d)}{C_{\varPi}(r_d)}\Big)^{1/3}r_d^{2/3}\frac{1}{\langle\epsilon^*\rangle_{\boldsymbol{x}}^<(t)^{1/3}}\Big(\frac{1}{\langle\epsilon^*\rangle_{\boldsymbol{x}}^<(t)^{1/3}}\frac{d\langle\epsilon^*\rangle_{\boldsymbol{x}}(t)}{dt}\Big)^<\Big].\end{aligned} \tag{5.33}$$

These expressions can be compared with similar studies. Yoshizawa (1994); Woodruff and Rubinstein (2006); Horiuti and Tamaki (2013) and Bos and Rubinstein (2017) consider the (spectral) cascade dynamics in terms of a decomposition into equilibrium and non-equilibrium parts, where the non-equilibrium part is represented as a perturbation expansion. Horiuti and Tamaki (2013) and Bos and Rubinstein (2017) combine this assumption with a strong Kovaznay closure ($D_{\mathrm{Kov}}=\mathit{const.}$) to arrive at the following non-equilibrium dynamics at first-order

$$\frac{\partial E(k,t)}{\partial t} = \frac{2}{3}\frac{1}{D_K^{2/3}}k^{-5/3}\frac{1}{\langle\epsilon\rangle_{\boldsymbol{x}}(t)(t)^{1/3}}\frac{d\langle\epsilon\rangle_{\boldsymbol{x}}(t)(t)}{dt}, \tag{5.34}$$

and the following energy spectrum at zeroth- and first-order

$$E(k,t) = \frac{1}{D_K^{2/3}}\langle\epsilon\rangle_{\boldsymbol{x}}(t)^{2/3}k^{-5/3}\Big[1+\frac{2}{3}\frac{1}{D_K^{2/3}}k^{-2/3}\frac{1}{\langle\epsilon\rangle_{\boldsymbol{x}}(t)^{4/3}}\frac{d\langle\epsilon\rangle_{\boldsymbol{x}}(t)}{dt}\Big]. \tag{5.35}$$

As there is no one-to-one correspondence between the spectral and physical space cascade dynamics and between the energy spectrum and the second-order structure function (Frisch, 1995), we will limit our comparison to three qualitative differences between (5.32)-(5.33) and (5.34)-(5.35). Such a qualitative comparison is supported by the physical space time-lag results in this chapter and the Fourier space time-lag results in the literature (see e.g. Goto and Vassilicos (2016a)); if time-lag effects are important in the energy cascade, they should be similarly predictable in both physical and Fourier spaces. Note that the scale/wavenumber dependencies of (5.32)-(5.34) and (5.33)-(5.35) are equal (disregarding C_{Π} and C_{Kov} r_d-variations for now).

The first qualitative difference between these expressions is the absence of low-pass filtering in (5.34)-(5.35). By developing (5.32)-(5.33) from the formalised time-lag hypothesis, we showed that it is only for the low-pass filtered dynamics a truncated series expansion of the non-equilibrium dynamics is applicable. The second qualitative difference is the neglect of the time-lag between interscale transfers and the energy spectrum in (5.35) compared to the presence of this effect in (5.33) in terms of $C_{\tau} - C_{\tau_u}$. This has the effect of overestimating the first-order non-equilibrium effect for the energy spectrum scaling. Finally, finite Reynolds number effects are discarded in (5.34)-(5.35) in terms of no $C_{\Pi}(=1)$ or D_K r_d-dependencies. One can expect that these three differences limit the accuracy of the Fourier space predictions (5.34)-(5.35). By starting with a Fourier space formalised time-lag hypothesis and repeating the steps in this section, one could arrive at more accurate Fourier space predictions and develop their limitations/applicability.

To summarise this section, our DNSs of low to moderate $\langle Re_{\lambda} \rangle_t$ forced homogeneous/periodic turbulence support the non-equilibrium predictions (5.32)-(5.33) (and the more general expressions (5.24)-(5.29b)), in particular at the lower end of $\langle \lambda \rangle_t < r_d < \langle L \rangle_t$. The key to arriving at these relations is our formalisation of the cascade time-lag idea. From this starting point, we develop under which conditions the formalised time-lag hypothesis can be used to develop simple non-equilibrium corrections to local equilibrium. An appropriate time-lagged relation between the interscale transfer rate and $\langle (|\delta \boldsymbol{u}|^2)^a \rangle_{\boldsymbol{x}}^{<}(r_d, t)$ is also required to develop non-equilibrium corrections to the second-order structure function scaling. Our physical space rather than Fourier space approach facilitates a similar assessment of cascade unsteadiness effects in other appropriate turbulent flow regions (see e.g. appendix D with (5.32)-(5.33) adapted to grid turbulence).

5.4 Time-lags and Dissipation Scaling Laws

We end this chapter by developing a new dissipation scaling law for forced homogeneous/periodic turbulence based on the phenomenology of a time-lagged energy cascade and the quasiperiodic turbulence evolution; typically in forced homogeneous/periodic turbulence the dissipation rate and the large-scale kinetic energy are in anti-phase with long time periods $\overline{T}$ of order $10 - 20T$ (and this behaviour can be understood in terms

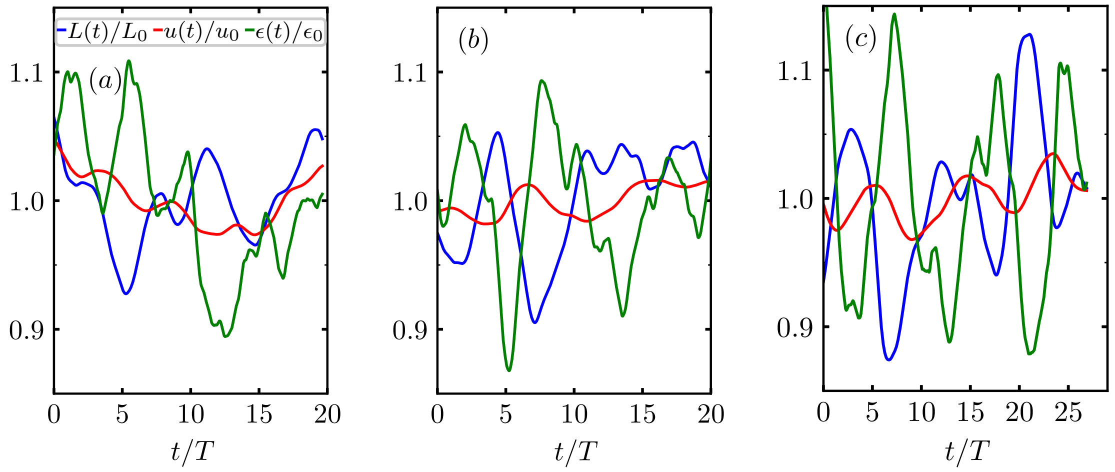

Figure 5.19: Time series of $u(t)/u_0$, $L(t)/L_0$ and $\epsilon(t)/\epsilon_0$. (a, b, c): (DNS2,DNS3,DNS4).

of a time-lagged cascade (Goto et al., 2017)). We think of this behaviour as composed of two phases: in the first phase there is more than average kinetic energy at the large scales and the dissipation rate is lower than average and vice versa in the second phase. We translate this large- and small-scale anti-correlation into a dissipation scaling, noting

$$L(t) = 3\pi/4 \int_0^\infty k^{-1} E(k,t)/K(t) dk, \tag{5.36a}$$

$$K(t) = \int_0^\infty E(k,t) dk, \tag{5.36b}$$

such that $L(t)/L_0$ (where $L_0 \equiv \langle L \rangle_t$) can be interpreted: the ratio of the large-scale energy to the total energy at time t relative to its average ratio (note the large-scale weighing in (5.36a) from k^{-1}). When $L(t)/L_0 > 1$, there is more than average energy among the large scales such that we expect less than average dissipation $\langle \epsilon \rangle_{\boldsymbol{x}}(t)/\epsilon_0 < 1$ (where $\epsilon_0 = \langle \epsilon \rangle_t$) and similarly when $L(t)/L_0 < 1$ we expect $\langle \epsilon \rangle_{\boldsymbol{x}}(t)/\epsilon_0 > 1$. This argument is restricted to the case of limited kinetic energy variations $K(t) \approx const.$ and note that the velocity r.m.s. $u(t) = \sqrt{2/3K(t)}$ has stronger intermediate-scale dependencies than $L(t)$.

The time series in figure 5.19 reiterate the statistical tendency of anti-phase $\langle \epsilon \rangle_{\boldsymbol{x}}(t)$ and $L(t)$ observed in forced homogeneous turbulence (Goto and Vassilicos, 2015, 2016a). Note the small $u(t)/u_0$ fluctuations in comparison in figures 5.19(b, c), which are neither in phase nor in anti-phase with $\langle \epsilon \rangle_{\boldsymbol{x}}(t)$ (where $u_0 = \langle u \rangle_t$). The ABC forcing time series (figure 5.19(a)) are different and seem to contain a time scale of the order of the sampling period $20T$. This seems related to the less pronounced quasiperiodic behaviour of DNS2 compared to DNS3-DNS4, measured in terms of correlation functions (see figure 5.8).

If one assumes that the above redistributive effect between large and small scales determines the dissipation scaling, which seems plausible in our DNSs DNS3-DNS4, one scaling which might capture this behaviour is the "redistributive dissipation scaling"

$$\frac{\langle \epsilon \rangle_{\boldsymbol{x}}(t) - \epsilon_0}{\epsilon_0} \sim -\frac{L(t) - L_0}{L_0}. \tag{5.37}$$

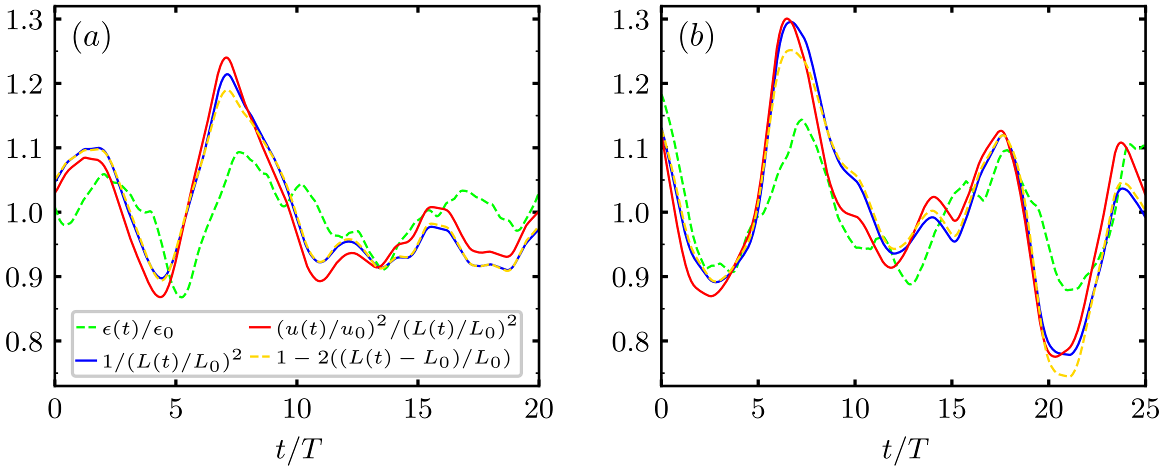

Figure 5.20: Time series related to the non-equilibrium and redistributive dissipation scalings, normalised by their time-average values. (a, b) $\langle Re_\lambda \rangle_t = (112, 174)$.

We use our DNSs to consider the performance of this scaling compared to the Taylor dissipation scaling law $\langle \epsilon \rangle_{\boldsymbol{x}}(t) \sim u(t)^3/L(t)$ (Taylor, 1935; Kolmogorov, 1941b) and the non-equilibrium dissipation scaling law (Goto and Vassilicos, 2015)

$$\frac{\langle \epsilon \rangle_{\boldsymbol{x}}(t)}{\epsilon_0} \sim \frac{(u(t)/u_0)^2}{(L(t)/L_0)^2}. \tag{5.38}$$

The correlation coefficients between the LHS and RHS of the redistributive, Taylor and non-equilibrium scaling laws in DNS3-DNS4 read $(0.53, 0.75)$, $(0.42, 0.61)$ and $(0.52, 0.75)$. The Taylor scaling is presumably outperformed by the redistributive and non-equilibrium scaling laws as it weighs $u(t)$ too heavily compared to $L(t)$. The relative importance of $u(t)$ and $L(t)$ can be assessed by considering their importance in the non-equilibrium dissipation scaling in figure 5.20. These time series show that the $(L(t)/L_0)^{-2}$ dependence (blue lines) is key in capturing the $\langle \epsilon \rangle_{\boldsymbol{x}}(t)/\epsilon_0$ temporal variations (green lines), while the inclusion of $(u(t)/u_0)^2$ (red lines) yields no clear improvement or deterioration. We tested the dissipation dependence on $u(t)$ further by calculating correlations for $\langle \epsilon \rangle_{\boldsymbol{x}}(t)/\epsilon_0 \sim (u(t)/u_0)^m$ with integer m and $|m| \leq 4$. These correlations do not exceed 0.01. The correlations with the three dissipation scalings are attributable to $L(t)$ for DNS3-DNS4.

The correlations with the redistributive and non-equilibrium scaling are very similar and seem to increase with the Reynolds number. This latter point might be explained by the phenomenology of a time-lagged cascade, underpinning the suggested $\langle \epsilon \rangle_{\boldsymbol{x}}(t)$ and $L(t)$ anti-phase behaviour, which should increase in validity as the range of scales increases. Concerning the close-to-identical behaviour of the non-equilibrium scaling and the redistributive scaling, this follows from the limited effect of $(u(t)/u_0)^2$ and the order 0.1 fluctuations of $L(t)/L_0$ around 1 such that

$$\frac{1}{(L(t)/L_0)^2} \approx 1 - 2\frac{L(t) - L_0}{L_0}. \tag{5.39}$$

If this first-order Taylor approximation of $(L(t)/L_0)^{-2}$ and $u(t) \approx u_0$ are inserted into the non-equilibrium scaling (5.38), one attains after re-arranging the redistributive scaling law (5.37). It is clear from figure 5.20 that this first-order Taylor approximation follows $(L(t)/L_0)^{-2}$ very closely in DNS3 and DNS4 (compare the blue and yellow lines). It follows that the non-equilibrium scaling reduces to the redistributive scaling in DNS3-DNS4. This is important as the redistributive scaling law is simpler (there is no $u(t)/u_0$ dependence and it is linear in $L(t)$) so it is easier to analyse and interpret. Given the circumstances in DNS3-DNS4, the non-equilibrium dissipation scaling can be interpreted as resulting from a time-lagged energy cascade undergoing quasiperiodic evolution (i.e. the justification of the redistributive scaling). $L(t)/L_0$ captures the large-scale behaviour and its small-scale anti-correlation tendency predicts the dissipation rate.

It must be emphasised that the justification of the redistributive scaling law is restricted to relatively limited temporal variations in kinetic energy $K(t) \approx const.$ At higher Reynolds numbers, the $K(t)$ temporal variations might be larger and make the non-equilibrium and redistributive scaling laws differ. The correlation coefficients with the redistributive, non-equilibrium and Taylor scaling laws for DNS2 read $(0.28, 0.64, 0.78)$. In this simulation with the time scale of order $20T$, the dissipation scaling behaviour can not be explained by redistribution (note however the anti-correlation tendency between $\epsilon(t)/\epsilon_0$ and $L(t)/L_0$ also in this DNS). The $u(t)/u_0$ and $\epsilon(t)/\epsilon_0$ behaviour with time scale $20T$ seem to have a similar phase. Hence, $u(t)/u_0$ correlates with $\epsilon(t)/\epsilon_0$ and the scaling which includes the strongest $u(t)/u_0$-dependency (the Taylor scaling) correlates most strongly with the dissipation. Long DNS integration periods would presumably yield similar dissipation scaling behaviour for DNS2 as with DNS3-DNS4.

The redistributive scaling might not be limited to forced homogeneous turbulence. One can argue that in the initial period of decaying homogeneous turbulence, the dissipation scales as in forced homogeneous turbulence due to the finite large-to-small-scale time-lag. This is suggested by the decaying homogeneous turbulence DNSs of Goto and Vassilicos (2016b) who found

$$\frac{\langle\epsilon\rangle_{\boldsymbol{x},E}(t)}{\epsilon_0} \sim \frac{(\langle u\rangle_E(t)/u_0)^2}{(\langle L\rangle_E(t)/L_0)^2} \tag{5.40}$$

satisfied for $t < 3T$, where L_0, u_0 and $\epsilon_0 \sim u_0^3/L$ are characteristic length, velocity and dissipation scales when the forcing was turned off at $t = 0$. In the DNSs of Goto and Vassilicos (2016b), the forcing was turned off when $\langle\epsilon\rangle_{\boldsymbol{x}}(t)/\epsilon_0$ reached a maximum such that $L(t)/L_0$ initially had a small value. One can expect the quasiperiodic evolution to next increase $\langle L\rangle_E(t)/L_0$, redistributing energy from small and intermediate scales to large scales, with a consequent reduction in $\langle\epsilon\rangle_{\boldsymbol{x},E}(t)/\epsilon_0$. This anti-correlation tendency can be represented by the non-equilibrium/redistributive dissipation scaling (the $\langle L\rangle_E(t)/L_0$ variations from unity are limited in this initial period (see their figure 1(a))). One might expect from the ubiquity of the non-equilibrium dissipation scaling law (Vassilicos, 2015) that this redistributive effect is rather common in turbulent flows. It remains to be determined whether the redistributive effect can explain at least some of these results.

We end this section by noting that the scaling behaviour and cascade dynamics in decaying homogeneous turbulence at times $t > 3T$ in Goto and Vassilicos (2016b) can also be explained by a time-lagged energy cascade. For times $t > 3T$ in Goto and Vassilicos (2016b) (i) the interscale transfer, dissipation and unsteadiness terms are all similar in size and decaying proportionally (this behaviour is denoted as "balanced non-equilibrium"). Moreover, for $t > T$ (ii) the large-scale interscale transfer scales as $\langle u \rangle_E(t)^3/\langle L \rangle_E(t)$ for $t > T$ such that the dissipation follows a Taylor scaling for $t > 3T$ (i.e. (i)-(ii) combined). Balanced non-equilibrium cascades were developed further in Steiros (2022) with non-equilibrium predictions of the cascade dynamics and energy spectrum scaling consistent with DNSs and grid turbulence experiments. It remains to explain why this transition to balanced non-equilibrium behaviour comes about and the time of this transition.

This question might be addressed with the argument of Bos et al. (2007) and our results. Bos et al. (2007) assumes the large-scale scaling (ii), a time-lagged cascade and power-law decay of $\langle u \rangle_E(t)$ and $\langle L \rangle_E(t)$. These assumptions result in a Taylor scaling and self-similar interscale transfer, dissipation and unsteadiness terms at times $t > T_0 + T_c$ (i.e. balanced non-equilibrium), where T_0 is the time (ii) is first valid and T_c is the time-lag between large-scale interscale transfer and dissipation. That is, if the cascade is time-lagged, the dissipation at e.g. $t = 0$ will scale according to the past behaviour at time $t \approx -\overline{\tau}(L_0)$ when the turbulence was still forced (i.e. non-equilibrium scaling). As far as the dissipation is concerned, the effect of turning off the forcing is not felt before the large scales have reacted/changed behaviour due to the force removal and this effect has been cascaded to the small scales. Our figure 5.15(a) suggests that the kinetic energy at scale $\langle L \rangle_t$ is only affected by a change in the interscale transfer/cascade dynamics after a time $\tau_u(\langle L \rangle_t) \approx T$, i.e. at time $t = T_0$ when (ii) is valid in Goto and Vassilicos (2016b). It takes approximately the time $T_c = \overline{\tau}(L_0) \approx 2T$ before this new large-scale behaviour affects the dissipation at time $t = 3T$, the time reported in Goto and Vassilicos (2016b).

In sum, the scaling behaviour in decaying homogeneous turbulence might be divided into an initial period $t < T_0 + T_c$ with redistributive scaling followed by a later period of Taylor/decay scaling $t > T_0 + T_c$ (before the final period of decay sets in (Batchelor, 1953)). The scaling behaviour differs for the redistributive period and the decay period, but they have in common that they can be explained in terms of a time-lagged energy cascade. The similar scaling behaviour in e.g. grid turbulence (Vassilicos, 2015) suggests that such a dual subdivision of the scaling behaviour might be beneficial to synthesise experimental/DNS results on dissipation scaling behaviour across turbulent flows.

5.5 Summary

The concept of a time-lag between larger-scale interscale transfer and dissipation is commonly employed qualitatively in studies of the turbulent energy cascade. In this chapter we propose a physical space formalisation of this concept for homogeneous/periodic turbulence denoted the formalised time-lag hypothesis. This hypothesis connects the present spatially averaged interscale transfer rate with the future spatially averaged dissipation rate and it is a generalisation of the cascade time-lag hypothesis of Bos et al. (2007), which is only intended in an ensemble-averaged sense for freely decaying homogeneous turbulence at large scales. Building on the argument in Lumley (1992), we argue that the physical basis for this hypothesis is a fluctuating, unsteady, inertial (i.e. no direct fluctuating effects of production, dissipation and diffusion) and unidirectional energy cascade.

The formalised time-lag hypothesis is consistent with the time/ensemble-averaged behaviour in homogeneous/periodic turbulence and it is able to predict approximately $80 - 90\%$ of the dissipation rate fluctuations at the Taylor scale in our low to moderate Reynolds number DNSs of forced homogeneous/periodic turbulence. This compares with $40-50\%$ of the dissipation fluctuations with local equilibrium. At scales approaching the integral scale or scales below the Taylor scale, the hypothesis is less accurate with a large part of the dissipation fluctuations unaccounted for. It is primarily the low-frequency quasiperiodic cascade imbalances between larger-scale interscale transfer and dissipation (Goto and Vassilicos, 2015; Goto et al., 2017) which is captured by the formalised time-lag hypothesis. The time-lag estimate must be sufficiently accurate to capture these low-frequency temporal variations and a simple delay estimate only dependent on scale r_d is able to achieve this accuracy in our DNSs. Our results indicate that the delay includes both cascading and diffusive components.

We used the formalised time-lag hypothesis to derive simple non-equilibrium corrections to local equilibrium. In practice, this requires the evolution of the dissipation rate over a delay time τ to be approximated by its truncated Taylor series. This is not feasible at and above the Taylor scale in our low to moderate Reynolds number DNSs with the dissipation rate evolving too rapidly compared to the time delay. However, this approach is feasible for the low-pass filtered dynamics and second-structure function scaling at time scales similar to and larger than the integral time scale T. In this case our predictions for the non-equilibrium dynamics are consistent with the DNSs with significant improvements over the no-time-lag predictions, in particular at scales close to the Taylor scale. When combined with an appropriate time-lagged closure between the low-pass filtered interscale transfer and $(\langle|\delta \boldsymbol{u}|^2\rangle_{\boldsymbol{x}}^a)^<$, we obtain highly accurate second-order structure function scalings at the lower end of $\langle\lambda\rangle_t < r_d < \langle L\rangle_t$. These predictions are similar to earlier non-equilibrium predictions (Horiuti and Tamaki, 2013; Bos and Rubinstein, 2017), but they are restricted to the low-pass filtered behaviour, they do account for finite Reynolds number effects from e.g. non-negligible large-scale energy injection and use a time-lagged Kovasznay closure to take into account the finite time-lag between interscale transfer and $(\langle|\delta \boldsymbol{u}|^2\rangle_{\boldsymbol{x}}^a)^<$. By developing non-equilibrium predictions from a clear physical basis (i.e. the formalised time-lag hypothesis), the limitations of our non-equilibrium predictions are clear. Moreover, by generalising the formalised time-lag hypothesis to more complex flows, non-equilibrium predictions can be developed more generally.

We used the phenomenology of a time-lagged energy cascade to motivate a new redistributive dissipation scaling law for forced homogeneous/periodic turbulence. This scaling law specifies an anti-correlation tendency between large-scale energy and energy dissipation from the large-to-small-scale quasiperiodic turbulence evolution (Goto et al., 2017). As energy becomes concentrated at large scales, the small-scale energy available for dissipation decreases and vice versa. The successful non-equilibrium dissipation scaling law (Goto and Vassilicos, 2015) reduces to the redistributive scaling law in our DNSs when the velocity r.m.s. have limited fluctuations relative to its average value and the integral length scale to its average value has fluctuations around 1 less than or order 0.1. Hence, the success of the non-equilibrium scaling law in our DNSs can be understood in terms of a time-lagged energy cascade undergoing quasiperiodic evolution. We showed that this new scaling along with the Taylor scaling, as derived by Bos et al. (2007) from time-lag considerations, can be used to tentatively synthesise the reported dissipation scalings in both forced and freely decaying homogeneous turbulence. These results suggest that a common feature underlying these dissipation scalings is a (non-equilibrium) time-lagged energy cascade.

6. Conclusion

The average cascade picture in statistically stationary and homogeneous/periodic turbulence is drastically different from the spatio-temporally fluctuating cascade dynamics hidden behind it. It makes limited sense to attempt to model an unrepresentative average cascade picture rather than attempt to model the underlying cascade dynamics which appear once the clouding effects of averages are lifted. In this thesis we have studied the local cascade dynamics (rather than the average cascade dynamics) in forced homogeneous/periodic turbulence in light of the objectives outlined in section 1.3.

In chapter 3 we used the Helmholtz decomposition to decompose the two-point cascade dynamics into solenoidal and irrotational KHMH equations. At scales $r_d > \langle \lambda \rangle_t$ our DNSs of forced homogeneous/periodic turbulence at low to moderate $\langle Re_\lambda \rangle_t$ show that the solenoidal cascade dynamics can be reduced to a balance between Lagrangian transport and solenoidal interscale transfer $\mathcal{A}_t + \mathcal{T}_{\overline{S}} \approx -\Pi'_{\overline{S}}$. This balance is a good approximation for most times and most locations. As more than average $|\delta \boldsymbol{u}|^2$ is cascaded from larger to smaller scales at a particular location, $|\delta \boldsymbol{u}|^2$ increases; and as more than average $|\delta \boldsymbol{u}|^2$ is inversely cascaded from smaller to larger scales, $|\delta \boldsymbol{u}|^2$ decreases. The solenoidal interscale transfer rate derives from non-local (in space) vortex stretching and tilting effects of its spatial vicinity. The fluctuation intensity of the Lagrangian transport $\mathcal{A}_t + \mathcal{T}_{\overline{S}}$ is much reduced by comparison to $\mathcal{A}_t$ and $\mathcal{T}_{\overline{S}}$ as a consequence of two-point sweeping (and increasingly so as the scale decreases). At relatively rare interscale transfer events, viscous effects are non-negligible in the cascade dynamics (together with $\Pi'_{\overline{S}}$ and $\mathcal{A}_t + \mathcal{T}_{\overline{S}}$) and our results indicate that viscous effects are essential for the negative skewness of $\Pi_{\overline{S}}$. The irrotational KHMH equation in homogeneous turbulence reduces to the exact $\Pi_{\overline{I}} = \mathcal{T}_{\overline{I}} = \mathcal{T}_p/2$, which explains the significant correlation between interscale transfer Π and pressure-velocity $\mathcal{T}_p$ found in Yasuda and Vassilicos (2018). The above key solenoidal KHMH terms and irrotational KHMH terms have typical fluctuations vastly exceeding the average cascade behaviour (characterised by $\langle \epsilon^* \rangle$) and typical dissipation fluctuations.

As we move to smaller scales $r_d < \langle \lambda \rangle_t$, the average cascade description includes effects of interscale transfer, scale space viscous diffusion and viscous dissipation. Our solenoidal KHMH analysis of a well-resolved DNS of forced homogeneous/periodic turbulence in chapter 4 shows that Lagrangian transport remains important at these scales. At low to intermediate levels of $(|\delta \boldsymbol{u}|^2)^a$ we find significant correlations between Lagrangian transport and interscale transfer and between Lagrangian transport and viscous effects

$\mathcal{D}^a$, but the correlations between interscale transfer and viscous effects are limited (and the correlations between interscale transfer and viscous dissipation/diffusion are similarly limited, in contrast with Frisch and Vergassola (1991)). There is a correlation tendency between viscous effects and interscale transfer at high $(|\delta \boldsymbol{u}|^2)^a$ events, but there are still significant correlations between $\mathcal{A}_t + \mathcal{T}_{\overline{S}}$ and these two KHMH terms. Hence, an average balance between interscale transfer and viscous effects at small scales is not typically satisfied locally in time and space. At low/high levels of $(|\delta \boldsymbol{u}|^2)^a$, physical space viscous diffusion tends to significantly increase/decrease $(|\delta \boldsymbol{u}|^2)^a$ locally.

The spatially averaged turbulent energy cascade we study in chapter 5 is the spatially averaged manifestation of the local cascade dynamics in chapters 3-4. The unsteady cascade dynamics can be formalised in terms of a time-lag hypothesis which connects the present spatially averaged interscale transfer to the future spatially averaged dissipation. The hypothesis is consistent with the average KHMH dynamics and is able to predict approximately $80 - 90\%$ of the dissipation fluctuations at scales close to the Taylor scale in our low to moderate Reynolds number DNSs of forced homogeneous/periodic turbulence. It is primarily the low-frequency cascade imbalances between larger-scale interscale transfer and dissipation which are captured by the hypothesis. We use this hypothesis to predict the low-pass filtered non-equilibrium cascade dynamics. This equilibrium/non-equilibrium decomposition of the cascade dynamics relies on a truncated Taylor expansion of the dissipation rate which is only possible for low-frequencies (i.e. order T^{-1} and below). We combine the low-frequency cascade dynamics with a time-lagged closure between interscale transfer and $(\langle|\delta \boldsymbol{u}|^2\rangle_{\boldsymbol{x}}^a)^<$ to obtain non-equilibrium corrections to the second-order structure function consistent with our DNSs. Our predictions have a clear physical basis in terms of the formalised time-lag hypothesis, making it relatively straightforward to assess their limitations/applicability and to develop generalisations for other turbulent flows. Finally, we used the phenomenology of a time-lagged energy cascade to justify a new redistributive dissipation scaling for forced homogeneous/periodic turbulence which performs identically to the successful non-equilibrium scaling in our low to moderate Reynolds number DNSs DNS3-DNS4. This scaling law captures the anti-correlation tendency between the energy dissipation and large-scale energy due to the quasiperiodic turbulence evolution.

Our results suggest that the local and spatially averaged cascade behaviour contains crucial insights into obtaining a deeper understanding of turbulent flows. Some of the research questions raised by our results are as follows:

- It is important to assess the applicability of the spatio-temporal cascade dynamics of chapters 3-4. For example, do the intermediate scale solenoidal and irrotational KHMH dynamics reduce to $\mathcal{A}_t + \mathcal{T}_{\overline{S}} \approx -\Pi'_{\overline{S}}$ and $\Pi_{\overline{I}} \approx \mathcal{T}_{\overline{I}} \approx \mathcal{T}_p/2$ in a range of turbulent flow regions and what are the Reynolds number effects? In more general, anisotropic turbulent flow regions redistribution of kinetic energy across the various $\delta u_i \delta u_i$ components are important (no summation over i). Solenoidal and irrotational evolution equations for these quantities can readily be developed and analysed by adopting the procedures in Hill (2002) and Gatti et al. (2020) to the irrotational and solenoidal NSD equations rather than the NSD equation.

- The combination of $\mathcal{A}_t + \mathcal{T}_{\overline{S}} \approx -\mathit{\Pi}'_{\overline{S}}$ and intense interscale transfer events imply concentrated regions of two-point kinetic energy $|\delta \boldsymbol{u}|^2$. Can a careful study of $\boldsymbol{a}_{\mathit{\Pi}_{\overline{S}}}$ in terms of its non-local dependence on vorticity stretching/compression and tilting reveal the vorticity dynamics which generates high $|\delta \boldsymbol{u}|^2$ concentrations? Moreover, can Lagrangian investigations of such high $|\delta \boldsymbol{u}|^2$ concentrations reveal if they get spatially mixed by turbulent transport less rapidly than they are cascaded to smaller scales? If so, such cascade behaviour could explain the intermittency build-up at decreasing intermediate scales as discussed in Kraichnan (1974).

- Our results in chapter 4 question the validity of a local balance between viscous dissipation/scale space diffusion and interscale transfer at small scales. In the future it will be important to develop estimates of the smallest turbulent length and time scales which are consistent with the local small-scale dynamics. In the regions with the highest small-scale two-point energy, the effect of Lagrangian transport in the dynamics is minimal. Thus, the prospect of a local balance between viscous effects and interscale transfer seems most promising in such regions with some correction(s) due to Lagrangian transport. Deeper insights into the small-scale dynamics in homogeneous/periodic turbulence might be obtained by studying the local KHMH dynamics affecting its coherent structures (Vincent and Meneguzzi, 1991; Ishihara et al., 2013). E.g. what are the typical KHMH dynamics affecting Burgers-like vortices? Such knowledge might be used to devise reduced-order models of small-scale turbulence and subsequent predictions of its smallest length and time scales.

- In the future it will be essential to assess the accuracy and applicability of the formalised time-lag hypothesis and its associated non-equilibrium predictions in forced and freely decaying homogeneous/periodic turbulence across a range of Reynolds numbers and forcings. To this end, the pseudospectral method developed in appendix C for the spatially and spherically averaged KHMH terms in homogeneous/periodic turbulence could prove useful, allowing for efficient in-situ calculations. This time-lag hypothesis and its associated predictions might explain the low-frequency non-equilibrium cascade dynamics and second-order structure function scaling behaviour in homogeneous/periodic turbulence. If the hypothesis and its associated non-equilibrium predictions prove accurate and widely applicable (in terms of Reynolds numbers and forcings), they might be extendable to other turbulent flow regions (see e.g. equations (5.12)-(5.13)). Investigations of the formalised time-lag hypothesis and non-equilibrium predictions could also be performed in terms of their Fourier space analogues to develop non-equilibrium corrections for the Fourier space cascade dynamics and the energy spectrum.

- Future LES subgrid-scale (SGS) models should benefit from detailed descriptions of spatially averaged interscale transfers (chapter 5) and local fluctuating dynamics of interscale and interspace energy transfers (chapter 3). These two contributions to interscale transfer dynamics suggest a mixed LES model, where the spatially averaged interscale transfer dynamics determines the dissipative part of the model and the local fluctuating dynamics determines the self-similarity part of the model (mixed models are in general required to provide a priori consistency of both SGS dissipation and mean stress (Li and Meneveau, 2004; Moser et al., 2021)).

  Time-lagged cascade dynamics can be implemented in a LES model similarly as in Horiuti and Tamaki (2013). They consider a one-equation model (Deardorff, 1974) for the SGS energy which evolves according to grid-scale kinetic energy temporal variations (and the eddy-viscosity is determined from the SGS energy). This model produces good a posteriori predictions in forced homogenous/periodic turbulence.

  The local cascade dynamics shows that LES models based on local equilibrium cannot be suitable for calculating fluctuations in subgrid stresses. On the other hand, the good correlations between subgrid stresses from similarity models and DNSs (Bardina et al., 1980; Cimarelli et al., 2019; Abbà et al., 2022) suggest that these models might indeed approximate (unawarely) at least some of the local cascade dynamics due to scale invariance/similarity (Meneveau and Katz, 2000), possibly the fact that $\mathcal{A}_t + \mathcal{T}_{\overline{S}} + \Pi'_{\overline{S}} \approx 0$ holds in most of the flow most of the time. This relation incorporates balancing between spatial fluxes and forward and backward interscale transfers, yet a recent work by Vela-Martín (2022a) argues that such spatial fluxes can be ignored by LES models. The importance of subgrid spatial transfers in facilitating local interscale transfers remains to be addressed in future works (the approach in Linkmann et al. (2018) might be used to compare the ability of LES models to capture/retain spatial transport effects to their accuracy).

- It will be important in the future to assess the redistributive dissipation scaling in forced homogeneous turbulence and in the initial period of freely decaying homogeneous turbulence in a range of Reynolds numbers and forcings to quantify the effect of redistribution in the scaling. If the dissipation mainly scales according to redistribution, it would provide a simple and possibly extendable account of the non-equilibrium scaling behaviour. One should assess if the phenomenology of a time-lagged energy cascade proves able to predict dissipation scaling transitions from redistributive/non-equilibrium scaling to Taylor/decay scaling. Such predictions would be of uttermost importance for RANS turbulent flow prediction methods, where the dissipation scaling is a crucial ingredient (Leschziner, 2016).

The issues raised in the above list suggest that further studies of spatio-temporally varying turbulent energy cascades might yield new insights into fundamental issues in turbulence theory and provide substantial improvements in turbulence modelling.

Bibliography

Abbà, A., Cimarelli, A. and Germano, M. (2022). Dynamic tensorial eddy viscosity model: Effects of compressibility and of complex geometry, *Physics of Fluids* **34**(2): 25109.

Alves Portela, F., Papadakis, G. and Vassilicos, J. C. (2017). The turbulence cascade in the near wake of a square prism, *Journal of Fluid Mechanics* **825**: 315–352.

Alves Portela, F., Papadakis, G. and Vassilicos, J. C. (2020). The role of coherent structures and inhomogeneity in near-field interscale turbulent energy transfers, *Journal of Fluid Mechanics* **896**: A16.

Aoyama, T., Ishihara, T., Kaneda, Y., Yokokawa, M., Itakura, K. and Uno, A. (2005). Statistics of energy transfer in high-resolution direct numerical simulation of turbulence in a periodic box, *Journal of the Physical Society of Japan* **74**(12): 3202–3212.

Baj, P., Alves Portela, F. and Carter, D. W. (2022). On the simultaneous cascades of energy, helicity, and enstrophy in incompressible homogeneous turbulence, *Journal of Fluid Mechanics* **952**: A20.

Ballouz, J. G., Johnson, P. L. and Ouellette, N. T. (2020). Temporal dynamics of the alignment of the turbulent stress and strain rate, *Physical Review Fluids* **5**(11): 114606.

Bardina, J., Ferziger, J. and Reynolds, W. (1980). Improved subgrid-scale models for large-eddy simulation, *13th Fluid and Plasma Dynamics Conference*, Fluid Dynamics and Co-located Conferences, American Institute of Aeronautics and Astronautics.

Batchelor, G. K. (1953). *The theory of homogeneous turbulence*, Cambridge University Press.

Batchelor, G. K. (1967). *An introduction to fluid dynamics*, Cambridge University Press.

Batchelor, G. K., Proudman, I. and Taylor, G. I. (1956). The large-scale structure of homogenous turbulence, *Philosophical Transactions of the Royal Society of London. Series A, Mathematical and Physical Sciences* **248**(949): 369–405.

Batchelor, G. K., Townsend, A. A. and Jeffreys, H. (1949). The nature of turbulent motion at large wave-numbers, *Proceedings of the Royal Society of London. Series A. Mathematical and Physical Sciences* **199**(1057): 238–255.

Bhatia, H., Norgard, G., Pascucci, V. and Bremer, P. (2013). The Helmholtz-Hodge decomposition—a survey, *IEEE Transactions on Visualization and Computer Graphics* **19**(8): 1386–1404.

Blackman, R. B. and Tukey, J. W. (1958). The measurement of power spectra from the point of view of communications engineering — Part II, *The Bell System Technical Journal* **37**(2): 485–569.

Bos, W. J. T. and Rubinstein, R. (2017). Dissipation in unsteady turbulence, *Physical Review Fluids* **2**(2): 22601.

Bos, W. J. T., Shao, L. and Bertoglio, J.-P. (2007). Spectral imbalance and the normalized dissipation rate of turbulence, *Physics of Fluids* **19**(4): 45101.

Canuto, C., Hussaini, M. Y., Quarteroni, A. and Zang, T. A. (1987). *Spectral methods in fluid dynamics*, Springer.

Cardesa, J. I., Vela-Martín, A., Dong, S. and Jiménez, J. (2015). The temporal evolution of the energy flux across scales in homogeneous turbulence, *Physics of Fluids* **27**(11): 111702.

Chevillard, L., Roux, S. G., Lévêque, E., Mordant, N., Pinton, J.-F. and Arnéodo, A. (2005). Intermittency of velocity time increments in turbulence, *Physical Review Letters* **95**(6): 64501.

Cimarelli, A., Abbà, A. and Germano, M. (2019). General formalism for a reduced description and modelling of momentum and energy transfer in turbulence, *Journal of Fluid Mechanics* **866**: 865–896.

Cimarelli, A., De Angelis, E., Jiménez, J. and Casciola, C. M. (2016). Cascades and wall-normal fluxes in turbulent channel flows, *Journal of Fluid Mechanics* **796**: 417–436.

Davidson, P. A. (2015). *Turbulence : an introduction for scientists and engineers*, 2nd edn, Oxford University Press.

Davidson, P. A., Kaneda, Y., Moffatt, K. and Sreenivasan, K. R. (2011). *A voyage through turbulence*, Cambridge University Press.

Davidson, P. A. and Pearson, B. R. (2005). Identifying turbulent energy distributions in real, rather than Fourier, space, *Physical Review Letters* **95**(21): 214501.

Deardorff, J. W. (1974). Three-dimensional numerical study of the height and mean structure of a heated planetary boundary layer, *Boundary-Layer Meteorology* **7**(1): 81–106.

Doan, N. A. K., Swaminathan, N., Davidson, P. A. and Tanahashi, M. (2018). Scale locality of the energy cascade using real space quantities, *Physical Review Fluids* **3**(8): 84601.

Domaradzki, J. A. and Carati, D. (2007). An analysis of the energy transfer and the locality of nonlinear interactions in turbulence, *Physics of Fluids* **19**(8): 85112.

Donzis, D. A., Yeung, P. K. and Sreenivasan, K. R. (2008). Dissipation and enstrophy in isotropic turbulence: Resolution effects and scaling in direct numerical simulations, *Physics of Fluids* **20**(4): 45108.

Dubrulle, B. (2019). Beyond Kolmogorov cascades, *Journal of Fluid Mechanics* **867**: P1.

Dubrulle, B. and Gibbon, J. D. (2021). A correspondence between the multifractal model of turbulence and the Navier-Stokes equations.
URL: *https://arxiv.org/abs/2102.00189*

Eyink, G. L. (2018). Review of the Onsager "ideal turbulence" theory, *arXivX* .
URL: *https://arxiv.org/abs/1803.02223*

Frigo, M. and Johnson, S. G. (2005). The design and implementation of FFTW3, *Proceedings of the IEEE* **93**(2): 216–231.

Frisch, U. (1995). *Turbulence: the legacy of A. N. Kolmogorov*, Cambridge University Press.

Frisch, U. and Vergassola, M. (1991). A prediction of the multifractal model: the intermediate dissipation range, *Europhysics Letters* **14**(5): 439–444.

Galanti, B. and Tsinober, A. (2000). Self-amplification of the field of velocity derivatives in quasi-isotropic turbulence, *Physics of Fluids* **12**(12): 3097–3099.

Gatti, D., Chiarini, A., Cimarelli, A. and Quadrio, M. (2020). Structure function tensor equations in inhomogeneous turbulence, *Journal of Fluid Mechanics* **898**: A5.

Gatti, D., Remigi, A., Chiarini, A., Cimarelli, A. and Quadrio, M. (2019). An efficient numerical method for the generalised Kolmogorov equation, *Journal of Turbulence* **20**(8): 457–480.

Gill, S. (1951). A process for the step-by-step integration of differential equations in an automatic digital computing machine, *Mathematical Proceedings of the Cambridge Philosophical Society* **47**(1): 96–108.

Goto, S. (2008). A physical mechanism of the energy cascade in homogeneous isotropic turbulence, *Journal of Fluid Mechanics* **605**: 355–366.

Goto, S., Saito, Y. and Kawahara, G. (2017). Hierarchy of antiparallel vortex tubes in spatially periodic turbulence at high Reynolds numbers, *Physical Review Fluids* **2**(6): 64603.

Goto, S. and Vassilicos, J. C. (2015). Energy dissipation and flux laws for unsteady turbulence, *Physics Letters A* **379**(16): 1144–1148.

Goto, S. and Vassilicos, J. C. (2016a). Local equilibrium hypothesis and Taylor's dissipation law, *Fluid Dynamics Research* **48**(2): 21402.

Goto, S. and Vassilicos, J. C. (2016b). Unsteady turbulence cascades, *Physical Review E* **94**(5): 53108.

Gotoh, T. and Kraichnan, R. H. (2004). Turbulence and Tsallis statistics, *Physica D: Nonlinear Phenomena* **193**(1): 231–244.

Gulitski, G., Kholmyansky, M., Kinzelbach, W., Lüthi, B., Tsinober, A. and Yorish, S. (2007). Velocity and temperature derivatives in high-Reynolds-number turbulent flows in the atmospheric surface layer. Part 2. Accelerations and related matters, *Journal of Fluid Mechanics* **589**: 83–102.

Helmholtz, H. (1867). LXIII. On Integrals of the hydrodynamical equations, which express vortex-motion, *The London, Edinburgh, and Dublin Philosophical Magazine and Journal of Science* **33**(226): 485–512.

Hill, R. J. (1997). Applicability of Kolmogorov's and Monin's equations of turbulence, *Journal of Fluid Mechanics* **353**: 67–81.

Hill, R. J. (2002). Exact second-order structure-function relationships, *Journal of Fluid Mechanics* **468**: 317–326.

Hill, R. J. and Thoroddsen, S. T. (1997). Experimental evaluation of acceleration correlations for locally isotropic turbulence, *Physical Review E* **55**(2): 1600–1606.

Hirsch, C. (2007). *Numerical computation of internal and external flows, volume 1: fundamentals of computational fluid dynamics*, 2nd edn, Butterworth-Heinemann.

Horiuti, K. and Ozawa, T. (2011). Multimode stretched spiral vortex and nonequilibrium energy spectrum in homogeneous shear flow turbulence, *Physics of Fluids* **23**(3): 35107.

Horiuti, K. and Tamaki, T. (2013). Nonequilibrium energy spectrum in the subgrid-scale one-equation model in large-eddy simulation, *Physics of Fluids* **25**(12): 125104.

Hussaini, M. Y. and Zang, T. A. (1987). Spectral methods in fluid dynamics, *Annual Review of Fluid Mechanics* **19**: 339–367.

Ishihara, T., Kaneda, Y. and Hunt, J. C. R. (2013). Thin shear layers in high Reynolds number turbulence—DNS results, *Flow, Turbulence and Combustion* **91**(4): 895–929.

Ishihara, T., Morishita, K., Yokokawa, M., Uno, A. and Kaneda, Y. (2016). Energy spectrum in high-resolution direct numerical simulations of turbulence, *Physical Review Fluids* **1**(8): 82403.

Iyer, K. P., Bonaccorso, F., Biferale, L. and Toschi, F. (2017). Multiscale anisotropic fluctuations in sheared turbulence with multiple states, *Physical Review Fluids* **2**(5): 52602.

Iyer, K. P., Sreenivasan, K. R. and Yeung, P. K. (2020). Scaling exponents saturate in three-dimensional isotropic turbulence, *Physical Review Fluids* **5**(5): 54605.

Kaneda, Y. and Ishihara, T. (2006). High-resolution direct numerical simulation of turbulence, *Journal of Turbulence* **7**: N20.

Kármán, T. and Howarth, L. (1938). On the statistical theory of isotropic turbulence, *Proceedings of the Royal Society of London. Series A - Mathematical and Physical Sciences* **164**(917): 192–215.

Khurshid, S., Donzis, D. A. and Sreenivasan, K. R. (2021). Slow spectral transfer and energy cascades in isotropic turbulence, *Journal of Fluid Mechanics* **908**: A21.

Kolmogorov, A. N. (1941a). Dissipation of energy in locally isotropic turbulence, *Doklady Akademii Nauk SSSR* **32**: 19–21.

Kolmogorov, A. N. (1941b). On the degeneration of isotropic turbulence in an incompressible viscous fluid, *Doklady Akademii Nauk SSSR* **31**: 319–323.

Kolmogorov, A. N. (1941c). The local structure of turbulence in incompressible viscous fluid for very large Reynolds numbers, *Doklady Akademii Nauk SSSR* **30**: 301–305.

Kolmogorov, A. N. (1962). A refinement of previous hypotheses concerning the local structure of turbulence in a viscous incompressible fluid at high Reynolds number, *Journal of Fluid Mechanics* **13**(1): 82–85.

Kovasznay, L. S. G. (1948). The spectrum of locally isotropic turbulence, *Physical Review* **73**(9): 1115–1116.

Kraichnan, R. H. (1959). The structure of isotropic turbulence at very high Reynolds numbers, *Journal of Fluid Mechanics* **5**(4): 497–543.

Kraichnan, R. H. (1974). On Kolmogorov's inertial-range theories, *Journal of Fluid Mechanics* **62**(2): 305–330.

Landau, L. D. and Lifshitz, E. M. (1987). *Fluid mechanics*, 2nd edn, Butterworth-Heinemann.

Lebedev, V. I. (1975). Values of the nodes and weights of ninth to seventeenth order gauss-markov quadrature formulae invariant under the octahedron group with inversion, *USSR Computational Mathematics and Mathematical Physics* **15**(1): 44–51.

Leschziner, M. (2016). *Statistical turbulence modelling for fluid dynamics - demystified : an introductory text for graduate engineering students*, Imperial College Press.

Leung, T., Swaminathan, N. and Davidson, P. A. (2012). Geometry and interaction of structures in homogeneous isotropic turbulence, *Journal of Fluid Mechanics* **710**: 453–481.

Li, Y. and Meneveau, C. (2004). Analysis of mean momentum flux in subgrid models of turbulence, *Physics of Fluids* **16**(9): 3483–3486.

Lin, C. C. (1949). Remarks on the spectrum of turbulence, *Proceedings of Symposia in Applied Mathematics* **1**: 81–89.

Linkmann, M. (2018). Effects of helicity on dissipation in homogeneous box turbulence, *Journal of Fluid Mechanics* **856**: 79–102.

Linkmann, M., Buzzicotti, M. and Biferale, L. (2018). Multi-scale properties of large eddy simulations: correlations between resolved-scale velocity-field increments and subgrid-scale quantities, *Journal of Turbulence* **19**(6): 493–527.

Linkmann, M. F. and Morozov, A. (2015). Sudden relaminarization and lifetimes in forced isotropic turbulence, *Physical Review Letters* **115**(13): 134502.

Lumley, J. L. (1992). Some comments on turbulence, *Physics of Fluids A: Fluid Dynamics* **4**(2): 203–211.

Machiels, L. (1997). Predictability of small-scale motion in isotropic fluid turbulence, *Physical Review Letters* **79**(18): 3411–3414.

Marati, N., Casciola, C. and Piva, R. (2004). Energy cascade and spatial fluxes in wall turbulence, *Journal of Fluid Mechanics* **521**: 191–215.

McComb, W. D., Linkmann, M. F., Berera, A., Yoffe, S. R. and Jankauskas, B. (2015). Self-organization and transition to turbulence in isotropic fluid motion driven by negative damping at low wavenumbers, *Journal of Physics A: Mathematical and Theoretical* **48**(25): 25FT01.

Meneveau, C. and Katz, J. (2000). Scale-invariance and turbulence models for large-eddy simulation, *Annual Review of Fluid Mechanics* **32**(1): 1–32.

Moffatt, H. K. (2002). G. K. Batchelor and the homogenization of turbulence, *Annual Review of Fluid Mechanics* **34**(1): 19–35.

Moffatt, H. K. (2014). Helicity and singular structures in fluid dynamics, *Proceedings of the National Academy of Sciences* **111**(10): 3663–3670.

Monin, A. S. and Yaglom, A. M. (1975). *Statistical fluid mechanics, volume II: mechanics of turbulence*, MIT Press.

Moser, R. D., Haering, S. W. and Yalla, G. R. (2021). Statistical properties of subgrid-scale turbulence models, *Annual Review of Fluid Mechanics* **53**(1): 255–286.

Nie, Q. and Tanveer, S. (1999). A note on third–order structure functions in turbulence, *Proceedings of the Royal Society of London. Series A: Mathematical, Physical and Engineering Sciences* **455**(1985): 1615–1635.

Obligado, M. and Vassilicos, J. C. (2019). The non-equilibrium part of the inertial range in decaying homogeneous turbulence, *Europhysics Letters* **127**(6): 64004.

Obukhov, A. M. (1941). On the energy distribution in the spectrum of a turbulent flow, *Doklady Akademii Nauk SSSR* **32**(1): 454–466.

Onsager, L. (1949). Statistical hydrodynamics, *Il Nuovo Cimento* **6**(2): 279–287.

Parisi, G. and Frisch, U. (1985). On the singularity structure of fully developed turbulence in Turbulence and predictability in geophysical fluid dynamics and climate dynamics, *Turbulence and Predictability of Geophysical Flows and Climate Dynamics, Proceedings of the International School of Physics Enrico Fermi*, pp. 84–87.

Patterson, G. S. and Orszag, S. A. (1971). Spectral calculations of isotropic turbulence: efficient removal of aliasing interactions, *Phys. Fluids* **14**(11): 2538–2541.

Patterson, G. S. and Orszag, S. A. (1972). Numerical simulation of three-dimensional homogeneous isotropic turbulence, *Physical Review Letters* **28**(2): 76–79.

Perot, B. and Moin, P. (1996). A new approach to turbulence modelling, *Proceedings CTR Summer program*, pp. 35–46.

Pinton, J.-F., Holdsworth, P. C. W. and Labbé, R. (1999). Power fluctuations in a closed turbulent shear flow, *Physical Review E* **60**(3): R2452–R2455.

Piomelli, U., Cabot, W. H., Moin, P. and Lee, S. (1991). Subgrid-scale backscatter in turbulent and transitional flows, *Physics of Fluids A: Fluid Dynamics* **3**(7): 1766–1771.

Podvigina, O. and Pouquet, A. (1994). On the non-linear stability of the 1:1:1 ABC flow, *Physica D: Nonlinear Phenomena* **75**(4): 471–508.

Pope, S. B. (2000). *Turbulent flows*, Cambridge University Press.

Prabhu, K. M. M. (2018). *Window functions and their applications in signal processing*, CRC Press.

Reynolds, O. (1883). XXIX. An experimental investigation of the circumstances which determine whether the motion of water shall be direct or sinuous, and of the law of resistance in parallel channels, *Philosophical Transactions of the Royal Society of London* **174**: 935–982.

Reynolds, O. (1895). IV. On the dynamical theory of incompressible viscous fluids and the determination of the criterion, *Philosophical Transactions of the Royal Society of London* **186**: 123–164.

Richardson, L. F. (1922). *Weather prediction by numerical process*, Cambridge University Press.

Rogallo, R. S. (1977). An ILLIAC program for the numerical solution of homogeneous, incompressible turbulence. Technical report TM73203, *NASA* .

Rogallo, R. S. (1981). Numerical experiments in homogeneous turbulence. Technical report TM81315, *NASA* .

Rosenberg, K. and McKeon, B. J. (2019). Efficient representation of exact coherent states of the Navier–Stokes equations using resolvent analysis, *Fluid Dynamics Research* **51**(1): 11401.

Sagaut, P. (2006). *Large eddy simulation for incompressible flows: an introduction*, 3rd edn, Springer.

Sagaut, P. and Cambon, C. (2018). *Homogeneous turbulence dynamics*, 2nd edn, Springer.

Sanderson, C. and Curtin, R. (2016). Armadillo: a template-based C++ library for linear algebra, *Journal of Open Source Software* **1**: 26.

Sanderson, C. and Curtin, R. (2018). A user-friendly hybrid sparse matrix class in C++, *Lecture Notes in Computer Science* **10931**: 422–430.

Sprössig, W. (2010). On Helmholtz decompositions and their generalizations—an overview, *Mathematical Methods in the Applied Sciences* **33**(4): 374–383.

Sreenivasan, K. R. (1998). An update on the energy dissipation rate in isotropic turbulence, *Physics of Fluids* **10**(2): 528–529.

Sreenivasan, K. R. and Antonia, R. A. (1997). The phenomenology of small-scale turbulence, *Annual Review of Fluid Mechanics* **29**(1): 435–472.

Steiros, K. (2022). Balanced nonstationary turbulence, *Physical Review E* **105**(3): 35109.

Stewart, A. M. (2012). Longitudinal and transverse components of a vector field, *Sri Lankan Journal of Physics* **12**: 33–42.

Tang, S. L., Antonia, R. A. and Djenidi, L. (2022). Transport equations for the normalized nth-order moments of velocity derivatives in grid turbulence, *Journal of Fluid Mechanics* **930**: A31.

Taylor, G. I. (1935). Statistical theory of turbulence, *Proceedings of the Royal Society A: Mathematical, Physical and Engineering Sciences* **151**(873): 421–444.

Taylor, G. I. (1938a). Production and dissipation of vorticity in a turbulent fluid, *Proceedings of the Royal Society of London. Series A - Mathematical and Physical Sciences* **164**(916): 15–23.

Taylor, G. I. (1938b). The spectrum of turbulence, *Proceedings of the Royal Society A: Mathematical, Physical and Engineering Sciences* **164**(919): 476–490.

Tennekes, H. (1975). Eulerian and Lagrangian time microscales in isotropic turbulence, *Journal of Fluid Mechanics* **67**(3): 561–567.

Tennekes, H. and Lumley, J. L. (1972). *A first course in turbulence*, MIT Press.

Thiesset, F., Danaila, L. and Antonia, R. A. (2014). Dynamical interactions between the coherent motion and small scales in a cylinder wake, *Journal of Fluid Mechanics* **749**: 201–226.

Townsend, A. A. (1976). *The structure of turbulent shear flow*, 2nd edn, Cambridge University Press.

Tsinober, A. (2009). *An informal conceptual introduction to turbulence*, 2nd edn, Springer.

Tsinober, A., Vedula, P. and Yeung, P. K. (2001). Random Taylor hypothesis and the behavior of local and convective accelerations in asotrophic turbulence, *Physics of Fluids* **13**(7): 1974–1984.

Tsuruhashi, T., Goto, S., Oka, S. and Yoneda, T. (2022). Self-similar hierarchy of coherent tubular vortices in turbulence, *Philosophical Transactions of the Royal Society A: Mathematical, Physical and Engineering Sciences* **380**(2226): 20210053.

Valente, P. C. and Vassilicos, J. C. (2014). The non-equilibrium region of grid-generated decaying turbulence, *Journal of Fluid Mechanics* **744**: 5–37.

Valente, P. C. and Vassilicos, J. C. (2015). The energy cascade in grid-generated non-equilibrium decaying turbulence, *Physics of Fluids* **27**(4): 45103.

Vassilicos, J. C. (2015). Dissipation in turbulent flows, *Annual Review of Fluid Mechanics* **47**(1): 95–114.

Vedula, P. and Yeung, P. K. (1999). Similarity scaling of acceleration and pressure statistics in numerical simulations of isotropic turbulence, *Physics of Fluids* **11**(5): 1208–1220.

Vela-Martín, A. (2021). The synchronisation of intense vorticity in isotropic turbulence, *Journal of Fluid Mechanics* **913**: R8.

Vela-Martín, A. (2022a). Subgrid-scale models of isotropic turbulence need not produce energy backscatter, *Journal of Fluid Mechanics* **937**: A14.

Vela-Martín, A. (2022b). The energy cascade as the origin of intense events in small-scale turbulence, *Journal of Fluid Mechanics* **937**: A13.

Vincent, A. and Meneguzzi, M. (1991). The spatial structure and statistical properties of homogeneous turbulence, *Journal of Fluid Mechanics* **225**: 1–20.

Wan, M., Xiao, Z., Meneveau, C., Eyink, G. L. and Chen, S. (2010). Dissipation-energy flux correlations as evidence for the Lagrangian energy cascade in turbulence, *Physics of Fluids* **22**(6): 61702.

Wissink, J. G. and Rodi, W. (2008). Numerical study of the near wake of a circular cylinder, *International Journal of Heat and Fluid Flow* **29**(4): 1060–1070.

Woodruff, S. L. and Rubinstein, R. (2006). Multiple-scale perturbation analysis of slowly evolving turbulence, *Journal of Fluid Mechanics* **565**: 95–103.

Wu, J., Zhou, Y. and Wu, J. (1996). Reduced stress tensor and dissipation and the transport of Lamb vector. Report 96-21 ICASE, *Technical report*, NASA Langley Research Center.

Xu, H., Ouellette, N. T., Vincenzi, D. and Bodenschatz, E. (2007). Acceleration correlations and pressure structure functions in high-Reynolds number turbulence, *Physical Review Letters* **99**(20): 204501.

Yasuda, T., Goto, S. and Kawahara, G. (2014). Quasi-cyclic evolution of turbulence driven by a steady force in a periodic cube, *Fluid Dynamics Research* **46**(6): 61413.

Yasuda, T. and Vassilicos, J. C. (2018). Spatio-temporal intermittency of the turbulent energy cascade, *Journal of Fluid Mechanics* **853**: 235–252.

Yeung, P. K., Pope, S. B., Lamorgese, A. G. and Donzis, D. A. (2006). Acceleration and dissipation statistics of numerically simulated isotropic turbulence, *Physics of Fluids* **18**(6): 65103.

Yeung, P. K., Sreenivasan, K. R. and Pope, S. B. (2018). Effects of finite spatial and temporal resolution in direct numerical simulations of incompressible isotropic turbulence, *Physical Review Fluids* **3**(6): 64603.

Yeung, P. K., Zhai, X. M. and Sreenivasan, K. R. (2015). Extreme events in computational turbulence, *Proceedings of the National Academy of Sciences* **112**(41): 12633–12638.

Yoffe, S. R. (2012). *Investigation of the transfer and dissipation of energy in isotropic turbulence*, PhD thesis, University of Edinburgh.

Yoshizawa, A. (1994). Nonequilibrium effect of the turbulent-energy-production process on the inertial-range energy spectrum, *Physical Review E* **49**(5): 4065–4071.

Appendices

A. Derivation of the KHMH Equation

In this appendix we derive the Kármán-Howarth-Monin-Hill (KHMH) equation from the incompressible Navier-Stokes equations. The derivation is a simplified version of the more general derivation of Hill (2002), who first derives the evolution equation for the tensor $\delta u_i \delta u_j$ before arriving at the evolution equation for $\delta u_i \delta u_i$ (i.e. the KHMH equation).

We first write the incompressible Navier-Stokes equations in two reference frames x_i^+ and x_i^- where the superscripts indicate the reference frame the velocity, pressure and body forcing is evaluated. These two reference frames are independent of each other. The Navier-Stokes equations at x_i^+ read

$$\frac{\partial u_i^+}{\partial x_i^+} = 0, \tag{A.1a}$$

$$\frac{\partial u_i^+}{\partial t} + u_j^+ \frac{\partial u_i^+}{\partial x_j^+} = -\frac{1}{\rho}\frac{\partial p^+}{\partial x_i^+} + \nu \frac{\partial^2 u_i^+}{\partial x_j^+ \partial x_j^+} + f_i^+, \tag{A.1b}$$

and at x_i^- read

$$\frac{\partial u_i^-}{\partial x_i^-} = 0, \tag{A.2a}$$

$$\frac{\partial u_i^-}{\partial t} + u_j^- \frac{\partial u_i^-}{\partial x_j^-} = -\frac{1}{\rho}\frac{\partial p^-}{\partial x_i^-} + \nu \frac{\partial^2 u_i^-}{\partial x_j^- \partial x_j^-} + f_i^-. \tag{A.2b}$$

The next step in the derivation is to derive an evolution for the velocity difference $\delta u_i = u_i^+ - u_i^-$. The symbol δ preceding a quantity ϕ denotes in general $\delta\phi = \phi^+ - \phi^-$. We introduce new reference frames x_i and r_i where

$$x_i = \frac{1}{2}(x_i^+ + x^-), \tag{A.3a}$$

$$r_i = x_i^+ - x_i^-. \tag{A.3b}$$

x_i denotes the centroid of x_i^+ and x_i^- and r_i their separation vector (see the illustration of these coordinate systems in figure 3.2). Note the inverse relations

$$x_i^+ = x_i + \frac{1}{2} r_i, \tag{A.4a}$$

$$x_i^- = x_i - \frac{1}{2} r_i. \tag{A.4b}$$

Before proceeding we develop some useful relations between derivatives in the frame (x_i^+, x_i^-) and the frame (x_i, r_i). We have from (A.3)-(A.4) that

$$\frac{\partial}{\partial x_i} = \frac{\partial}{\partial x_j^+}\frac{\partial x_j^+}{\partial x_i} + \frac{\partial}{\partial x_j^-}\frac{\partial x_j^-}{\partial x_i}, \tag{A.5a}$$

$$= \delta_{ij}\frac{\partial}{\partial x_j^+} + \delta_{ij}\frac{\partial}{\partial x_j^-}, \tag{A.5b}$$

$$= \frac{\partial}{\partial x_i^+} + \frac{\partial}{\partial x_i^-}, \tag{A.5c}$$

where δ_{ij} is the Kronecker delta. We also have

$$\frac{\partial}{\partial r_i} = \frac{1}{2}\left(\frac{\partial}{\partial x_i^+} - \frac{\partial}{\partial x_i^-}\right), \tag{A.6}$$

and the inverse relationships

$$\frac{\partial}{\partial x_i^\pm} = \frac{1}{2}\frac{\partial}{\partial x_i} \pm \frac{\partial}{\partial r_i}. \tag{A.7}$$

Finally, the following relationship for the Laplacians will be useful below

$$\frac{\partial^2}{\partial x_j^+ \partial x_j^+} + \frac{\partial^2}{\partial x_j^- \partial x_j^-} = 2\frac{\partial^2}{\partial r_j \partial r_j} + \frac{1}{2}\frac{\partial^2}{\partial x_j \partial x_j}. \tag{A.8}$$

We subtract the NS equations at x_i^- (A.2b) from the NS equations at x_i^+ (A.1b), which yields

$$\frac{\partial \delta u_i}{\partial t} + u_j^+\frac{\partial u_i^+}{\partial x_j^+} - u_j^-\frac{\partial u_i^-}{\partial x_j^-} = -\frac{1}{\rho}\frac{\partial p^+}{\partial x_i^+} + \frac{1}{\rho}\frac{\partial p^-}{\partial x_i^-} + \nu\frac{\partial^2 u_i^+}{\partial x_j^+ \partial x_j^+} - \nu\frac{\partial^2 u_i^-}{\partial x_j^- \partial x_j^-} + \delta f_i. \tag{A.9}$$

We rewrite the non-linear, pressure and viscous terms in (A.9) in the reference frame (x_i, r_i). As $\partial/\partial x_j^+ \phi^- = \partial/\partial x_j^- \phi^+ = 0$, we can express the non-linear term as

$$u_j^+\frac{\partial u_i^+}{\partial x_j^+} - u_j^-\frac{\partial u_i^-}{\partial x_j^-} = u_j^+\frac{\partial(u_i^+ - u_i^-)}{\partial x_j^+} - u_j^-\frac{\partial(u_i^- - u_i^+)}{\partial x_j^-}, \tag{A.10a}$$

$$= u_j^+\frac{\partial \delta u_i}{\partial x_j^+} + u_j^-\frac{\partial \delta u_i}{\partial x_j^-}, \tag{A.10b}$$

$$= \frac{u_j^+ + u_j^-}{2}\frac{\partial \delta u_i}{\partial x_j} + \delta u_j\frac{\partial \delta u_i}{\partial r_j}, \tag{A.10c}$$

where we used (A.7) to go from (A.10b) to (A.10c). We can rewrite the pressure term as

$$-\frac{1}{\rho}\frac{\partial p^+}{\partial x_i^+}+\frac{1}{\rho}\frac{\partial p^-}{\partial x_i^-}=-\frac{1}{\rho}\frac{\partial \delta p}{\partial x_i^+}+\frac{1}{\rho}\frac{\partial \delta p}{\partial x_i^-}, \tag{A.11a}$$

$$=-\frac{1}{\rho}\frac{\partial \delta p}{\partial x_i}, \tag{A.11b}$$

and the viscous term as

$$\nu\frac{\partial^2 u_i^+}{\partial x_j^+\partial x_j^+}-\nu\frac{\partial^2 u_i^-}{\partial x_j^-\partial x_j^-}=\nu\frac{\partial^2 \delta u_i}{\partial x_j^+\partial x_j^+}+\nu\frac{\partial^2 \delta u_i}{\partial x_j^-\partial x_j^-}, \tag{A.12a}$$

$$=2\nu\frac{\partial^2 \delta u_i}{\partial r_j\partial r_j}+\frac{\nu}{2}\frac{\partial^2 \delta u_i}{\partial x_j\partial x_j}, \tag{A.12b}$$

where we used (A.8) to arrive at the final expression. We insert (A.10c), (A.11b) and (A.12b) into (A.9) to obtain the following NS difference equations

$$\frac{\partial \delta u_i}{\partial t}+\frac{u_j^+ + u_j^-}{2}\frac{\partial \delta u_i}{\partial x_j}+\delta u_j\frac{\partial \delta u_i}{\partial r_j}=-\frac{1}{\rho}\frac{\partial \delta p}{\partial x_i}+2\nu\frac{\partial^2 \delta u_i}{\partial r_j\partial r_j}+\frac{\nu}{2}\frac{\partial^2 \delta u_i}{\partial x_j\partial x_j}+\delta f_i. \tag{A.13}$$

We derive an evolution equation for $\delta u_i\delta u_i=|\delta \boldsymbol{u}|^2$ by contracting (A.13) with $2\delta u_i$

$$\frac{\partial |\delta \boldsymbol{u}|^2}{\partial t}+\frac{u_j^+ + u_j^-}{2}\frac{\partial |\delta \boldsymbol{u}|^2}{\partial x_j}+\delta u_j\frac{\partial |\delta \boldsymbol{u}|^2}{\partial r_j}=-\frac{2}{\rho}\frac{\partial (\delta p\delta u_i)}{\partial x_i}+2\delta u_i\Big(2\nu\frac{\partial^2 \delta u_i}{\partial r_j\partial r_j}+\frac{\nu}{2}\frac{\partial^2 \delta u_i}{\partial x_j\partial x_j}\Big)+2\delta u_i\delta f_i, \tag{A.14}$$

where we used incompressibility to write the pressure-velocity term in conservative form. The final task before arriving at the KHMH equation is to rewrite the viscous terms. We first note that for $\phi=\phi(z_i)$, we have in general

$$\phi\frac{\partial^2 \phi}{\partial z_j z_j}=\frac{1}{2}\frac{\partial^2 \phi^2}{\partial z_j\partial z_j}+\frac{\partial \phi}{\partial z_j}\frac{\partial \phi}{\partial z_j}. \tag{A.15}$$

If we use this expression for the viscous terms we have

$$2\delta u_i\Big(2\nu\frac{\partial^2 \delta u_i}{\partial r_j\partial r_j}+\frac{\nu}{2}\frac{\partial^2 \delta u_i}{\partial x_j\partial x_j}\Big)=2\nu\frac{\partial^2 |\delta \boldsymbol{u}|^2}{\partial r_j\partial r_j}+\frac{\nu}{2}\frac{\partial^2 |\delta \boldsymbol{u}|^2}{\partial x_j\partial x_j}+4\nu\frac{\partial \delta u_i}{\partial r_j}\frac{\partial \delta u_i}{\partial r_j}+\nu\frac{\partial \delta u_i}{\partial x_j}\frac{\partial \delta u_i}{\partial x_j}. \tag{A.16}$$

We rewrite the two rightmost terms in the RHS of (A.16) in the (x_i^+, x_i^-) frame by use of (A.5)-(A.6) to obtain

$$4\nu\frac{\partial \delta u_i}{\partial r_j}\frac{\partial \delta u_i}{\partial r_j}+\nu\frac{\partial \delta u_i}{\partial x_j}\frac{\partial \delta u_i}{\partial x_j}=2\nu\big[(\frac{\partial u_i^+}{\partial x_j^+})^2+(\frac{\partial u_i^-}{\partial x_j^-})^2\big]. \tag{A.17}$$

We insert (A.17) into (A.16) which we insert into (A.14) to obtain the KHMH equation

$$\frac{\partial|\delta\boldsymbol{u}|^2}{\partial t} + \frac{u_j^+ + u_j^-}{2}\frac{\partial|\delta\boldsymbol{u}|^2}{\partial x_j} + \delta u_j\frac{\partial|\delta\boldsymbol{u}|^2}{\partial r_j} = -\frac{2}{\rho}\frac{\partial(\delta p\delta u_i)}{\partial x_i}$$
$$+ 2\nu\frac{\partial^2|\delta\boldsymbol{u}|^2}{\partial r_j\partial r_j} + \frac{\nu}{2}\frac{\partial^2|\delta\boldsymbol{u}|^2}{\partial x_j\partial x_j} + 2\nu\big[(\frac{\partial u_i^+}{\partial x_j^+})^2 + (\frac{\partial u_i^-}{\partial x_j^-})^2\big] + 2\delta u_i\delta f_i. \quad \text{(A.18)}$$

Note that we only assumed the incompressible Navier-Stokes equation to arrive at the KHMH equation. The formulation (A.18) of the KHMH equation is preferable to e.g. (A.14) as this formulation lends itself to the physical interpretation of the various terms we give in section 3.1.4. All derivatives are written in the frame (x_i, r_i) (except the viscous dissipation) and all terms appear as differences (δu_i, δp, δf_i) except the advection velocity $(u_j + u_j)/2$. Similarly, the NS difference formulation (A.13) we use in section 3.1.3 is preferable over e.g. the NS difference formulation (A.9). To more easily recognise the connection between the various NS, NSD and KHMH terms, we have listed them according to their underlying NS/NSD physical mechanisms in table A.1.

One can calculate the KHMH and NSD terms in physical space with DNS data by rewriting them in terms of the (x_i^+, x_i^-) frame with e.g. the KHMH time-derivative and NSD pressure gradient terms given as

$$\frac{\partial|\delta\boldsymbol{u}|^2}{\partial t} = 2\delta u_i(\frac{\partial u_i^+}{\partial t} - \frac{\partial u_i^-}{\partial t}), \quad \text{(A.19)}$$

$$-\frac{1}{\rho}\frac{\partial\delta p}{\partial x_i} = -\frac{1}{\rho}(\frac{\partial p^+}{\partial x_i^+} - \frac{\partial p^-}{\partial x_i^-}). \quad \text{(A.20)}$$

To sample fields or derivatives at x_i^+ (or x_i^-), the same quantities can be calculated at the surrounding grid points and then be interpolated to x_i^+ with some interpolation scheme (see section 2.3 for more details on the KHMH post-processing).

Physical mechanism	**NS**	**NSD**	**KHMH**
Time-derivative	$\boldsymbol{a}_l = \partial \boldsymbol{u}/\partial t$	$\delta \boldsymbol{a}_l = \boldsymbol{a}_l^+ - \boldsymbol{a}_l^-$	$\mathcal{A}_t = 2\delta \boldsymbol{u} \cdot \delta \boldsymbol{a}_l$
Non-linearity	$\boldsymbol{a}_c = \boldsymbol{u} \cdot \nabla_{\boldsymbol{x}} \boldsymbol{u}$	$\delta \boldsymbol{a}_c = \boldsymbol{a}_c^+ - \boldsymbol{a}_c^-$	$\mathcal{A}_c = 2\delta \boldsymbol{u} \cdot \delta \boldsymbol{a}_c$
Solenoidal non-linearity	$\boldsymbol{a}_{c_S} = (\boldsymbol{u} \cdot \nabla_{\boldsymbol{x}} \boldsymbol{u})_S$	$\delta \boldsymbol{a}_{c_S} = \boldsymbol{a}_{c_S}^+ - \boldsymbol{a}_{c_S}^-$	$\mathcal{A}_{c_S} = 2\delta \boldsymbol{u} \cdot \delta \boldsymbol{a}_{c_S}$
Irrotational non-linearity	$\boldsymbol{a}_{c_I} = (\boldsymbol{u} \cdot \nabla_{\boldsymbol{x}} \boldsymbol{u})_I$	$\delta \boldsymbol{a}_{c_I} = \boldsymbol{a}_{c_I}^+ - \boldsymbol{a}_{c_I}^-$	$\mathcal{A}_{c_I} = 2\delta \boldsymbol{u} \cdot \delta \boldsymbol{a}_{c_I}$
Physical transport	$[\boldsymbol{a}_c]$	$\boldsymbol{a}_{\mathcal{T}} = \frac{1}{2}(\boldsymbol{u}^+ + \boldsymbol{u}^-) \cdot \nabla_{\boldsymbol{x}} \delta \boldsymbol{u}$	$\mathcal{T} = 2\delta \boldsymbol{u} \cdot \boldsymbol{a}_{\mathcal{T}}$
Solenoidal physical transport	$[\boldsymbol{a}_{c_S}]$	$\boldsymbol{a}_{\mathcal{T}_{\overline{S}}} = \frac{1}{2}((\boldsymbol{u}^+ + \boldsymbol{u}^-) \cdot \nabla_{\boldsymbol{x}} \delta \boldsymbol{u})_{\overline{S}}$	$\mathcal{T}_{\overline{S}} = 2\delta \boldsymbol{u} \cdot \boldsymbol{a}_{\mathcal{T}_{\overline{S}}}$
Irrotational physical transport	$[\boldsymbol{a}_{c_I}]$	$\boldsymbol{a}_{\mathcal{T}_{\overline{I}}} = \frac{1}{2}((\boldsymbol{u}^+ + \boldsymbol{u}^-) \cdot \nabla_{\boldsymbol{x}} \delta \boldsymbol{u})_{\overline{I}}$	$\mathcal{T}_{\overline{I}} = 2\delta \boldsymbol{u} \cdot \boldsymbol{a}_{\mathcal{T}_{\overline{I}}}$
Interscale transfer	$[\boldsymbol{a}_c]$	$\boldsymbol{a}_{\Pi} = \frac{1}{2}(\boldsymbol{u}^+ + \boldsymbol{u}^-) \cdot \nabla_{\boldsymbol{x}} \delta \boldsymbol{u}$	$\Pi = 2\delta \boldsymbol{u} \cdot \boldsymbol{a}_{\Pi}$
Solenoidal interscale transfer	$[\boldsymbol{a}_{c_S}]$	$\boldsymbol{a}_{\Pi_{\overline{S}}} = \frac{1}{2}((\boldsymbol{u}^+ + \boldsymbol{u}^-) \cdot \nabla_{\boldsymbol{x}} \delta \boldsymbol{u})_{\overline{S}}$	$\Pi_{\overline{S}} = 2\delta \boldsymbol{u} \cdot \boldsymbol{a}_{\Pi_{\overline{S}}}$
Irrotational interscale transfer	$[\boldsymbol{a}_{c_I}]$	$\boldsymbol{a}_{\Pi_{\overline{I}}} = \frac{1}{2}((\boldsymbol{u}^+ + \boldsymbol{u}^-) \cdot \nabla_{\boldsymbol{x}} \delta \boldsymbol{u})_{\overline{I}}$	$\Pi_{\overline{I}} = 2\delta \boldsymbol{u} \cdot \boldsymbol{a}_{\Pi_{\overline{S}}}$
Pressure gradient	$\boldsymbol{a}_p = -1/\rho \nabla_{\boldsymbol{x}} p$	$\delta \boldsymbol{a}_p = \boldsymbol{a}_p^+ - \boldsymbol{a}_p^-$	$\mathcal{T}_p = 2\delta \boldsymbol{u} \cdot \delta \boldsymbol{a}_p$
Viscosity	$\boldsymbol{a}_\nu = \nu \nabla_{\boldsymbol{x}}^2 \boldsymbol{u}$	$\delta \boldsymbol{a}_\nu = \boldsymbol{a}_\nu^+ - \boldsymbol{a}_\nu^-$	$\mathcal{D} = 2\delta \boldsymbol{u} \cdot \delta \boldsymbol{a}_\nu$
Forcing	$\boldsymbol{f}$	$\delta \boldsymbol{f} = \boldsymbol{f}^+ - \boldsymbol{f}^-$	$\mathcal{I} = 2\delta \boldsymbol{u} \cdot \delta \boldsymbol{f}$
Total acceleration	$\boldsymbol{a} = \boldsymbol{a}_p + \boldsymbol{a}_\nu$	$\delta \boldsymbol{a} = \boldsymbol{a}^+ - \boldsymbol{a}^-$	$\mathcal{A} = 2\delta \boldsymbol{u} \cdot \delta \boldsymbol{a}$
Physical space diffusion		$[\delta \boldsymbol{a}_\nu]$	$\mathcal{D}_{x,\nu} = \frac{\nu}{2} \nabla_{\boldsymbol{x}}^2 \lvert\delta \boldsymbol{u}\rvert^2$
Scale space diffusion		$[\delta \boldsymbol{a}_\nu]$	$\mathcal{D}_{r,\nu} = 2\nu \nabla_{\boldsymbol{r}}^2 \lvert\delta \boldsymbol{u}\rvert^2$
Two-point pseudo-dissipation		$[\delta \boldsymbol{a}_\nu]$	$\epsilon^* = 2\nu((\partial u_i^+/\partial x_k^+)^2$ $+(\partial u_i^-/\partial x_k^-)^2))$

Table A.1: Specification of Navier-Stokes (NS), Navier-Stokes-Difference (NSD) and Kármán-Howarth-Monin-Hill (KHMH) notation and listing of analogue NS, NSD and KHMH terms according to their physical mechanisms. Most NSD terms $\delta \boldsymbol{q}$ are related to their NS analogue $\boldsymbol{q}$ in terms of $\delta \boldsymbol{q} = \boldsymbol{q}^+ - \boldsymbol{q}^-$, where $\boldsymbol{q}^\pm$ is $\boldsymbol{q}$ evaluated at $\boldsymbol{x} \pm \boldsymbol{r}/2$ with $\boldsymbol{x}$ being the centroid position and $\boldsymbol{r}$ the separation vector. Some NSD terms do not have a direct NS analogue as e.g. $\boldsymbol{a}_{\mathcal{T}}$ and $\boldsymbol{a}_{\Pi}$ which are related indirectly to the non-linear term $\delta \boldsymbol{a}_c = \boldsymbol{a}_{\mathcal{T}} + \boldsymbol{a}_{\Pi}$ (and such indirect relationships are highlighted with square brackets). Most KHMH terms $\mathcal{Q}(\boldsymbol{x}, \boldsymbol{r}, t)$ are directly related to a NSD analogue $\boldsymbol{q}(\boldsymbol{x}, \boldsymbol{r}, t)$ as $\mathcal{Q} = 2\delta \boldsymbol{u} \cdot \boldsymbol{q}$. Some of the viscosity-related KHMH terms are indirectly related to the viscous NSD term $\delta \boldsymbol{a}_\nu$ as $2\delta \boldsymbol{u} \cdot \delta \boldsymbol{a}_\nu = \mathcal{D} = \mathcal{D}_{x,\nu} + \mathcal{D}_{r,\nu} - \epsilon$ (and these indirect relationships are highlighted with square brackets.) Subscripts S and I denote solenoidal and irrotational parts in physical space, while subscripts $\overline{S}$ and $\overline{I}$ denote irrotational and solenoidal parts in centroid space (see chapter 3 for more details).

B. Helmholtz-decomposed Dynamics in Fourier Space

In this appendix we first list the Helmholtz decomposition for periodic fields. Second, we show how this decomposition relates to the more general solution to the Helmholtz decomposition in the case of incompressible fields and fields which can be written as gradients of scalar fields. (These results are important to connect the general irrotational and solenoidal KHMH equations and the irrotational and solenoidal KHMH equations specific to homogeneous/periodic turbulence (see section 3.4).) Thirdly, we show that the difference of a periodic Helmholtz decomposed term $\boldsymbol{q}$ in physical space equals the Helmholtz decomposed term $\delta\boldsymbol{q}$ in centroid space and finally we show that $\boldsymbol{a}_{\Pi_{\overline{I}}}(\boldsymbol{x},\boldsymbol{r},t) = \boldsymbol{a}_{\mathcal{T}_{\overline{I}}}(\boldsymbol{x},\boldsymbol{r},t)$ in homogeneous/periodic turbulence (see section 3.1.3).

We first demonstrate that the longitudinal part of a periodic vector field equals the irrotational part of the vector field and that the transverse part of a periodic vector field equals its solenoidal part. Let $\boldsymbol{q}(\boldsymbol{x},t)$ be a periodic, twice continuously differentiable 3D vector field with the Helmholtz decomposition $\boldsymbol{q}(\boldsymbol{x},t) = \boldsymbol{q}_I(\boldsymbol{x},t) + \boldsymbol{q}_S(\boldsymbol{x},t)$, where $\boldsymbol{q}_I(\boldsymbol{x},t) = -\nabla_{\boldsymbol{x}}\phi(\boldsymbol{x},t)$, $\boldsymbol{q}_S(\boldsymbol{x},t) = \nabla_{\boldsymbol{x}} \times \boldsymbol{B}(\boldsymbol{x},t)$. The scalar and vector potentials ϕ and $\boldsymbol{B}$ are unique within constants when $\nabla_{\boldsymbol{x}} \cdot \boldsymbol{q}$ and $\nabla_{\boldsymbol{x}} \times \boldsymbol{q}$ are known in the domain and $\boldsymbol{q}$ is known at the boundary (Bhatia et al., 2013). $\boldsymbol{q}(\boldsymbol{x},t)$ has the corresponding Fourier representation $\widehat{\boldsymbol{q}}(\boldsymbol{k},t)$, which can be decomposed into a component parallel to $\boldsymbol{k}$ (the longitudinal field $\widehat{\boldsymbol{q}}^L$) and transverse to $\boldsymbol{k}$ (the transverse field $\widehat{\boldsymbol{q}}^T$) (Stewart, 2012)

$$\widehat{\boldsymbol{q}}^L(\boldsymbol{k},t) = \frac{\boldsymbol{k}[\widehat{\boldsymbol{q}}(\boldsymbol{k},t)\cdot\boldsymbol{k}]}{k^2}, \quad \widehat{\boldsymbol{q}}^T(\boldsymbol{k},t) = \widehat{\boldsymbol{q}}(\boldsymbol{k},t) - \widehat{\boldsymbol{q}}^L(\boldsymbol{k},t). \tag{B.1}$$

We define the scalar field $\Phi(\boldsymbol{x},t)$ as

$$\Phi(\boldsymbol{x},t) = \sum_{\boldsymbol{k}} \frac{\widehat{\boldsymbol{q}}(\boldsymbol{k},t)\cdot i\boldsymbol{k}}{k^2} e^{i\boldsymbol{k}\cdot\boldsymbol{x}}, \tag{B.2}$$

such that its Fourier modes read

$$\widehat{\Phi}(\boldsymbol{k},t) = \frac{\widehat{\boldsymbol{q}}(\boldsymbol{k},t)\cdot i\boldsymbol{k}}{k^2}. \tag{B.3}$$

We can write the inverse Fourier transform of $\widehat{\boldsymbol{q}}^L$ as

$$\boldsymbol{q}^L(\boldsymbol{x},t) = \sum_{\boldsymbol{k}} -i\boldsymbol{k}[\frac{\widehat{\boldsymbol{q}}(\boldsymbol{k},t)\cdot i\boldsymbol{k}}{k^2}]e^{i\boldsymbol{k}\cdot\boldsymbol{x}}, \tag{B.4}$$

$$= \sum_{\boldsymbol{k}} -i\boldsymbol{k}\widehat{\Phi}(\boldsymbol{k},t)e^{i\boldsymbol{k}\cdot\boldsymbol{x}}, \tag{B.5}$$

$$= -\nabla_{\boldsymbol{x}}\Phi(\boldsymbol{x},t), \tag{B.6}$$

such that $\boldsymbol{q}^L$ can be written as the gradient of a scalar potential. Per the uniqueness of the Helmholtz decomposition $\Phi = \phi$ within a constant with $\boldsymbol{q}_I = \boldsymbol{q}^L$. From this and $\boldsymbol{q} = \boldsymbol{q}_I + \boldsymbol{q}_S = \boldsymbol{q}^L + \boldsymbol{q}^T$ it follows that $\boldsymbol{q}_S = \boldsymbol{q}^T$, which is what we wanted to demonstrate.

We next connect the Helmholtz decomposition of periodic fields to a very general Helmholtz decomposition in the cases of incompressible fields and fields which are gradients of scalar fields. The Helmholtz decomposition can be written (Sprössig, 2010)

$$\boldsymbol{q}_{IV}(\boldsymbol{x},t) = \frac{1}{4\pi}\int_V d\boldsymbol{y}\frac{\boldsymbol{x}-\boldsymbol{y}}{|\boldsymbol{x}-\boldsymbol{y}|^3}[\nabla_{\boldsymbol{y}}\cdot\boldsymbol{q}(\boldsymbol{y},t)], \tag{B.7a}$$

$$\boldsymbol{q}_{IB}(\boldsymbol{x},t) = -\frac{1}{4\pi}\int_S dS_{\boldsymbol{y}}\frac{\boldsymbol{x}-\boldsymbol{y}}{|\boldsymbol{x}-\boldsymbol{y}|^3}[\widehat{\boldsymbol{n}}_{\boldsymbol{y}}\cdot\boldsymbol{q}(\boldsymbol{y},t)], \tag{B.7b}$$

$$\boldsymbol{q}_{SV}(\boldsymbol{x},t) = -\frac{1}{4\pi}\int_V d\boldsymbol{y}\frac{\boldsymbol{x}-\boldsymbol{y}}{|\boldsymbol{x}-\boldsymbol{y}|^3}\times[\nabla_{\boldsymbol{y}}\times\boldsymbol{q}(\boldsymbol{y},t)], \tag{B.7c}$$

$$\boldsymbol{q}_{SB}(\boldsymbol{x},t) = \frac{1}{4\pi}\int_S dS_{\boldsymbol{y}}\frac{\boldsymbol{x}-\boldsymbol{y}}{|\boldsymbol{x}-\boldsymbol{y}|^3}\times[\widehat{\boldsymbol{n}}_{\boldsymbol{y}}\times\boldsymbol{q}(\boldsymbol{y},t)]. \tag{B.7d}$$

where $\boldsymbol{q}_I = \boldsymbol{q}_{IV} + \boldsymbol{q}_{IB}$, $\boldsymbol{q}_S = \boldsymbol{q}_{SV} + \boldsymbol{q}_{SB}$ and $\widehat{\boldsymbol{n}}_{\boldsymbol{y}}$ denotes the unit surface normal at $\boldsymbol{y}$ and $dS_{\boldsymbol{y}}$ is the differential surface element at $\boldsymbol{y}$. In the case of a field $\boldsymbol{q}(\boldsymbol{x},t)$ which is incompressible $\nabla_{\boldsymbol{x}}\cdot\boldsymbol{q}(\boldsymbol{x},t) = 0$, it follows that $\widehat{\boldsymbol{q}}(\boldsymbol{k},t)\cdot\boldsymbol{k} = 0$ for every $\boldsymbol{k}$. By inspection of (B.1), it is clear that this condition yields $\widehat{\boldsymbol{q}}^L(\boldsymbol{k},t) = 0$ for every $\boldsymbol{k}$ such that $\widehat{\boldsymbol{q}}(\boldsymbol{k},t) = \widehat{\boldsymbol{q}}(\boldsymbol{k},t)^T$. By applying the Fourier transform to this relation and applying $\boldsymbol{q}^T(\boldsymbol{x},t) = \boldsymbol{q}_S(\boldsymbol{x},t)$ from above, we have that $\boldsymbol{q}(\boldsymbol{x},t) = \boldsymbol{q}_S(\boldsymbol{x},t)$ for incompressible periodic vector fields. In the case of $\boldsymbol{q}(\boldsymbol{x},t) = \nabla_{\boldsymbol{x}}\psi(\boldsymbol{x},\boldsymbol{t})$, where $\psi(\boldsymbol{x},t)$ is some scalar field, we have that $\widehat{\boldsymbol{q}}(\boldsymbol{k},t) = i\boldsymbol{k}\widehat{\psi}(\boldsymbol{k},t)$. If we insert this expression into the definition of $\widehat{\boldsymbol{q}}^L(\boldsymbol{k},t)$, it follows that $\widehat{\boldsymbol{q}}(\boldsymbol{k},t) = \widehat{\boldsymbol{q}}^L(\boldsymbol{k},t)$, which implies that $\boldsymbol{q}(\boldsymbol{x},t) = \boldsymbol{q}_I(\boldsymbol{x},t)$. If these properties are combined with equations (B.7a)-(B.7d), we obtain the following simplifications: A periodic incompressible vector field has $\boldsymbol{q}_{IB} = \boldsymbol{q}_{IV} = 0$ and a periodic vector field that can be written as a gradient of a scalar field has $\boldsymbol{q}_{SB} = \boldsymbol{q}_{SV} = 0$.

We next demonstrate that $\delta\boldsymbol{q}_I = \delta\boldsymbol{q}_{\overline{I}}$ and $\delta\boldsymbol{q}_S = \delta\boldsymbol{q}_{\overline{S}}$ for a periodic vector field $\boldsymbol{q}$ (i.e. the difference of a periodic Helmholtz decomposed term $\boldsymbol{q}$ in physical space equals the Helmholtz decomposed term $\delta\boldsymbol{q}$ in centroid space). The field $\boldsymbol{q}$ has the Fourier representation

$$\boldsymbol{q}(\boldsymbol{x},t) = \sum_{\boldsymbol{k}}\widehat{\boldsymbol{q}}(\boldsymbol{k},t)e^{i\boldsymbol{k}\cdot\boldsymbol{x}}, \tag{B.8}$$

with the shifted fields

$$\boldsymbol{q}^+(\boldsymbol{x},\boldsymbol{r},t) = \boldsymbol{q}(\boldsymbol{x}+\boldsymbol{r}/2,t) = \sum_{\boldsymbol{k}} \widehat{\boldsymbol{q}}(\boldsymbol{k},t)e^{i\boldsymbol{k}\cdot(\boldsymbol{x}+\boldsymbol{r}/2)}, \tag{B.9a}$$

$$\boldsymbol{q}^-(\boldsymbol{x},\boldsymbol{r},t) = \boldsymbol{q}(\boldsymbol{x}-\boldsymbol{r}/2,t) = \sum_{\boldsymbol{k}} \widehat{\boldsymbol{q}}(\boldsymbol{k},t)e^{i\boldsymbol{k}\cdot(\boldsymbol{x}-\boldsymbol{r}/2)}, \tag{B.9b}$$

which have the Fourier coefficients

$$\widehat{\boldsymbol{q}^+}(\boldsymbol{k},\boldsymbol{r},t) = \widehat{\boldsymbol{q}}(\boldsymbol{k},t)e^{i\boldsymbol{k}\cdot\boldsymbol{r}/2}, \tag{B.10a}$$

$$\widehat{\boldsymbol{q}^-}(\boldsymbol{k},\boldsymbol{r},t) = \widehat{\boldsymbol{q}}(\boldsymbol{k},t)e^{-i\boldsymbol{k}\cdot\boldsymbol{r}/2}. \tag{B.10b}$$

From the definition of the irrotational part of a vector field in (B.1), it follows

$$\delta\boldsymbol{q}_I(\boldsymbol{x},\boldsymbol{r},t) = \boldsymbol{q}_I^+(\boldsymbol{x},\boldsymbol{r},t) - \boldsymbol{q}_I^-(\boldsymbol{x},\boldsymbol{r},t), \tag{B.11a}$$

$$= \sum_{\boldsymbol{k}} [\widehat{\boldsymbol{q}_I^+}(\boldsymbol{k},\boldsymbol{r},t) - \widehat{\boldsymbol{q}_I^-}(\boldsymbol{k},\boldsymbol{r},t)]e^{i\boldsymbol{k}\cdot\boldsymbol{x}}, \tag{B.11b}$$

$$= \sum_{\boldsymbol{k}} \frac{\boldsymbol{k}}{k^2}[\widehat{\boldsymbol{q}}(\boldsymbol{k},t)\cdot\boldsymbol{k}](e^{i\boldsymbol{k}\cdot\boldsymbol{r}/2} - e^{-i\boldsymbol{k}\cdot\boldsymbol{r}/2})e^{i\boldsymbol{k}\cdot\boldsymbol{x}}, \tag{B.11c}$$

$$= \sum_{\boldsymbol{k}} \frac{\boldsymbol{k}}{k^2}[\widehat{\boldsymbol{q}}(\boldsymbol{k},t)\cdot\boldsymbol{k}]2i\sin(\boldsymbol{k}\cdot\boldsymbol{r}/2)e^{i\boldsymbol{k}\cdot\boldsymbol{x}}. \tag{B.11d}$$

Similarly, we can write

$$\delta\boldsymbol{q}(\boldsymbol{x},\boldsymbol{r},t) = \boldsymbol{q}^+(\boldsymbol{x},\boldsymbol{r},t) - \boldsymbol{q}^-(\boldsymbol{x},\boldsymbol{r},t), \tag{B.12a}$$

$$= \sum_{\boldsymbol{k}} \widehat{\boldsymbol{q}}(\boldsymbol{k},t)2i\sin(\boldsymbol{k}\cdot\boldsymbol{r}/2)e^{i\boldsymbol{k}\cdot\boldsymbol{x}}, \tag{B.12b}$$

and then calculate its irrotational centroid part

$$\delta\boldsymbol{q}_{\overline{I}}(\boldsymbol{x},\boldsymbol{r},t) = \sum_{\boldsymbol{k}} \frac{\boldsymbol{k}}{k^2}[\widehat{\boldsymbol{q}}(\boldsymbol{k},t)\cdot\boldsymbol{k}]2i\sin(\boldsymbol{k}\cdot\boldsymbol{r}/2)e^{i\boldsymbol{k}\cdot\boldsymbol{x}}, \tag{B.13}$$

which shows that $\delta\boldsymbol{q}_I(\boldsymbol{x},\boldsymbol{r},t) = \delta\boldsymbol{q}_{\overline{I}}(\boldsymbol{x},\boldsymbol{r},t)$. By combining this with $\delta\boldsymbol{q} = \delta\boldsymbol{q}_I + \delta\boldsymbol{q}_S = \delta\boldsymbol{q}_{\overline{I}} + \delta\boldsymbol{q}_{\overline{S}}$, we have also $\delta\boldsymbol{q}_S(\boldsymbol{x},\boldsymbol{r},t) = \delta\boldsymbol{q}_{\overline{S}}(\boldsymbol{x},\boldsymbol{r},t)$, which is what we wanted to show.

We end this appendix by showing that $\boldsymbol{a}_{\Pi_{\overline{I}}}(\boldsymbol{x},\boldsymbol{r},t) = \boldsymbol{a}_{\mathcal{T}_{\overline{I}}}(\boldsymbol{x},\boldsymbol{r},t)$ in homogeneous/periodic turbulence. First, we list the following expressions for the vectors and tensors related to these two terms in Fourier space

$$\widehat{\delta u_j}(\boldsymbol{k},\boldsymbol{r},t) = 2i\sin(\boldsymbol{k}\cdot\boldsymbol{r}/2)\widehat{u}_j(\boldsymbol{k},t), \tag{B.14a}$$

$$(\widehat{u_j^+ + u_j^-})/2(\boldsymbol{k},\boldsymbol{r},t) = \cos(\boldsymbol{k}\cdot\boldsymbol{r}/2)\widehat{u}_j(\boldsymbol{k},t), \tag{B.14b}$$

$$\widehat{\frac{\partial\delta u_i}{\partial r_j}}(\boldsymbol{k},\boldsymbol{r},t) = ik_j\cos(\boldsymbol{k}\cdot\boldsymbol{r}/2)\widehat{u}_i(\boldsymbol{k},t), \tag{B.14c}$$

$$\widehat{\frac{\partial\delta u_i}{\partial x_j}}(\boldsymbol{k},\boldsymbol{r},t) = -2k_j\sin(\boldsymbol{k}\cdot\boldsymbol{r}/2)\widehat{u}_i(\boldsymbol{k},t). \tag{B.14d}$$

By use of these equations, we have that the Fourier coefficients of the transport terms read (see section 2.1.1 for more details on non-linear terms and convolution sums)

$$\widehat{\boldsymbol{a}_{\mathcal{T}}}(\boldsymbol{k},\boldsymbol{r},t) = \sum_{\boldsymbol{k}=\boldsymbol{k}'+\boldsymbol{k}''} -2\sin(\boldsymbol{k}''\cdot\boldsymbol{r}/2)\cos(\boldsymbol{k}'\cdot\boldsymbol{r}/2)\widehat{u}_j(\boldsymbol{k}')k_j''\widehat{\boldsymbol{u}}(\boldsymbol{k}''), \tag{B.15a}$$

$$\widehat{\boldsymbol{a}_{\mathit{\Pi}}}(\boldsymbol{k},\boldsymbol{r},t) = \sum_{\boldsymbol{k}=\boldsymbol{k}'+\boldsymbol{k}''} -2\sin(\boldsymbol{k}'\cdot\boldsymbol{r}/2)\cos(\boldsymbol{k}''\cdot\boldsymbol{r}/2)\widehat{u}_j(\boldsymbol{k}')k_j''\widehat{\boldsymbol{u}}(\boldsymbol{k}''). \tag{B.15b}$$

Their irrotational parts are given per (B.1)

$$\widehat{\boldsymbol{a}_{\mathcal{T}_{\bar{I}}}}(\boldsymbol{k},\boldsymbol{r},t) = -\frac{\boldsymbol{k}}{k^2}\sum_{\boldsymbol{k}=\boldsymbol{k}'+\boldsymbol{k}''} 2\sin(\boldsymbol{k}''\cdot\boldsymbol{r}/2)\cos(\boldsymbol{k}'\cdot\boldsymbol{r}/2)\widehat{u}_j(\boldsymbol{k}')k_j''\widehat{u}_l(\boldsymbol{k}'')k_l', \tag{B.16a}$$

$$\widehat{\boldsymbol{a}_{\mathit{\Pi}_{\bar{I}}}}(\boldsymbol{k},\boldsymbol{r},t) = -\frac{\boldsymbol{k}}{k^2}\sum_{\boldsymbol{k}=\boldsymbol{k}'+\boldsymbol{k}''} 2\sin(\boldsymbol{k}'\cdot\boldsymbol{r}/2)\cos(\boldsymbol{k}''\cdot\boldsymbol{r}/2)\widehat{u}_j(\boldsymbol{k}')k_j''\widehat{u}_l(\boldsymbol{k}'')k_l'. \tag{B.16b}$$

If we employ the trigonometric identity $\sin x\cos y = \frac{1}{2}[\sin(x+y)+\sin(x-y)]$, we get

$$\widehat{\boldsymbol{a}_{\mathcal{T}_{\bar{I}}}}(\boldsymbol{k},\boldsymbol{r},t) = -\frac{\boldsymbol{k}}{k^2}\sum_{\boldsymbol{k}=\boldsymbol{k}'+\boldsymbol{k}''} [\sin(\boldsymbol{k}\cdot\boldsymbol{r}/2)+\sin(\boldsymbol{k}''\cdot\boldsymbol{r}/2-\boldsymbol{k}'\cdot\boldsymbol{r}/2)]\widehat{u}_j(\boldsymbol{k}')k_j''\widehat{u}_l(\boldsymbol{k}'')k_l', \tag{B.17a}$$

$$\widehat{\boldsymbol{a}_{\mathit{\Pi}_{\bar{I}}}}(\boldsymbol{k},\boldsymbol{r},t) = -\frac{\boldsymbol{k}}{k^2}\sum_{\boldsymbol{k}=\boldsymbol{k}'+\boldsymbol{k}''} [\sin(\boldsymbol{k}\cdot\boldsymbol{r}/2)-\sin(\boldsymbol{k}''\cdot\boldsymbol{r}/2-\boldsymbol{k}'\cdot\boldsymbol{r}/2)]\widehat{u}_j(\boldsymbol{k}')k_j''\widehat{u}_l(\boldsymbol{k}'')k_l'. \tag{B.17b}$$

Consider the term $\sin(\boldsymbol{k}''\cdot\boldsymbol{r}/2-\boldsymbol{k}'\cdot\boldsymbol{r}/2)\widehat{u}_j(\boldsymbol{k}')k_j''\widehat{u}_l(\boldsymbol{k}'')k_l'$. If one adds this term with the wavenumber triad $\boldsymbol{k}' = \boldsymbol{k}^a$ and $\boldsymbol{k}'' = \boldsymbol{k}^b \neq \boldsymbol{k}^a$ with the same term with the wavenumber triad $\boldsymbol{k}' = \boldsymbol{k}^b$ and $\boldsymbol{k}'' = \boldsymbol{k}^a$ the result is zero. Furthermore, in the case of $\boldsymbol{k}^a = \boldsymbol{k}^b$ this term is zero per incompressibility. That is, this term does not contribute instantaneously in the above expressions such that we attain what we wanted to demonstrate

$$\widehat{\boldsymbol{a}_{\mathcal{T}_{\bar{I}}}}(\boldsymbol{k},\boldsymbol{r},t) = \widehat{\boldsymbol{a}_{\mathit{\Pi}_{\bar{I}}}}(\boldsymbol{k},\boldsymbol{r},t) = -\frac{\boldsymbol{k}}{k^2}\sin(\boldsymbol{k}\cdot\boldsymbol{r}/2)\sum_{\boldsymbol{k}=\boldsymbol{k}'+\boldsymbol{k}''}\widehat{u}_j(\boldsymbol{k}')k_j''\widehat{u}_l(\boldsymbol{k}'')k_l'. \tag{B.18}$$

C. Spatially Averaged KHMH Terms in Fourier Space

The spatially averaged KHMH equation in homogeneous turbulence (see section 5.1) reads

$$\langle \mathcal{A}_t \rangle_{\boldsymbol{x}} + \langle \Pi \rangle_{\boldsymbol{x}} = \langle \mathcal{D}_{r,\nu} \rangle_{\boldsymbol{x}} - \langle \epsilon^* \rangle_{\boldsymbol{x}} + \langle \mathcal{I} \rangle_{\boldsymbol{x}}. \tag{C.1}$$

In the following we derive expressions for efficient and accurate evaluations of the spatially averaged KHMH terms in (C.1) by adapting the derivation of Gatti et al. (2019) to homogeneous/periodic turbulence.

We start with some preliminary expressions which will be useful later. The velocity field $u_i(\boldsymbol{x},t)$ can be written in terms of $\widehat{u}_i(\boldsymbol{k},t)$ as

$$u_i(\boldsymbol{x},t) = \sum_{\boldsymbol{k}} \widehat{u}_i(\boldsymbol{k},t) e^{i\boldsymbol{k}\cdot\boldsymbol{x}}, \tag{C.2}$$

and the velocity fields at $\boldsymbol{x} \pm \boldsymbol{r}/2$ (see appendix B) can be written as

$$u_i^{\pm}(\boldsymbol{x},\boldsymbol{r},t) = \sum_{\boldsymbol{k}} \widehat{u}_i(\boldsymbol{k},t) e^{\pm i\boldsymbol{k}\cdot\boldsymbol{r}/2} e^{i\boldsymbol{k}\cdot\boldsymbol{x}}. \tag{C.3}$$

We can express from (C.3) $\langle u_i^+(\boldsymbol{x},\boldsymbol{r},t) u_j^-(\boldsymbol{x},\boldsymbol{r},t)\rangle_{\boldsymbol{x}}$ as (in the following we drop for brevity the $u_i^{\pm}$ and $f_i^{\pm}$ dependency on $(\boldsymbol{x},\boldsymbol{r},t)$ and the $\widehat{u}_i$ and $\widehat{f}_i$ dependency on t)

$$\begin{aligned}
\langle u_i^+ u_j^- \rangle_{\boldsymbol{x}} &= \langle \sum_{\boldsymbol{k}} \widehat{u}_i(\boldsymbol{k}) e^{i\boldsymbol{k}\cdot\boldsymbol{r}/2} e^{i\boldsymbol{k}\cdot\boldsymbol{x}} \sum_{\boldsymbol{k}'} \widehat{u}_j(\boldsymbol{k}') e^{-i\boldsymbol{k}'\cdot\boldsymbol{r}/2} e^{i\boldsymbol{k}'\cdot\boldsymbol{x}} \rangle_{\boldsymbol{x}}, && \text{(C.4a)}\\
&= \langle \sum_{\boldsymbol{k}} \sum_{\boldsymbol{k}'} \widehat{u}_i(\boldsymbol{k}) \widehat{u}_j(\boldsymbol{k}') e^{i(\boldsymbol{k}-\boldsymbol{k}')\cdot\boldsymbol{r}/2} e^{i(\boldsymbol{k}+\boldsymbol{k}')\cdot\boldsymbol{x}} \rangle_{\boldsymbol{x}}, && \text{(C.4b)}\\
&= \sum_{\boldsymbol{k}} \widehat{u}_i(\boldsymbol{k}) \widehat{u}_j^*(\boldsymbol{k}) e^{i\boldsymbol{k}\cdot\boldsymbol{r}}, && \text{(C.4c)}
\end{aligned}$$

where the final line follows from the orthogonality of Fourier modes (Canuto et al., 1987) ($\langle e^{i(\boldsymbol{k}+\boldsymbol{k}')\cdot\boldsymbol{x}}\rangle_{\boldsymbol{x}}$ equals zero for $\boldsymbol{k}' \neq -\boldsymbol{k}$ and unity for $\boldsymbol{k}' = -\boldsymbol{k}$) and the reality of u_j which requires $\widehat{u}_j(-\boldsymbol{k}) = \widehat{u}_j^*(\boldsymbol{k})$ (and $\widehat{u}_j^*(\boldsymbol{k})$ is the complex conjugate of $\widehat{u}_j(\boldsymbol{k})$). By repeating the steps in (C.4) for $\langle u_i^+ u_j^+ \rangle_{\boldsymbol{x}}$ and $\langle u_i^- u_j^- \rangle_{\boldsymbol{x}}$, it follows that $\langle u_i^+ u_j^+ \rangle_{\boldsymbol{x}} = \langle u_i^- u_j^- \rangle_{\boldsymbol{x}} = \langle u_i u_j \rangle_{\boldsymbol{x}}$.

We next express the spatially averaged KHMH terms which only involve products of two u_i and/or f_i components (i.e. all the terms in (C.1) except $\langle \Pi \rangle_{\boldsymbol{x}}$). The spatially averaged time derivative term can be written in the semi-discrete form

$$\begin{aligned}
\langle \mathcal{A}_t \rangle_{\boldsymbol{x}}(\boldsymbol{r}, t) &= \frac{\partial}{\partial t} \langle \delta u_i \delta u_i \rangle_{\boldsymbol{x}}, && \text{(C.5a)} \\
&= \frac{\partial}{\partial t} \big(\langle u_i^+ u_i^+ \rangle_{\boldsymbol{x}} - 2 \langle u_i^+ u_i^- \rangle_{\boldsymbol{x}} + \langle u_i^- u_i^- \rangle_{\boldsymbol{x}} \big), && \text{(C.5b)} \\
&= \frac{\partial}{\partial t} \big(2 \langle u_i u_i \rangle_{\boldsymbol{x}} - 2 \langle u_i^+ u_i^- \rangle_{\boldsymbol{x}} \big), && \text{(C.5c)} \\
&= 2 \frac{\partial}{\partial t} \sum_{\boldsymbol{k}} \widehat{u}_i(\boldsymbol{k}) \widehat{u}_i^*(\boldsymbol{k}) \big(1 - e^{i\boldsymbol{k}\cdot\boldsymbol{r}} \big), && \text{(C.5d)}
\end{aligned}$$

and the forcing term can be developed similarly as

$$\begin{aligned}
\langle \mathcal{I} \rangle_{\boldsymbol{x}}(\boldsymbol{r}, t) &= 2 \langle \delta u_i \delta f_i \rangle_{\boldsymbol{x}}, && \text{(C.6a)} \\
&= 2 \big(\langle u_i^+ f_i^+ \rangle_{\boldsymbol{x}} - \langle u_i^+ f_i^- \rangle_{\boldsymbol{x}} - \langle f_i^+ u_i^- \rangle_{\boldsymbol{x}} + \langle u_i^- f_i^- \rangle_{\boldsymbol{x}} \big), && \text{(C.6b)} \\
&= 2 \big(2 \sum_{\boldsymbol{k}} \widehat{u}_i(\boldsymbol{k}) \widehat{f}_i^*(\boldsymbol{k}) - \widehat{u}_i(\boldsymbol{k}) \widehat{f}_i^*(\boldsymbol{k}) e^{i\boldsymbol{k}\cdot\boldsymbol{r}} - \widehat{u}_i(\boldsymbol{k}) \widehat{f}_i^*(\boldsymbol{k}) e^{-i\boldsymbol{k}\cdot\boldsymbol{r}} \big), && \text{(C.6c)} \\
&= 2 \sum_{\boldsymbol{k}} \widehat{u}_i(\boldsymbol{k}) \widehat{f}_i^*(\boldsymbol{k}) (2 - e^{i\boldsymbol{k}\cdot\boldsymbol{r}} - e^{-i\boldsymbol{k}\cdot\boldsymbol{r}}). && \text{(C.6d)}
\end{aligned}$$

The spatially averaged viscous diffusion in scale space term can be expressed as

$$\begin{aligned}
\langle \mathcal{D}_{r,\nu} \rangle_{\boldsymbol{x}}(\boldsymbol{r}, t) &= 2\nu \frac{\partial^2}{\partial r_l^2} \langle \delta u_i \delta u_i \rangle_{\boldsymbol{x}}, && \text{(C.7a)} \\
&= 4\nu \frac{\partial^2}{\partial r_l^2} \sum_{\boldsymbol{k}} \widehat{u}_i(\boldsymbol{k}) \widehat{u}_i^*(\boldsymbol{k}) \big(1 - e^{i\boldsymbol{k}\cdot\boldsymbol{r}} \big), && \text{(C.7b)} \\
&= 4\nu \sum_{\boldsymbol{k}} k^2 \widehat{u}_i(\boldsymbol{k}) \widehat{u}_i^*(\boldsymbol{k}) e^{i\boldsymbol{k}\cdot\boldsymbol{r}}, && \text{(C.7c)}
\end{aligned}$$

where we used the expression developed for $\langle \delta u_i \delta u_i \rangle_{\boldsymbol{x}}$ in (C.5) to go from (C.7a) to (C.7b) (and $k^2 = k_l k_l$). Similarly as for the velocity tensor $\langle u_i u_j \rangle_{\boldsymbol{x}}$, it is easy to show that $\langle (\partial u_i^+ / \partial x_j^+)^2 \rangle_{\boldsymbol{x}} = \langle (\partial u_i^- / \partial x_j^-)^2 \rangle_{\boldsymbol{x}} = \langle (\partial u_i / \partial x_j)^2 \rangle_{\boldsymbol{x}}$. This allows us to write the spatially averaged two-point pseudo-dissipation rate as

$$\begin{aligned}
\langle \epsilon^* \rangle_{\boldsymbol{x}}(t) &= 4\nu \langle \frac{\partial u_i}{\partial x_j} \frac{\partial u_i}{\partial x_j} \rangle_{\boldsymbol{x}}, && \text{(C.8a)} \\
&= 4\nu \langle \sum_{\boldsymbol{k}} \widehat{u}_i(\boldsymbol{k}) i k_j e^{i\boldsymbol{k}\boldsymbol{x}} \sum_{\boldsymbol{k}'} \widehat{u}_i(\boldsymbol{k}') i k_j' e^{i\boldsymbol{k}'\boldsymbol{x}} \rangle_{\boldsymbol{x}}, && \text{(C.8b)} \\
&= 4\nu \sum_{\boldsymbol{k}} k^2 \widehat{u}_i(\boldsymbol{k}) \widehat{u}_i^*(\boldsymbol{k}). && \text{(C.8c)}
\end{aligned}$$

We can write the spatially averaged interscale transfer rate in terms of velocity triple correlations as

$$\langle \mathit{\Pi} \rangle_{\boldsymbol{x}}(\boldsymbol{r}, t) = \frac{\partial}{\partial r_j} \langle \delta u_j \delta u_i \delta u_i \rangle_{\boldsymbol{x}}, \tag{C.9a}$$

$$= \frac{\partial}{\partial r_j} \langle u_i^+ u_i^+ u_j^+ - 2u_i^+ u_j^+ u_i^- + u_j^+ u_i^- u_i^- - u_i^+ u_i^+ u_j^- + 2u_i^+ u_i^- u_j^- - u_i^- u_i^- u_j^- \rangle_{\boldsymbol{x}}. \tag{C.9b}$$

We write the leftmost term in the RHS of (C.9b) as

$$\langle u_i^+ u_i^+ u_j^+ \rangle_{\boldsymbol{x}} = \langle \sum_{\boldsymbol{k}} \langle u_i^+ u_i^+ \rangle_{\boldsymbol{k}} e^{i\boldsymbol{k}\cdot\boldsymbol{x}} \sum_{\boldsymbol{k}'} \widehat{u}_j(\boldsymbol{k}') e^{i\boldsymbol{k}'\cdot\boldsymbol{x}} e^{i\boldsymbol{k}'\cdot\boldsymbol{r}/2} \rangle_{\boldsymbol{x}}, \tag{C.10a}$$

$$= \sum_{\boldsymbol{k}} \langle u_i^+ u_i^+ \rangle_{\boldsymbol{k}} \widehat{u}_j^*(\boldsymbol{k}) e^{-i\boldsymbol{k}\cdot\boldsymbol{r}/2}, \tag{C.10b}$$

where

$$\langle u_i^+ u_i^+ \rangle_{\boldsymbol{k}} = \frac{1}{N^3} \sum_{\boldsymbol{x}} u_i^+ u_i^+ e^{-i\boldsymbol{k}\cdot\boldsymbol{x}}, \tag{C.11a}$$

$$= \sum_{\boldsymbol{k}'} \sum_{\boldsymbol{k}''} \widehat{u}_i(\boldsymbol{k}') \widehat{u}_i(\boldsymbol{k}'') e^{i(\boldsymbol{k}'+\boldsymbol{k}'')\cdot\boldsymbol{r}/2} \frac{1}{N^3} \sum_{\boldsymbol{x}} e^{i(\boldsymbol{k}'+\boldsymbol{k}''-\boldsymbol{k})\cdot\boldsymbol{x}}, \tag{C.11b}$$

$$= e^{i\boldsymbol{k}\cdot\boldsymbol{r}/2} \sum_{\boldsymbol{k}=\boldsymbol{k}'+\boldsymbol{k}''} \widehat{u}_i(\boldsymbol{k}') \widehat{u}_i(\boldsymbol{k}'') = e^{i\boldsymbol{k}\cdot\boldsymbol{r}/2} \langle u_i u_i \rangle_{\boldsymbol{k}}, \tag{C.11c}$$

such that

$$\langle u_i^+ u_i^+ u_j^+ \rangle_{\boldsymbol{x}} = \sum_{\boldsymbol{k}} \langle u_i u_i \rangle_{\boldsymbol{k}} \widehat{u}_j^*(\boldsymbol{k}), \tag{C.12}$$

(and note the notation $\langle \phi \rangle_{\boldsymbol{k}} = \widehat{\phi}(\boldsymbol{k})$). When going from (C.11b) to (C.11c), we assume that aliasing errors are zero or taken appropriate care of. E.g., if one applies the full dealiasing technique of Patterson and Orszag (1971) to $\langle u_i^+ u_i^+ \rangle_{\boldsymbol{k}}$, equation (C.11c) follows (see also section 2.1.1). Thus, we only need to use this technique once at every time step to calculate $\langle u_i u_i \rangle_{\boldsymbol{k}}$ rather than for every $\langle u_i^+ u_i^+ \rangle_{\boldsymbol{k}}$ (i.e. for every $\boldsymbol{r}$ at every time step).

We can repeat the above procedure for the five remaining terms in (C.9b) with the only differences being the sign in front of $\boldsymbol{r}$ in (C.10b) and (C.11c) and the velocity component indices (i.e. i or j). The five remaining terms read

$$-2\langle u_i^+ u_j^+ u_i^- \rangle_{\boldsymbol{x}} = -2 \sum_{\boldsymbol{k}} \langle u_i u_j \rangle_{\boldsymbol{k}} \widehat{u}_i^*(\boldsymbol{k}) e^{i\boldsymbol{k}\cdot\boldsymbol{r}}, \tag{C.13a}$$

$$\langle u_j^+ u_i^- u_i^- \rangle_{\boldsymbol{x}} = \sum_{\boldsymbol{k}} \langle u_i u_i \rangle_{\boldsymbol{k}} \widehat{u}_j^*(\boldsymbol{k}) e^{-i\boldsymbol{k}\cdot\boldsymbol{r}}, \tag{C.13b}$$

$$\langle u_i^+ u_i^+ u_j^- \rangle_{\boldsymbol{x}} = \sum_{\boldsymbol{k}} \langle u_i u_i \rangle_{\boldsymbol{k}} \widehat{u}_j^*(\boldsymbol{k}) e^{i\boldsymbol{k}\cdot\boldsymbol{r}}, \tag{C.13c}$$

$$2\langle u_i^+ u_i^- u_j^- \rangle_{\boldsymbol{x}} = 2 \sum_{\boldsymbol{k}} \langle u_i u_j \rangle_{\boldsymbol{k}} \widehat{u}_i^*(\boldsymbol{k}) e^{-i\boldsymbol{k}\cdot\boldsymbol{r}}, \tag{C.13d}$$

$$-\langle u_i^- u_j^- u_i^- \rangle_{\boldsymbol{x}} = -\sum_{\boldsymbol{k}} \langle u_i u_i \rangle_{\boldsymbol{k}} \widehat{u}_j^*(\boldsymbol{k}). \tag{C.13e}$$

Clearly, $\langle u_i^+u_i^+u_j^+\rangle_{\boldsymbol{x}}$ cancels with $-\langle u_i^-u_j^-u_i^-\rangle_{\boldsymbol{x}}$. Moreover, the contributions to $\langle \mathit{\Pi}\rangle_{\boldsymbol{x}}$ from (C.13b) and (C.13c) equal zero from incompressibility ($k_j\widehat{u}_j^*(\boldsymbol{k}) = 0$). This leaves only the contributions from (C.13a) and (C.13d), which yield the following expression

$$\begin{aligned}
\langle \mathit{\Pi}\rangle_{\boldsymbol{x}}(\boldsymbol{r},t) &= \frac{\partial}{\partial r_j}\big(-2\sum_{\boldsymbol{k}}\langle u_iu_j\rangle_{\boldsymbol{k}}\widehat{u}_i^*(\boldsymbol{k})e^{i\boldsymbol{k}\cdot\boldsymbol{r}} + 2\sum_{\boldsymbol{k}}\langle u_iu_j\rangle_{\boldsymbol{k}}\widehat{u}_i^*(\boldsymbol{k})e^{-i\boldsymbol{k}\cdot\boldsymbol{r}}\big), && \text{(C.14a)}\\
&= 2\frac{\partial}{\partial r_j}\sum_{\boldsymbol{k}}\langle u_iu_j\rangle_{\boldsymbol{k}}\widehat{u}_i^*(\boldsymbol{k})\big(e^{-i\boldsymbol{k}\cdot\boldsymbol{r}} - e^{i\boldsymbol{k}\cdot\boldsymbol{r}}\big), && \text{(C.14b)}\\
&= 2\sum_{\boldsymbol{k}}\langle u_iu_j\rangle_{\boldsymbol{k}}\widehat{u}_i^*(\boldsymbol{k})(-2ik_j\cos(\boldsymbol{k}\cdot\boldsymbol{r})), && \text{(C.14c)}\\
&= 4\sum_{\boldsymbol{k}}\cos(\boldsymbol{k}\cdot\boldsymbol{r})k_j\Im[\langle u_iu_j\rangle_{\boldsymbol{k}}\widehat{u}_i^*(\boldsymbol{k})], && \text{(C.14d)}
\end{aligned}$$

where the final line follows from only considering the real part of (C.14c) and $\Im[z]$ denotes the imaginary part of z.

In light of the above expressions, the calculation of spatially averaged KHMH terms at time t can be subdivided into two steps. Firstly, one obtains the required vector/tensor fields in Fourier space. $\widehat{f}_i(\boldsymbol{k},t)$ and $\widehat{u}_i(\boldsymbol{k},t)$ are required and $\widehat{u}_i(\boldsymbol{k})$ is required at different times to calculate the time-derivative in (C.5) (we use a first-order forward difference). The tensor $\langle u_iu_j\rangle_{\boldsymbol{k}}$ must be calculated with an appropriate method which removes aliasing errors (we use the method of Patterson and Orszag (1971)). This step has the same complexity as a DNS time step $\mathcal{O}(N^3\log_2 N)$. Secondly, the above fields are used in expressions (C.5d)-(C.6d)-(C.7c)-(C.8c)-(C.14d) to calculate the non-zero spatially averaged KHMH terms at a total N_r separation vectors $\boldsymbol{r}$. This second step, which has complexity $\mathcal{O}(N^3N_r)$, is typically more computationally demanding than the first step as typically $N_r \gg \log_2(N)$. The second step can be performed more efficiently if one is interested in spherical averages. Applying a spherical average to these expressions, yields

$$\begin{aligned}
\langle \mathcal{A}_t\rangle_{\boldsymbol{x}}^a(r_d,t) &= 2\frac{\partial}{\partial t}\sum_{\boldsymbol{k}}\widehat{u}_i(\boldsymbol{k},t)\widehat{u}_i^*(\boldsymbol{k},t)\big(1-\sin(kr_d)/(kr_d)\big), && \text{(C.15a)}\\
\langle \mathit{\Pi}\rangle_{\boldsymbol{x}}^a(r_d,t) &= 4\sum_{\boldsymbol{k}}k_j\Im[\langle u_iu_j\rangle_{\boldsymbol{k}}(t)\widehat{u}_i^*(\boldsymbol{k},t)]\sin(kr_d)/(kr_d), && \text{(C.15b)}\\
\langle \mathcal{D}_{r,\nu}\rangle_{\boldsymbol{x}}^a(r_d,t) &= 4\nu\sum_{\boldsymbol{k}}k^2\widehat{u}_i(\boldsymbol{k},t)\widehat{u}_i^*(\boldsymbol{k},t)\sin(kr_d)/(kr_d), && \text{(C.15c)}\\
\langle \epsilon^*\rangle_{\boldsymbol{x}}(t) &= 4\nu\sum_{\boldsymbol{k}}k^2\widehat{u}_i(\boldsymbol{k},t)\widehat{u}_i^*(\boldsymbol{k},t), && \text{(C.15d)}\\
\langle \mathcal{I}\rangle_{\boldsymbol{x}}^a(r_d,t) &= 4\sum_{\boldsymbol{k}}\widehat{u}_i(\boldsymbol{k},t)\widehat{f}_i^*(\boldsymbol{k},t)(1-\sin(kr_d)/(kr_d)). && \text{(C.15e)}
\end{aligned}$$

If the total number of considered scales $N_{r_d} \lesssim \log_2(N)$, we have that the second calculation step is similarly or less expensive than the first calculation step. In this case, the calculation of the KHMH terms (C.15) at one time step has complexity $\mathcal{O}(N^3\log_2 N)$.

D. Time-lags and Grid Turbulence

In this appendix we adapt our non-equilibrium cascade dynamics and second-order structure function scaling (5.32)-(5.33) to grid turbulence by use of Taylor's hypothesis (Taylor, 1938b; Tsinober, 2009). This results in some interesting expressions, qualitatively consistent with experiments/DNSs, which shed led light on the relative importance of advection to interscale transfer in grid turbulence. We start with some preliminary expressions/relations. Let $\boldsymbol{u}$ denote the fluctuating velocity field and U denote the unidirectional mean flow in direction x. We define the KHMH unsteadiness, advection and dissipation terms as:

$$\mathcal{A}_t(\boldsymbol{x},\boldsymbol{r},t) = \partial/\partial t(|\delta\boldsymbol{u}|^2); \tag{D.1a}$$

$$\mathcal{A}(\boldsymbol{x},\boldsymbol{r},t) = U\partial/\partial x(|\delta\boldsymbol{u}|^2); \tag{D.1b}$$

$$\epsilon^*(\boldsymbol{x},\boldsymbol{r},t) = 2\nu\big[(\partial u_i^+/\partial x_j^+)^2 + (\partial u_i^-/\partial x_j^-)^2\big]. \tag{D.1c}$$

Taylor's hypothesis states that $\partial/\partial t = -U\partial/\partial x$ when $u/U \ll 1$ where u is the $\boldsymbol{u}$ r.m.s. If we apply this transformation to the low-pass filtered time-derivative term, we have

$$\langle\mathcal{A}_t^a\rangle_{\boldsymbol{x}}^<(x,t) = \frac{\partial}{\partial t}\langle(|\delta\boldsymbol{u}|^2)^a\rangle_{\boldsymbol{x}}^<, \tag{D.2a}$$

$$= -U\frac{\partial}{\partial x}\langle(|\delta\boldsymbol{u}|^2)^a\rangle_{\boldsymbol{x}}^<, \tag{D.2b}$$

$$= -\langle\mathcal{A}^a\rangle_{\boldsymbol{x}}^<(x,t), \tag{D.2c}$$

(where $\mathcal{A}$ is the advection term). We rewrite similarly the following term as

$$\frac{1}{\langle\epsilon^*\rangle_{\boldsymbol{x}}^<}\frac{d\langle\epsilon^*\rangle_{\boldsymbol{x}}^<}{dt} = -U\frac{1}{\langle\epsilon^*\rangle_{\boldsymbol{x}}^<}\frac{d\langle\epsilon^*\rangle_{\boldsymbol{x}}^<}{dx}, \tag{D.3a}$$

$$= \frac{U}{L_\epsilon}, \tag{D.3b}$$

where $L_\epsilon(x,t) > 0$ is the dissipation length scale of change. We also rewrite the dissipation rate in terms of the velocity r.m.s., the integral length scale and the normalised dissipation coefficient

$$\langle\epsilon^*\rangle_{\boldsymbol{x}}^<(x,t) = C_\epsilon(x,t)\frac{u(x,t)^3}{L(x,t)}. \tag{D.4}$$

We only consider the first-order corrections to local equilibrium. If we use (D.2)-(D.3)-(D.4) in the expression for the non-equilibrium dynamics (5.32), we obtain at first-order

$$-\frac{\langle \mathcal{A}^a \rangle_{\boldsymbol{x}}^{<}(x,t)}{\langle \epsilon^* \rangle_{\boldsymbol{x}}^{<}(x,t)} \approx C_\tau \big(\frac{C_{\text{Kov}}}{C_\Pi C_\epsilon}\big)^{1/3} * (\frac{r_d}{L})^{2/3} * \frac{1}{u/U} * \frac{L}{L_\epsilon}. \tag{D.5}$$

This expression allows for a simple interpretation. The local delay reads (see (5.31))

$$\tau^* = C_\tau r_d^{2/3} * (C_{\text{Kov}}/C_\Pi)^{1/3} * (\langle \epsilon^* \rangle_{\boldsymbol{x}}^{<})^{-1/3} = C_\tau (C_{\text{Kov}}/(C_\Pi C_\epsilon))^{1/3} * (r_d/L)^{2/3} * L/u, \tag{D.6}$$

and the advection time scale reads $T_a \sim L_\epsilon/U$. It follows that the RHS of (D.5) is proportional to the ratio of the delay to the advection time scale τ^*/T_a. When this ratio is significant, we have a non-equilibrium cascade as the energy is advected more or similarly rapidly downstream as it is being cascaded to small scales. This expression can also be interpreted in terms of $x_{\tau^*}/L_\epsilon = \tau^* U/L_\epsilon$ where $x_{\tau^*} = \tau^* U$ is the distance the energy at scale r_d is advected before it is dissipated. If x_{τ^*} is similar or larger than L_ϵ, the cascade is in non-equilibrium. If $(C_{\text{Kov}}/C_\Pi)^{1/3}$ behaves as in forced homogeneous turbulence, the expression (D.5) have an approximate linear r_d-scaling (see figure 5.7(*a*)). This would be consistent with the grid turbulence experiments in Valente and Vassilicos (2015) where $\langle \mathcal{A} \rangle_t^a / \langle \epsilon^* \rangle_t \sim -0.1$ at $r_d/\langle L \rangle_t \sim 0.1$ and $\langle \mathcal{A} \rangle_t^a / \langle \epsilon^* \rangle_t \sim -1$ at $r_d/\langle L \rangle_t \sim 1$ (see their figure 11b). Moreover, in the initial downstream region the turbulence intensity u/U decreases from 6% to 3% over a relatively short distance (see figure 5 of Valente and Vassilicos (2014)) with a downstream increase in $-\langle \mathcal{A} \rangle_t^a / \langle \epsilon^* \rangle_t$ (see figure 11b of Valente and Vassilicos (2015)).

We use expressions (D.2)-(D.3)-(D.4) to express the energy scaling (5.33) as

$$\frac{\langle (|\delta \boldsymbol{u}|^2)^a \rangle_{\boldsymbol{x}}^{<}(x,t)}{u(x,t)^2} \approx \big(\frac{C_\epsilon C_\Pi}{C_{\text{Kov}}}\big)^{2/3} (\frac{r_d}{L})^{2/3} * \Big[1 + \frac{2}{3}(C_\tau - C_{\tau_u}) \big(\frac{C_{\text{Kov}}}{C_\Pi C_\epsilon}\big)^{1/3} * (\frac{r_d}{L})^{2/3} * \frac{1}{u/U} * \frac{L}{L_\epsilon}\Big]. \tag{D.7}$$

The first-order correction has the same interpretation as above. It is interesting that non-equilibrium is minimised in regions with high turbulence intensity. This behaviour is consistent with studies reporting a relatively clear $-5/3$ scaling of the energy spectrum in the very near field (with high turbulence intensity) and a less clear power-law behaviour downstream (with lower turbulence intensity) (Wissink and Rodi, 2008; Alves Portela et al., 2017). The expressions (D.5)-(D.7) seem to contain some non-trivial qualitative features of the cascade dynamics and energy scaling consistent with experimental/DNS results.

Finally, with regards to the dissipation scaling in grid turbulence (see Vassilicos (2015)), a similar argument can be applied as for freely decaying homogeneous/periodic turbulence in section 5.4. Note that the analogue to the time $t = 0$ in grid turbulence is the point x_0 where production effects first become negligible at large scales.